

Dissertation zur Erlangung des Doktorgrades  
der Fakultät für Chemie und Pharmazie  
der Ludwig-Maximilians-Universität München

Synthesis and Characterization of Triazine-Based  
Frameworks for Light-Driven Hydrogen Evolution

Katharina Schwinghammer  
aus  
Weilheim in OB, Deutschland  
2016



### Erklärung

Diese Dissertation wurde im Sinne von § 7 der Promotionsordnung vom 28. November 2011 von Frau Prof. Dr. Bettina V. Lotsch betreut.

### Eidesstattliche Versicherung

Diese Dissertation wurde eigenständig und ohne unerlaubte Hilfe erarbeitet.

Stuttgart, 31.05.2016

.....  
Katharina Schwinghammer

Dissertation eingereicht am

1. Gutachter:

2. Gutachter:

Mündliche Prüfung am

25.04.2016

Prof. Dr. Bettina V. Lotsch

Prof. Dr. Jürgen Senker

24.05.2016





*Für meine Eltern, Freunde und große Liebe*



## Danksagung

Mein tiefster Dank gilt meiner Doktormutter Prof. B. Lotsch, da sie mich in ihrem aufblühenden und herzlichen Arbeitskreis aufgenommen hat. Mit ihrem Ehrgeiz, ihrer Beharrlichkeit, ihrem Intellekt und auch ihrer Empathie hat sie mich während der Arbeit stets angespornt. Sie gilt für mich als Inspiration sowohl innerhalb als auch außerhalb der Institutsmauern. Ich möchte mich dafür bedanken, dass ich einerseits genug Freiraum hatte meinen Ideen nachzugehen und gleichzeitig immer die Möglichkeit hatte an ihre Bürotür zu klopfen um nach Rat zu fragen.

Prof. J. Senker danke ich für die Übernahme des Koreferats und für die erfolgreiche Zusammenarbeit während der letzten Jahre. Seine Expertise bezüglich der Festkörper-NMR-Spektroskopie, sein Equipment und sein Arbeitskreis – insbesondere seine überaus kompetente, ambitionierte und liebenswerte Doktorandin Maria Mesch – haben dieser Arbeit den nötigen Schliff gegeben. Ich hoffe für unsere neuen Doktoranden, dass unsere CN-Treffen weiterhin organisiert werden, da man so eine Menge voneinander lernen kann.

Prof. W. Schnick, Prof. C. Scheu, Prof. D. Johrendt und Prof. K. Karaghiosoff danke ich für die Bereitschaft, als weitere Prüfer zur Verfügung zu stehen.

Darüber hinaus möchte ich mich bei Dr. H. Klauk bedanken, da er als mein Zweitbetreuer für meine Arbeit und meine persönlichen Belange immer ein offenes Ohr hatte.

Ein besonderer Dank gilt:

- Meinen Mentoren Dr. Stephan Hug, Brian Tuffy und Dr. Vincent Lau. Alle drei haben sehr viel Zeit in meine Bildung investiert, obwohl sie es nicht mussten und vor allem deswegen bin ich ihnen zutiefst dankbar.
- Meinen Koautoren Brian Tuffy, Maria Mesch, Dr. Eva Wirnhier, Dr. Charlotte Martineau, Prof. Francis Taulelle, Dr. Christian Ziegler, Viola Duppel, Dr. Linus Stegbauer, Dr. Stephan Hug und Dr. D. Fischer.
- Meinen Praktikanten Frederik Broszeit, Peter Swekis, Christina Sondermann und Leonard Moser für ihre hart erbrachte Arbeit, ihre investierte Zeit, ihren Ehrgeiz, die schöne und erfolgreiche Zusammenarbeit und ihren Beistand.
- Meinen ehemaligen und momentanen Münchner Gruppenmitgliedern Dr. Stephan Hug, Dr. Sebastian Junggeburch, Dr. Hongji Wang, Dr. Ida Pavlichenko, Dr. Annekathrin Ranft, Dr. Erik Flügel, Dr. Linus Stegbauer, Dr. Christian Ziegler, Dr. Stephan Werner, Katalin Szendrei, Olaf Alberto von Mankowski, Dr. Li Shen und Dr. Cheng Li. Vor allem danke ich Ida und Anna, die ich für immer in meinem Herzen trage.
- Meiner zweiten „Mama“ und Freundin Claudia Kamella, Viola Duppel, Roland Eger, Willi Hölle, Friedrich Kögel und Prof. Jürgen Köhler für ihre liebevolle Aufnahme in unsere Gruppe in Stuttgart.

- Meinen weiteren Stuttgarter Kollegen Marie-Luise Schreiber, Daniel Weber, Dr. Vincent Lau (Dr. Meow Meow), Dr. Vijay Vyas, Primin Ganter, Xiuping Gao, Frederik Haase, Tanja Holzmann, Filip Podjaski, Dr. Leslie Schoop, Brian Tuffy, Dr. Olalla Sánchez-Sobrado und Dr. Alexander Kuhn. Sie haben mit mir die Höhen und Tiefen, die man während seiner Doktorarbeit durchlebt, durchlitten. Vor allem Tanja und Chrissi haben mir täglich die Sonnenseite des Lebens vor Augen geführt und meinen Alltag mit Monden, Sternen und anderen Himmelskörpern versüßt.
- Unserem Charmeur Dr. Reinhard Kremer und seiner Gruppe für die lustigen Anekdoten, wie auch anderen netten Bekanntschaften aus dem Institut.
- Marie-Luise Schreiber, Dr. Mitsuharu Konuma und Christine Stefani für die unzähligen Messungen, die sie für mich durchgeführt haben und Christoph Hohmann für mein Cover (<3).

Insbesondere danke ich meinen Freunden außerhalb des Instituts, die mich stets auf andere Gedanken gebracht haben, damit ich wieder genug Energie hatte, um mich auf die Arbeit zu konzentrieren.

Den größten Dank möchte ich jedoch meinen Eltern Gabriele und Georg und Vasilis widmen. Ohne ihre finanzielle wie auch seelische Stütze hätte ich dieses Langzeitprojekt nicht geschafft. Ich liebe euch von ganzem Herzen.

*Leider lässt sich eine wahrhafte Dankbarkeit mit Worten nicht ausdrücken.*

Johann Wolfgang von Goethe

*Probleme sind Gelegenheiten zu zeigen, was man kann.*

Edward Kennedy Ellington



# Content

Chapter I.....	1
1 Introduction .....	1
1.1 Fossil fuels and nuclear energy.....	1
1.2 Renewable energy.....	2
1.3 Alternative photocatalysts.....	8
Chapter II.....	15
2 Background .....	15
2.1 Carbon nitrides.....	15
2.2 Challenges in photocatalysis.....	33
2.3 Covalent organic frameworks as photocatalysts.....	35
2.4 Project aims.....	36
Chapter III .....	47
3 Poly(triazine imide) as photocatalyst.....	47
3.1 Co-polymerization of PTI .....	47
3.2 Surface engineering through exfoliation .....	59
3.3 Investigations on the catalytically relevant sites of PTI .....	68
Chapter IV .....	83
4 Covalent organic frameworks .....	83
4.1 TFPT-COF as photocatalyst.....	83
4.2 Oligomers of the archetype covalent-triazine framework CTF-1 .....	93
Chapter V .....	111
5 Summary .....	111
5.1 PTI/LiCl as a new triazine-based 2D carbon nitride photocatalyst .....	111
5.2 Rational design of a photocatalytically active COF .....	115
5.3 Polymerization degree & photocatalytic activity illustrated on CTF-1.....	116

Chapter VI.....	119
6 Conclusion and Outlook .....	119
Chapter VII .....	125
7 Appendix.....	125
7.1 Supporting information.....	125
7.2 Photocatalysis – calculations.....	196
7.3 List of publications and statement of contribution.....	203
7.4 Contributions to conferences .....	207
7.5 List of abbreviations .....	208



# Chapter I

## 1 Introduction

Ever since the dawn of mankind, energy carriers were required to keep people warm, safe and supplied with food. To fulfill their needs, biomass in the form of plants and bones was sufficient for a very long time. The combustion of biomass did not have any negative effect on the environment. The carbon dioxide which was released to nature was reabsorbed into plants to produce energy-rich organic carbohydrates through photosynthesis.

With the invention of the first steam engine in 1698 and the start of the industrial revolution, high efficiency energy carriers in the form of fossil fuels (coal, oil and gas) were used to cover the world's energy consumption.<sup>1</sup> With the increasing energy consumption and the deforestation, the carbon dioxide level of the atmosphere rose, resulting in a dangerous warming of the globe.

Paradoxically, the energy consumption not only increases with the human population but with the efficiency of an engine as reported by *W. S. Jevons*.<sup>1,2</sup> In detail, in the year 1860 the world consumed  $5 \cdot 10^{12}$  kWh yr<sup>-1</sup> with a global population of 1.2 billion.<sup>1,3</sup> Nowadays, 7.1 billion people live on earth and consume  $156 \cdot 10^{12}$  kWh yr<sup>-1</sup>.<sup>4,5</sup> While the population increased about six times, the energy demand grew by a factor of 30, which can be explained by higher energy efficiency leading to cheaper energy usage, and an increase in economic growth.<sup>1,6</sup>

### 1.1 Fossil fuels and nuclear energy

As fossil fuels are products of dead organisms which naturally decompose over millions of years, their depletion is much faster than new ones are created. Still, 82 % of energy used nowadays can be traced back to fossil fuels, which can be considered as a primary energy source.<sup>7</sup> While biomass and mineral coals were used exclusively at the beginning of the industrialization period,<sup>1</sup> crude oil represents the biggest share currently with natural gas having an increasing share.<sup>1,8</sup> The need for replacement of coal is attributed to environmental concerns since its combustion gives rise to the highest emission of carbon dioxide and other pollutants within fossil fuels.<sup>7,9</sup> Carbon dioxide accounts for 9 % – 26 % of the greenhouse effect and is mainly responsible for global warming.<sup>10</sup> Crude oil, as a flexible and easy to transport fuel, is indispensable for petrochemical industries and the

leading tradable commodity. However, the price range has a high volatility which is due to the large geopolitical tensions in the areas of greatest reserves (e.g. Venezuela, Saudi Arabia, Iran, and Iraq). Natural gas is the cleanest of fossil fuels with increasing proven reserves and is efficient enough for power generation. Nonetheless, the long supply routes of natural gas require high cost of infrastructure.

Already in 1954, the first nuclear reactor was commissioned and the nuclear industry started. Nuclear energy seems to solve energy and environmental problems as no carbon dioxide is produced, while at the same time it is a very efficient energy source.<sup>7</sup> Several grave nuclear power plant accidents including the *Three Mile Island* accident in 1979, the *Chernobyl* disaster in 1986 or the latest *Fukushima Daiichi* nuclear disaster in 2011, as well as concerns about the final waste disposal are the reasons why other zero-emission energy sources have to be explored.<sup>7</sup> The next chapter introduces one promising candidate for the generation of zero-emission fuel.

## 1.2 Renewable energy

The extract from *L'Île mystérieuse* (shown below) affirms that already in the 19<sup>th</sup> century people worried about running out of fossil fuels. This emphasizes that a drastic change in the energy economy from fossil fuels and nuclear power to renewable energy carriers is indispensable and should be tackled as long as fossil fuels are still available.<sup>1</sup>

*“One day all the coal will be used up. What will they burn in the place of coal?”*  
*“Water,” replied Cyrus Smith. “but decomposed into its basic elements. Water will be employed as a fuel, hydrogen and oxygen will furnish an inexhaustible source of heat and light. As long as this earth is inhabited, it will provide for the needs of its inhabitants. Water is the coal of the future.”*

*L'Île mystérieuse (J. Verne, 1874)*

Renewable energy comes from infinite resources such as rain, wind, tides, waves, geothermal heat and sunlight, and contributes currently 19 % of our global energy generation based on *REN21's 2014* report.<sup>11,12</sup> Commonly, these forms of energy are immediately converted into heat and electricity. However, these sources deliver a power flow that varies according to the daily and seasonal cycles. Therefore, the storage in the form of synthetic energy carriers such as hydrogen or hydrocarbons is needed which also makes their transport to consumers easier.

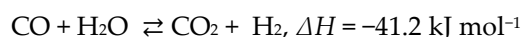
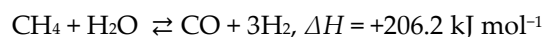
### 1.2.1 Hydrogen

Hydrogen is an ideal alternative energy carrier due to its high specific energy of 142 MJ kg<sup>-1</sup> (compared to coal: 15 MJ kg<sup>-1</sup> – 33 MJ kg<sup>-1</sup>)<sup>13</sup> which originates from its low molecular weight and its strong covalent binding (bond dissociation energy: 436 kJ mol<sup>-1</sup>).<sup>14,15</sup> Hydrogen oxidizes to water when combusted which justifies its designation as green energy

source. In addition, no living matter is needed for the generation of hydrogen which allows large scale production in a very short period of time.<sup>1,16</sup> However, safety issues and storage problems still cast a shadow over hydrogen as the future fuel.<sup>1</sup>

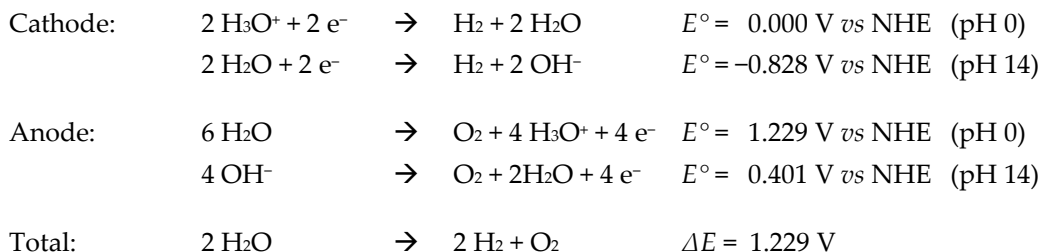
#### Exemplary routes for hydrogen generation:

- In small scale, hydrogen can be formed by adding diluted acids or water to base metals (*e.g.* Zn) or alkali metals (*e.g.* Li) (redox reaction).<sup>17</sup>
- The crudest way to produce hydrogen is to heat water above 3730 °C, where water dissociates to molecular and atomic hydrogen, oxygen and hydroxyl ions (thermal decomposition).<sup>18</sup> This route is considered dangerous for large scale production, since at such extreme temperatures hydrogen and oxygen cannot be separated quickly enough.<sup>1,16</sup>
- In industry, hydrogen is commonly generated by steam reforming in a two-step process (see reaction below). In the presence of a metal-based catalyst (such as Ni) and at high temperatures (700 °C – 1100 °C) and pressure, hydrocarbons (*e.g.* methane) are converted to hydrogen in excess of steam. To increase the hydrogen yield, carbon monoxide (the byproduct from the first reaction) is exposed to more steam to form additional hydrogen (water-gas shift reaction) and carbon dioxide.<sup>19,20</sup>



- While steam reforming is usually applied for low-boiling crude oil fractions, the partial oxidation approach exploits the high-boiling ones. In both cases, toxic carbon monoxide is formed as a side-product.<sup>19-21</sup>
- In the 1980s, the Norwegian company *Kværner* developed a way to dissociate hydrocarbons to hydrogen and pure carbon (rather than carbon dioxide) within a plasma oven at 1600 °C.<sup>22-24</sup> Waste heat-induced hydrogen formation is efficient for industrial applications. However, this method seems dangerous and disadvantageous when applied on a small scale (*e.g.* hydrogen car) due to the necessary high temperatures.<sup>1,16</sup>
- High temperatures and carbon monoxide can be avoided by means of electrolysis (see reaction below). Here, electricity is used to endothermically split water into hydrogen and oxygen in the presence of an electrocatalyst in the stoichiometric ratio of 2:1 ( $\Delta H^0 = +571.8 \text{ kJ mol}^{-1}$  at  $T = 25 \text{ °C}$ ,  $p = 1.013 \times 10^5 \text{ Pa}$ ).<sup>25-27</sup> Currently, yield efficiencies of over 80 % are reached in industry (basic 25 % – 30 % KOH solution,  $T = 70 \text{ °C} - 90 \text{ °C}$ , 1.90 V, 0.15 A cm<sup>-2</sup> – 0.5 A cm<sup>-2</sup>).<sup>25-27</sup>

The standard electrode potentials ( $E^0$ ) presented here are given in reference to the normal hydrogen electrode (NHE), where the potential of the H<sup>+</sup>/H<sub>2</sub> redox couple (pH 0) is defined as the zero-point.



In detail, the reference cathode is a platinum electrode flushed with hydrogen gas at atmospheric pressure and at a temperature of 298.15 K. 1 mol L<sup>-1</sup> HCl is used as electrolyte. This leads to an adsorption of the hydrogen molecules on the platinum's surface. At constant temperature and pressure, the electrode potentials ( $E$ ) still depend on the pH values according to the *Nernst equation*<sup>27</sup> (equation 1). Here,  $R$  denotes the molar gas constant  $R = 8.31447 \text{ J mol}^{-1} \text{ K}^{-1}$ ,  $T$  the absolute temperature in K (298.15 K),  $z_e$  the number of transferred electrons,  $F$  the Faraday constant ( $F = 96385.34 \text{ C mol}^{-1}$ ),  $a$  the activity of the redox-couple and  $c$  (and  $d$ ) the prefactor of the oxidation (reduction) site.

$$\begin{aligned}
 E &= E^\circ + \frac{RT}{z_e F} \ln \frac{(a_{\text{Ox}})^c}{(a_{\text{Red}})^d} = E^\circ + \frac{0.059 \text{ V}}{z_e} \log_{10} \frac{(a_{\text{Ox}})^c}{(a_{\text{Red}})^d} \approx E^\circ + \frac{0.059 \text{ V}}{z_e} \lg \frac{(c_{\text{Ox}})^c}{(c_{\text{Red}})^d} \\
 &= 0 + \frac{0.059 \text{ V}}{2} \lg \frac{(\text{H}_3\text{O}^+)^2}{(\text{H}_2)^1} = 0 + 0.059 \text{ V} \cdot \lg(c(\text{H}_3\text{O}^+)) = -0.059 \text{ V pH} \quad (1)
 \end{aligned}$$

The presented list above shows that nowadays, hydrogen can be successfully produced on a large scale. However, hydrogen can only be considered as a renewable energy carrier when it is produced either directly or indirectly from a renewable source such as solar, hydro or wind power.<sup>1,16</sup> The next chapter explains the light-driven formation of hydrogen by water reduction.

### 1.2.2 Photocatalytic water splitting

The necessity of heat or electricity points out that energy is required for water splitting.<sup>28</sup> In 1972, *Hondo and Fujishima*<sup>29</sup> demonstrated on a single-crystal rutile TiO<sub>2</sub> photo anode and a platinum cathode that electrochemical water splitting can be catalyzed by the illumination with UV-light (Figure 1.1). TiO<sub>2</sub> as a typical semiconductor exhibits a valence and a conduction band which are separated by an energy gap of 3.0 eV – 3.2 eV (anatase: 3.2 eV, brookite: 3.1 eV and rutile: 3.0 eV).<sup>30-34</sup> When TiO<sub>2</sub> is illuminated by light with energies  $\geq 3.0 \text{ eV}$ , electrons of the valence band can be promoted to the conduction band level while leaving “holes” behind. Unfortunately, the photo-generated electrons quickly recombine with the holes and release the energy in the form of unproductive heat or photons. However, once an anodic potential is applied through an external circuit, the excited electrons migrate through the bulk to reach the platinum counter electrode. Here, these electrons are good reducing agents and can reduce water/protons to molecular hydrogen. This is only possible because the conduction band of TiO<sub>2</sub> is more negative (anatase:  $-0.29 \text{ V vs NHE}$  at pH 0)<sup>35</sup> than the reduction energy level of water ( $0.00 \text{ V vs NHE}$  at pH

0). Concurrently, the holes in the valence band can oxidize water/hydroxyl ions to hydroxyl radicals, reactive oxygen species or oxygen on the surface of the TiO<sub>2</sub> photoelectrode since the valence band is more positive (anatase: 2.91 V *vs* NHE at pH 0) than the oxidation energy level of water (1.23 V *vs* NHE at pH 0).<sup>28,29,35-38</sup>

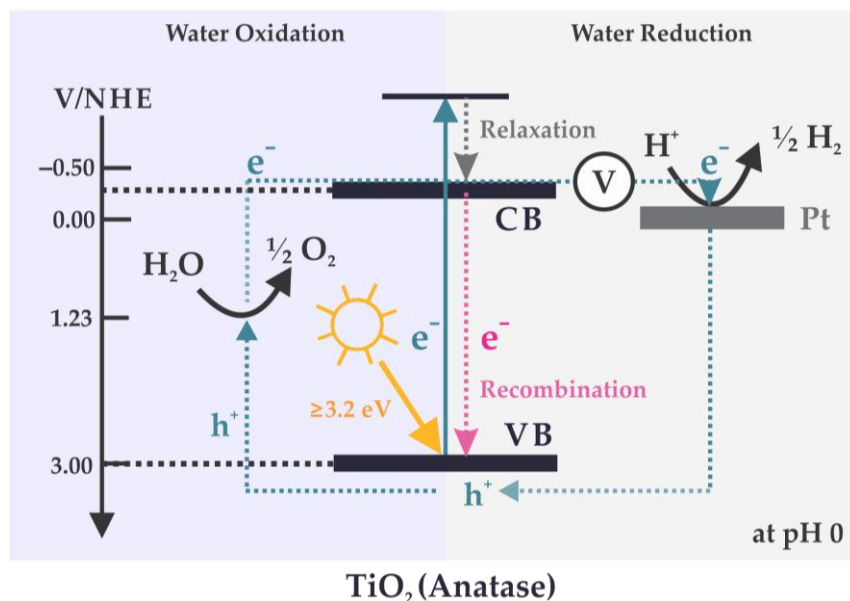


**Figure 1.1** Schematic photoelectrochemical splitting of water into hydrogen and oxygen with the help of TiO<sub>2</sub> and an external circuit which hinders charge recombination (magenta).

TiO<sub>2</sub> particulates by themselves cannot photocatalytically evolve hydrogen due to the large overpotential on their surface. To solve this problem, the TiO<sub>2</sub> surface can be loaded with co-catalysts of noble metals such as platinum.<sup>35</sup> Noble metals are preferably used as co-catalysts due to their high exchange current densities  $i_0$  (in A m<sup>-2</sup>) and low *Tafel slope* values  $A$  (in V) which results in low overpotentials ( $\Delta V$ ) (see *Tafel equation* (2);  $i$ : current density in A m<sup>-2</sup>).<sup>39</sup> The exchange current density can be considered as the spontaneous reaction rate between H<sup>+</sup>/H<sub>2</sub> at equilibrium and, thus, represents the inherent activity of the catalyst. The *Tafel slope* displays the voltage increase needed to increase the current by an order of magnitude.<sup>39</sup>

$$\Delta V = A \times \ln\left(\frac{i}{i_0}\right) \quad (2)$$

Platinum requires the lowest overpotential, which is the reason why it is the most widely used hydrogen evolution co-catalyst.<sup>35</sup> A co-catalyst can thus serve as active site for the hydrogen production on the photocatalyst's surface (Figure 1.2).<sup>35</sup> Additionally, co-catalysts can also trap excited electrons due to a larger driving force caused by their larger work functions (e.g. Pt: 1.21 V *vs* NHE at pH 0)<sup>35</sup> compared to the semiconductor (TiO<sub>2</sub>: -0.29 V *vs* NHE at pH 0).<sup>35</sup> Often, this phenomenon is described by the formation of a Schottky barrier at the metal/TiO<sub>2</sub> interface.<sup>35</sup> Here, electrons migrate from the TiO<sub>2</sub> surface to the noble metal until a thermodynamic equilibrium is reached, *i.e.* until their Fermi levels are aligned. The photoinduced electrons can shift the Fermi levels of TiO<sub>2</sub>

which leads to a continuous migration of the electrons from TiO<sub>2</sub> to the noble metal where they react with water. The photoinduced hole is then free to diffuse to the TiO<sub>2</sub> surface and the electron-hole-recombination is suppressed.<sup>35</sup> However, this holds true only for large platinum particles or films. If the diameters of the metal particles are similar to the depletion width of the semiconductor (as it is in our case here), the semiconductor/liquid junction dominates the band bending in the semiconductor and not the co-catalyst.<sup>40</sup> In addition, the surface plasmon resonances of the nanoparticulate noble metals can further excite electrons which are located either at the metal or semiconductor (CB) site and contribute to the photocatalytic activity.<sup>41-43</sup> Nevertheless, noble metals are expensive and non-abundant. Further, Pt (for instance) can catalyze the backward reaction of H<sub>2</sub> and O<sub>2</sub> to water which leads to lower efficiencies. Current research focuses on more ecologically benign, efficient, durable and cost-effective co-catalysts such as NiO<sub>x</sub>,<sup>42,44-48</sup> MoS<sub>2</sub>,<sup>49</sup> RuO<sub>x</sub><sup>42,44,50-54</sup> or molecular metal complexes which allow better charge transfer.<sup>55-62</sup>

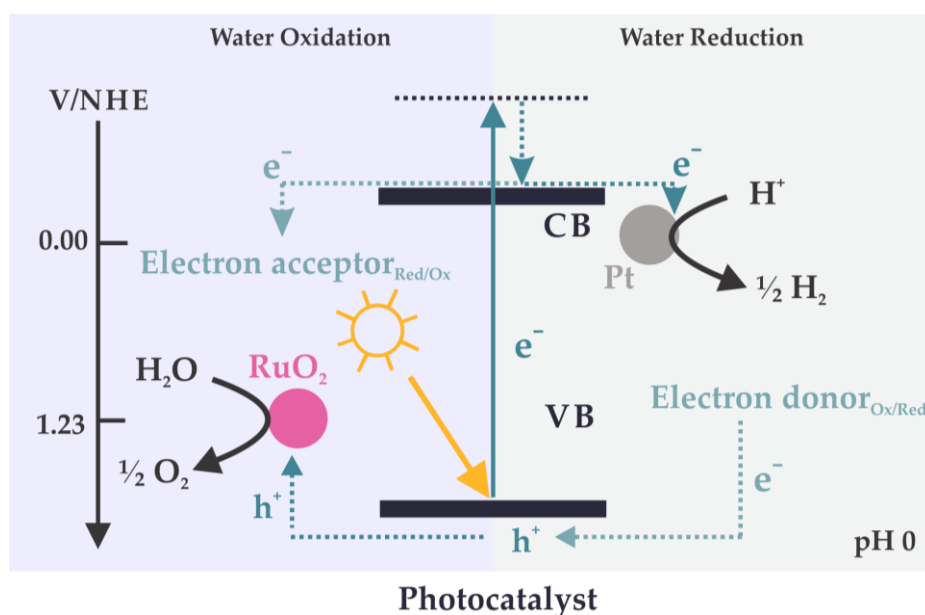


**Figure 1.2** Schematic showing the photocatalytic splitting of water into hydrogen and oxygen with the help of co-catalysts and sacrificial agents. The violet tinted region presents the water oxidation mechanism. The right side shows the water reduction process.

Charge recombination can be further suppressed by the addition of suitable sacrificial agents. In the case of water reduction/oxidation, electron donors/acceptors which are more easily oxidized/reduced compared to water are used (Figure 1.2). These molecular compounds react irreversibly with the photogenerated holes/electrons instead of water. Hence, a direct recombination of the charges can be avoided and the remaining charges more easily react with water. Since the sacrificial agents are consumed, a continuous addition is required to sustain gas evolution.<sup>35</sup> The addition of such sacrificial agents allows to decouple the water oxidation and reduction process and, for instance, to study the reduction process as the rate-limiting step.<sup>63</sup> Commonly, organic compounds such as triethanolamine (TEoA or TEA), methanol (MeOH), ethanol, lactic acid, sodium ascorbate,

formaldehyde, and EDTA are used as electron donors. In the case of chalcogenide photocatalyst systems, also sulfide ions such as  $S^{2-}$  and  $SO_3^{2-}$  are used as well to prevent corrosion of the chalcogenide itself.<sup>65</sup> The oxidation potential of the electron donors has an influence on the hydrogen production efficiency (Figure 1.3). The more negative the redox potential of the electron donor, the more efficient the hydrogen production.<sup>64</sup> For instance, using triethanolamine in a photocatalytic system typically leads to higher hydrogen evolution rates compared to MeOH since the driving force for accepting the “hole” on the photoexcited catalyst is enhanced.<sup>64</sup> Note, however, that since the oxidation potentials of commonly used electron donors such as TEOA are higher than the potential for  $H^+/H_2$ , the occurring reactions are not of endothermic nature anymore. The sacrificial agent has further an influence on the pH conditions of the photocatalytic system which directly influences the redox potentials of the photocatalyst (see *Nernst* equation, Chapter 1.2.1). With TEOA a basic environment can be created (pH 10-11; 10 vol% aqueous TEOA solution) while MeOH leads to a neutral or slightly acidic conditions (pH 6; 10 vol%).

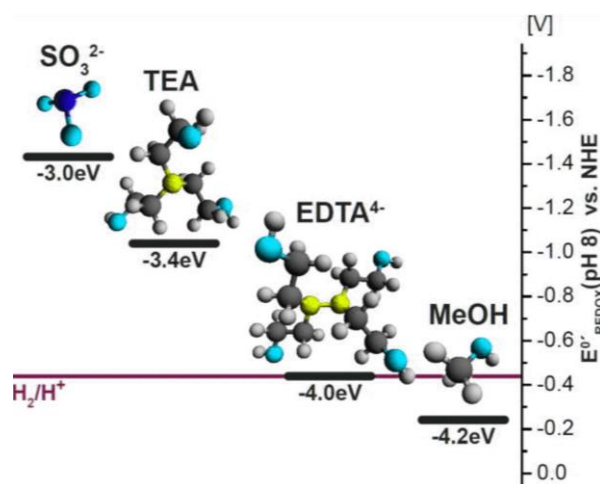


**Figure 1.3** Redox potentials of some commonly used electron donors. Adapted with permission from the reference.<sup>64</sup> Copyright 2012, AIP Publishing LLC.

For high water oxidation efficiencies, suitable electron acceptors are necessary, such as silver nitrate ( $AgNO_3$ ) and sodium persulfate ( $Na_2S_2O_8$ ).<sup>65-67</sup> In the best case, environmental pollutants are chosen as sacrificial agents which are decomposed while hydrogen/oxygen is produced photocatalytically. Some of these sacrificial agents have to be chosen with caution. For instance, it is known that TEOA is light sensitive and may form photoactive charge transfer complexes with some photocatalysts constructed on nitrogen-containing heterocycles (which are used as photocatalysts in this work, see Chapter 2).<sup>68-70</sup> In addition, the oxidation of triethanolamine or other alcohols leads to the formation of radicals (Figure 1.4). When these radicals are further oxidized by directly injecting an electron either into the conduction band of the photocatalyst or directly to the platinum centers, then extra electrons are located in the excited state. These electrons can also reduce water and form hydrogen which is not due to the action of the photocatalyst. The detected photocatalytic activity of the photocatalyst might not be reflective of the true performance of the photocatalyst, also known as the current doubling effect.<sup>71,72</sup>

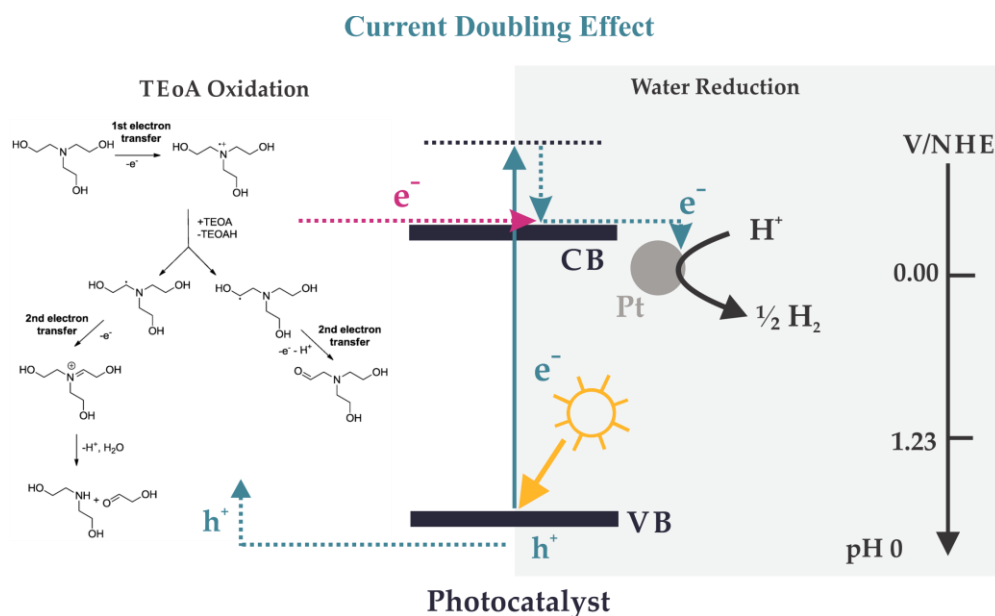


**Figure 1.4** TEoA oxidation can lead to an extra electron in the conduction band of the photocatalysts and thus, higher amount of produced hydrogen. The suggested reaction sequence for the oxidation of TEoA is reprinted from the reference.<sup>69</sup>

### 1.3 Alternative photocatalysts

Until now,  $\text{TiO}_2$  (mostly in the form of anatase or anatase–rutile mixtures, *e.g.* the commercially available P25)<sup>73</sup> is widely used as a photocatalyst due to its abundance, long-term stability, sustainability and low-cost production.<sup>33,35,44,73-75</sup> Its large band gap of  $3.0 \text{ eV} - 3.2 \text{ eV}$ <sup>31,33,34</sup> demands that  $\text{TiO}_2$  must be illuminated with UV-light, which contributes only 3 % – 6 % to the solar spectrum at sea level (Figure 1.3).<sup>28,76</sup>

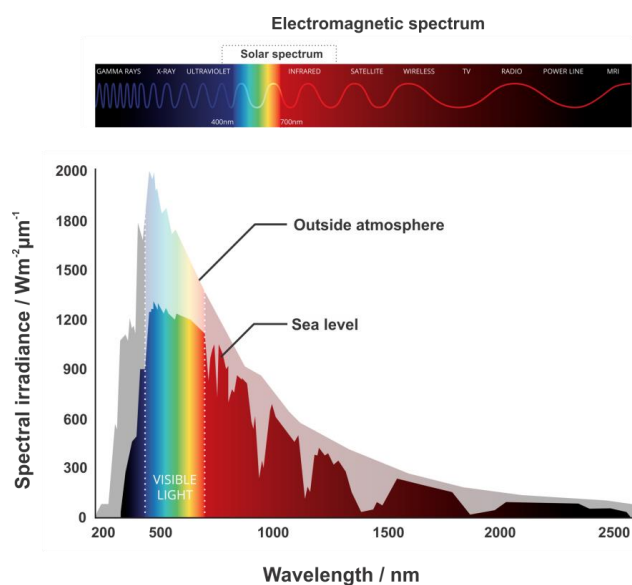


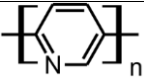
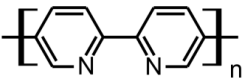
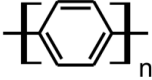
**Figure 1.3** Electromagnetic spectrum from gamma rays to radio frequencies (top). Solar spectrum outside the atmosphere and at sea level (bottom). The region of visible light is highlighted. Adapted with permission from Nate Christopher / Fondriest Environmental.<sup>77</sup>



However, about 50 % of the solar energy derives from visible light, so an ideal photocatalyst should exhibit a band gap lower than 3 eV to work efficiently with solar light.<sup>28,44</sup> At the same time, the band gap should be wider than 1.23 eV to fulfil the thermodynamic requirements for photocatalytic water splitting (see Chapter 1.2.1) and actually even larger than 2 eV to accumulate sufficient driving force to overcome the overpotential.<sup>44</sup> Hence, semiconductors with a band gap between 2 eV and 3 eV are needed for photocatalytic water splitting. In the literature, this is often realized by simply optimizing the band gap of TiO<sub>2</sub>.<sup>44</sup> However, band gap tuning of TiO<sub>2</sub> is limited (with regards to adjusting the band levels), therefore the development of novel photocatalysts are a focal point in modern materials chemistry. A plethora of alternative photocatalysts are known which can generally be classified into inorganic (*e.g.* d<sup>0</sup> metal oxides: Ti<sup>4+</sup>, Zr<sup>4+</sup> and Nb<sup>5+</sup>, d<sup>10</sup>: In<sup>3+</sup>, Ga<sup>3+</sup> and Ge<sup>4+</sup>; f<sup>0</sup> metal oxides: Ce<sup>4+</sup>; non-oxides: InP, GaN and β-Ge<sub>3</sub>N<sub>4</sub>; (oxy)sulfides: ZnS and CdS)<sup>28,44</sup> and organic compounds (which will be discussed in the following).<sup>67,78-87</sup>

These organic photocatalysts can achieve high hydrogen evolution rates. However, only a low amount of oxygen is usually detected since the oxidation of water requires four electrons compared to the water reduction which is a two-electron process. Due to the complexity (which involves the kinetically demanding consecutive transfer of four electrons and also a rearrangement of multiple bonds and the formation of the O-O bond) and the high oxidation potential required to oxidize water, this half reaction is currently considered to be the bottleneck for organic photocatalytic systems. For successful water oxidation, organic photocatalysts are required with valence bands providing sufficient overpotential. In addition, high-energy intermediates are formed during the water oxidation process which can damage and degrade the photocatalyst itself.<sup>88</sup> Therefore, it is crucial to compare the photocatalyst before and after the photocatalytic process to ensure its integrity. The benefits of organic-based photocatalysts lie in their accessibility, abundance, light weight, and relatively facile band gap tuning. The idea of using organic materials for photocatalysis dates back to early investigations on semiconducting polymers such as poly(pyridine-2,5-diyl) (PPD),<sup>82</sup> poly(2,2'-bipyridine-5,5'-diyl) (PBPD)<sup>81</sup> and poly(*p*-phenylene) (PPP)<sup>83</sup> (see Table 1.1) which clearly suffered from low long-term stability. Still, the research on these polymers carried on, resulting in optimized 1D polymeric photocatalysts producing up to 3680 μmol H<sub>2</sub> per hour per gram recently.<sup>89</sup> Also, co-polymers of benzene and pyrene building-blocks have recently been identified as attractive photocatalysts.<sup>80,84,86,87</sup> However, the most established organic photocatalysts remain the carbon nitrides, which will be presented in detail in Chapter 2.1. In addition, this thesis introduces the most recent organic photocatalytic system, the covalent organic frameworks (COFs) (Chapter 2.2).

**Table 1.1** Photocatalytic results for hydrogen evolution of the above mentioned organic polymers and the conditions under which they have been tested.

photocatalyst	co-catalyst	electron donor	illumination wavelength	activity
 PPD, ref. <sup>82</sup>	RuCl <sub>3</sub>	MeOH- triethylamine	>400 nm	~250 μmol H <sub>2</sub> h <sup>-1</sup> g <sup>-1</sup> ; 0.21 % (450 nm)
 PBPD, ref. <sup>81</sup>	[Pt(bpy) <sub>2</sub> ](NO <sub>3</sub> ) <sub>2</sub> · H <sub>2</sub> O	MeOH- triethylamine	>320 nm	TON/Pt: 490
 PPP, ref. <sup>83</sup>	—	diethylamine	>290 nm	~104 μmol H <sub>2</sub> h <sup>-1</sup> g <sup>-1</sup>
fluorene-type polymers, ref. <sup>89</sup>	possibly Pd-traces; no additional co-catalyst	MeOH- triethylamine	>420 nm	≤3680 μmol H <sub>2</sub> h <sup>-1</sup> g <sup>-1</sup> 2.3 % (420 nm)
pyrene-type co-polymers, ref. <sup>86</sup>	possibly Pd-traces; no additional co-catalyst	diethylamine	visible light	>170 μmol H <sub>2</sub> h <sup>-1</sup> g <sup>-1</sup>

## Bibliography

- (1) A. Züttel, A. Remhof, A. Borgschulte, O. Friedrichs, *Philos. Trans. Roy. Soc. Ser. A* **2010**, 368, 3329.
- (2) W. S. Jevons, *The Coal Question: An Inquiry Concerning the Progress of the Nation, and the Probable Exhaustion of Our Coal-Mines*, (1866) 2<sup>nd</sup> ed., London: Macmillan and Co, **1865**.
- (3) M. Kremer, *Q. J. Econ.* **1993**, 108, 681.
- (4) *World Population Prospects: The 2012 Revision*, UN, Dept. of Economic and Social Affairs, Population Division, **2013**.
- (5) International Energy Agency, *Key World Energy Statistics: 2014*.
- (6) H. D. Saunders, *Energ. J.* **1992**, 13, 1944.
- (7) *World Energy Council, WEC Survey of Energy Resources 1995, World Energy Resources 2013 and WEC World Energy Scenarios to 2050*, **2013**.
- (8) *Statistical Review of World Energy*, BP, London, **2013**.
- (9) *CO<sub>2</sub> Emission from Fuel Combustion - Highlights*, International Energy Agency, , **2014**.
- (10) J. T. Kiehl, K. E. Trendberth, *Bull. Amer. Meteor. Soc.* **1997**, 78, 197.
- (11) O. Ellabban, H. Abu-Rub, F. Blaabjerg, *Renew. Sust. Energ. Rev.* **2014**, 39, 748.
- (12) *REN21 - Renewable Energy Policy Network for the 21<sup>st</sup> Century*, Institute for Sustainable Energy Policies, **2014**.
- (13) B. Cooper, *The Science and Technology of Coal and Coal Utilization*, 1<sup>st</sup> ed., Springer US, **1984**.
- (14) U. Bossel, B. Eliasson, *Energy and The Hydrogen Economy*, **2003**.
- (15) G. Herzberg, A. Monfils, *J. Mol. Spectr.* **1960**, 5, 482.

- (16) A. Züttel, A. Borgschulte, L. Schlapbach, *Hydrogen as a Future Energy Carrier*, Wiley-VCH Verlag GmbH & Co. KGaA: Weinheim, **2008**.
- (17) J. Strähle, E. Schweda, *Lehrbuch der analytischen und präparativen anorganischen Chemie*, 15<sup>th</sup> ed., S. Hirzel Verlag Stuttgart: Leipzig, **2002**.
- (18) A. Steinfeld, R. Palumbo, *Solar thermochemical process technology*, NY: Academic Press: New York, **2001**; Vol. 15.
- (19) N. W. Johanson, M. H. Spritzer, G. T. Hong, W. S. Rickman, *2001 U.S. DOE Hydrogen Program Review*, National Renewable Energy Laboratory: Baltimore, Maryland, **2001**.
- (20) M. A. Alaa-Eldin, J. R. Grace, C. J. Lim, S. S. Elnashaie, *US Patent* **1994**; Vol. 5,326,550.
- (21) L. Hartmann, K. Lucka, H. Köhne, *J. Power Sources* **2003**, 118, 286.
- (22) S. Lynam, J. Hugdahl, R. Hildrum, *Carbon Black World* Nice, France, **1996**.
- (23) L. Fulcheri, Y. Schwob, *Int. J. Hydrogen Energy* **1995**, 20, 197.
- (24) B. Gaudernack, S. Lynam, *Int. J. Hydrogen Energy* **1998**, 23, 1087.
- (25) G. Sandstede, *Möglichkeiten zur Wasserstoff-Erzeugung mit verminderter Kohlendioxid-Emission für zukünftige Energiesysteme*, VCH-Verlagsgesellschaft Weinheim: Weinheim, **1993**; Vol. 63.
- (26) C. J. Winter, J. Nitsch, *Wasserstoff als Energieträger: Technik, Systeme, Wirtschaft*, Springer Verlag Berlin Heidelberg, **1986**.
- (27) P. W. Atkins, J. d. Paula, *Physikalische Chemie*, 4<sup>th</sup> ed., Wiley-VCH Verlag GmbH & Co. KGaA: Weinheim, **2006**.
- (28) T. Hisatomi, J. Kubota, K. Domen, *Chem. Soc. Rev.* **2014**, 43, 7520.
- (29) A. Fujishima, K. Honda, *Nature* **1972**, 238, 37.
- (30) A. D. Paola, M. Bellardita, L. Palmisano, *Catalysts* **2013**, 3, 36.
- (31) D. O. Scanlon, C. W. Dunnill, J. Buckeridge, S. A. Shevlin, A. J. Logsdail, S. M. Woodley, C. R. A. Catlow, M. J. Powell, R. G. Palgrave, I. P. Parkin, G. W. Watson, T. W. Keal, P. Sherwood, A. Walsh, A. A. Sokol, *Nat. Mater.* **2013**, 12, 798.
- (32) D. Reyes-Coronado, G. Rodríguez-Gattorno, M. E. Espinosa-Pesqueira, C. Cab, R. d. Coss, G. Oskam, *Nanotechnology* **2008**, 19, 145605.
- (33) M. Anpo, *Environmentally Benign Photocatalysts: Applications of Titanium Oxide-based Materials*, Springer: New York, **2010**.
- (34) M. Landmann, E. Rauls, W. G. Schmidt, *J. Phys.: Condens. Matter* **2012**, 24, 195503.
- (35) D. Y. C. Leung, X. Fu, C. Wang, M. Ni, M. K. H. Leung, X. Wang, X. Fu, *ChemSusChem* **2010**, 3, 681.
- (36) M. S. Wrighton, *Acc. Chem. Res.* **1979**, 12, 303.
- (37) A. J. Bard, *Science* **1980**, 207, 139.
- (38) J. M. Coronado, F. Fresno, M. D. Hernández-Alonso, *Design of Advanced Photocatalytic Materials for Energy and Environmental Applications*, Springer: London, **2013**.
- (39) P. C. K. Vesborg, B. Seger, I. Chorkendorff, *J. Phys. Chem. Lett.* **2015**, 6, 951.
- (40) M. G. Walter, E. L. Warren, J. R. McKone, S. W. Boettcher, Q. Mi, E. A. Santori, N. S. Lewis, *Chem. Rev.* **2010**, 110, 6446.
- (41) Z. Zhao, Y. Sun, F. Dong, *Nanoscale* **2015**, 7, 15.
- (42) J. Yang, D. Wang, H. Han, C. Li, *Acc. Chem. Res.* **2013**, 46, 1900.

- (43) [http://www.pro-physik.de/details/news/8230601/Direkter\\_Elektronentransfer\\_durch\\_Plasmonen.html](http://www.pro-physik.de/details/news/8230601/Direkter_Elektronentransfer_durch_Plasmonen.html), accessed on 1<sup>st</sup> of February 2016.
- (44) X. Chen, S. Shen, L. Guo, S. S. Mao, *Chem. Rev.* **2010**, *110*, 6503.
- (45) C.-C. Hu, H. Teng, *J. Catal.* **2010**, *272*, 1.
- (46) S. H. Kim, J.-H. Kang, S.-W. Ryu, *J. Nanosci. Nanotechnol.* **2014**, *14*, 7903.
- (47) K. Domen, S. Naito, T. Onishi, K. Tamaru, M. Soma, *J. Phys. Chem.* **1982**, *86*, 3657.
- (48) T. Sreethawong, Y. Suzuki, S. Yoshikawa, *Int. J. Hydrogen Energy* **2005**, *30*, 1053.
- (49) X. Zong, H. Yan, G. Wu, G. Ma, F. Wen, L. Wang, C. Li, *J. Am. Chem. Soc.* **2008**, *130*, 7176.
- (50) Y. Ebina, N. Sakai, T. Sasaki, *J. Phys. Chem. B* **2005**, *109*, 17212.
- (51) H. Kadowaki, N. Saito, H. Nishiyama, H. Kobayashi, Y. Shimodaira, Y. Inoue, *J. Phys. Chem. C* **2007**, *111*, 439.
- (52) N. Arai, N. Saito, H. Nishiyama, Y. Shimodaira, H. Kobayashi, Y. Inoue, K. Sato, *J. Phys. Chem. C* **2008**, *112*, 5000.
- (53) J. Sato, N. Saito, Y. Yamada, K. Maeda, T. Takata, J. N. Kondo, M. Hara, H. Kobayashi, K. Domen, Y. Inoue, *J. Am. Chem. Soc.* **2005**, *127*, 4150.
- (54) K. Teramura, K. Maeda, T. Saito, T. Takata, N. Saito, Y. Inoue, K. Domen, *J. Phys. Chem. B* **2005**, *109*, 21915.
- (55) Y. Hou, B. L. Abrams, P. C. K. Vesborg, M. E. Björketun, K. Herbst, L. Bech, A. M. Setti, C. D. Damsgaard, T. Pedersen, O. Hansen, J. Rossmeisl, S. Dahl, J. K. Nørskov, I. Chorkendorff, *Nat. Mater.* **2011**, *10*, 434.
- (56) S. W. Seo, S. Park, H.-Y. Jeong, S. H. Kim, U. Sim, C. W. Lee, K. T. Nam, K. S. Hong, *Chem. Commun.* **2012**, *48*, 10452.
- (57) M. de Respinis, K. S. Joya, H. J. M. De Groot, F. D'Souza, W. A. Smith, R. van de Krol, B. Dam, *J. Phys. Chem. C* **2015**, *119*, 7275.
- (58) Y. Sun, J. P. Bigi, N. A. Piro, M. L. Tang, J. R. Long, C. J. Chang, *J. Am. Chem. Soc.* **2011**, *133*, 9212.
- (59) S. W. Sheehan, J. M. Thomsen, U. Hintermair, R. H. Crabtree, G. W. Brudvig, C. A. Schmuttenmaer, *Nat. Commun.* **2015**, *6*.
- (60) C. A. Caputo, M. A. Gross, V. W. Lau, C. Cavazza, B. V. Lotsch, E. Reisner, *Angew. Chem. Int. Ed.* **2014**, *53*, 11538.
- (61) J. Ran, J. Zhang, J. Yu, M. Jaroniec, S. Z. Qiao, *Chem. Soc. Rev.* **2014**, *43*, 7787.
- (62) K. E. Karakitsou, X. E. Verykios, *J. Phys. Chem.* **1993**, *97*, 1184.
- (63) J. C. Colmenares, *Green Chemistry and Sustainable Technology*, Xu, Y.-J., Ed., Springer-Verlag: Berlin Heidelberg, **2016**.
- (64) M. J. Berr, P. Wagner, S. Fischbach, A. Vaneski, J. Schneider, A. S. Sussha, A. L. Rogach, F. Jäckel, J. Feldmann, *Appl. Phys. Lett.* **2012**, *100*, 223903.
- (65) J. Schneider, D. W. Bahnemann, *J. Phys. Chem. Lett.* **2013**, *4*, 3479.
- (66) M. Bowker, *Green Chem.* **2011**, *13*, 2235.
- (67) X. Wang, K. Maeda, A. Thomas, K. Takanabe, G. Xin, J. M. Carlsson, K. Domen, M. Antonietti, *Nat. Mater.* **2009**, *8*, 76.
- (68) M. Ash, I. Ash, *Handbook of Green Chemicals*, Synapse Information Resources, **2004**.

- (69) R. Reithmeier, C. Bruckmeier, B. Rieger, *Catalysts* **2012**, *2*, 544.
- (70) M. Z. Hoffman, D. R. Prasad, G. Jones, V. Malba, *J. Am. Chem. Soc.* **1983**, *105*, 6360.
- (71) N. Hykaway, W. M. Sears, H. Morisaki, S. R. Morrison, *J. Phys. Chem.* **1986**, *90*, 6663.
- (72) M. Fujishima, K. Tanaka, N. Sakami, M. Wada, K. Morii, T. Hattori, Y. Sumida, H. Tada, *J. Phys. Chem. C* **2014**, *118*, 8917.
- (73) Anatase is reported to be photocatalytically superior to rutile and brookite (despite its larger band gap) due to its higher surface adsorption capacity, lower charge carrier recombination rate caused by its convenient indirect band gap and smaller grain sizes (extrinsic reason). J. Zhang, P. Zhou, J. Liu, J. Yu, *Phys. Chem. Chem. Phys.* **2014**, *16*, 20382.
- (74) R. Abe, K. Sayama, K. Domen, H. Arakawa, *Chem. Phys. Lett.* **2001**, *344*, 339.
- (75) M. V. Rao, K. Rajeshwar, V. R. P. Verneker, J. DuBow, *J. Phys. Chem.* **1980**, *84*, 1987.
- (76) B. Ohtani, *Chem. Lett.* **2008**, *37*, 216.
- (77) K. Fitsch, C. Kemker, Fundamentals of Environmental Measurements, *Solar Radiation and Photosynthetically Active Radiation 2014*, <http://www.fondriest.com/environmental-measurements/parameters/weather/photosynthetically-active-radiation/>, accessed on 17<sup>th</sup> of September 2015
- (78) J. Zhu, P. Xiao, H. Li, S. A. C. Carabineiro, *ACS Appl. Mater. Interfaces* **2014**, *6*, 16449.
- (79) K. Maeda, X. Wang, Y. Nishihara, D. Lu, M. Antonietti, K. Domen, *J. Phys. Chem. C* **2009**, *113*, 4940.
- (80) S. Cao, J. Low, J. Yu, M. Jaroniec, *Adv. Mater.* **2015**, *27*, 2150.
- (81) T. Maruyama, T. Yamamoto, *J. Phys. Chem. B* **1997**, *101*, 3806.
- (82) S. Matsuoka, T. Kohzuki, Y. Kuwana, A. Nakamura, S. Yanagida, *J. Chem. Soc. Perkin Trans.* **1992**, *2*, 679.
- (83) S. Yanagida, A. Kabumoto, K. Mizumoto, C. Pac, K. Yoshino, *J. Chem. Soc., Chem. Commun.* **1985**, 474.
- (84) K. Schwinghammer, B. Tuffy, M. B. Mesch, E. Wirnhier, C. Martineau, F. Taulelle, W. Schnick, J. Senker, B. V. Lotsch, *Angew. Chem. Int. Ed.* **2013**, *52*, 2435.
- (85) D. Dontsova, S. Pronkin, M. Wehle, Z. Chen, C. Fettkenhauer, G. Clavel, M. Antonietti, *Chem. Mater.* **2015**, *27*, 5170.
- (86) R. S. Sprick, J.-X. Jiang, B. Bonillo, S. Ren, T. Ratvijitvech, P. Guiglion, M. A. Zwijnenburg, D. J. Adams, A. I. Cooper, *J. Am. Chem. Soc.* **2015**, *137*, 3265.
- (87) L. Stegbauer, K. Schwinghammer, B. V. Lotsch, *Chem. Sci.* **2014**, *5*, 2789.
- (88) M. D. Kärkäs, O. Verho, E. V. Johnston, B. Åkermark, *Chem. Rev.* **2014**, *114*, 11863.
- (89) R. S. Sprick, B. Bonillo, R. Clowes, P. Guiglion, N. J. Brownbill, B. J. Slater, F. Blanc, M. A. Zwijnenburg, D. J. Adams, A. I. Cooper, *Angew. Chem. Int. Ed.* **2016**, *55*, 1792.



# Chapter II

## 2 Background

### 2.1 Carbon nitrides

#### 2.1.1 History

Carbon nitrides (systematically named as ammonocarbonic acids) are known since the discovery of “melon” by the Swedish chemist *J. J. Berzelius* in 1830<sup>1</sup> who has synthesized amorphous melon by the pyrolysis of mercury thiocyanate  $\text{Hg}(\text{SCN})_2$  (back then known as the Pharaoh’s serpents).<sup>2</sup> *J. Liebig* repeated several of *J. J. Berzelius*’ experiments, yet started from  $\text{NH}_4(\text{SCN})$ , which yielded products of higher purity. Next to melon, he identified and named<sup>3</sup> various triazine- and heptazine-based molecular compounds such as melamine (1,3,5-triazine-2,4,6-triamine), melam ( $N^2$ -(4,6-diamino-1,3,5-triazine-2-yl)-1,3,5-triazine-2,4,6-triamine), melem (2,5,8-triamino-tri-*s*-triazine), ammeline (4,6-diamino-2-hydroxy-1,3,5-triazine) and ammelide (6-amino-2,4-dihydroxy-1,3,5-triazine) (see Figure 2.1 for the general formula), some of which are tent intermediates (and derivatives) of the thermal polycondensation of melon (see Scheme 2.1).<sup>1</sup>

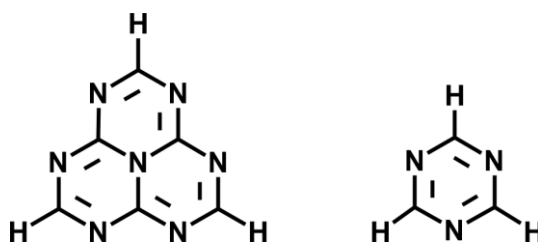
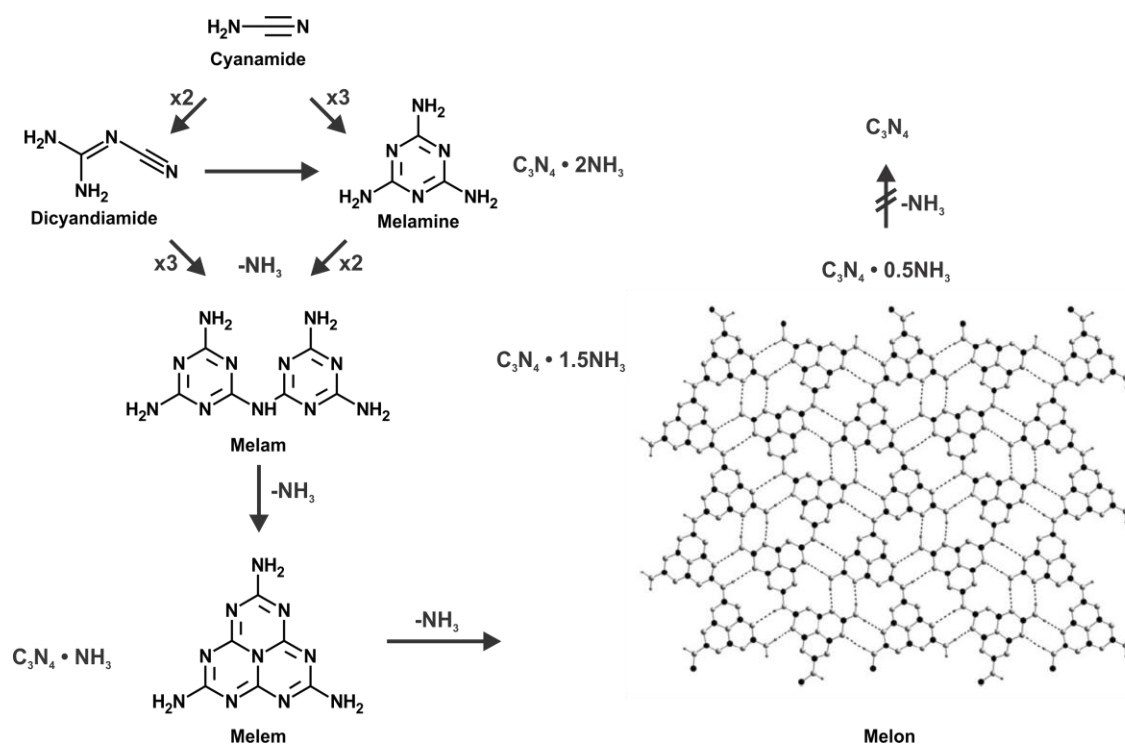


**Figure 2.1** Structures of *s*-heptazine or tri-*s*-triazine (left) and *s*-triazine (right).

Many of these materials and their salts<sup>4</sup> or hydrate phases,<sup>5</sup> which have been found during the 19<sup>th</sup> century, remained unidentified regarding their molecular and crystal structures. In the cases of the higher-condensed phases, the low solubility and the low crystallinity hindered the elucidation of their structures.<sup>6-8</sup> Melamine<sup>9</sup> and cyanuric acid<sup>10,11</sup> (2,4,6-trihydroxy-1,3,5-triazine) were the first compounds that could be fully characterized due to early single-crystal X-ray diffraction (XRD) investigations. After years in oblivion, *R. Franklin*<sup>4</sup> introduced the concept of ammonocarbonic acids ( $x \text{C}_3\text{N}_4 \cdot y \text{NH}_3$ ) in 1922 and many of the “old” compounds were reinvestigated. *L. Pauling* and *J. H. Sturdivant*<sup>12</sup> were especially interested in the possibility of the formation of a heptazine (tri-*s*-triazine) nucleus which led to speculations as to whether melon might consist of heptazine cores ra-

ther than triazine building blocks. This mystery has been finally solved in 2007 by *Schnick and co-workers*<sup>13</sup> with the help of electron diffraction in combination with advanced solid state nuclear magnetic resonance (ssNMR) spectroscopy on crystalline melon samples. The results showed that melon (poly(aminoimino)heptazine) consists of layers made up from zigzag-type one-dimensional (1D) chains of NH-bridged melem monomers that are tightly linked by hydrogen bonds (see Scheme 2.1).<sup>13</sup> Melon ( $C_3N_4 \cdot 0.5 NH_3$ ) and not  $C_3N_4$  is the final product of the (simple) thermal polycondensation process. However, it had often been attempted to synthesize the hydrogen-free, purely  $sp^2$ -bonded binary carbon nitride  $C_3N_4$  which has firstly been described by *R. Franklin* in 1922.<sup>4,13</sup>



**Scheme 2.1** Simplified thermal condensation path of cyanamide, resulting in melon as the final deammonation product.<sup>13-15</sup> The structure of melon is reproduced with permission from 2007 WILEY-VCH Verlag GmbH & Co. KGaA, Weinheim (licence number: 3800290814770).<sup>13</sup>

Still, the polymerization process is not yet fully understood in detail. However, it is possible to mention some important reaction steps (see Scheme 2.1).<sup>13-16</sup> As suitable carbon nitride precursors, different nitrogen-rich compounds and mixtures thereof such as cyanamide, dicyandiamide, melamine and (thio)urea can be named due to their preorganized C/N/H motifs (having no C-C or C-H, but exclusively N-C and N-H bonds) and easy accessibility. When heated, these non-cyclic precursors form melamine (and derivatives of melamine) which is a thermally stable compound (up to 350 °C)<sup>17,18</sup> and, hence, constitutes a thermodynamic sink favorable over a wide range of conditions.<sup>7,19</sup> Melam can be considered as composed of two condensed melamine units and is the product of the deammonation process of guanylmelamine and dicyandiamide.<sup>19</sup> It is formed at about 350 °C as a relatively short-lived intermediate (without ammonia back pressure, leading to rapid transformation into melem) and has been elucidated in 2007 by *Lotsch et al.*<sup>20</sup> At higher



temperatures, the heptazine nucleus is formed: First in the form of melamine-melem (2:1, 1:1 and 1:3) adduct phases<sup>21</sup> and melem<sup>1,22,23</sup> and finally, when the condensation process has further advanced into 1D chains of fused melem units, *i.e.*, the already mentioned melon.<sup>1,13</sup> As a side phase a holey heptazine-based 2D network containing embedded melamine molecules, known as poly(heptazine imide) (PHI), has been synthesized in small yields and characterized.<sup>24</sup> Above 500 °C melon decomposes and starts degrading into volatiles (NH<sub>3</sub>, C<sub>2</sub>N<sub>2</sub> and HCN).<sup>25</sup>

After the prediction by *Liu and Cohen*<sup>26-28</sup> of extremely high bulk moduli ( $B$ ) for the dense sp<sup>3</sup>-bonded hydrogen-free C<sub>3</sub>N<sub>4</sub> phases (especially  $\beta$ -C<sub>3</sub>N<sub>4</sub>:  $B = 4.27$  Mbar;  $B_{\text{diamond}} = 4.43$  Mbar), a “harder-than-diamond” fever, followed by a resurrection of carbon nitride chemistry, occurred in the 1990s.<sup>29,30</sup> The interest in these compounds blossomed and motivated scientists to synthesize the binary C<sub>3</sub>N<sub>4</sub> which turned out to be very difficult, if not impossible. In analogy to diamond, further theoretical calculations indicated that the graphitic ( $g$ ) phase of C<sub>3</sub>N<sub>4</sub>, which should be thermodynamically more stable, could be transformed to the dense 3D structure by high pressure and high temperature (HP-HT) synthesis.<sup>31</sup> In many experimental attempts, several groups tried to obtain  $g$ - and dense C<sub>3</sub>N<sub>4</sub> through HP-HT,<sup>32-36</sup> solid state<sup>37-41</sup> and solvothermal synthesis,<sup>42-45</sup> chemical<sup>46</sup> and physical vapor deposition<sup>47</sup> (CVD and PVD) and through thermal polycondensation/decomposition paths.<sup>48-51</sup> With one exception (see below),<sup>52</sup> none of the presented materials purely consist of carbon and nitrogen in a stoichiometric ratio of 3:4. Usually, amorphous products were synthesized. Some rare examples show high crystallinity but still contain residues of hydrogen and partly oxygen.<sup>13,24,32,34-36,40,52-55</sup> For simplicity, these (CN)<sub>x</sub> compounds were still called carbon nitrides in the literature, and in this thesis, this terminology will be used as well. Over the last years, some crystalline (CN)<sub>x</sub> could be identified among the already mentioned melon and PHI, for which either the combination of relatively high temperature and pressure was needed, or the use of salt melts.

For instance, in a laser-heated diamond-anvil cell, a three-dimensional (3D) carbon nitride network has been synthesized starting with dicyandiamide under HP-HT conditions by *Boehler and co-workers* in 2007.<sup>34</sup> The obtained carbon nitride imide C<sub>2</sub>N<sub>2</sub>(NH) crystallizes in a defect Wurtzite-type structure.

The first purely triazine-based carbon nitride, C<sub>6</sub>N<sub>9</sub>H<sub>3</sub> · HCl (hereinafter also referred to as “PTI/HCl”) has been synthesized in 2001 by *Wolf and co-workers* in a piston cylinder apparatus using a mixture of melamine and cyanuric chloride as precursors.<sup>32</sup> The compression of this layered compound above 40 GPa results in a pillared-layered carbon nitride material composed of a backbone of sp<sup>2</sup> and sp<sup>3</sup> hybridized carbon and nitrogen atoms.<sup>53</sup> A similar compound is poly(triazine imide) (PTI), C<sub>6</sub>N<sub>9</sub>(H<sub>x</sub>Li<sub>1-x</sub>)<sub>3</sub> · LiCl (PTI/LiCl), which has been initially synthesized under ionothermal conditions by *Thomas and co-workers*<sup>35</sup> but was fully characterized by *Wirnhier et al.*<sup>36</sup>

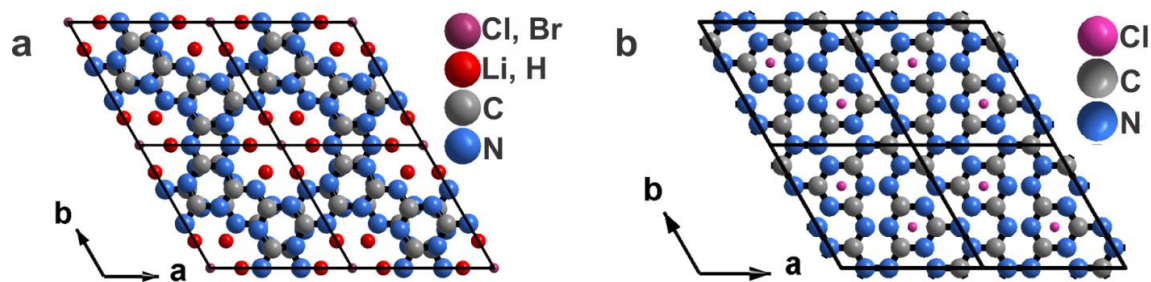


**Figure 2.2** Idealized crystal structure of two stacked layers of (a) Li/H containing PTI intercalated with chloride (ICSD 422088)<sup>36</sup> and bromide (CCDC 902173)<sup>56</sup> ions and (b) C<sub>6</sub>N<sub>9</sub>H<sub>3</sub>·HCl (PTI/HCl)<sup>32</sup> viewed along the *c*-direction.

Until recently, PTI was the only existing crystalline two-dimensional (2D) carbon nitride network known. It is composed of imide-linked triazine units forming layers which are stacked in an ABA-type fashion, with cations (protons, lithium and partially potassium ions) and anions (chlorine or bromine ions) situated in the channels running along the stacking direction along the *c*-axis (Figure 2.2).<sup>36,57</sup> Bojdys and co-workers have also reported on PTI/LiF which has been synthesized by treating PTI/LiBr with NH<sub>4</sub>F. PTI/LiF occurred as a side-phase next to PTI/LiBr and seems to crystallize in the PTI/HCl form.<sup>56</sup> Depending on which ions are intercalated, a change in the stacking distance appears (PTI/HCl: 3.22 Å,<sup>32</sup> PTI/LiF: 3.32 Å,<sup>56</sup> PTI/LiCl: 3.36 Å,<sup>35,36</sup> PTI/LiBr: 3.52 Å; bigger ions lead to larger stacking distances)<sup>56</sup> which has a significant influence on its electronic and absorption properties. PTI has also been synthesized in ZnCl<sub>2</sub>-based salt melts which resulted in PTI/ZnO cluster composites.<sup>58</sup>

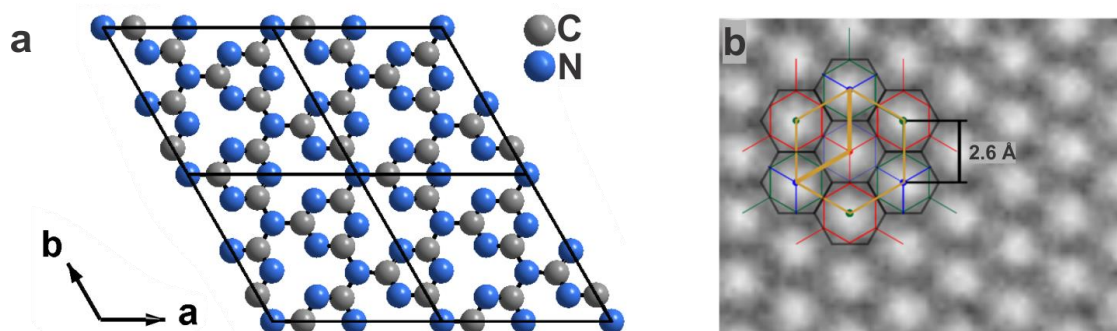


**Figure 2.3** (a) Idealized crystal structure of one layer of TGCN. (b) A TEM image of a single macroscopic TGCN film, adapted with permission from 2014 WILEY-VCH Verlag GmbH & Co. KGaA, Weinheim (licence number: 3755350729716).<sup>52</sup>

In 2014, *Bojdys and co-workers*<sup>52</sup> have once more reported on a crystalline, triazine-based graphitic carbon nitride (TGCN) with an ABC-type layered structure, which in contrast to PTI should exclusively consist of covalently-linked sp<sup>2</sup>-hybridized carbon and nitrogen atoms (Figure 2.3). The elemental analysis data show residues of 0.51 wt% of hydrogen which has been assigned to residual water. Clear impurities of potassium, bromine and adventitious carbon have been detected. The TEM data indicate that a triazine-based carbon nitride has been synthesized (in the form of a thin film). However, the NH-regions are slightly active in the IR and Raman spectra. Paradoxically, even though a band gap of 1.6 eV – 2.0 eV has been extracted, the optical appearance of the TGCN flakes is of metallic

character. Due to its narrow band gap, TGCN could be applied as a novel metal-free semiconductor in electronic devices (*e.g.* in transistors or solar cells), but not for full photocatalytic water splitting.<sup>52,59</sup>

### 2.1.2 Melon as photocatalyst for water splitting

While monomeric carbon nitrides (*e.g.* melamine and melem) are wide band gap semiconductors ( $\geq 3.5$  eV) giving rise to their white color, yellow-colored melon exhibits a band gap of 2.7 eV.<sup>60</sup> Its narrow band gap and the calculated band potentials render melon a suitable candidate for overall photocatalytic water splitting. In 2009, *Antonietti, Domen and co-workers*<sup>60</sup> showed for the first time that the amorphous form of melon is able to split water with the help of sacrificial agents when illuminated with visible light ( $\lambda > 420$  nm). Its moderate and fluctuating hydrogen evolution rate of  $0.1 \mu\text{mol h}^{-1}$  to  $4 \mu\text{mol h}^{-1}$  could be increased and stabilized with the addition of platinum as co-catalyst (Figure 2.4(a)).

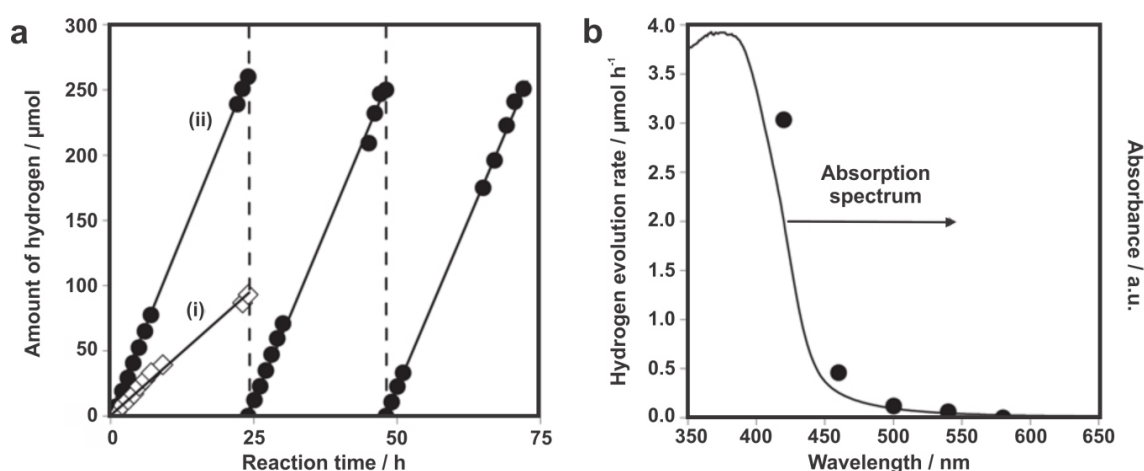


**Figure 2.4** (a) Produced hydrogen over 75 hour for a 10 vol% aq. TEOA/amorphous melon dispersion when illuminated with visible light (i: before and ii: after 3.0 wt% Pt-loading). Every 24 hours the reactor was evacuated to avoid saturation. (b) Action spectrum of the same sample using a 10 vol% aq. MeOH solution. Adapted with permission from Macmillan Publishers Ltd: Nature Materials,<sup>60</sup> copyright 2008 (licence number: 3755370969507).

Then,  $770 \mu\text{mol H}_2$  after 72 h of illumination were accumulated resulting in a hydrogen evolution rate of  $107 \mu\text{mol h}^{-1} \text{g}^{-1}$ . It was also reported that  $\text{RuO}_2$ -modified melon is capable of oxidizing water, albeit just  $8 \mu\text{mol O}_2$  were detected after 9 h of ( $\lambda > 420$  nm) illumination ( $9 \mu\text{mol h}^{-1} \text{g}^{-1}$ ), proving the oxidation of water being the problematic reaction.<sup>3</sup> As explained in Chapter 1.3, the oxidation of water is a four-electron-four-proton process and is hence, kinetically limited. In addition, the valence band potential is not offering enough overpotential (600 mV) for the water oxidation process.<sup>60,61</sup>

This pioneering work indicated that for high photocatalytic activities it is necessary to optimize four factors such as catalyst- and co-catalyst-loading, the choice of suitable sacrificial agent, pH conditions as well as the choice of wavelengths with which the catalyst is illuminated (Figure 2.4(b)).<sup>60</sup> The concentration of the photocatalyst-dispersion is important since the hydrogen evolution rates first increase with increasing concentration

until they start to saturate and then to decline due to scattering effects and thus, disturbed light absorption.<sup>62,63</sup> Henceforth, the hydrogen evolution rates will be given normalized to mass (per gram) to facilitate a comparison between the different presented photocatalysts.

### 2.1.3 Photocatalytic mechanism in carbon nitride photocatalysis

While it is experimentally proven that amorphous melon is capable of splitting water under visible light illumination, a clear theoretical explanation of its activity does not exist to date. This may be aggravated by misconceptions regarding the structure of carbon nitrides as well as limited interaction between theorists and experimentalists, since the calculations are often based on fully condensed structure models of melon. To be more precise, melon has often been modelled as a 2D system while actually being a 1D polymer.<sup>64-73</sup> This fallacy may result from the fact that melon-type carbon nitrides are often erroneously named “g-C<sub>3</sub>N<sub>4</sub>”, a term excessively used in the literature.<sup>60</sup> Moreover, photoactive melon is not crystalline but an ill-defined polymer with terminal sites and structural defects which are not properly studied. Such misconceptions will hamper precise theoretical calculations and may even explain obvious discrepancies between computational and experimental results.

In the following, a summary of the theoretical (DFT) and experimental results (spectroscopic) regarding the band gaps and band potentials as well as proposed photocatalytic mechanism will be given for the prototypical carbon nitrides: Heptazine-based 1D melon, triazine-based 2D PTI and (hypothetical) heptazine- and triazine-based graphitic carbon nitride.

#### Melon

In 2009, *Antonietti and co-workers*<sup>60</sup> demonstrated experimentally by UV-Vis spectroscopy that the optical band gap of amorphous melon is about 2.7 eV which is large enough to realize complete water splitting. According to their density functional theory (DFT) calculations (using the software CASTEP)<sup>74</sup> on different reaction intermediates along the condensation path, the electronic band gap decreases from the melem molecule (3.5 eV) to the 1D polymerized melon (2.6 eV) (Figure 2.5(a), grey arrow).<sup>60</sup> The theorized band gap is in agreement with the one experimentally extracted. In a later publication, *Cheng and co-workers*<sup>75</sup> computed an even narrower (direct) band gap of 2.34 eV for 1D melon (these calculations were carried out using the Vienna simulation package).<sup>76,77</sup> A large vacuum space of 15 Å between two neighboring melon sheets was constructed to avoid stacking interactions. The discrepancies of the two band gap values are attributed to the different methods (and corrections) used for the calculations. To the best of our knowledge, no other band gap calculations have been performed on 1D melon.

The computations presented in the original paper<sup>60</sup> showed further that melon exhibits a highly anisotropic band structure with low band dispersion (hence high charge carrier effective masses) and with a *direct band gap* at the  $\Gamma$  point (Figure 2.5(a)). Its valence band derives from the HOMO levels of the melem building blocks, *i.e.* the nitrogen  $p_z$  orbitals of

the peripheral nitrogens of the heptazine ring (Figure 2.5(c)). The carbon atoms (as  $p_z$  orbitals) create the LUMO levels and are hence assumed to be the reduction sites carrying the photogenerated electrons (Figure 2.5(b)). For photocatalysis, not only the band gap itself but the absolute potentials of the energy bands are essential. Since the valence and conduction band of melon theoretically straddle the proton reduction/water oxidation potential, melon should be capable to completely split water.<sup>60</sup> However, one should bear in mind that these calculations are based on vacuum conditions, thus excluding real solvation effects. Therefore, *Antonietti and co-workers*<sup>78</sup> tried to explore experimentally the valence and conduction band edge positions through the photoelectrochemical determination of the flat band potential (onset potential for photocurrent). A sufficient potential of  $-0.83$  V and  $1.83$  V *vs* NHE at pH 0 was estimated for the conduction and valence band edges, respectively.

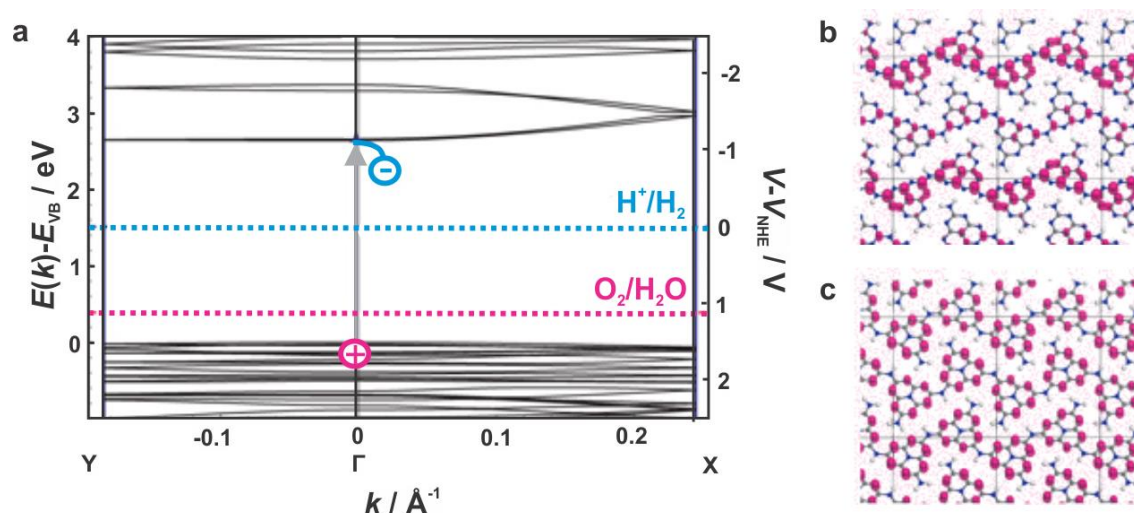


**Figure 2.5** (a) DFT band structure for 1D melon calculated along the chain ( $\Gamma$ -X direction) and perpendicular to the chain (Y- $\Gamma$  direction). The position of the water reduction level  $H^+/H_2$  is indicated by the dashed blue line and the oxidation potential  $O_2/H_2O$  is indicated by the magenta dashed line. The Kohn-Sham orbitals (b) of the conduction band and (c) of the valence band of melon. Adapted with permission from Macmillan Publishers Ltd: Nature Materials, copyright 2008 (licence number: 3755370969507).<sup>60</sup>

Following publications have shown that the optical band gap of melon correlates with the temperature it has been synthesized and thus, the polycondensation degree. Melon (or rather melem oligomers) obtained at  $400$  °C displayed an absorption edge about  $410$  nm, while materials synthesized at  $650$  °C exhibited a red-shifted absorption edge at  $520$  nm.<sup>79,80</sup> Hence, the optical band gap of melon can vary between  $2.4$  eV –  $3.1$  eV depending on the polymerization degree.<sup>81</sup> Therefore, *Butchosa et al.*<sup>82</sup> studied the optical properties of melon (or rather melem clusters; see Figure 2.6) in various condensation states by computational methods (DFT/TD-DFT).



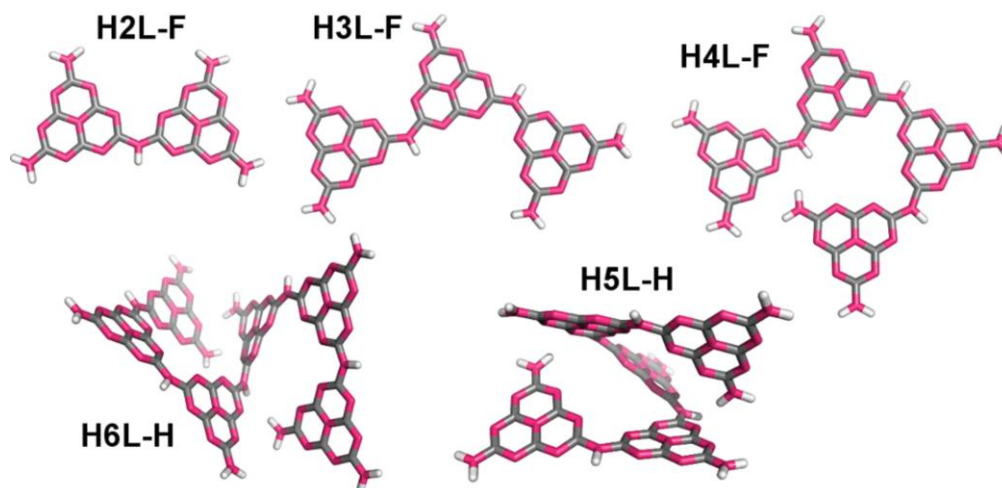


**Figure 2.6** The linear melon oligomer clusters (in gas phase) used for the calculations of *Butchosa et al.* Adapted with permission from the reference.<sup>82</sup> Copyright 2014, American Chemical Society.

Their calculations suggested that for an extended absorption in the visible region, a certain oligomeric length is necessary. Further, the absorption spectra of melon show a red-shift with increasing polymer length and stacking order suggesting higher photocatalytic activities for the highly condensed samples. However, *Lau et al.*<sup>25</sup> could verify experimentally that the oligomeric forms of melon are actually more photocatalytically active than the extended polymer despite their lower absorption in the visible regime. This points out that besides the band potentials and energy gap as well as the light harvesting properties of the photocatalyst, “functional defects” (such as the terminal sites) are important to investigate since they can improve the interaction with the co-catalyst and the kinetics of charge transfer and, thus, the photocatalytic activity.

Complementary to the absorption properties, it is important to look at the photoluminescent (PL) behavior of a photocatalyst to deeply study its optical properties. PL (fluorescence and phosphorescence) occurs due to light emission after photon absorption (radiative decay pathway). The amount of emitted light depends on the number of populated excited states after photoabsorption. The number of populated excited states can vary upon the excitation wavelength. As the decay rate has radiative and non-radiative contributions,

$$\Gamma_{tot} = \Gamma_{rad} + \Gamma_{non} \quad (3)$$

each of them can be attributed to the time constant:

$$\frac{1}{\tau_{PL}} = \frac{1}{\tau_{rad}} + \frac{1}{\tau_{non}} \quad (4)$$

where  $\tau_{rad}$  and  $\tau_{non}$  are the radiative and non-radiative recombination times, respectively.<sup>83</sup> Responsible for radiative recombination processes in semiconductors are the recombinations of free charge carriers, free, bound and localized excitons (exciton: excited quasiparticle in a solid, which is formed by a Coulomb-bound electron-hole pair).<sup>84</sup> Non-

radiative recombination processes can occur due to *e.g.* carrier capture by defects or Auger recombinations and are detrimental for photocatalysis.<sup>83</sup> Charge transfer can either lead to radiative or non-radiative processes. In the case of a dominant radiative recombination process, a fast decay rate of the PL signal after light absorption (pico-nanosecond range) would indicate a short charge carrier lifetime (*e.g.* of electron-hole pairs). However, the radiative recombination process plays only a minor role in carbon nitrides, hence, light absorption leads mostly to non-radiative processes.<sup>85</sup>

*Merschjann et al.*<sup>86,87</sup> investigated the photoluminescence behavior of melon (and mesoporous melon) which shows relatively strong emission at 440 nm – 520 nm, covering almost the whole visible range. The broad PL signal width is caused by the ill-defined nature of the sample. Highly condensed melon samples (synthesized at a reaction temperature of 610 °C) show a red-shifted photoluminescence signal (maximum at 480 nm) compared to low condensed samples (synthesized at 490 °C; maximum at 460 nm).<sup>86</sup> The high reaction temperature seems to correlate with a decreased layer stacking of melon and an increasing overlap of the  $\pi$ -orbitals perpendicular to the aromatic systems.<sup>86</sup> The mean lifetimes of the photoluminescence emission is in the range of a few nanoseconds, which suggests the initial formation of singlet excitons directly after excitation (see Figure 27).<sup>86</sup> Further, a transport mechanism has been suggested. First, the singlet excitons dissociate into singlet polaron pairs (Coulomb bound pair of a negative and a positive polaron, situated on different molecules)<sup>84</sup> on neighboring sheets and further dissociate into free polarons (a charge – electron or hole – plus a distortion of the charge's surroundings).<sup>84,87</sup> It has been shown that the PL lifetimes decrease non-linearly with the (increasing) process temperature and decreasing layer distance of melon (see Figure 2.8(a,b)). Therefore, a hopping mechanism of the charges (in a Brownian motion-type movement) perpendicular to the aromatic system was assumed.<sup>86</sup> This was also justified due to the large intrachain hopping activation energies of >1 eV and presumably an even higher energy barrier with regards to intraplanar hopping. Still, an additional transport within the sheets might be possible.<sup>87</sup> In general, the highly non-linear decrease of the PL lifetimes points to a fairly complex relaxation behavior and probably an interaction between radiative and non-radiative relaxation processes.<sup>86</sup> The low radiative efficiency of the melon samples arise from non-radiative relaxation formed triplet excitons.<sup>87</sup> The hopping rates declined with increasing layer stacking (Figure 2.7(c,d)) and measured to be in the range of  $10^9 \text{ s}^{-1}$ , leading to low combined electronic mobilities (of electron and hole polarons) of about  $10^{-6} \text{ cm}^2 \text{ V}^{-1} \text{ s}^{-1} - 10^{-4} \text{ cm}^2 \text{ V}^{-1} \text{ s}^{-1}$  which are common for conducting organic polymers.<sup>87</sup>

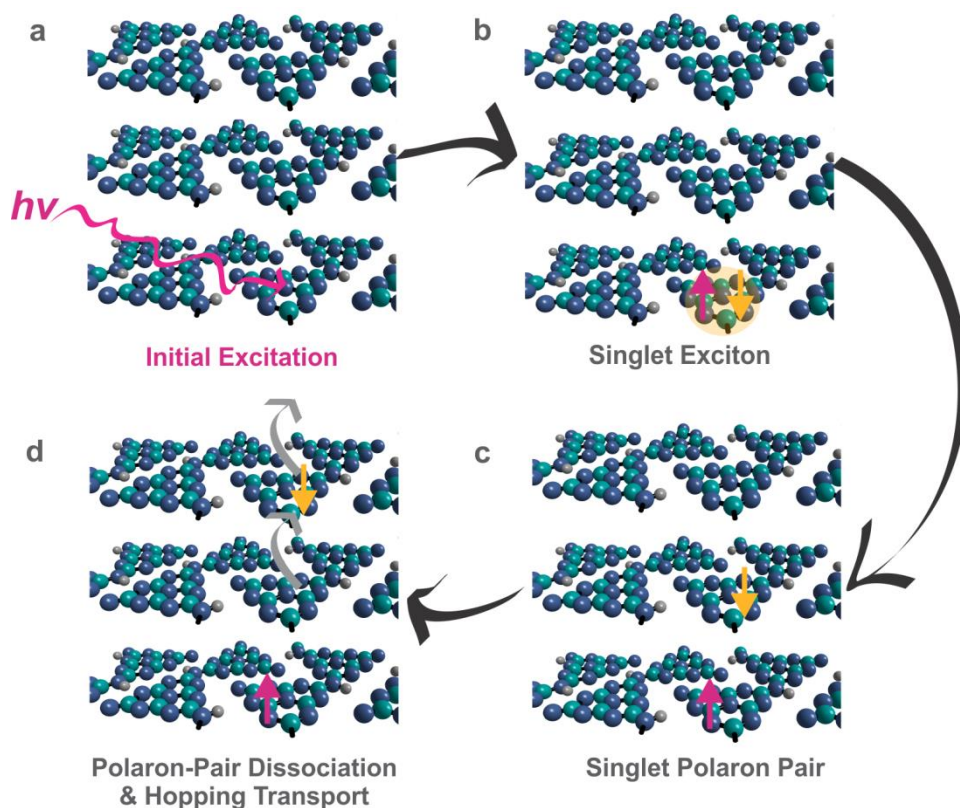


**Figure 2.7** Proposed excitation and transport mechanism of melon: (a) Photoexcitation, (b) generation of singlet excitons, (c) dissociation of singlet excitons into singlet polaron pairs on neighboring sheets and (d) polaron-pair dissociation and the diffusive Brownian motion of the free polarons along the  $c$ -direction.<sup>73</sup>

One would assume that a higher hopping rate would subsequently lead to higher photocatalytic activities. *Merschjann et al.*<sup>87</sup> detected apparent correlations between the hopping rate (or inverse time constant of the PL decay) and the measured concentration of photoinduced charge carriers, as well as photocatalytic activity (see Figure 2.8(d)). However, the photocatalytic activity (and the concentration of photoinduced charge carriers) largely depends on the absorption coefficient of the samples and their surface area. While the surface area could be measured, the absorption coefficient could not be determined due to light scattering. Therefore, a definite answer about the correlation between mobility and activity could not be given.

To summarize the results of *Merschjann et al.*,<sup>86</sup> a molecular singlet exciton is generated when melon is irradiated with UV light, which is highly confined to the network-constituting monomer due to insufficient orbital overlap and, hence, limited conjugation between the heptazine building blocks of the polymer strand. A separation of the electron-hole pairs was discussed to be unlikely at room temperature due to the very high exciton binding energies (approximately 800 meV). Thus, these excitons dissociate into free polarons which travel perpendicular to the aromatic systems *via* diffuse hopping and the rate decreases with increasing layer stacking distance. To conclude, melon behaves effectively as a monomer in contrast to classical semiconductor systems.<sup>86</sup>



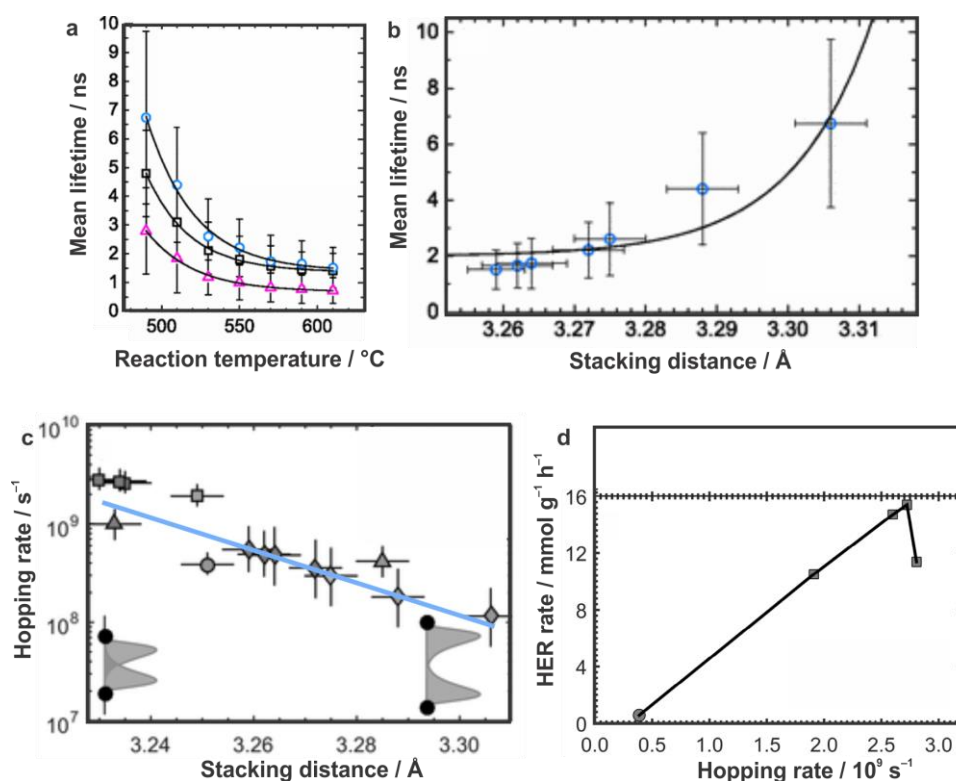


**Figure 2.8** Decreasing PL mean lifetime of melon with (a) increasing reaction temperature and (b) decreasing stacking distance.<sup>86</sup> (c) Correlation of the stacking distances of various melon samples with the hopping rates. (d) No reliable correlation between the photocatalytic activity and the hopping rates can be given (also due to missing absorption coefficient values) according to the reference.<sup>87</sup> Adapted with permission from 2016 John Wiley and Sons (licence number: 3825241351008).

### Poly(triazine imide)

Less information on the electronic structure can be found for the 2D triazine-based carbon nitride PTI. Initially,<sup>88</sup> an optical band gap of 2.6 eV has been extracted for crystalline PTI/LiCl from the UV/Vis diffuse reflectance spectrum which is narrower than the one of polymeric melon (2.7 eV).<sup>60</sup> Moewes, Scheu, Schnick and co-workers<sup>89</sup> carried out deeper studies on the electronic structure on PTI depending on its ion loading by a combination of X-ray absorption/emission and electron energy-loss spectroscopy in a transmission electron microscope (TEM). A band gap of 2.2 eV has been estimated for PTI when it is fully loaded with lithium and chloride ions (Figure 2.9(a)), which is narrower than the one observed experimentally.

Similar to melon, the highest-energy nitrogen states of PTI are responsible for photoabsorption, as N  $2p$  sites also contribute to the conduction band minimum.<sup>89</sup> In contrast to melon, the N  $2p$  states of PTI can split due to the lithium-coordination to the nitrogen-bridge which introduces additional states just below the valence band maximum. However, the position of the valence band maximum remains unchanged. The introduced lithium, leads to a reduction of the conduction band minimum which consists of hybridized C and N  $2p$  states, with C dominating. Hence, a high lithium content leads in total to a narrowing of the band gap (of 0.4 eV). The chlorine loading does not affect the

valence band maximum. However, the splitting of the N  $2p$  states at the valence band maximum allows an increased hybridization between the lithium-coordinated imide-linkage with the low binding energy Cl  $2p$  states (the valence electron density is illustrated in Figure 2.9(b)). This finding suggests that the photocatalytic activity of PTI might be controllable by ion loading, especially with regards to the lithium content.

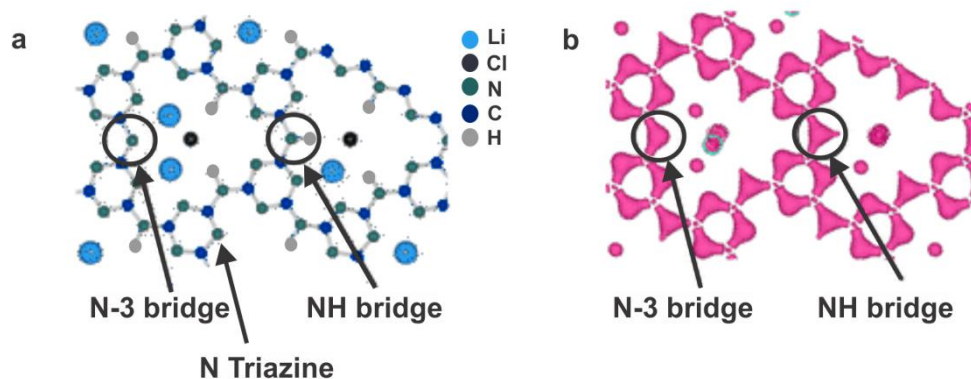


**Figure 2.9** (a) Fully Li loaded PTI/LiCl model showing three different nitrogen sites: the triazine nitrogen and the bridging nitrogen with either two neighboring Li atoms (N-3) or as NH group. (b) The N-3 site gives a different valence electron density.<sup>3</sup> Adapted with permission from the reference.<sup>89</sup> Copyright 2016, American Chemical Society.

Deifallah *et al.*<sup>90</sup> performed further calculations on a single-layer PTI and PTI/HCl sheet (flat geometry). A large electronic band gap of 5.16 eV has been calculated for PTI between the valence band maximum (unshielded electron pairs on the nitrogens) and the bottom of the conduction band ( $\pi^*$  levels of the triazine ring). When loaded with HCl (protonation of the triazine nitrogen), the band gap decreases to 4.12 eV due to the presence of additional bands just above the valence band due to chlorine loading.

### Two dimensional graphitic carbon nitride

The electronic structure of  $g$ - $C_3N_4$  has been studied on models constructed either on triazine or heptazine building blocks (Figure 2.10). While both versions should be thermodynamically capable to reduce and oxidize water, the heptazine-based carbon nitrides should be more suitable for photocatalysis due to its red-shifted absorption edge. However, the triazine-based structures seem to have a larger thermodynamic driving force for proton reduction than the heptazine-based compounds. On the other hand, the heptazine-based compounds seem to be more suitable to perform water oxidation. In general, a stronger red-shift has been observed for the graphitic than the linear structures (Figure 2.6). Stacking as well as extension of the oligomeric length seems to red-shift the absorption edge. The effect of stacking appears larger for the triazine-based models.<sup>82</sup>

While a heptazine-based graphitic  $C_3N_4$  has not been synthesized without doubts so far, no experimental values can be given. However, *Bojdys and co-workers*<sup>52</sup> could experimentally estimate a band gap of roughly 1.6 eV – 2.0 eV for (almost hydrogen-free) triazine-based  $g$ - $C_3N_4$ . The following table lists several band gap values for hypothetical heptazine- and triazine based  $g$ - $C_3N_4$  found in the literature (calculated with different methods and based on different stacking behaviors).

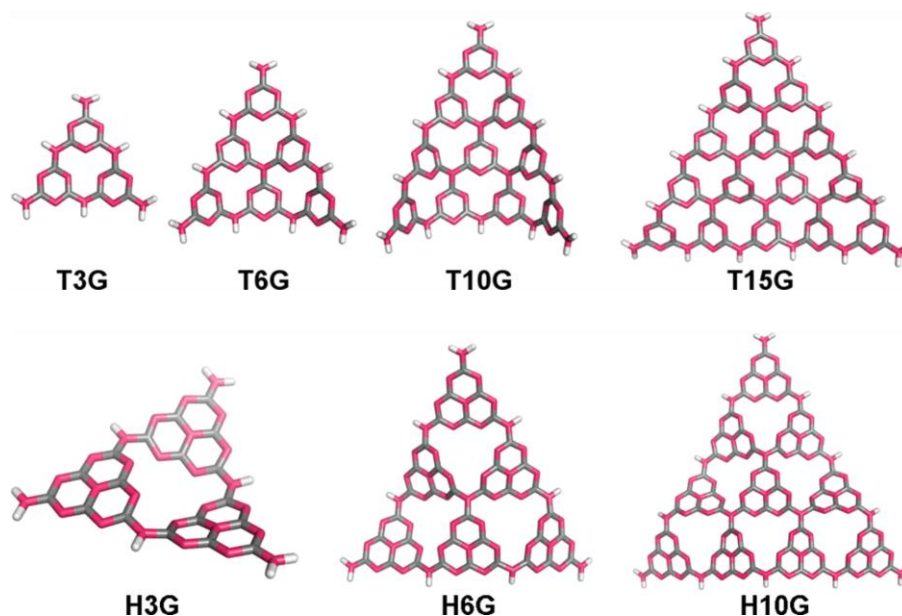
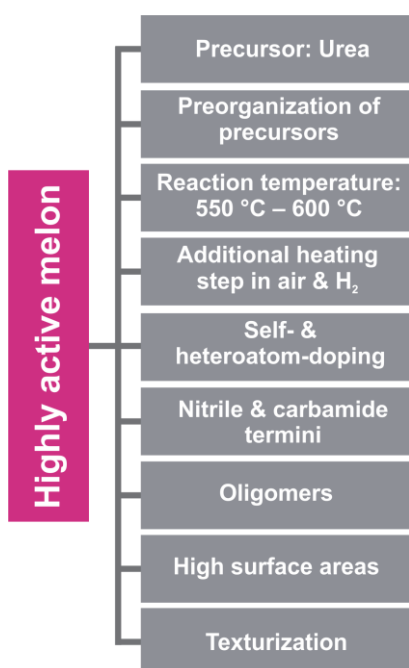


**Figure 2.10** Model clusters of triazine- (top) and heptazine-based (bottom)  $g\text{-C}_3\text{N}_4$ . Adapted with permission from the reference.<sup>82</sup> Copyright 2014, American Chemical Society.

**Table 2.1** Various band gap values of heptazine- and triazine-based  $g\text{-C}_3\text{N}_4$  taken from the references.

reference	heptazine-based	triazine-based	band gap (eV)	method
60	infinite sheet		2.1 (direct)	CASTEP <sup>74</sup>
67	x		2.7 (indirect)	PAW, GGA-PBE, VASP, <sup>76</sup> HSE06,
67		x	3.3 (direct)	
91		x	3.0 (AB-stack) 2.6 (AA-stack)	WIEN2K package, LDA-CA, GGA-PBE, EV-GGA, mBJ
90		x	2.9–4.1	CRYSTAL06 code, hybrid B3LYP functional, LDA
90	x		3.0–3.8	
68	x		1.2–1.5 (indirect)	VASP, PAW, PBE, CASTEP, PWUS-PW91, GGA, LDA-CAPZ
71	x		1	VASP (GGA-LDA)
73	x		2.9–3.1 (depending on the stacking order)	VASP, PAW, vdW-DF, GW, Hartree-Fock

## 2.1.4 Methods to improve the photocatalytic activity of carbon nitrides



**Scheme 2.2** Several methods discussed in the literature, which benefit the synthesis of highly active melon.

The photocatalytic activity of carbon nitrides in general and for melon in particular strongly depend on the synthesis conditions such as reaction temperature,<sup>79,80,92,93</sup> reaction time,<sup>94</sup> applied pressure,<sup>95</sup> synthetic atmosphere<sup>95</sup> and choice of precursor.<sup>95-97</sup> For instance, conventionally synthesized (brown) crystalline melon is photocatalytically inactive (measurements performed within our research group) while ill-defined carbon nitrides show a reasonable photocatalytic activity.<sup>88,98</sup> From classical photocatalysis it is known that high crystallinity is beneficial for charge transport since defect states might operate as scattering sites and recombination centers.<sup>99-104</sup> On the other hand, the so-called “defects”, including carbon-nitrogen substitutions, incorporation of oxygen-impurities or dangling terminal sites can dramatically change the density of states by adjusting the redox potentials or by introducing additional energy levels.<sup>95</sup> They might also be the reason for changes in morphology (such as particle size and porosity), improved wettability of the photocatalyst, or better attachment of the co-catalyst and reactants on the surface of the photocatalyst and therefore, quicker charge transfer (see Chapter 4.2). In detail, *Lau et al.*<sup>25</sup> have shown that a large quantity of terminal sites, which correlates with the polymerization degree, is beneficial for melon. It has often been reported that the photocatalytic activity of melon reaches its maximum at a reaction temperature of roughly 550 °C – 600 °C while usually only short reaction times of about 4 h are applied, implying incomplete polymerization and an increased level of unreacted terminal sites.<sup>95</sup>

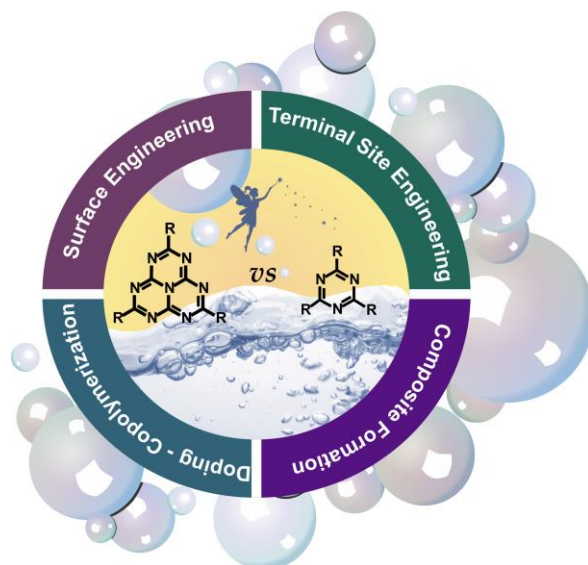


**Figure 2.11** Summarized methods to improve the photocatalytic activity of carbon nitrides.

Through an additional calcination step under special conditions (half-closed crucible), the activity can be further enhanced. This is explained by thermal oxidation of melon, sometimes along with exfoliation or modification of the surface termini.<sup>105</sup> It has also been shown that ultra-long calcination times (> 500 h) can result in very active samples which display surprisingly high crystallinity.<sup>106</sup> Heating the samples in a hydrogen atmosphere was reported to result in higher activities. The samples displayed a narrower band gap compared to melon samples heated in air which has been reasoned by a reduction of the amino-groups.<sup>75</sup> Clearly, the applied conditions resulted in more ill-defined samples, a partial decomposition of the heptazine cores and possible delamination.

As already mentioned, the choice of the precursor is crucial. Urea-derived melon samples are more active compared to the melamine- and dicyandiamide-based ones, probably owing to the carbamide terminal sites and higher surface areas.<sup>95,96,107</sup> In contrast, it has been reported that amine and imino groups have a negative influence on the photocatalytic activity of melon.<sup>98</sup>

In addition, a pre-organization of the precursors before heating seems also to be beneficial for highly active materials. The pre-organization of the precursors improves the crystallinity of the products.<sup>108,109</sup>

The activity of the carbon nitrides has been enhanced not only through reaction control but also by a series of specific modifications. For instance, an increase of the surface area by porosity engineering through soft<sup>110-112</sup> and hard templating methods,<sup>113-116</sup> by changing the condensation process, *e.g.* by sulfuric acid treated melamine,<sup>117,118</sup> and by exfoliation/delamination of the carbon nitride layers results in a larger number of accessible active sites.<sup>105,119-123</sup> However, excessively thinning down the carbon nitrides (< 2 nm) can result in a widening of the band gaps due to quantum size confinement effects.<sup>67</sup>

While an enlargement of the surface area leads to a better access to the terminal sites, texturization of carbon nitrides in the form of hollow spheres<sup>109,124,125</sup> and 1D nanostructures<sup>126-130</sup> can improve light harvesting. Also doping or intercalation with specific heteroatoms of metallic (Zn, Fe, Mn, Co, Ni, Cu, Eu, Pt, Pd, Li, Na and K)<sup>89,131-140</sup> and non-metallic elements (B, S, F, O, I, P, H, C, N and Cl)<sup>66,68,89,141-151</sup> or by co-polymerization<sup>88,108,152-156</sup> with a series of organic molecules has a significant influence on the absorption properties, defect levels and band edges and thus the photocatalytic activity (see Figure 2.12). However, good light harvesting properties do not necessarily make a semiconductor a more active photocatalyst.

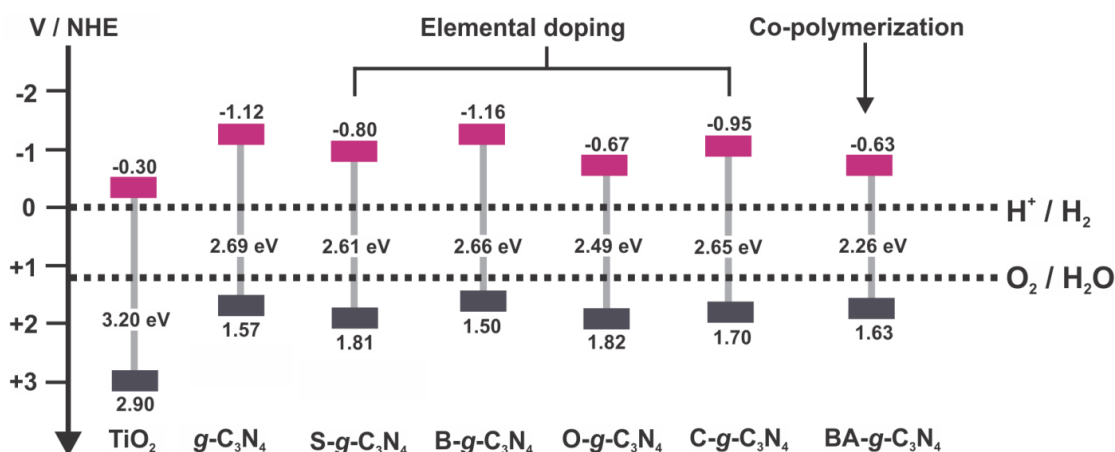


**Figure 2.12** Schematic illustration of the band structures of typical samples of melon in comparison to TiO<sub>2</sub> (from left to right): Pristine melon, S-, B-, O- and C-doped melon and melon which was co-polymerized with barbituric acid (BA). Adapted with permission from 2015 WILEY-VCH Verlag GmbH & Co. KGaA, Weinheim (licence number: 3756411023958).<sup>95</sup>

Another method to enhance the activity of carbon nitrides is the formation of hybrids and heterojunction systems to either improve light harvesting or charge transfer.<sup>95</sup> Carbon nitride-based composites with several carbon materials (*e.g.* graphene,<sup>157-159</sup> reduced graphene oxide,<sup>160</sup> fullerene,<sup>161</sup> carbon nanotubes,<sup>142</sup> carbon black<sup>162</sup> and carbon nanodots),<sup>163</sup> inorganic semiconductors (*e.g.* TiO<sub>2</sub>,<sup>164-169</sup> WO<sub>3</sub>,<sup>170,171</sup> Fe<sub>2</sub>O<sub>3</sub><sup>172</sup> and ZnO<sup>172-174</sup>) and organic semiconductors (*e.g.* poly(3-hexylthiophene)<sup>175</sup> and poly-pyrrole),<sup>176</sup> dyes,<sup>177</sup>  $\alpha$ -sulfur,<sup>178</sup> red phosphor<sup>179</sup> and carbon nitrides (thiourea-derived C<sub>3</sub>N<sub>4</sub>/urea-derived C<sub>3</sub>N<sub>4</sub>)<sup>180,181</sup> have been created.<sup>182</sup> In Table 2.1, the best carbon nitride-based systems for photocatalytic water reduction so far are listed along with some essential experimental details. Unfortunately, a fair comparison between different laboratories is practically impossible. Therefore, the activity is typically given related to a reference sample (usually non-modified melon) measured under identical conditions. The next chapter (Chapter 2.2) will give further insights into challenges in photocatalysis and presents a suggested protocol for the experimental setup.

To conclude, carbon nitrides have been widely used and studied as light-element photocatalysts. High photocatalytic activities can already be achieved but there is still scope for improvement. The carbon nitrides suffer from their limited structural variety as they are composed of exclusively triazine or heptazine building blocks. In addition, their lack of crystallinity and generally low intrinsic surface are major disadvantages. Chapter 2.3 introduces a novel photocatalyst which belongs to the category of covalent organic frameworks, which offers a greater toolbox for modifications.

**Table 2.1** A variety of carbon nitride-based photocatalysts for visible-light induced water reduction. Grey-highlighted photocatalysts produce more than 2000  $\mu\text{mol H}_2 \text{ h}^{-1} \text{ g}^{-1}$  or are over 10 times more active compared to their reference. Note that since these catalysts were measured under different conditions, they cannot be compared directly.

precursor* -derived photocatalyst, synthesis conditions, literature	co-catalyst	sacrificial donor	irradiation (wavelength)	activity in $\text{H}_2 /$ $\mu\text{mol h}^{-1} \text{ g}^{-1},$ AQE / % (wavelength)	activity in $\text{H}_2 / \mu\text{mol}$ $\text{h}^{-1} \text{ g}^{-1}$ of a reference catalyst, synthesis conditions (if different from the photocatalyst)	enhancement in activity relative to reference
<b>Melon</b>						
D*-melon <sup>60</sup>	3.0 wt% Pt	10 vol% TEoA	> 420 nm, 300 W Xe lamp	107, 0.1 (420–460 nm)	-	-
U*-melon, 600 °C, air <sup>96</sup>	3.0 wt% Pt	13 vol% TEoA	$\geq 395 \text{ nm},$ 300 W Xe lamp	3300	300 (D*-melon) 500 (thiourea- melon) 142.3 (C*-melon)	11 7 23
oligomeric M*-melon, 450 °C, 12 h, air <sup>25</sup>	~0.9 wt% Pt	10 vol% MeOH (pH 7 0.1 M PBS)	> 420 nm, 300 W Xe lamp	270 0.1 (400 nm)	45 (polymeric M*- melon, 550 °C, 12 h, Ar)	6
melon nanosheets, liquid sonication <sup>119</sup>	3.0 wt% Pt	10 vol% TEoA	> 420 nm, 300 W Xe lamp	1860, 3.75 (420 nm)	200	9
melon nanosheets, thermal oxidation	3.0 wt% Pt	10 vol% TEoA	> 420 nm, 300 W Xe lamp	1300	200	7
D*-melon nanosheets, 550 °C, 4 h, chemical exfoliation <sup>118</sup>	3 wt% Pt	10 vol% TEoA	> 420 nm, 500 W Xe lamp, 40.0 mW $\text{cm}^{-2}$	230	90 (D*-melon)	3
U*-melon nanosheets, 500 °C, 8 h, Ar <sup>183</sup>	0.5 wt% Pt	15 vol% TEoA	> 420 nm, 300 W Xe lamp	1400, 2.6 (420 nm)	450 (U*-melon nanosheets, 1 h)	3
D*-melon, 550 °C, 4 h, N <sub>2</sub> treated for 2 h with H <sub>2</sub> at 550 °C <sup>184</sup>	3 wt% Pt	10 vol% TEoA	> 420 nm, 350 W Hg arc lamp, 15 °C	960	92 (D*-melon, air) 90 (D*-melon)	10 11
U*-melon, 550 °C, 4 h, treated with 0.001 M NaOH <sup>185</sup>	3 wt% Pt	10 vol% TEoA	> 420 nm, 300 W Xe lamp	2433	1100 (U*-melon)	2
N-doped M*-melon, 550 °C, 4 h, air <sup>150</sup>	3.0 wt% Pt	10 vol% TEoA	> 400 nm, 300 W Xe lamp	554	98 (M*-melon)	6
N-deficient M*-melon, 520 °C, 4 h, Ar <sup>186</sup>	1 wt% Pt	10 vol% TEoA	> 420 nm, 300 W Xe lamp	316	105 (M*-melon)	3
S-doped D*-melon, 550 °C, 4 h <sup>66</sup>	6.0 wt% Pt	10% TEoA	> 420 nm, 300 W Xe lamp, T $\leq 9$ °C	~340	~60 (D*-melon)	6
10 % Zn-doped melon, 550 °C, 4 h <sup>187</sup>	0.5 wt% Pt	19 vol% MeOH	$\geq 420 \text{ nm},$ 200 W Xe lamp	298	28 (D*-melon)	11
mesoporous-C*-melon, 550 °C, 4 h, from hard-templating <sup>188</sup>	Pt	10 vol% TEOA	> 420 nm, 500 W HBO	1490	-	-
mesoporous-C*-melon, 550 °C, 4 h, from soft-templating (SBA-15) <sup>116</sup>	Pt	10 vol% TEoA	> 420 nm, 500 W HBO	850	-	-
N-doped tantalic acid sensitized U*-melon, 400 °C, 2 h, air <sup>189</sup>	Pt	19 vol% MeOH	$\geq 410 \text{ nm},$ 300 W Xe lamp, 27 mW $\text{cm}^{-2}$	71, 4.8 (420 nm) at 940 $\mu\text{W cm}^{-2}$	20 (U*-melon)	4
F-doped D*-melon, 550 °C, 4 h, through NH <sub>4</sub> F treatment <sup>143</sup>	3.0 wt% Pt	10 vol% TEoA	> 420 nm, 500 W HBO	120–130	50–60 (D*-melon)	2
0.03 quinoline- incorporated U*-melon, 550 °C, 2 h <sup>190</sup>	3.0 wt% Pt	10 vol% TEoA	> 420 nm, < 780 nm, 300 W Xe lamp	4360	1110 (U*-melon)	4
ABN-doped melon <sup>153</sup>	Pt		> 420 nm, 300 W Xe lamp	1470	-	-
barbituric acid-doped D*- melon, 550 °C, 4 h <sup>152</sup>	Pt	10 vol% TEoA	> 420 nm, 500 W HBO	294	65 (D*-melon)	5
C*-melon nanorods, 600 °C, 4 h, N <sub>2</sub> <sup>126</sup>	3.0 wt% Pt	10 vol% TEoA	> 420 nm, 300 W Xe lamp	~1680	560 (C*-melon)	3
U*-melon, 550 °C, 3 h, air <sup>163</sup>	4.8 x 10 <sup>-3</sup> conc. C- nanodots	without	> 420 nm, 300 W Xe lamp	575, 16 (420 nm)	-	-
M*-melon, 550 °C, 4 h, N <sub>2</sub> <sup>157</sup>	1.5 wt% Pt, 1 wt% graphene	25 vol% MeOH	> 400 nm, Xe arc lamp	451	147 (M-melon)	3
C*-melon, 550 °C, 4 h, N <sub>2</sub> <sup>191</sup>	1.0 wt% Pt, 2 wt% MWCNTs	25 vol% MeOH	> 400 nm, Xe arc lamp	76	20 (C*-melon)	4
U*-melon, 550 °C, 3 h, air <sup>176</sup>	3.0 wt% Pt, 1.5 wt% polypyrrole nanoparticles	pure water	> 400 nm, 300 W Xe lamp	154	3 (U*-melon)	50



mesoporous-U*-melon, 600 °C, 43 h, air + 0.4 mM Eosin Y <sup>192</sup>	1.0 wt% Pt	15 vol% TEoA pH 7	≥ 420 nm, 250 W HP Hg lamp	3850, 24.0 (≥ 420 nm)	-	-
U*-melon nanosheets, 550 °C, 4 h + erythrosin B (1:2) <sup>107</sup>	1.25 wt% Pt	5 vol% TEoA, pH 9	> 420 nm, 300 W Xe lamp	6525	451 (U*-melon nanosheets, 1 wt% Pt)	15
U*-melon + Zn- <i>tri</i> -PcNc <sup>193</sup>	0.5 wt% Pt	50 mM ascorbic acid	≥ 500 nm, 300 W Xe lamp, 328.4 mW cm <sup>-2</sup>	12520, 1.85 (700 nm)	-	-
U*-melon, 550 °C, 4 h, Ar + 70 wt% red P <sup>179</sup>	0.5 wt% Pt	0.1 M, pH 4.0, L-ascorbic acid	> 420 nm, 300 W Xe lamp	1000	340 (U*-melon)	3
D*-melon, 550 °C, 4 h, N <sub>2</sub> + S-doped D*-melon <sup>181</sup>	Pt	10 vol% TEoA	> 420 nm, 300 W Xe lamp	~6500	~250 (D*-melon)	26
melon <sup>194</sup>	0.5 mol% Ni(OH) <sub>2</sub>	10 vol% TEoA	> 400 nm, 350 W Xe lamp, 180 mW cm <sup>-2</sup>	152, 1.1	-	-
mesoporous-C*-melon, 550 °C, 4 h <sup>195</sup>	0.2 wt% MoS <sub>2</sub>	10 vol% lactic acid	> 420 nm, 300 W Xe lamp	1030, 2.1 (420 nm)	240 (mesoporous-C*-melon, 0.5 wt% Pt)	4
mesoporous-U*-melon, 550 °C, 4 h <sup>196</sup>	1.1 wt% NiS	15 vol% TEoA, pH 11.0	> 420 nm, 300 W Xe lamp	482, 1.9 (440 nm)	2 (mesoporous-U*-melon)	241
melon <sup>197</sup>	(2.0 wt% Ni) [Ni(TEoA) <sub>2</sub> ]Cl <sub>2</sub>	10 vol% TEoA	> 400 nm, 500 W Xe lamp	2435, 1.51 (400 nm)	(melon, 2 wt% Pt); (AQE: 1.83 % (400 nm))	no
M*-melon, 600 °C, 4 h, Ar + SrTiO <sub>3</sub> :Rh <sub>0.3 mol%</sub> (20:80 wt%) <sup>198</sup>	0.5 wt% Pt	20 vol% MeOH	> 415 nm, 300 W Xe lamp	2233, 5.5 (410 nm)	107 (M*-melon)	21
U*-melon, 500–520 °C, 4 h, air + 10 wt% WO <sub>3</sub> <sup>199</sup>	2 wt% Pt	10 vol% TEoA	> 420 nm, 300 W Xe lamp	66, 0.90 (405 nm)	27 (U*-melon); AQE: 0.34 % (405 nm)	2
M*-melon, 520 °C, 4 h, air + 0.05 wt% Cu <sub>2</sub> O <sup>200</sup>	3.0 wt% Pt	10 vol% TEoA	> 420 nm, 300 W Xe lamp	241	142 (M*-melon)	2
M*-melon, 500–520 °C, 4 h, air + 10 wt% In <sub>2</sub> O <sub>3</sub> <sup>201</sup>	0.5 wt% Pt	0.1 M L-ascorbic acid (pH = 4.0)	> 420 nm, 300 W Xe lamp, 200 mW cm <sup>-2</sup>	198	38 (M*-melon)	5
<b>PTI</b>						
D*-PTI, LiCl/KCl, 12 h in Ar at 400 °C, 24 h in NH <sub>3</sub> at 600 °C <sup>88</sup>	2.3 wt% Pt	10 vol% TEoA	≥ 420 nm, 300 W Xe lamp	864	722 (D*-melon, 600 °C, 4 h, air)	>1
amorphous D*-PTI, LiCl/KCl, 12 h, 500 °C, Ar/air <sup>88</sup>	2.3 wt% Pt	10 vol% TEoA	≥ 420 nm, 300 W Xe lamp	1080	722 (D*-melon, 600 °C, 4 h, air)	>1
4AP-doped amorphous D*-PTI, LiCl/KCl, 12 h, 500 °C, Ar/air <sup>88</sup>	2.3 wt% Pt	10 vol% TEoA	≥ 420 nm, 300 W Xe lamp	4907	864 (D*-PTI), 722 (D*-melon, 600 °C, 4 h, air), 1080 (amorphous D*-PTI)	6 6 5
D*-PTI nanosheets, LiCl/KCl, 12 h in Ar at 400 °C, 24 h in NH <sub>3</sub> at 600 °C <sup>122</sup>	2.3 wt% Pt	10 vol% TEoA	≥ 420 nm, 300 W Xe lamp	1750, 1.3 (400 nm)	430 (D-PTI)	4
C*-PTI, 500 °C, air, 0.2 Li/C mol% <sup>202</sup>	5 wt% Pt	10 vol% TEoA	> 420 nm, 300 W Xe lamp	~ 46	~ 76 (C*-melon, 500 °C, air)	no
PTI, (LiCH <sub>2</sub> O/KCl/NaCl (1:1:1)): (15:1), 500 °C, 1 h <sup>139</sup>	3 wt% Pt	10 vol% TEoA	≥ 420 nm, 300 W Xe lamp	3460, 21.2 (420 nm)	100 (D*-melon, 550 °C, 4h)	35
TAP-doped M*-PTI (0.13:1 mol%) <sup>108</sup>	3 wt% Pt	10 vol% TEoA	> 420 nm, 300 W Xe lamp	8160	600 (melon), 880 (M*-PTI)	14 9
3-Amino-1,2,4-triazole-5-thiol, LiCl/KCl, 600 °C, 4 h, N <sub>2</sub> <sup>203</sup>	3 wt% Pt	10 vol% TEoA pH = 10.8	50 W LED	1220	660 (mesoporous-melon), 0 (D*-PTI, LiCl/KCl, 550 °C), 132 (guanazole, LiCl/KCl, 550 °C), 163 (M*-PTI)	2 total 9
M*-PTI, NaCl/KCl/LiCl, 500 °C, 2 h <sup>162</sup>	3 wt% Pt, 0.5 wt% C black	25 vol% MeOH	> 420 nm	689	163 (M*-PTI)	4
PTI/HCl, HP, HT <sup>90</sup>	Pt	10 vol% MeOH	> 400 nm, 300 W Xe lamp	0	115 (D*-M-melon, 550 °C, 15 h, N <sub>2</sub> ), 0 (D*-PTI, LiCl/KCl, 400 °C for 6 h in N <sub>2</sub> , 600 °C for 12 h, NH <sub>3</sub> )	

\*Precursors: Melamine (M), dicyandiamide (D), urea (U) and cyanamide (C).



## 2.2 Challenges in photocatalysis

After the initial paper on the photocatalytic activity of melon, numerous publications followed which reported on competitive hydrogen evolution rates. However, a fair comparison is basically impossible due to missing standards. So far, there is no consensus on how to measure the photocatalytic activity in a standardized fashion, not just for carbon nitrides but for any heterogeneous photocatalytic systems. Several articles aimed to discuss these problems with the goal to improve the quality of the research work and scientific papers in the field of photocatalysis. Here, I want to refer to the personal commentary of *B. Ohtani*<sup>204</sup> and *J.-M. Herrmann*<sup>205</sup> on the preparation of articles and misconceptions occurring in photocatalysis and the problem of normalization and comparing rates or photonic efficiencies from *T. Maschmeyer & M. Che*<sup>63</sup> and *H. Kisch*.<sup>206</sup> A “best practice” recommendation (published by others and based on the research performed herein) is given below in order to provide a guideline for future researchers in this field:

- Photo- and co-catalyst loading should be optimized, which also depends on the design of the photoreactor (see Figure 2.13).<sup>62</sup> The amount of catalysts and concentration should be presented in the manuscript, as well as the illuminated surface area and the reactor design.<sup>63</sup> Continuous stirring to provide stability of the suspensions is absolutely necessary for heterogeneous photocatalytic systems.<sup>207</sup>

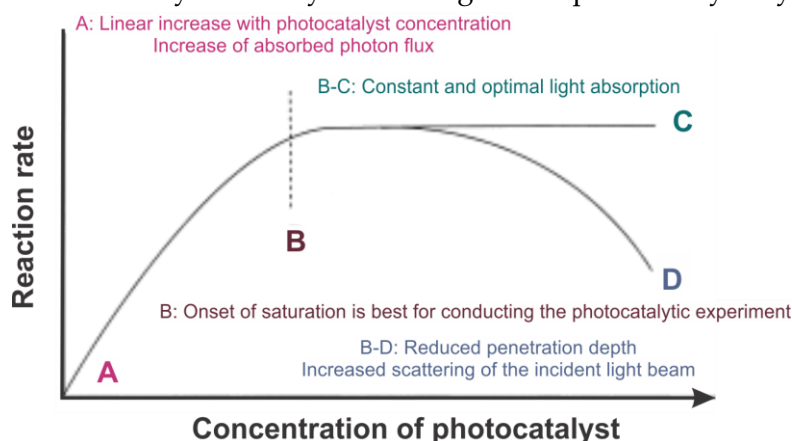


**Figure 2.13** Dependence of the reaction rate on the photocatalyst concentration. Adapted with permission from John Wiley and Sons, 2016 (licence number 3825421251768).<sup>206</sup>

- Over-powered lamps should be avoided, especially with small photoreactors since the head space might get oversaturated with hydrogen.<sup>63</sup> The intensity and intensity profile of the lamp should be as similar to sunlight as possible (solar simulator or AM conditions) and should explicitly be given in the manuscript. Since we (in this work) saw significant differences in the intensity profiles of commercially available cut-off mirrors/filters as well as light bulbs (and altering), it is helpful to show the intensity profiles in the publication.<sup>204</sup>
- The experiments should be performed under well-defined conditions of temperature (25 °C) and pressure (atmospheric) (keep in mind the *Nernst* equation, Chap-

ter 1.2.1, the *Le Chatelier's* principle and the temperature-dependent solubility of hydrogen/oxygen in water).<sup>63</sup>

- Maximum quantum yield can only be obtained at full coverage of the photocatalyst's active sites with the reactants. Apparent quantum yields (AQEs)/photonic efficiencies (see Chapter 7.2) should be given, but are only accurate if the light intensity is low and properly measured, and the catalyst loading is saturated such that all photons are absorbed. Otherwise, the AQE values are underestimated.<sup>63</sup> The AQE results are sometimes pushed to the limits by surrounding the photoreactor with a reflecting surface (*e.g.* aluminum foil) or by using inner-radiation, which should be explicitly stated in the experimental details.<sup>63</sup>
- A purchasable reference sample should be used for comparing the results.<sup>204</sup> Table 2.1 (Chapter 2.1.4) shows that the photocatalytic activity of "non-modified" amorphous melon varies drastically depending on the reaction conditions used during synthesis. It has been suggested to use purchasable P25 and purchasable melon (Nicanite).<sup>61</sup>
- Dye discoloration is not sufficient to prove the photocatalytic activity of a novel photocatalyst. Since the mechanism of dye degradation is complicated, the efficiency of the photocatalytic reaction cannot be measured. The consumption of a dye (measured with a spectrophotometer) is no clear proof for a photocatalytic process. The presence of dyes can even lead to dye sensitization. An action spectrum is therefore needed.<sup>204,208</sup> Continuous gas detection by a well calibrated chromatograph and correct product identification should be the method of choice.<sup>204</sup>
- The choice of sacrificial agent is crucial. Triethanolamine seems the most effective electron donor for many organic-based photocatalysts but it should be used with particular caution since it is light-sensitive.<sup>209</sup> Further, any alcohol containing electron donor (*e.g.* methanol) can cause current doubling effects such that at least half of the detected hydrogen is formed through the oxidation of the electron donor and the subsequent transfer of extra electrons into the conduction band of the photocatalyst.<sup>210</sup> Additional tests with other electron donors (such as acetate, which has no current doubling effect) should be performed to prove the photocatalytic activity of the novel photocatalyst.
- The pH values before and after photocatalysis should be given and controlled since the pH has an influence on the water splitting potential (see *Nernst* equation, Chapter 1.2.1) and band bending.
- The photocatalyst should be extensively analyzed before and after photocatalysis.<sup>204</sup> Most of the used carbon nitrides are rather ill-defined samples for which the nature of the terminal sites or the polymer length are not discussed. In some cases, the continuous stirring in water might even lead to partial delamination of 2D photocatalysts.

- Surface area values of samples should be given since higher activities can often solely be traced back to higher surface areas (and thus, more accessible active sites).<sup>204</sup>
- Adhesion and distribution of the co-catalyst on the photocatalyst as well as its oxidation state (or crystallite sites) should be known since they have an influence on the proton reduction capability.<sup>211</sup> The initially used amount of co-catalyst might differ from the actual concentration deposited on the catalyst.

### 2.3 Covalent organic frameworks as photocatalysts

Covalent organic frameworks (COFs), a relatively new class of 2D and 3D organic polymers, are light-weight, crystalline, and porous solids. Several COFs are 2D systems and show interesting absorption properties for photocatalysis, which allows a comparison with the already presented photocatalytically active carbon nitrides. Their chemical versatility and easy tunability is determined by the building blocks used and augmented by post-synthesis modifications. COFs are synthesized by the assembly of molecular building units which are linked by reversible bond-forming reactions (dynamic covalent chemistry) to yield periodic and porous frameworks. By combining several of these building blocks (Figure 2.14), an inexhaustible number of COFs can be built, which differ in their material properties and applications.<sup>212,213</sup> Thus, it is possible, in principle, to rationally design a suitable photocatalyst with good light-harvesting and charge transfer properties, high surface areas (hence, accessible active sites), and low weight. In addition, COFs may be able to capture the hydrogen (and oxygen) gas which is formed during water splitting, which could be an interesting solution to the challenge of hydrogen storage and gas separation.<sup>212,213</sup>

In 2005, *Yaghi and co-workers*<sup>212</sup> presented the first COFs which have been synthesized through the condensation of phenyl diboronic acids (termed COF-1) or phenyl diboronic acid and hexahydroxytriphenylene (termed COF-5). The formation of COFs by the condensation of boronic acids still belongs to the most popular COF synthesis routes. Thus far, COFs have been assembled through several linkages which can be categorized as boron-based (boronate, borosilicate, boron acid anhydrides and borazine), nitrogen nucleophile-based (hydrazone, imine, squaraine, azine, phenazine and imide) as well as triazine/heptazine-based linkages. While most of these interconnections are rather unstable under aqueous conditions (*e.g.* boron-based and imine), the imide-, hydrazone- and triazine/heptazine-bridged COFs could be applied for photocatalytic water splitting.<sup>214</sup> The extensive studies on carbon nitrides clearly emphasizes the important role of triazines (and also heptazines) for photocatalysis even though their function is yet not fully understood. Therefore, this thesis includes our investigations on triazine-based COFs next to those of the carbon nitride PTI. Triazine-based COFs can either be synthesized by directly starting from a triazine-containing building block or through the formation of a triazine-linkage during synthesis. When the triazine unit is formed by a (Lewis-acid

catalyzed) trimerization reaction of a nitrile-terminated building block, then the COF is referred to as covalent triazine framework (CTF) (for an exemplary synthesis see Chapter 4.2).<sup>215-221</sup>

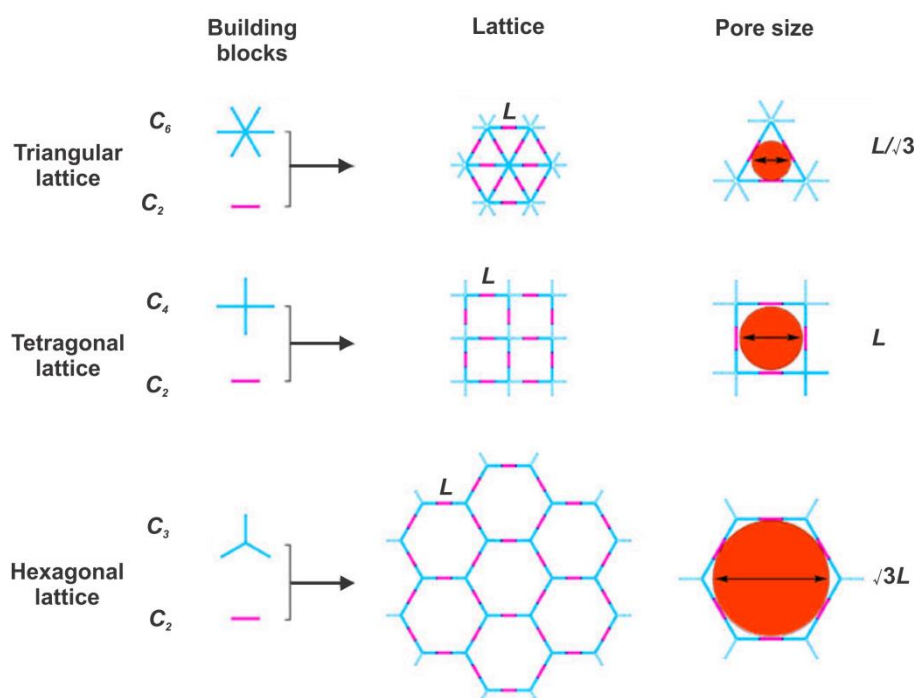


**Figure 2.14** Possible assembly of planar COFs out of  $C_2$ ,  $C_3$ ,  $C_4$  and  $C_6$  symmetric building blocks.<sup>222</sup>

To conclude, in this chapter the synthesis and structure of melon, its intermediates and PTI has been presented. It has further been discussed that melon is (theoretically and experimentally) photocatalytically active and that its activity can be improved by a series of techniques (Chapter 2.1.4). It has been pointed out that the comparison of the photocatalytic activities from different laboratories is challenging and that photocatalytic experiments should be performed under well-defined conditions (Chapter 2.2). Also PTI and triazine-containing covalent organic frameworks have been theorized to be potential candidates for water splitting. These two triazine-based material classes form the basis of this work. The following chapter delves deeper into the aims of this thesis and gives an overview of the the following chapters.

## 2.4 Project aims

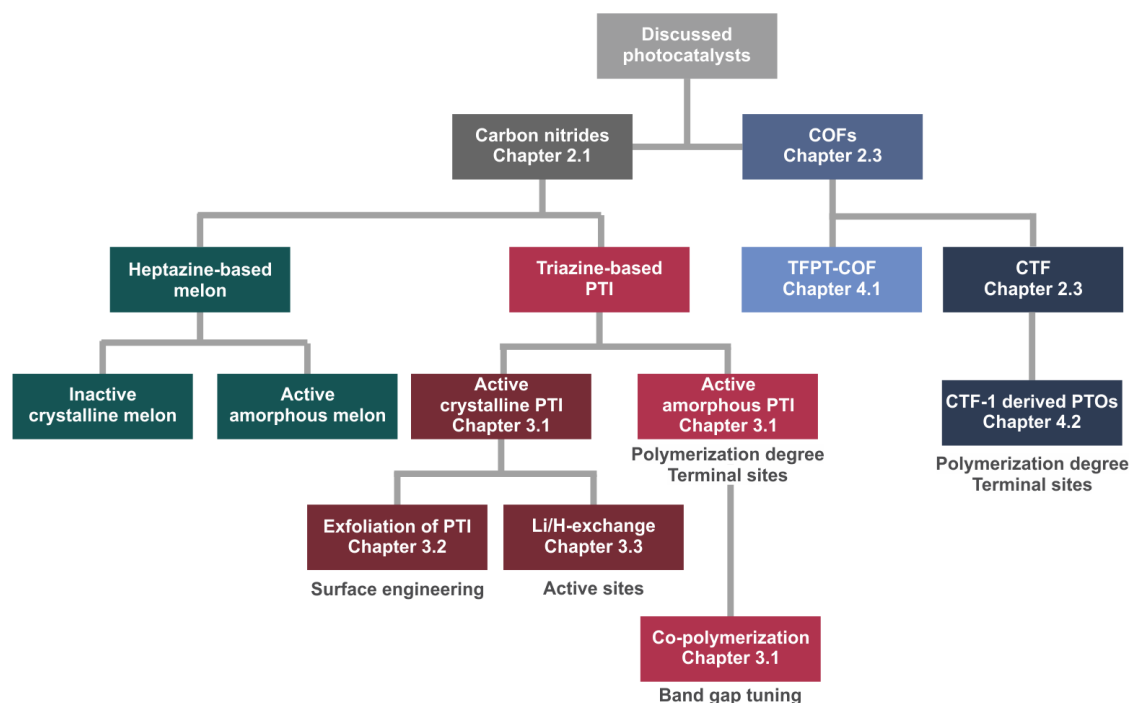
This thesis is providing first insights into triazine-based photocatalysts. PTI as an exemplary triazine-based compound is comprehensively discussed in this thesis and compared with the reference material melon which in contrast to PTI is based on heptazine-building blocks.

Therefore, the crystalline carbon nitride PTI/LiCl has been synthesized and its photocatalytic activity was tested for light-induced hydrogen evolution (Chapter 3.1). The results were compared with the commonly used amorphous melon (“g- $C_3N_4$ ”). After intro-

ducing crystalline PTI/LiCl as a new class of “green” photocatalysts, its moderate activity has been further improved. Its absorption properties have been studied and modified to result in a higher photocatalytic activity. Overall, the following aspects were explored to increase the activity of PTI/LiCl:

- 1 Lowering its crystallinity and band gap modulation by a co-polymerization process of dicyandiamide (PTI-precursor) with pyrimidine-based molecules: 4-amino-2,6-dihydropyrimidine, barbituric acid, triaminopyrimidine and 2-amino-4,6-dihydropyrimidine, which correlates with an increased surface area and amount of terminal sites (Chapter 3.1).
- 2 Extension of the surface area of PTI and interface with the electrolyte by aqueous exfoliation (Chapter 3.2).
- 3 Cationic and anionic exchange of PTI/LiCl,Br for the investigation on the catalytically relevant sites of PTI (Chapter 3.3).

The resulting products were thoroughly characterized by a multitude of analytical methods. Special attention has been paid to identifying the triazine-building block in the ill-defined products and to preventing photocorrosion during the photocatalytic experiment.



**Scheme 2.3** Overview of the conducted projects and the corresponding Chapters.

In order to gain a deeper understanding of the role of these triazine units, two other triazine-based compounds belonging to the class of covalent organic frameworks or covalent triazine frameworks are investigated for photocatalytic water splitting, namely 1,3,5-*tris*-(4-formyl-phenyl)triazine (TFPT)-COF and CTF-1 (Chapter 4). The scheme shown above serves as an orientation for the projects that were conducted.

## Bibliography

- (1) J. Liebig, *Annalen* **1834**, *10*, 1.
- (2) T. L. Davis, *J. Chem. Educ.* **1940**, *17*, 268.
- (3) 0.01 M silver nitrate as electron acceptor, 3.0 wt% RuO<sub>2</sub>-loading and 0.2 g La<sub>2</sub>O<sub>3</sub> as pH 8-9 buffer were used. X. Wang, K. Maeda, A. Thomas, K. Takanahe, G. Xing, J. M. Carlsson, K. Domen, M. Antonietti, *Nat. Chem.* **2009**, *8*, 76.
- (4) E. C. Franklin, *J. Am. Chem. Soc.* **1922**, *44*, 486.
- (5) W. Henneberg, *Ann. Chem. Pharm.* **1859**, *73*, 228.
- (6) B. V. Lotsch, *PhD thesis*, Ludwig-Maximilians-Universität, **2006**.
- (7) A. Sattler, *PhD thesis*, Ludwig-Maximilians-Universität, **2010**.
- (8) J. Klason, *J. Prakt. Chem.* **1886**, *33*, 285.
- (9) E. W. Hughes, *J. Am. Chem. Soc.* **1941**, *63*, 1737.
- (10) E. H. Moerman, N. F. Wiebenga, *Z. Krist.* **1938**, *99*, 217.
- (11) E. H. Wiebenga, *J. Am. Chem. Soc.* **1952**, *74*, 6156.
- (12) L. Pauling, J. H. Sturdivant, *Proceedings of the National Academy of Sciences of the United States of America* **1937**, *23*, 615.
- (13) B. V. Lotsch, M. Döblinger, J. Sehnert, L. Seyfarth, J. Senker, O. Oeckler, W. Schnick, *Chem. Eur. J.* **2007**, *13*, 4969.
- (14) W. H. Tolleson, G. W. Diachenko, D. Folmer, D. Doell, D. Heller, *Background Paper on the Chemistry of Melamine Alone and in Combination with Related Compounds*, WHO, **2009**.
- (15) Y. Wang, X. Wang, M. Antonietti, *Angew. Chem.* **2012**, *124*, 70.
- (16) A. Schwarzer, T. Saplinova, E. Kroke, *Coord. Chem. Rev.* **2013**, *257*, 2032.
- (17) B. Bann, S. A. Miller, *Chem. Rev.* **1958**, *58*, 131.
- (18) D. R. Lide, *CRC Handbook of Chemistry and Physics, Internet Version*, CRC Press: Boca Raton, FL, **2005**.
- (19) H. Bieling, M. Radüchel, G. Wenzel, H. Beyer, *J. Prakt. Chem.* **1965**, *28*, 325.
- (20) B. V. Lotsch, W. Schnick, *Chem. Eur. J.* **2007**, *13*, 4956.
- (21) A. Sattler, S. Pagano, M. Zeuner, A. Zurawski, D. Gunzelmann, J. Senker, K. Müller-Buschbaum, W. Schnick, *Chem. Eur. J.* **2009**, *15*, 13161.
- (22) A. Sattler, W. Schnick, *Z. Anorg. Allg. Chem.* **2006**, *632*, 238.
- (23) B. Jürgens, E. Irran, J. Senker, P. Kroll, H. Müller, W. Schnick, *J. Am. Chem. Soc.* **2003**, *125*, 10288.
- (24) M. Dobliger, B. V. Lotsch, J. Wack, J. Thun, J. Senker, W. Schnick, *Chem. Commun.* **2009**, 1541.
- (25) V. W.-h. Lau, M. B. Mesch, V. Duppel, V. Blum, J. Senker, B. V. Lotsch, *J. Am. Chem. Soc.* **2015**, *137*, 1064.
- (26) A. Y. Liu, M. L. Cohen, *Science* **1989**, *245*, 841.
- (27) A. Y. Liu, M. L. Cohen, *Phys. Rev. B* **1990**, *41*, 10727.
- (28) A. Y. Liu, R. M. Wentzcovitch, *Phys. Rev. B* **1994**, *50*, 10362.
- (29) R. C. DeVries, *Mat. Res. Innovat.* **1997**, *1*, 161.

- (30) M. M. Chaudhri, Y. Y. Lim, *Nat. Mater.* **2005**, *4*, 4.
- (31) D. M. Teter, R. J. Hemley, *Science* **1996**, *271*, 53.
- (32) Z. Zhang, K. Leinenweber, M. Bauer, L. A. J. Garvie, P. F. McMillan, G. H. Wolf, *J. Am. Chem. Soc.* **2001**, *123*, 7788.
- (33) P. V. Zinin, L. C. Ming, S. K. Sharma, S. M. Hong, Y. Xie, T. Irifune, T. Shinmei, *Journal of Physics: Conference Series* **2008**, *121*, 062002.
- (34) E. Horvath-Bordon, R. Riedel, P. F. McMillan, P. Kroll, G. Miehe, P. A. van Aken, A. Zerr, P. Hoppe, O. Shebanova, I. McLaren, S. Lauterbach, E. Kroke, R. Boehler, *Angew. Chem. Int. Ed.* **2007**, *46*, 1476.
- (35) M. J. Bojdys, J.-O. Müller, M. Antonietti, A. Thomas, *Chem. Eur. J.* **2008**, *14*, 8177.
- (36) E. Wirnhier, M. Döblinger, D. Gunzelmann, J. Senker, B. V. Lotsch, W. Schnick, *Chem. Eur. J.* **2011**, *17*, 3213.
- (37) S. Tragl, K. Gibson, J. Glaser, V. Duppel, A. Simon, H. J. Meyer, *Solid State Commun.* **2007**, *141*, 529.
- (38) X. Lu, L. Gai, D. Cui, Q. Wang, X. Zhao, X. Tao, *Mater. Lett.* **2007**, *61*, 4255.
- (39) J. L. Zimmerman, R. Williams, V. N. Khabashesku, J. L. Margrave, *Nano Lett.* **2001**, *1*, 731.
- (40) T. Komatsu, *Macromol. Chem. Phys.* **2001**, *202*, 19.
- (41) Y. Gu, L. Chen, L. Shi, J. Ma, Z. Yang, Y. Qian, *Carbon* **2003**, *41*, 2674.
- (42) Y.-J. Bai, B. Lü, Z.-G. Liu, L. Li, D.-L. Cui, X.-G. Xu, Q.-L. Wang, *Journal of Crystal Growth* **2003**, *247*, 505.
- (43) Q. Guo, Y. Xie, X. Wang, S. Zhang, T. Hou, S. Lv, *Chem. Commun.* **2004**, 26.
- (44) Q. Guo, Y. Xie, X. Wang, S. Lv, T. Hou, X. Liu, *Chem. Phys. Lett.* **2003**, *380*, 84.
- (45) H. Montigaud, B. Tanguy, G. Demazeau, I. Alves, S. Courjault, *J. Mater. Sci.* **2000**, *35*, 2547.
- (46) J. Kouvetakis, M. Todd, B. Wilkens, A. Bandari, N. Cave, *Chem. Mater.* **1994**, *6*, 811.
- (47) P. Wang, T. Takeno, K. Adachi, H. Miki, T. Takagi, *Applied Surface Science* **2012**, *258*, 6576.
- (48) B. V. Lotsch, W. Schnick, *Chem. Mater.* **2006**, *18*, 1891.
- (49) Y. C. Zhao, D. L. Yu, H. W. Zhou, Y. J. Tian, O. Yanagisawa, *J. Mater. Sci.* **2005**, *40*, 2645.
- (50) D. R. Miller, J. R. Holst, E. G. Gillan, *Inorg. Chem.* **2007**, *46*, 2767.
- (51) E. G. Gillan, *Chem. Mater.* **2000**, *12*, 3906.
- (52) G. Algara-Siller, N. Severin, S. Y. Chong, T. Björkman, R. G. Palgrave, A. Laybourn, M. Antonietti, Y. Z. Khimiyak, A. V. Krasheninnikov, J. P. Rabe, U. Kaiser, A. I. Cooper, A. Thomas, M. J. Bojdys, *Angew. Chem.* **2014**, *126*, 7580.
- (53) P. F. McMillan, V. Lees, E. Quirico, G. Montagnac, A. Sella, B. Reynard, P. Simon, E. Bailey, M. Deifallah, F. Corà, *J. Solid State Chem.* **2009**, *182*, 2670.
- (54) T. Komatsu, *J. Mater. Chem.* **2001**, *11*, 802.
- (55) L. Yang, P. W. May, L. Yin, R. Brown, T. B. Scott, *Chem. Mater.* **2006**, *18*, 5058.
- (56) S. Y. Chong, J. T. A. Jones, Y. Z. Khimiyak, A. I. Cooper, A. Thomas, M. Antonietti, M. J. Bojdys, *J. Mater. Chem. A* **2013**, *1*, 1102.
- (57) W.-r. Lee, Y.-S. Jun, J. Park, G. D. Stucky, *J. Mater. Chem. A* **2015**, *3*, 24232.
- (58) C. Fettkenhauer, J. Weber, M. Antonietti, D. Dontsova, *RSC Adv.* **2014**, *4*, 40803.

- (59) E. Kroke, *Angew. Chem. Int. Ed.* **2014**, *53*, 11134.
- (60) X. Wang, K. Maeda, A. Thomas, K. Takanahe, G. Xin, J. M. Carlsson, K. Domen, M. Antonietti, *Nat. Mater.* **2009**, *8*, 76.
- (61) V. W. Lau, K. Schwinghammer, B. Lotsch, *Chem. Soc. Rev.* **2016**.
- (62) V. W. Lau, *PhD thesis*, University of Sydney, **2011**.
- (63) T. Maschmeyer, M. Che, *Angew. Chem. Int. Ed.* **2010**, *49*, 1536.
- (64) J. Wirth, R. Neumann, M. Antonietti, P. Saalfrank, *Phys. Chem. Chem. Phys.* **2014**, *16*, 15917.
- (65) X. Zhang, X. Xie, H. Wang, J. Zhang, B. Pan, Y. Xie, *J. Am. Chem. Soc.* **2013**, *135*, 18.
- (66) G. Liu, P. Niu, C. Sun, S. C. Smith, Z. Chen, G. Q. Lu, H.-M. Cheng, *J. Am. Chem. Soc.* **2010**, *132*, 11642.
- (67) H. Zhang, X. Zuo, H. Tang, G. Li, Z. Zhou, *Phys. Chem. Chem. Phys.* **2015**, *17*, 6280.
- (68) X. Ma, Y. Lv, J. Xu, Y. Liu, R. Zhang, Y. Zhu, *J. Phys. Chem. C* **2012**, *116*, 23485.
- (69) H.-Z. Wu, L.-M. Liu, S.-J. Zhao, *Phys. Chem. Chem. Phys.* **2014**, *16*, 3299.
- (70) F. Wu, Y. Liu, G. Yu, D. Shen, Y. Wang, E. Kan, *J. Phys. Chem. Lett.* **2012**, *3*, 3330.
- (71) S. M. Aspera, M. David, H. Kasai, *Jpn. J. Appl. Phys.* **2010**, *49*, 115703.
- (72) S. Sergey, Z. Sebastian, *J. Phys.: Condens. Matter* **2013**, *25*, 085507.
- (73) S. Zuluaga, L.-H. Liu, N. Shafiq, S. M. Rupich, J.-F. Veyan, Y. J. Chabal, T. Thonhauser, *Phys. Chem. Chem. Phys.* **2015**, *17*, 957.
- (74) J. S. Clark, D. M. Segall, J. C. Pickard, J. P. Hasnip, I. J. M. Probert, K. Refson, C. M. Payne, *Zeitschrift für Kristallographie - Crystalline Materials* **2005**; Vol. 220, 567.
- (75) P. Niu, L.-C. Yin, Y.-Q. Yang, G. Liu, H.-M. Cheng, *Adv. Mater.* **2014**, *26*, 8046.
- (76) G. Kresse, J. Furthmüller, *Physical Review B* **1996**, *54*, 11169.
- (77) J. P. Perdew, K. Burke, M. Ernzerhof, *Physical Review Letters* **1996**, *77*, 3865.
- (78) Y. Zhang, M. Antonietti, *Chem. Asian J.*, *5*, 1307.
- (79) J. Liu, T. Zhang, Z. Wang, G. Dawson, W. Chen, *J. Mater. Chem.* **2011**, *21*, 14398.
- (80) A. B. Jorge, D. J. Martin, M. T. S. Dhanoa, A. S. Rahman, N. Makwana, J. Tang, A. Sella, F. Corà, S. Firth, J. A. Darr, P. F. McMillan, *J. Phys. Chem. C* **2013**, *117*, 7178.
- (81) T. Tyborski, C. Merschjann, S. Orthmann, F. Yang, M. C. Lux-Steiner, S.-N. Th, *Journal of Physics: Condensed Matter* **2012**, *24*, 162201.
- (82) C. Butchosa, P. Guiglion, M. A. Zwijnenburg, *J. Phys. Chem. C* **2014**, *118*, 24833.
- (83) S. K. Zhang, H. Lu, W. B. Wang, B. B. Das, N. Okoye, M. Tamargo, R. R. Alfano, *J. Appl. Phys.* **2007**, *101*, 023111.
- (84) <http://blog.disorderedmatter.eu/2008/04/15/polaron-polaron-pair-exciton-exciplex/>; accessed on 1<sup>st</sup> of February **2016**
- (85) J. Schneider, M. Matsuoka, M. Takeuchi, J. Zhang, Y. Horiuchi, M. Anpo, D. W. Bahnemann, *Chem. Rev.* **2014**, *114*, 9919.
- (86) C. Merschjann, T. Tyborski, S. Orthmann, F. Yang, K. Schwarzburg, M. Lublow, M. C. Lux-Steiner, T. Schedel-Niedrig, *Phys. Rev. B* **2013**, *87*, 205204.
- (87) C. Merschjann, S. Tschierlei, T. Tyborski, K. Kailasam, S. Orthmann, D. Hollmann, T. Schedel-Niedrig, A. Thomas, S. Lochbrunner, *Adv. Mater.* **2015**, *27*, 7993.



- (88) K. Schwinghammer, B. Tuffy, M. B. Mesch, E. Wirnhier, C. Martineau, F. Taulelle, W. Schnick, J. Senker, B. V. Lotsch, *Angew. Chem. Int. Ed.* **2013**, *52*, 2435.
- (89) E. J. McDermott, E. Wirnhier, W. Schnick, K. S. Viridi, C. Scheu, Y. Kauffmann, W. D. Kaplan, E. Z. Kurmaev, A. Moewes, *J. Phys. Chem. C* **2013**, *117*, 8806.
- (90) M. Deifallah, P. F. McMillan, F. Corà, *J. Phys. Chem. C* **2008**, *112*, 5447.
- (91) A. H. Reshak, S. A. Khan, S. Auluck, *RSC Adv.* **2014**, *4*, 6957.
- (92) S. C. Yan, Z. S. Li, Z. G. Zou, *Langmuir* **2009**, *25*, 10397.
- (93) G. Zhang, J. Zhang, M. Zhang, X. Wang, *J. Mater. Chem.* **2012**, *22*, 8083.
- (94) F. Dong, Z. Wang, Y. Sun, W.-K. Ho, H. Zhang, *J. Colloid Interf. Sci.* **2013**, *401*, 70.
- (95) S. Cao, J. Low, J. Yu, M. Jaroniec, *Adv. Mater.* **2015**, *27*, 2150.
- (96) D. J. Martin, K. Qiu, S. A. Shevlin, A. D. Handoko, X. Chen, Z. Guo, J. Tang, *Angew. Chem. Int. Ed.* **2014**, *53*, 9240.
- (97) W. Zhang, Q. Zhang, F. Dong, Z. Zhao, *Int. J. Photoenergy* **2013**, *2013*, 9.
- (98) P. Wu, J. Wang, J. Zhao, L. Guo, F. E. Osterloh, *J. Mater. Chem. A* **2014**, *2*, 20338.
- (99) P. Pichat, *Photocatalysis and Water Purification - From Fundamentals to Recent Applications*, Wiley-VCH Weinheim, Germany, **2013**.
- (100) S. Bakardjieva, V. Stengl, L. Szatmary, J. Subrt, J. Lukac, N. Murafa, D. Niznansky, K. Cizek, J. Jirkovsky, N. Petrova, *J. Mater. Chem.* **2006**, *16*, 1709.
- (101) J. Wu, X. Lü, L. Zhang, Y. Xia, F. Huang, F. Xu, *J. Alloys Compd.* **2010**, *496*, 234.
- (102) B. Tryba, M. Toyoda, A. W. Morawski, R. Nonaka, M. Inagaki, *Appl. Catal. B* **2007**, *71*, 163.
- (103) A. L. Linsebigler, G. Lu, J. T. Yates, *Chem. Rev.* **1995**, *95*, 735.
- (104) X. Chen, S. Shen, L. Guo, S. S. Mao, *Chem. Rev.* **2010**, *110*, 6503.
- (105) P. Niu, L. Zhang, G. Liu, H.-M. Cheng, *Adv. Funct. Mater.* **2012**, *22*, 4763.
- (106) H. Wang, *PhD thesis*, University of Munich, LMU, **2013**.
- (107) Y. Wang, J. Hong, W. Zhang, R. Xu, *Catal. Sci. Technol.* **2013**, *3*, 1703.
- (108) M. K. Bhunia, K. Yamauchi, K. Takanabe, *Angew. Chem. Int. Ed.* **2014**, *53*, 11001.
- (109) M. Shalom, S. Inal, C. Fettkenhauer, D. Neher, M. Antonietti, *J. Am. Chem. Soc.* **2013**, *135*, 7118.
- (110) H. Yan, *Chem. Commun.* **2012**, *48*, 3430.
- (111) J. Xu, Y. Wang, Y. Zhu, *Langmuir* **2013**, *29*, 10566.
- (112) M. Zhang, J. Xu, R. Zong, Y. Zhu, *Appl. Catal. B* **2014**, *147*, 229.
- (113) F. Goettmann, A. Fischer, M. Antonietti, A. Thomas, *Angew. Chem. Int. Ed.* **2006**, *45*, 4467.
- (114) Y. Cui, J. Zhang, G. Zhang, J. Huang, P. Liu, M. Antonietti, X. Wang, *J. Mater. Chem.* **2011**, *21*, 13032.
- (115) Y. Cui, J. Huang, X. Fu, X. Wang, *Catal. Sci. Technol.* **2012**, *2*, 1396.
- (116) X. Chen, Y.-S. Jun, K. Takanabe, K. Maeda, K. Domen, X. Fu, M. Antonietti, X. Wang, *Chem. Mater.* **2009**, *21*, 4093.
- (117) H. Yan, Y. Chen, S. Xu, *Int. J. Hydrogen Energy* **2012**, *37*, 125.
- (118) J. Xu, L. Zhang, R. Shi, Y. Zhu, *J. Mater. Chem. A* **2013**, *1*, 14766.

- (119) S. Yang, Y. Gong, J. Zhang, L. Zhan, L. Ma, Z. Fang, R. Vajtai, X. Wang, P. M. Ajayan, *Adv. Mater.* **2013**, *25*, 2452.
- (120) M. J. Bojdys, N. Severin, J. P. Rabe, A. I. Cooper, A. Thomas, M. Antonietti, *Macromol. Rapid Comm.* **2013**, *34*, 850.
- (121) X. She, H. Xu, Y. Xu, J. Yan, J. Xia, L. Xu, Y. Song, Y. Jiang, Q. Zhang, H. Li, *J. Mater. Chem. A* **2014**, *2*, 2563.
- (122) K. Schwinghammer, M. B. Mesch, V. Duppel, C. Ziegler, J. Senker, B. V. Lotsch, *J. Am. Chem. Soc.* **2014**, *136*, 1730.
- (123) F. Cheng, J. Yan, C. Zhou, B. Chen, P. Li, Z. Chen, X. Dong, *J. Colloid Interf. Sci.* **2016**, *468*, 103.
- (124) J. Sun, J. Zhang, M. Zhang, M. Antonietti, X. Fu, X. Wang, *Nat. Commun.* **2012**, 1139.
- (125) Y. S. Jun, E. Z. Lee, X. Wang, W. H. Hong, G. D. Stucky, A. Thomas, *Adv. Funct. Mater.* **2013**, *23*, 3661.
- (126) X.-H. Li, J. Zhang, X. Chen, A. Fischer, A. Thomas, M. Antonietti, X. Wang, *Chem. Mater.* **2011**, *23*, 4344.
- (127) X.-H. Li, X. Wang, M. Antonietti, *Chem. Sci.* **2012**, *3*, 2170.
- (128) X. Bai, L. Wang, R. Zong, Y. Zhu, *J. Phys. Chem. C* **2013**, *117*, 9952.
- (129) Y. Cui, Z. Ding, X. Fu, X. Wang, *Angew. Chem. Int. Ed.* **2012**, *51*, 11814.
- (130) M. Tahir, C. Cao, F. K. Butt, F. Idrees, N. Mahmood, Z. Ali, I. Aslam, M. Tanveer, M. Rizwan, T. Mahmood, *J. Mater. Chem. A* **2013**, *1*, 13949.
- (131) H. Pan, Y.-W. Zhang, V. B. Shenoy, H. Gao, *ACS Catal.* **2011**, *1*, 99.
- (132) X. Wang, X. Chen, A. Thomas, X. Fu, M. Antonietti, *Adv. Mater.* **2009**, *21*, 1609.
- (133) Z. Ding, X. Chen, M. Antonietti, X. Wang, *ChemSusChem* **2011**, *4*, 274.
- (134) J. Tian, Q. Liu, A. M. Asiri, A. H. Qusti, A. O. Al-Youbi, X. Sun, *Nanoscale* **2013**, *5*, 11604.
- (135) X. Song, H. Tao, L. Chen, Y. Sun, *Mater. Lett.* **2014**, *116*, 265.
- (136) S. Hu, R. Jin, G. Lu, D. Liu, J. Gui, *RSC Adv.* **2014**, *4*, 24863.
- (137) S. Tonda, S. Kumar, S. Kandula, V. Shanker, *J. Mater. Chem. A* **2014**, *2*, 6772.
- (138) Y. Bing, L. Qiuye, I. Hideo, K. Tetsuya, Y. Jinhua, *Sci. Technol. Adv. Mater.* **2011**, *12*, 034401.
- (139) H. Gao, S. Yan, J. Wang, Y. A. Huang, P. Wang, Z. Li, Z. Zou, *Phys. Chem. Chem. Phys.* **2013**, *15*, 18077.
- (140) D. Xu, X. Li, J. Liu, L. Huang, *J. Rare Earths* **2013**, *31*, 1085.
- (141) J. Zhang, J. Sun, K. Maeda, K. Domen, P. Liu, M. Antonietti, X. Fu, X. Wang, *Energy Environ. Sci.* **2011**, *4*, 675.
- (142) L. Ge, C. Han, X. Xiao, L. Guo, Y. Li, *Mater. Res. Bull.* **2013**, *48*, 3919.
- (143) Y. Wang, Y. Di, M. Antonietti, H. Li, X. Chen, X. Wang, *Chem. Mater.*, *22*, 5119.
- (144) Y. Wang, J. Zhang, X. Wang, M. Antonietti, H. Li, *Angew. Chem. Int. Ed.*, *49*, 3356.
- (145) G. Zhang, M. Zhang, X. Ye, X. Qiu, S. Lin, X. Wang, *Adv. Mater.* **2014**, *26*, 805.
- (146) J. Li, B. Shen, Z. Hong, B. Lin, B. Gao, Y. Chen, *Chem. Commun.* **2012**, *48*, 12017.
- (147) G. Dong, K. Zhao, L. Zhang, *Chem. Commun.* **2012**, *48*, 6178.
- (148) L. Zhang, X. Chen, J. Guan, Y. Jiang, T. Hou, X. Mu, *Mater. Res. Bull.* **2013**, *48*, 3485.

- (149) Y. Zhang, A. Thomas, M. Antonietti, X. Wang, *J. Am. Chem. Soc.* **2008**, 131, 50.
- (150) J. Fang, H. Fan, M. Li, C. Long, *J. Mater. Chem. A* **2015**, 3, 13819.
- (151) S. Liu, D. Li, H. Sun, H. M. Ang, M. O. Tadé, S. Wang, *J. Colloid Interf. Sci.*
- (152) J. Zhang, X. Chen, K. Takanahe, K. Maeda, K. Domen, J. D. Epping, X. Fu, M. Antonietti, X. Wang *Angew. Chem.* **2010**, 122, 451.
- (153) J. Zhang, G. Zhang, X. Chen, S. Lin, L. Möhlmann, G. Dołęga, G. Lipner, M. Antonietti, S. Blechert, X. Wang, *Angew. Chem. Int. Ed.* **2012**, 51, 3183.
- (154) G. Zhang, X. Wang, *J. Catal.* **2013**, 307, 246.
- (155) J. Zhang, M. Zhang, S. Lin, X. Fu, X. Wang, *J. Catal.* **2014**, 310, 24.
- (156) S. Chu, Y. Wang, Y. Guo, J. Feng, C. Wang, W. Luo, X. Fan, Z. Zou, *ACS Catal.* **2013**, 3, 912.
- (157) Q. Xiang, J. Yu, M. Jaroniec, *J. Phys. Chem. C* **2011**, 115, 7355.
- (158) A. Du, S. Sanvito, Z. Li, D. Wang, Y. Jiao, T. Liao, Q. Sun, Y. H. Ng, Z. Zhu, R. Amal, S. C. Smith, *J. Am. Chem. Soc.* **2012**, 134, 4393.
- (159) X. Li, Y. Dai, Y. Ma, S. Han, B. Huang, *Phys. Chem. Chem. Phys.* **2014**, 16, 4230.
- (160) Y. Li, H. Zhang, P. Liu, D. Wang, Y. Li, H. Zhao, *Small* **2013**, 9, 3336.
- (161) B. Chai, X. Liao, F. Song, H. Zhou, *Dalton Trans.* **2014**, 43, 982.
- (162) Z. Wu, H. Gao, S. Yan, Z. Zou, *Dalton Trans.* **2014**, 43, 12013.
- (163) J. Liu, Y. Liu, N. Liu, Y. Han, X. Zhang, H. Huang, Y. Lifshitz, S.-T. Lee, J. Zhong, Z. Kang, *Science* **2015**, 347, 970.
- (164) X. Zhou, F. Peng, H. Wang, H. Yu, Y. Fang, *Chem. Commun.* **2011**, 47, 10323.
- (165) H. Yan, H. Yang, *J. Alloys Compd.* **2011**, 509, L26.
- (166) X. Zhou, B. Jin, L. Li, F. Peng, H. Wang, H. Yu, Y. Fang, *J. Mater. Chem.* **2012**, 22, 17900.
- (167) J. Wang, W.-D. Zhang, *Electrochim. Acta* **2012**, 71, 10.
- (168) B. Chai, T. Peng, J. Mao, K. Li, L. Zan, *Phys. Chem. Chem. Phys.* **2012**, 14, 16745.
- (169) K. Sridharan, E. Jang, T. J. Park, *Appl. Catal. B* **2013**, 142–143, 718.
- (170) L. Huang, H. Xu, Y. Li, H. Li, X. Cheng, J. Xia, Y. Xu, G. Cai, *Dalton Trans.* **2013**, 42, 8606.
- (171) Y. Zang, L. Li, Y. Zuo, H. Lin, G. Li, X. Guan, *RSC Adv.* **2013**, 3, 13646.
- (172) S. Ye, L.-G. Qiu, Y.-P. Yuan, Y.-J. Zhu, J. Xia, J.-F. Zhu, *J. Mater. Chem. A* **2013**, 1, 3008.
- (173) Y. Wang, R. Shi, J. Lin, Y. Zhu, *Energy Environ. Sci.* **2011**, 4, 2922.
- (174) J.-X. Sun, Y.-P. Yuan, L.-G. Qiu, X. Jiang, A.-J. Xie, Y.-H. Shen, J.-F. Zhu, *Dalton Trans.* **2012**, 41, 6756.
- (175) H. Yan, Y. Huang, *Chem. Commun.* **2011**, 47, 4168.
- (176) Y. Sui, J. Liu, Y. Zhang, X. Tian, W. Chen, *Nanoscale* **2013**, 5, 9150.
- (177) K. Takanahe, K. Kamata, X. Wang, M. Antonietti, J. Kubota, K. Domen, *Phys. Chem. Chem. Phys.* **2010**, 12, 13020.
- (178) W. Wang, J. C. Yu, D. Xia, P. K. Wong, Y. Li, *Environ. Sci. Technol.* **2013**, 47, 8724.
- (179) Y.-P. Yuan, S.-W. Cao, Y.-S. Liao, L.-S. Yin, C. Xue, *Appl. Catal. B* **2013**, 140–141, 164.

- (180) F. Dong, Z. Zhao, T. Xiong, Z. Ni, W. Zhang, Y. Sun, W.-K. Ho, *ACS Appl. Mater. Interfaces* **2013**, *5*, 11392.
- (181) J. Zhang, M. Zhang, R.-Q. Sun, X. Wang, *Angew. Chem. Int. Ed.* **2012**, *51*, 10145.
- (182) Z. Zhao, Y. Sun, F. Dong, *Nanoscale* **2015**, *7*, 15.
- (183) Y.-P. Yuan, W.-T. Xu, L.-S. Yin, S.-W. Cao, Y.-S. Liao, Y.-Q. Tng, C. Xue, *Int. J. Hydrogen Energy* **2013**, *38*, 13159.
- (184) X. Li, G. Hartley, A. J. Ward, P. A. Young, A. F. Masters, T. Maschmeyer, *J. Phys. Chem. C* **2015**, *119*, 14938.
- (185) X. L. Wang, W. Q. Fang, H. F. Wang, H. Zhang, H. Zhao, Y. Yao, H. G. Yang, *J. Mater. Chem. A* **2013**, *1*, 14089.
- (186) Z. Hong, B. Shen, Y. Chen, B. Lin, B. Gao, *J. Mater. Chem. A* **2013**, *1*, 11754.
- (187) Y. Bing, L. Qiuye, I. Hideo, K. Tetsuya, Y. Jinhua, *Science and Technology of Advanced Materials* **2011**, *12*, 034401.
- (188) X. Wang, K. Maeda, X. Chen, K. Takanaabe, K. Domen, Y. Hou, X. Fu, M. Antonietti, *J. Am. Chem. Soc.* **2009**, *131*, 1680.
- (189) Q. Li, B. Yue, H. Iwai, T. Kako, J. Ye, *J. Phys. Chem. C* **2010**, *114*, 4100.
- (190) X. Fan, L. Zhang, R. Cheng, M. Wang, M. Li, Y. Zhou, J. Shi, *ACS Catal.* **2015**, *5*, 5008.
- (191) L. Ge, C. Han, *Appl. Catal. B* **2012**, *117–118*, 268.
- (192) S. Min, G. Lu, *J. Phys. Chem. C* **2012**, *116*, 19644.
- (193) X. Zhang, L. Yu, C. Zhuang, T. Peng, R. Li, X. Li, *ACS Catal.* **2014**, *4*, 162.
- (194) J. Yu, S. Wang, B. Cheng, Z. Lin, F. Huang, *Catal. Sci. Technol.* **2013**, *3*, 1782.
- (195) Y. Hou, A. B. Laursen, J. Zhang, G. Zhang, Y. Zhu, X. Wang, S. Dahl, I. Chorkendorff, *Angew. Chem. Int. Ed.* **2013**, *52*, 3621.
- (196) J. Hong, Y. Wang, Y. Wang, W. Zhang, R. Xu, *ChemSusChem* **2013**, *6*, 2263.
- (197) J. Dong, M. Wang, X. Li, L. Chen, Y. He, L. Sun, *ChemSusChem* **2012**, *5*, 2133.
- (198) H. W. Kang, S. N. Lim, D. Song, S. B. Park, *Int. J. Hydrogen Energy* **2012**, *37*, 11602.
- (199) H. Katsumata, Y. Tachi, T. Suzuki, S. Kaneco, *RSC Adv.* **2014**, *4*, 21405.
- (200) J. Chen, S. Shen, P. Guo, M. Wang, P. Wu, X. Wang, L. Guo, *Appl. Catal. B* **2014**, *152–153*, 335.
- (201) S.-W. Cao, X.-F. Liu, Y.-P. Yuan, Z.-Y. Zhang, Y.-S. Liao, J. Fang, S. C. J. Loo, T. C. Sum, C. Xue, *Appl. Catal. B* **2014**, *147*, 940.
- (202) Y. Ham, K. Maeda, D. Cha, K. Takanaabe, K. Domen, *Chem. Asian J.* **2013**, *8*, 218.
- (203) D. Dontsova, S. Pronkin, M. Wehle, Z. Chen, C. Fettkenhauer, G. Clavel, M. Antonietti, *Chem. Mater.* **2015**, *27*, 5170.
- (204) B. Ohtani, *Chem. Lett.* **2008**, *37*, 216.
- (205) J.-M. Herrmann, *J. Photochem. Photobiol. A* **2010**, *216*, 85.
- (206) H. Kisch, *Angew. Chem. Int. Ed.* **2010**, *49*, 9588.
- (207) M. Schwarze, D. Stellmach, M. Schroder, K. Kailasam, R. Reske, A. Thomas, R. Schomacker, *Phys. Chem. Chem. Phys.* **2013**, *15*, 3466.
- (208) M. Rochkind, S. Pasternak, Y. Paz, *Molecules* **2014**, *20*, 88.

- (209) M. Ash, I. Ash, *Handbook of Green Chemicals*, 2nd ed., Synapse Information Resources, Inc. : Endicott, NY, **2004**.
- (210) J. Schneider, D. W. Bahnemann, *J. Phys. Chem. Lett.* **2013**, *4*, 3479.
- (211) J. Yang, D. Wang, H. Han, C. Li, *Acc. Chem. Res.* **2013**, *46*, 1900.
- (212) A. P. Côté, A. I. Benin, N. W. Ockwig, M. O'Keeffe, A. J. Matzger, O. M. Yaghi, *Science* **2005**, *310*, 1166.
- (213) O. M. Yaghi, M. O'Keeffe, N. W. Ockwig, H. K. Chae, M. Eddaoudi, J. Kim, *Nature* **2003**, *423*, 705.
- (214) F. Haase, Communication about COF-linkages.
- (215) P. Kuhn, M. Antonietti, A. Thomas, *Angew. Chem. Int. Ed.* **2008**, *47*, 3450.
- (216) K. Kamiya, R. Kamai, K. Hashimoto, S. Nakanishi, *Nat. Commun.* **2014**, *5*.
- (217) T. Wang, K. Kailasam, P. Xiao, G. Chen, L. Chen, L. Wang, J. Li, J. Zhu, *Microporous and Mesoporous Materials* **2014**, *187*, 63.
- (218) X. Jiang, P. Wang, J. Zhao, *J. Mater. Chem. A* **2015**, *3*, 7750.
- (219) S. Hug, M. B. Mesch, H. Oh, N. Popp, M. Hirscher, J. Senker, B. V. Lotsch, *J. Mater. Chem. A* **2014**, *2*, 5928.
- (220) P. Katekomol, J. Roeser, M. Bojdys, J. Weber, A. Thomas, *Chem. Mater.* **2013**, *25*, 1542.
- (221) F. Chang, J. Guo, G. Wu, L. Liu, M. Zhang, T. He, P. Wang, P. Yu, P. Chen, *RSC Adv.* **2015**, *5*, 3605.
- (222) S. Dalapati, M. Addicoat, S. Jin, T. Sakurai, J. Gao, H. Xu, S. Irle, S. Seki, D. Jiang, *Nat. Commun.* **2015**, *6*.



## Chapter III

### 3 Poly(triazine imide) as photocatalyst

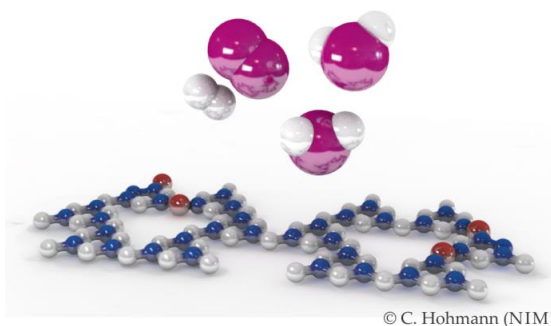
#### 3.1 Co-polymerization of PTI

##### Triazine-based carbon nitrides for visible-light driven hydrogen evolution

Katharina Schwinghammer, Brian Tuffy, Maria B. Mesch, Eva Wirnhier, Charlotte Martineau, Francis Taulelle, Wolfgang Schnick, Jürgen Senker and Bettina V. Lotsch

Published in: *Angew. Chem.* **2013**, *125*, 2495–2499; *Angew. Chem. Int. Ed.* **2013**, *52*, (2435–2439); DOI: 10.1002/anie.201206817.

Keywords: Carbon nitrides; copolymerization; photocatalysis; triazines; water splitting



#### Abstract

A new dimension: The doping of amorphous poly(triazine imide) (PTI) through ionothermal copolymerization of dicyandiamide with 4-amino-2,6-dihydropyrimidine (4AP) results in triazine-based carbon nitrides with increased photoactivity for water splitting compared to crystalline poly(triazine imide) (PTI/Li<sup>+</sup>Cl<sup>-</sup>) and melon-type carbon nitrides. This family of carbon nitride semiconductors has potential as low-cost, environmentally clean photocatalysts for solar fuel production.

### 3.1.1 Introduction

The development of catalysts that enable the direct conversion of solar energy into chemical energy has been defined as one of the major challenges of modern materials chemistry. Hydrogen generated by photochemical water splitting has been identified as a promising energy carrier that offers a high energy density while being environmentally clean.<sup>1</sup> Nevertheless, to realize a light-driven hydrogen-based economy, the exploration of new materials for highly efficient, stable, economically viable, and environmentally friendly photocatalysts is required.

To date, numerous inorganic semiconductors have been developed for water splitting, most of them being transition metal compounds containing heavy metals such as La, Bi, Ta, or Nb, which impede scalability, increase cost, and add complexity.<sup>2</sup> Recently, attention has been attracted to a new class of metal-free photocatalysts, comprising polymeric melon-type carbon nitrides (CNs) based on imide-bridged heptazine units (see Figure 3.1(a)).<sup>3</sup> CNs are readily accessible, light weight, stable, and low-cost compounds that offer an attractive alternative to metal-rich catalysts while still maintaining efficient photoactivity.<sup>4</sup> Thermal condensation of CNs forms a wide variety of chemical species that differ substantially with respect to their degree of condensation, hydrogen content, crystallinity, and morphology.<sup>5,6</sup> The chemical modification of CNs by molecular “dopants” has resulted in a number of CN materials with improved photocatalytic activity.<sup>7</sup> Although the evidence is largely empirical, the property enhancement presumably originates from subtle modifications of the parent structures by incorporation of heteroatoms as well as structural defects, to give rise to enhanced absorption in the visible light range and a more complete exploitation of the solar energy spectrum.

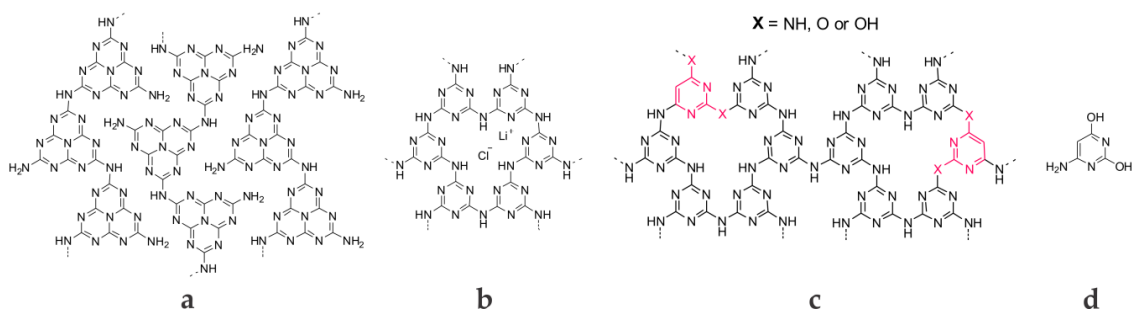


**Figure 3.1** Chemical structures of (a) melon, (b) PTI/LiCl (idealized structure), (c) aPTI-4AP<sub>16%</sub> (proposed structure), and (d) the dopant 4AP.

In contrast to all known CN photocatalysts, which are composed of heptazine building blocks, poly(triazine imide) (PTI/LiCl) is the only structurally characterized 2D CN network featuring imide-linked triazine units (see Figure 3.1(b)).<sup>8,9</sup> Owing to its high level of crystallinity, PTI/LiCl lends itself as an excellent model system to study photocatalytic activity towards water splitting as a function of the number of building blocks, the composition, and the degree of structural perfection of the system. Herein, we present a new generation of CN photocatalysts based on triazine building blocks and demonstrate their



enhanced photocatalytic activity in comparison to heptazine-based CNs. Moreover, we show that their performance can be amplified by small-molecule doping, thus rendering them the most active non-metal photocatalysts for the hydrogen evolution reaction that have been reported to date.

### 3.1.2 Results and discussion

As a starting point, we synthesized crystalline PTI/LiCl as a model structure for triazine-based CNs in a two-step ionothermal synthesis according to the procedure of *Wirnhier et al.*<sup>8,9</sup> To study the effect of crystallinity on the photocatalytic activity, we also synthesized an amorphous variant of PTI (aPTI), through a one-step ionothermal synthesis involving a LiCl/KCl salt melt. We used 4-amino-2,6-dihydroxypyrimidine (4AP) (Figure 3.1(d)) as the dopant because of its structural similarity to melamine and higher carbon and oxygen content. The photocatalytic activity of the as-prepared CNs was compared with that of crystalline PTI/LiCl and of heptazine-based raw melon (7.1 Supporting information).

The XRD patterns of the aPTI samples confirm their amorphous character by the absence of sharp reflections (Figure S1, 7.1 Supporting information), which are present in the XRD patterns of crystalline PTI/LiCl. However, the FTIR spectra of the synthesized aPTI CNs are still largely similar to that of PTI/LiCl<sup>8</sup> (Figure 3.2(d) and Figure S2–3, 7.1 Supporting information), as they contain a band at 810 cm<sup>-1</sup> (ring sextant out of plane bending) and a fingerprint region between 1200 cm<sup>-1</sup> and 1620 cm<sup>-1</sup> that is dominated by  $\nu(\text{C-NH-C})$  and  $\nu(\text{C=N})$  stretching vibrations.<sup>5,10</sup> Doping with 4AP gives rise to less well-defined IR bands, thereby indicating a decrease in the structural order. In addition, in the spectra of 16 % and 32 % doped PTI there is a band at 914 cm<sup>-1</sup> that can be assigned to aromatic C–H bending vibrations of the dopant (Figure S3, 7.1 Supporting information). Interestingly, the bands at 2160 cm<sup>-1</sup>, 1730 cm<sup>-1</sup>, and around 1200 cm<sup>-1</sup>, which are seen in the spectrum of aPTI and partially in those of the doped samples, point to the presence of terminal nitrile groups as well as oxygen containing functionalities, such as C=O and C–O.

Elemental analysis (EA) indicates the molar ratio C/N = 0.68 for PTI/LiCl, whereas the C/N ratios of the aPTI samples are slightly increased for those synthesized at elevated temperatures, indicating either a higher degree of condensation or an increase of oxygen incorporation (Table S1, 7.1 Supporting information). Notably, the amount of Li and Cl is lower in doped and non-doped aPTI than in crystalline PTI/LiCl, whereas the oxygen content is significantly higher, consistent with the IR results. This finding is worth noting as the amount of carbon and oxygen atoms in CNs is likely to play an essential role in the activity of CN photocatalysts.<sup>11</sup> By increasing the amount of 4AP incorporated in the doped PTI from 2 % to 64 % the C/N ratio increases from 0.69 to 1.13, respectively (Table S2, 7.1 Supporting information). In summary, the EA and IR results suggest that both carbon and oxygen atoms are incorporated into the amorphous materials, most likely

through replacement of one of the ring or bridging nitrogen atoms, as proposed in Figure 3.1(c).

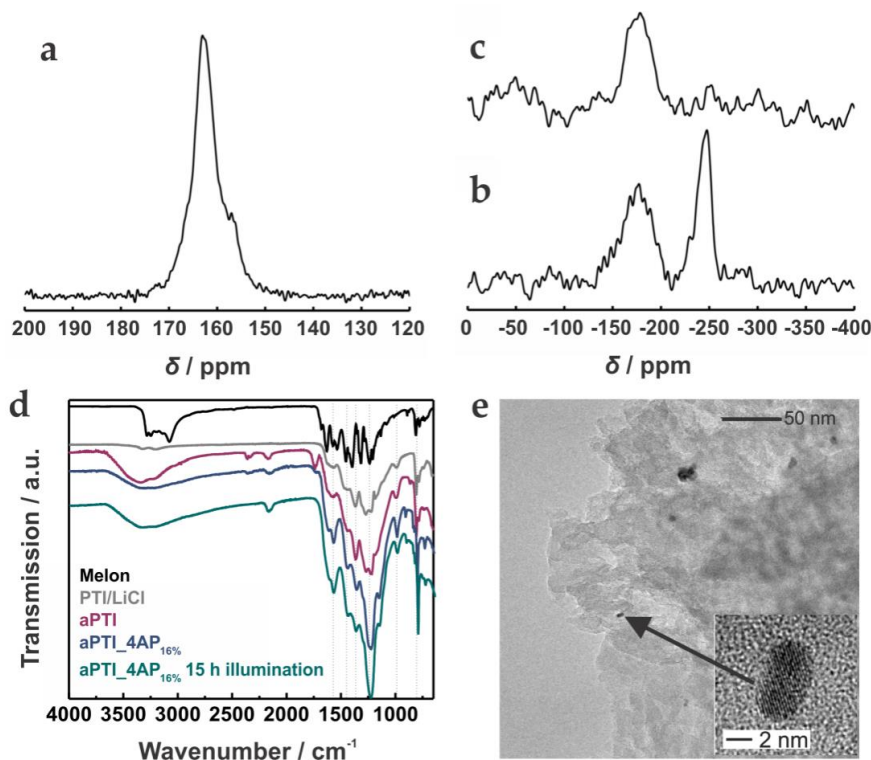


**Figure 3.2**  $^{13}\text{C}$  CP-MAS NMR spectrum (10 kHz) (a),  $^{15}\text{N}$  CPPI-MAS NMR spectrum (6 kHz, inversion time = 400 ms) (b) and  $^{15}\text{N}$  CP-MAS NMR spectrum (10 kHz) of aPTI-4AP<sub>16%</sub> (c). FTIR spectra of aPTI-4AP<sub>16%</sub> synthesized at 550 °C before and after 15 h illumination, compared to crystalline PTI/LiCl, aPTI<sub>500 °C</sub>, and melon (d). A typical image of 2.3 wt% Pt-loaded PTI-4AP<sub>8%</sub> after illumination for 3 h under visible light ( $\lambda \geq 420$  nm) (e) and at higher magnification (inset).

The  $^{13}\text{C}$  and  $^{15}\text{N}$  cross-polarization magic-angle spinning (CP-MAS) NMR spectra (Figure 3.1(a,c)) for aPTI doped with 16 % 4AP and synthesized at 550 °C (aPTI-4AP<sub>16%</sub>) provide additional information about the structural composition of the material derived from copolymerization with 4AP. Both spectra are similar to those of PTI/LiCl (Figure S4, 7.1 Supporting information),<sup>8,9</sup> albeit with significantly increased line width (full width at half maximum (FWHM)) of 1.5 kHz compared to 600 Hz) owing to the less ordered character of the materials (Figure S1, 7.1 Supporting information). The  $^{15}\text{N}$  CP-MAS spectrum shows two broad signal groups centered around -175 ppm and -245 ppm. The former group is typical for tertiary ring nitrogen atoms ( $\text{N}_{\text{tert}}$ ; from the outer ring nitrogen atoms of heptazine or triazine rings), whereas the latter is characteristic of bridging NH groups. A very weak signal around -280 ppm indicates that only a small amount of terminal  $\text{NH}_2$  groups is present, hence a melon-type structure seems very unlikely. However, to further corroborate this hypothesis and identify the type of heterocycle formed under the conditions used — triazine *versus* heptazine — we recorded a  $^{15}\text{N}$  cross polarization polarization inversion (CPPI)<sup>12</sup> NMR spectrum of aPTI-4AP<sub>16%</sub> (Figure 3.2(b)) with an inversion time of 400 ms. Under such conditions, resonances of the NH groups are reduced to zero intensity whereas signals of  $\text{NH}_2$  units will be inverted. In contrast, the  $^{15}\text{N}$  signals of tertiary nitro-

gen atoms are expected to remain largely unaffected. Hence, the unique signal for the central nitrogen atom,  $N_c$ , of a heptazine ring between  $-220$  ppm and  $-240$  ppm can unequivocally be identified.<sup>5</sup> The absence of any signals in the  $^{15}\text{N}$  CPPI spectrum (Figure 3.2(b)) in the region between  $-200$  ppm and  $-300$  ppm therefore strongly suggests the absence of heptazine units within the detection limit of roughly 10 % – 15 %. The markedly different intensity ratios in the  $^{13}\text{C}$  CP-MAS spectrum of aPTI-4AP<sub>16%</sub> (Figure 3.2(a)) compared to those in the  $^{13}\text{C}$  CP-MAS spectrum of PTI/LiCl, and the broad asymmetric high-field flank of the signal between  $-140$  ppm and  $-170$  ppm in the  $^{15}\text{N}$  CP-MAS spectrum (Figure 3.2(c)) may indicate partial incorporation of pyrimidine into the PTI framework during copolymerization, which is not observed for PTI/LiCl.<sup>8,9</sup>

The brown color of crystalline PTI/LiCl indicates substantial absorption in the visible range of the spectrum. More specifically, the material absorbs largely in the UV region, yet additional absorption takes place in the blue part of the visible region and there is a gradual decrease in absorption toward higher wavelengths (Figure 3.3(b) and Figure S5, 7.1 Supporting information). The absorption spectra of aPTI synthesized at  $400$  °C –  $600$  °C show bands that are comparable to those in the spectrum of melon, thus rendering the color of the materials similar to that of melon (Figure 3.3(b)). When the reaction temperature is increased, the color of aPTI changes from cream ( $400$  °C) to yellow ( $500$  °C), suggesting enhanced absorption in the visible region. The absorption of aPTI<sub>500 °C</sub>, which is synthesized at a reaction temperature of  $500$  °C, is strongly red-shifted compared to that of crystalline PTI/LiCl, thereby representing further improvement in the visible-light absorption (Figure S5, 7.1 Supporting information). With increasing amounts of dopant the color of the 4AP-doped CNs gets darker, changing from yellow (2 %) to red-brown (64 %); this color change correlates well with the red-shift observed in the absorption spectra (Figure S6, 7.1 Supporting information).

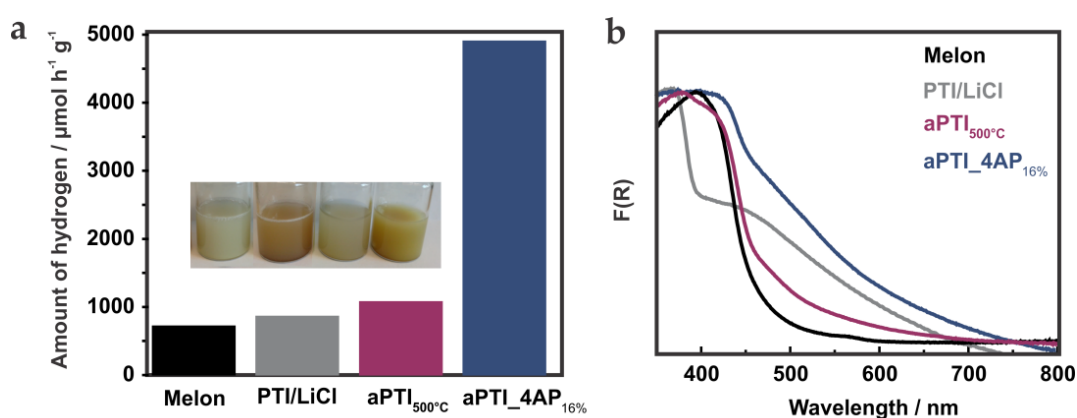


**Figure 3.3** Photocatalytic activity towards visible-light induced hydrogen production using 2.3 wt% Pt and 10 mg of photocatalyst dispersed in 10 mL of 10 vol% TEoA (a). UV-Vis spectra and color of the water/TEoA suspensions (inset in a) of aPTI-4AP<sub>16%</sub> synthesized at  $550$  °C compared to crystalline PTI/LiCl, aPTI synthesized at  $500$  °C, and melon (b).

The inherent 2D architecture of crystalline PTI/LiCl gives rise to an expanded  $\pi$ -electron system, lower band-gap, and enhanced absorption as compared to the 1D polymer

melon, and thus renders PTI/LiCl a promising photocatalyst that may even outperform the heptazine-based semiconductors. In fact, hydrogen production of  $864 \mu\text{mol h}^{-1} \text{g}^{-1}$  (ca. 15 % error) was measured for crystalline PTI/LiCl in the presence of a Pt co-catalyst and triethanolamine (TEoA) as sacrificial electron donor; this result equates to an enhancement of approximately 20 % compared to synthesized raw melon (see 7.1 Supporting information;  $722 \mu\text{mol h}^{-1} \text{g}^{-1}$ ) and is comparable to “g-C<sub>3</sub>N<sub>4</sub>” synthesized at 600 °C (synthesis according to *Zhang et al.*; <sup>7a</sup>  $844 \mu\text{mol h}^{-1} \text{g}^{-1}$ ). The photocatalytic activity of the amorphous CNs synthesized in an open system in the temperature range 400 °C – 600 °C showed that the highest activity was achieved for the CN synthesized at a reaction temperature of 500 °C ( $1080 \mu\text{mol h}^{-1} \text{g}^{-1}$ ); this activity corresponds to an approximately 50 % enhancement compared to that of raw melon (see Table 3.1).

**Table 3.1** Physicochemical properties and photocatalytic activity of different Pt/CN<sub>x</sub> species for the hydrogen evolution reaction driven by visible light.

catalyst	surface area / $\text{m}^2 \text{g}^{-1}$	C/N molar ratio	hydrogen evolution rate / $\mu\text{mol h}^{-1} \text{g}^{-1}$	apparent quantum efficiency / %
PTI/LiCl	37	0.68	864	0.60
melon	18	0.62	722	0.50
aPTI <sub>500°C</sub>	122	0.69	1080	0.75
aPTI-4AP <sub>16%</sub>	60	0.82	4907	3.40

Although the above results show a moderate improvement of the photocatalytic activity of PTI-derived materials compared to melon-based ones, when PTI is doped with 4AP the increase in the photoactivity of PTI is a function of the doping level and synthesis temperature. By increasing the temperature from 400 °C to 600 °C, an optimum photocatalytic activity was measured for the material synthesized at 550 °C (Figure S9, 7.1 Supporting information). When the content of 4AP was increased from 2 % to 64 %, the highest photocatalytic activity of  $4907 \mu\text{mol h}^{-1} \text{g}^{-1}$  (3.4 % [420 nm – 460 nm] apparent quantum efficiency) was detected for 16 % doped aPTI, synthesized at 550 °C (aPTI-4AP<sub>16%</sub>) (Figure S9, 7.1 Supporting information and Table 3.1). In essence, the photocatalytic activity of PTI/LiCl can be enhanced by 5–6 times upon doping with 4AP in a simple one-pot reaction. 4AP doping of crystalline PTI/LiCl leads to no apparent photocatalytic activity. Also, as a control experiment, pure 4AP was shown to be photocatalytically inactive by itself and under ionothermal or thermal treatment. Water oxidation experiments in which O<sub>2</sub> evolution was measured, carried out in the presence of a Co<sub>3</sub>O<sub>4</sub> co-catalyst, did not yield substantial amounts of oxygen, thus suggesting that either water oxidation is thermodynamically unfeasible or that the reaction conditions need to be further optimized.

A typical TEM micrograph shows that the surface morphology of doped aPTI is layered and platelet-like (Figure 3.2(d) and Figure S7, 7.1 Supporting information). The crystallite size and composition of the platinum nanoparticles deposited on the carbon nitride cata-

lyst *in situ* were studied by TEM and EDX. The results reveal that the photoinduced reduction of the co-catalyst results in well-dispersed nanoparticles roughly 5 nm in diameter.

N<sub>2</sub> sorption measurements allow us to quantify the impact of the surface area (SA) of the catalysts on the photocatalytic activity. In Table 3.1, the measured specific Brunauer–Emmett–Teller (BET) SAs indicate a weak correlation between SA and activity, but the increased photoactivity in the doped species cannot be rationalized by an increased SA alone.

As seen in Figure 3.3, the aPTI-4AP<sub>16%</sub> photocatalyst yields an orange-brown suspension and its diffuse reflectance spectrum spans across the visible region. It is therefore instructive to examine the wavelength-specific hydrogen production to determine which wavelengths actively contribute to the H<sub>2</sub> evolution. In the wavelength dependence graph (Figure 16), the absorption is overlaid with the wavelength specific hydrogen evolution. The hydrogen production rate falls off at 450 nm – 500 nm, thus indicating that the majority of photons contributing to the hydrogen production are at  $\lambda < 500$  nm. It is suggested that the active absorption follows the band edge observed between 430 nm and 440 nm. This band is similar to that seen for the other PTI compounds although red-shifted by the 4AP doping. The broad absorption profile suggests the existence of intra band gap electronic states at various energies, which could arise from the incorporated 4AP (Figure S3, 7.1 Supporting information). However, as Figure 3.4 infers, not all electronic states – especially those associated with absorption at higher wavelengths – contribute to the hydrogen evolution but may rather act as traps and quenching sites for excitons.

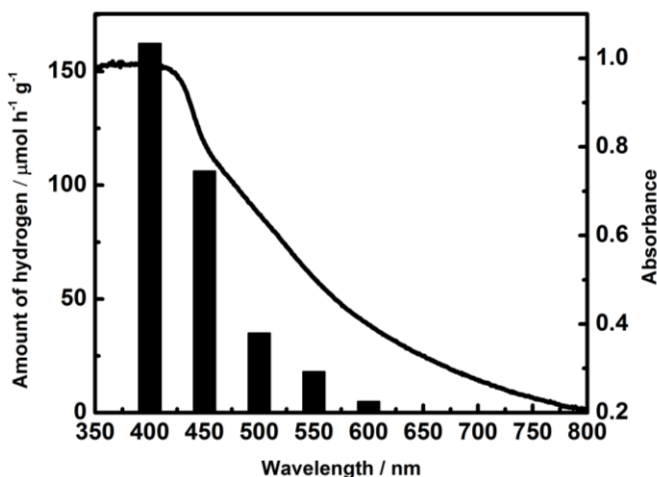


**Figure 3.4** Overlay of UV-Vis F(R) spectrum and wavelength-specific hydrogen production (black bars) of aPTI-4AP<sub>16%</sub> in 10 vol% TEOA and 2.3 wt% Pt using 40 nm FWHM band-pass filters.

We therefore envision that through active control of the number and position of defects in the material, photocatalysts with further enhanced activity can rationally be designed. Nevertheless, the increased visible-light activity up to approximately 500 nm in doped PTI results in a significant improvement over its undoped or crystalline counterparts and is a contributing factor to its high photoactivity.

### 3.1.3 Conclusion

In conclusion, we have reported a new family of 2D triazine-based carbon nitrides that shows substantial visible light-induced hydrogen production from water, and in this regard rivals the benchmark heptazine-derived photocatalysts. With external quantum efficiencies as high as 3.4 %, the amorphous carbon- and oxygen-enriched poly(triazine imide) species not only outperform melon-type photocatalysts, but also crystalline PTI by 5 to 6 times. Consistent with previous results,<sup>13</sup> we have demonstrated that a rather low level of structural definition and the introduction of defects up to a certain doping level (16 % for 4-amino-2,6-dihydroxypyrimidine) tend to enhance the photoactivity of the catalysts.

We believe that the diverse range of available organic and inorganic dopants will allow the rational design of a broad set of triazine-based CN polymers with controlled functions, thus opening new avenues for the development of light-harvesting semiconductors. The easily adjustable structural and electronic properties of CN polymers render them particularly versatile for solar energy applications.

### 3.1.4 Further co-polymerization experiments

Since the ionothermal co-polymerization reactions with 16 % 4AP and dicyandiamide resulted in highly photocatalytically active materials, further co-polymerization reactions with 16 % 2-amino-4,6-dihydroxypyrimidine (2AP), 2,4,6-triaminopyrimidine (TAP) and barbituric acid (BA) were carried out. The chemical structures of the dopants are depicted in Figure 3.5 and resemble the core unit of PTI, which should favor the incorporation of the dopant. The synthesis was carried out at the optimal conditions described before, using an argon atmosphere and a reaction temperature of 550 °C. The samples were heated twice for six hours at the peak temperature and were ground in-between to achieve homogenous condensation. The co-polymers were tested under identical photocatalytic conditions (see 7.1 Supporting information); thus a direct comparison is possible. The results are compared to amorphous PTI co-polymerized with melamine, which should result in simple amorphous PTI, and amorphous PTI synthesized exclusively with dicyandiamide.

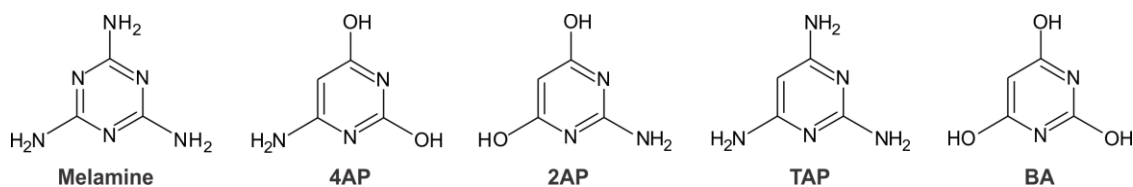


**Figure 3.5** Chemical structures of the dopants: melamine, 4AP, 2AP, TAP and BA (from left to right).

According to PXRD and IR spectroscopy, no significant differences can be detected between the products (Figure 3.6). All samples are rather ill-defined materials and show residual nitrile groups in addition to the characteristic PTI bands due to incomplete condensation or cyclo-reversion of the triazine ring during synthesis. Compared to melamine-



doped amorphous PTI, the 2AP, 4AP, TAP and BA co-polymerized samples exhibit an additional reflection at  $8.2^\circ 2\theta$ . This reflection might be attributed to partial potassium intercalation within the C,N-plane.<sup>15</sup> All doped amorphous samples show a larger potassium (up to 11 wt%) than lithium (0.4 wt%) content in contrast to crystalline PTI/LiCl.

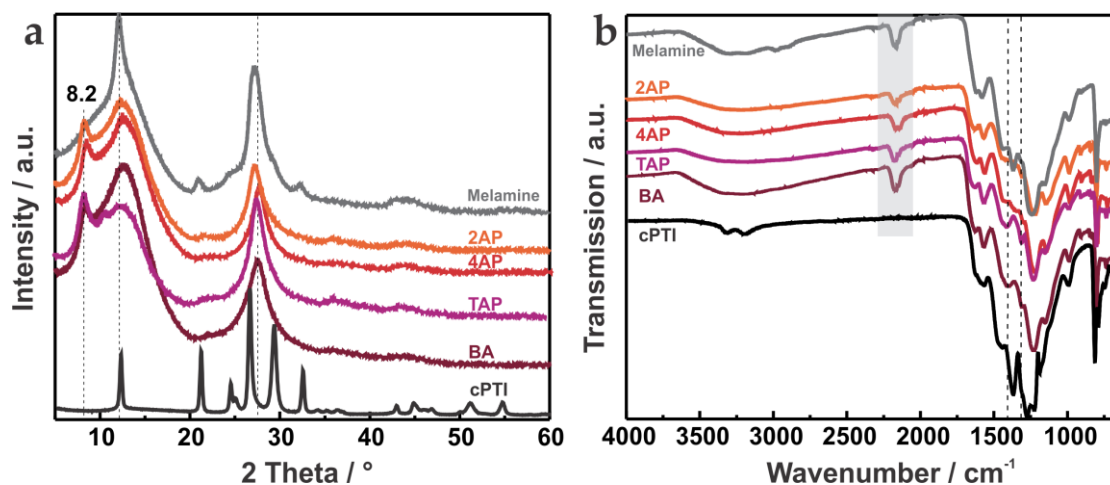


**Figure 3.6** PXRD patterns (a) and IR spectra (b) of the aPTI samples co-polymerized with melamine, 2AP, 4AP, TAP and BA, compared to crystalline PTI.

**Table 3.2** Elemental analysis of the melamine, 2AP, 4AP, TAP and BA co-polymerized amorphous PTI samples compared to non-doped amorphous PTI.

dopant	C [wt%]	N [wt%]	H [wt%]	rest [wt%]	C/N [wt.]
no dopant	27.8	47.5	2.2	22.5	0.58
melamine	30.1	48.7	2.4	18.8	0.62
4AP	29.6	44.3	2.7	23.4	0.67
2AP	29.0	44.4	1.9	24.7	0.65
TAP	30.0	44.1	2.4	23.5	0.68
BA	29.9	42.7	2.5	24.9	0.70

Unlike the PXRD and IR results, the samples differ in their elemental composition (Table 3.2). All samples show an increased C/N weight ratio compared to non-doped amorphous PTI synthesized under identical conditions. Even melamine-doped PTI shows a higher C/N ratio compared to non-doped PTI which might be due to two reasons: Melamine as precursor might lead to more condensed products compared to dicyandiamide, or to incipient carbonization. As expected, doping with 4AP, 2AP, TAP and BA lead to samples with larger C/N weight ratios and thus, carbon content, compared to melamine co-polymerized PTI. The differences in the C/N ratios of the doped samples demonstrate that either the quantity of inserted dopants varies or partial carbonization might take place as a side reaction. The BA- and TAP-co-polymerized samples exhibit higher C/N ratios compared to the 2AP- and 4AP-doped samples. A similar trend shows their melting/decomposition temperatures: BA:  $248^\circ\text{C} - 252^\circ\text{C}$ ,<sup>16</sup> TAP:  $249^\circ\text{C} - 251^\circ\text{C}$ ,<sup>17</sup> 2AP:  $> 300^\circ\text{C}$ <sup>18</sup> and 4AP:  $\geq 360^\circ\text{C}$ .<sup>19</sup> It seems that the hydroxy-contents of the dopants do

not affect the doped products since no additional oxygen (in form of the residue) has been detected.

As in the case for the 4AP-doped amorphous PTI, doping with 2AP, BA and TAP results in an increase of the photocatalytic activity compared to non-doped amorphous PTI ( $10.8 \mu\text{mol h}^{-1}$ ) (Figure 3.7). The co-polymerization with melamine does not have a large impact on the photocatalytic activity of PTI. A slightly enhanced activity is noticed for melamine-doped PTI compared to pure dicyandiamide-derived PTI, which might be due to its higher condensation degree (see elemental analysis). However, the enhancement is within the detection error of 15 % and is therefore not significant. It further seems that doping with 4AP, 2AP and TAP results in materials with similarly high activity, while BA-doped amorphous PTI is slightly less active. This might be associated with the large C/N ratio of the BA-doped sample and its darker color indicating progressed carbonization. Since the hydroxyl-containing 2AP and 4AP samples are very active, we do not relate the low activity of BA-doped PTI with its high hydroxyl-content. The difference in the photocatalytic activities might more likely be associated with the polymerization degree of the samples, quantity of inserted dopants and degree of degradation of PTI itself as well as its dopants. However, this should be analyzed in the future. Note that meanwhile, TAP- ( $\text{H}_2$  evolution) and BA-doping (dye degradation) of PTI have been shown to increase the photocatalytic activity of PTI.<sup>20</sup>

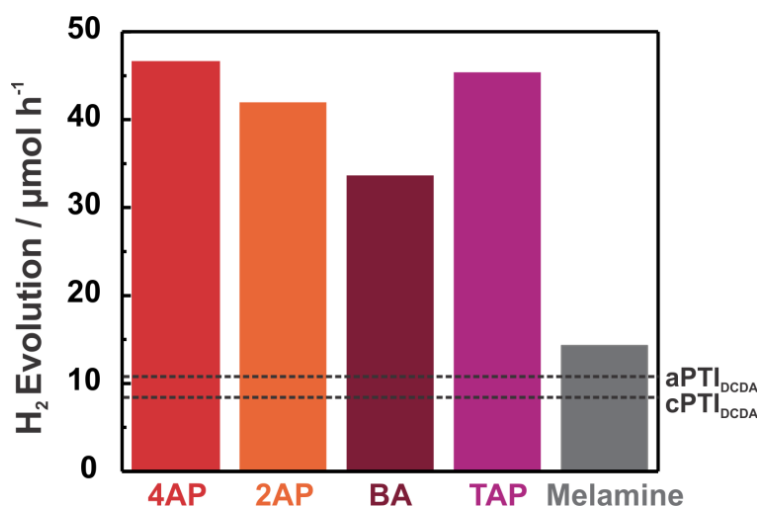


**Figure 3.7** Hydrogen evolution rates after three hours of illumination for 10 mg of 4AP, 2AP, BA and TAP-doped amorphous PTI samples compared to PTI co-polymerized with melamine. Measurement was performed in a 10 vol% aqueous TEoA solution, with  $6 \mu\text{L}$  of  $\text{H}_2\text{PtCl}_6$  (2.3 wt% Pt) under visible light ( $\geq 420 \text{ nm}$ ) illumination.

To conclude, it has been shown that the photocatalytic activity of amorphous PTI can be enhanced by co-polymerizing the precursor dicyanamide not only with 4AP, but also other melamine-related heterocyclic compounds of increased carbon content, such as 2AP, BA and TAP. The slight difference in the photocatalytic activities of the doped samples might be associated with the condensation degree of PTI, the quantity of inserted dopants, degree of carbonization and the amount and quality of platinum coordination. It further



seems that the hydroxyl-groups do not explicitly affect the photocatalytic activities of doped PTI. These preliminary experiments and results presented herein are repeated, vigorously developed, and discussed in *L. Moser's* bachelor thesis.<sup>21</sup> In addition, further experiments with other dopants, such as urea, ammeline, ammelide, cyanuric chloride and cyanuric acid should be performed in the future.

## Bibliography

- (1) X. Chen, S. Shen, L. Guo, S. S. Mao, *Chem. Rev.* **2010**, *110*, 6503.
- (2) H. Tong, S. Ouyang, Y. Bi, N. Umezawa, M. Oshikiri, J. Ye, *Adv. Mater.* **2012**, *24*, 229.
- (3) (a) X. Wang, K. Maeda, A. Thomas, K. Takanabe, G. Xing, J. M. Carlsson, K. Domen, M. Antonietti, *Nat. Mater.* **2009**, *8*, 76; (b) E. Kroke, M. Schwarz, E. Horath-Bordon, P. Kroll, B. Noll, A. D. Norman, *New J. Chem.* **2002**, *26*, 508.
- (4) (a) Y. Wang, X. Wang, M. Antonietti, *Angew. Chem.* **2012**, *124*, 70; *Angew. Chem. Int. Ed.* **2012**, *51*, 68; (b) Y. Zheng, J. Liu, J. Liang, M. Jaroniec, S. Z. Qiao, *Energy Environ. Sci.* **2012**, *5*, 6717.
- (5) (a) B. V. Lotsch, M. Döblinger, J. Sehnert, L. Seyfarth, J. Senker, O. Oeckler, W. Schnick, *Chem. Eur. J.* **2007**, *13*, 4969; (b) L. Seyfarth, J. Seyfarth, B. V. Lotsch, W. Schnick, J. Senker, *Phys. Chem. Chem. Phys.* **2010**, *12*, 2227; (c) B. Jürgens, E. Irran, J. Senker, P. Kroll, H. Müller, W. Schnick, *J. Am. Chem. Soc.* **2003**, *125*, 10288.
- (6) (a) D. Mitoraj, H. Kisch, *Chem. Eur. J.* **2010**, *16*, 261; (b) E. Kroke, M. Schwarz, *Coord. Chem. Rev.* **2004**, *248*, 493; (c) G. Goglio, D. Foy, G. Demazeau, *Mater. Sci. Eng. R* **2008**, *58*, 195; (d) X. Li, J. Zhang, L. Shen, Y. Ma, W. Lei, Q. Cui, G. Zou, *Appl. Phys. A* **2009**, *94*, 387.
- (7) (a) J. Zhang, X. Chen, K. Takanabe, K. Maeda, K. Domen, J. D. Epping, X. Fu, M. Antonietti, X. Wang, *Angew. Chem.* **2010**, *122*, 451; *Angew. Chem. Int. Ed.* **2010**, *49*, 441; (b) Q. Li, B. Yue, H. Iwai, T. Kako, J. Ye, *J. Phys. Chem. C* **2010**, *114*, 4100; (c) Y. Zhang, A. Thomas, M. Antonietti, X. Wang, *J. Am. Chem. Soc.* **2009**, *131*, 50; (d) H. Yan, Y. Huang, *Chem. Commun.* **2011**, *47*, 4168.
- (8) E. Wirnhier, M. Döblinger, D. Gunzelmann, J. Senker, B. V. Lotsch, W. Schnick, *Chem. Eur. J.* **2011**, *17*, 3213.
- (9) M. J. Bojdys, J.-O. Müller, M. Antonietti, A. Thomas, *Chem. Eur. J.* **2008**, *14*, 8177.
- (10) (a) B. V. Lotsch, W. Schnick, *Chem. Mater.* **2006**, *18*, 1891; (b) A. I. Finkel'shtein, *Opt. Spektrosk.* **1959**, *6*, 33; (c) M. Takimoto, *Kogyo Kagaku Zasshi* **1961**, *64*, 1452; (d) M. Takimoto, *Nippon Kagaku Zasshi* **1964**, *85*, 159; (e) D. A. Long, *J. Raman Spectrosc.* **2004**, *35*, 905; (f) B. V. Lotsch, W. Schnick, *Chem. Eur. J.* **2007**, *13*, 4956.
- (11) (a) P. Niu, G. Liu, H.-M. Cheng, *J. Phys. Chem. C* **2012**, *116*, 11013; (b) A. Thomas, A. Fischer, F. Goettmann, M. Antonietti, J.-O. Müller, R. Schlögl, J. M. Carlsson, *J. Mater. Chem.* **2008**, *18*, 4893; (c) A. V. Semencha, L. N. Blinov, *Glass Phys. Chem.* **2010**, *36*, 199; (d) X. Q. Gong, A. Selloni, M. Batzill, U. Diebold, *Nat. Mater.* **2006**, *5*, 665; (e) M. K. Nowotny, L. R. Sheppard, T. Bak, J. Nowotny, *J. Phys. Chem. C* **2008**, *112*, 5275.
- (12) (a) X. Wu, K. W. Zilm, *J. Magn. Reson. Ser. A* **1993**, *102*, 205; (b) C. Gervais, F. Babonneau, J. Maquet, C. Bonhomme, D. Massiot, E. Framery, M. Vaultier, *Magn. Reson. Chem.* **1998**, *36*, 407.
- (13) (a) X. Chen, L. Liu, P. Y. Yu, S. S. Mao, *Science* **2011**, *331*, 746; (b) M. Alvaro, E. Carbonell, V. Fornés, H. García, *ChemPhysChem* **2006**, *7*, 200; (c) G. Zhang, J. Zhang, M. Zhang, X. Wang, *J. Mater. Chem.* **2012**, *22*, 8083.

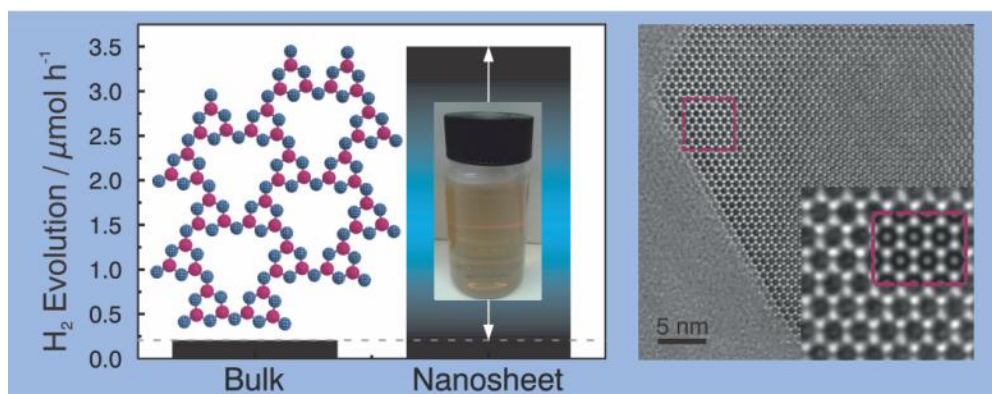
- (14) While this paper was in review, complementary data on the photocatalytic water splitting of crystalline PTI were published: Y. Ham, K. Maeda, D. Cha, K. Takanabe, K. Domen, *Chem. Asian J.* **2013**, *8*, 218.
- (15) (a) D. Dontsova, S. Pronkin, M. Wehle, Z. Chen, C. Fettkenhauer, G. Clavel, M. Antonietti, *Chem. Mater.* **2015**, *27*, 5170. (b) H. Gao, S. Yan, J. Wang, Y. A. Huang, P. Wang, Z. Li, Z. Zou, *Phys. Chem. Chem. Phys.* **2013**, *15*, 18077.
- (16) [www.sigmaaldrich.com](http://www.sigmaaldrich.com), CAS number: 67-62-7, accessed on 18<sup>th</sup> of January **2016**.
- (17) [www.sigmaaldrich.com](http://www.sigmaaldrich.com), CAS number: 1004-38-7, accessed on 18<sup>th</sup> of January **2016**.
- (18) [www.sigmaaldrich.com](http://www.sigmaaldrich.com), CAS number: 56-09-7, accessed on 18<sup>th</sup> of January **2016**.
- (19) [www.sigmaaldrich.com](http://www.sigmaaldrich.com), CAS number: 873-83-6, accessed on 18<sup>th</sup> of January **2016**.
- (20) (a) H. Zou, Y. Xuehua, J. Ren, X. Wu, Y. Dai, D. Sha, J. Pan, J. Liu, *J. Materiomics* **2015**, *1*, 340. (b) M. K. Bhunia, K. Yamauchi, K. Takanabe, *Angew. Chem. Int. Ed.* **2014**, *53*, 11001. (c) M. K. Bhunia, S. Melissen, S. M. R. Parida, P. Sarawade, J.-M. Basset, D. H. Anjum, O. F. Mohammed, P. Sautet, T. L. Bahers, K. Takanabe, *Chem. Mater.* **2015**, *27*, 8237.
- (21) L. Moser, *Bachelor thesis*, University of Munich, **2015**.

## 3.2 Surface engineering through exfoliation

### Crystalline carbon nitride nanosheets for improved visible-light hydrogen evolution

Katharina Schwinghammer, Maria B. Mesch, Viola Duppel, Christian Ziegler, Jürgen Senker and Bettina V. Lotsch

Published in: *J. Am. Chem. Soc.* **2014**, *136*, 1730–1733; DOI: 10.1021/ja411321s.



#### Abstract

Nanosheets of a crystalline 2D carbon nitride were obtained by ionothermal synthesis of the layered bulk material poly(triazine imide), PTI, followed by one-step liquid exfoliation in water. Triazine-based nanosheets are 1 nm – 2 nm in height and afford chemically and colloidally stable suspensions under both basic and acidic conditions. We use solid-state NMR spectroscopy of isotopically enriched, restacked nanosheets as a tool to indirectly monitor the exfoliation process and carve out the chemical changes occurring upon exfoliation, as well as to determine the nanosheet thickness. PTI nanosheets show significantly enhanced visible-light driven photocatalytic activity toward hydrogen evolution compared to their bulk counterpart, which highlights the crucial role of morphology and surface area on the photocatalytic performance of carbon nitride materials.

#### 3.2.1 Introduction

The exploration of highly efficient photocatalysts has been fuelled by the prospect of converting sustainable solar energy into clean chemical fuels.<sup>1</sup> In this context, carbon nitrides have emerged as promising metal-free visible-light photocatalysts owing to their abundance, stability, and chemical tunability.<sup>2</sup> Recently, we<sup>3</sup> and others<sup>4</sup> independently discovered a new type of carbon nitride photocatalyst, poly(triazine imide) (PTI/LiCl),<sup>5a,b</sup> which rivals the benchmark carbon nitride based on heptazine building blocks, known as melon<sup>6</sup> and often loosely called graphitic carbon nitride, *g*-C<sub>3</sub>N<sub>4</sub>.<sup>2,7</sup> In contrast to melon (“*g*-C<sub>3</sub>N<sub>4</sub>”), PTI is a crystalline species and represents the only structurally characterized two-dimensional (2D) carbon nitride network known to date.<sup>5</sup> The layers are composed of imide-

linked triazine units (Figure 3.8(a)) and are stacked in an ABA-type fashion, separated by weak van der Waals forces, with lithium and chloride ions situated in channels running along the stacking direction (Figure 3.8(b)).<sup>5b</sup> In the past, various strategies, such as doping with heteroatom<sup>8</sup> or organic molecules,<sup>3,9</sup> interfacing with other semiconductors or dyes to create heterojunctions,<sup>10</sup> and morphology-tuning<sup>8c,11</sup> have been used to increase the photocatalytic activity of carbon nitrides. In this regard, the exfoliation of carbon nitrides into ultrathin nanosheets has been shown to enhance the photocatalytic activity due to surface and quantum confinement effects.<sup>12</sup> Since the seminal discovery of graphene,<sup>13</sup> it has been well-established that delamination of 2D layered materials such as MoS<sub>2</sub><sup>14</sup> and WS<sub>2</sub><sup>15</sup> may entail unique physicochemical properties, including ultrahigh charge carrier mobilities and pronounced changes in the band structure. Likewise, delamination of layered photocatalysts into 2D sheets may be advantageous for promoting photocatalytic efficiency, both *via* the exposure of active sites and optimized light harvesting, charge separation and percolation.<sup>12a-c,16</sup> In contrast to melon-type carbon nitrides which have been exfoliated recently,<sup>12a</sup> PTI is highly crystalline and a true 2D material,<sup>5b,12d</sup> which lends itself as an excellent model system to explore both structural effects and photocatalytic activity as a function of the exfoliation state.

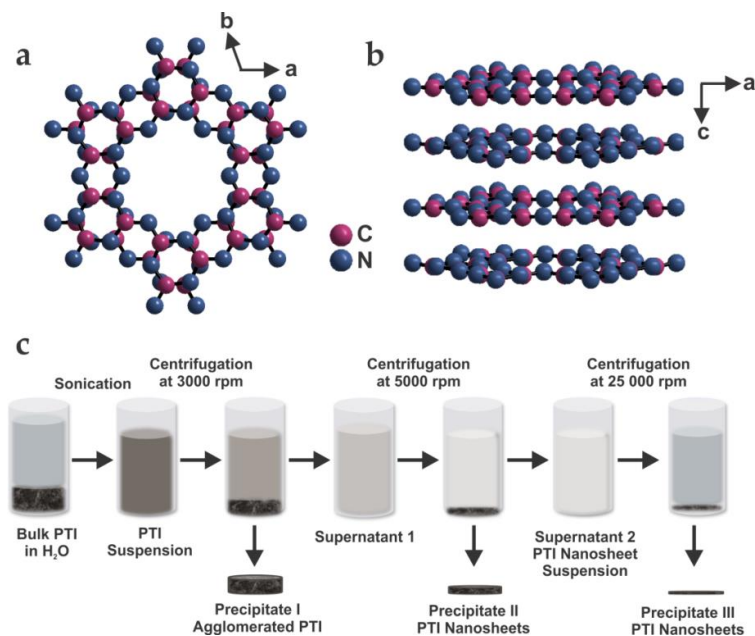


**Figure 3.8** Idealized PTI structure (lithium/chloride intercalation omitted for clarity) viewed along the *c*-axis (a) and the slightly tilted *b*-axis (b). Scheme of the exfoliation process and product labeling (c).

Layered materials such as graphite and boron nitride can be exfoliated when the enthalpy of mixing is minimized, which is the case when the surface energies of the nanosheet and solvent match.<sup>17</sup> Zhang *et al.*<sup>12b</sup> calculated the surface energy of *g*-C<sub>3</sub>N<sub>4</sub> as 115 mJ m<sup>-2</sup>, which matches well with the surface energy of water (~102 mJ m<sup>-2</sup>).<sup>17c</sup> In addition, the terminal hydrogen atoms of the carbon nitrides prefer polar solvents, which upon hydrogen bond formation will cause swelling and exfoliation of the bulk carbon nitrides

on a large scale.<sup>12b</sup> Recently, *Bojdys et al.* reported<sup>12d</sup> that bromide intercalated PTI can be exfoliated by intercalation of potassium and subjecting the intercalate to water. The resulting thin sheets show large lateral sizes in the micrometer range, which however is expected to be unfavorable for photocatalysis due to the relatively small surface area and exposed number of active sites.

Here we demonstrate the one-step synthesis of crystalline PTI nanosheets by "green" liquid phase exfoliation in water, without the need for additives, toxic solvents or preintercalation steps. Remarkably, facile exfoliation in water leads to highly crystalline nanosheets of 1 nm – 2 nm in thickness, which show significantly increased photocatalytic efficiency for visible-light driven hydrogen evolution compared to bulk crystalline PTI.

### 3.2.2 Results and Discussion

Crystalline PTI/LiCl was suspended in water (2 mg mL<sup>-1</sup>) and sonicated for 15 h at room temperature (Figure 3.8(c)). The dispersion was centrifuged at 3000 rpm to remove aggregates (Precipitate I), giving rise to a homogeneous dispersion of PTI nanosheets. To further separate the suspension according to the degree of exfoliation, a fraction of the aqueous suspension was further centrifuged at 5000 rpm (Precipitate II) to yield a nanosheet suspension with a higher degree of exfoliation compared to Precipitate I. The supernatant remaining after this centrifugation step, showing the maximum degree of exfoliation, was kept for analysis of the suspended nanosheets (Supernatant 2, 0.2 mg mL<sup>-1</sup>). Finally, the nanosheets were precipitated by centrifugation at 25000 rpm and subjected to analysis in order to compare the suspended nanosheets (Supernatant 2) *vs* their restacked form (Precipitate III). The labeling scheme of the different nanosheet fractions is outlined in Figure 3.8(c).

The well-dispersed PTI nanosheets (Supernatant 2) in water are negatively charged, with a zeta potential of -54.0 mV and a pH of 10.5. This observation is consistent with the fact that deprotonated, bridging imide moieties are present which are charge-compensated by Li ions, giving rise to dynamic lithium proton exchange with water and, hence, to the observed basic character of the suspension caused by lithium hydroxide. The brownish dispersion is highly stable, showing no signs of precipitation even after being stored for 2 months, in line with the high negative surface charge. Interestingly, the surface charge is minimal (point of zero charge) at pH 5.4 and reversed at lower pH with a zeta potential of +30 mV at pH 2 (Figure S11, 7.1 Supporting information). Thus, the nanosheets are stable both at low (< 3) and high pH values (> 8), which can be rationalized by the overall amphoteric character of the ring and bridging nitrogen functions in the PTI backbone.

Having ascertained the state of dispersion and stability of the suspensions, the thickness of as-prepared PTI nanosheets (Supernatant 2) was investigated by atomic force microscopy (AFM). According to *Wirnhier et al.* bulk PTI is built up from hollow microtubes

whose walls are composed of an oriented assembly of hexagonal prismatic crystallites with lateral sizes of about 60 nm.<sup>5b</sup> AFM images of the nanosheet suspension (Supernatant 2) and the corresponding height profile display exfoliated crystallites with lateral sizes of less than 100 nm and a height of 1 nm – 2 nm, indicating the exfoliated nanosheets are composed of only a few carbon nitride layers, taking into account a water shell likely surrounding the nanosheets (Figure 3.9(a) and discussion below).

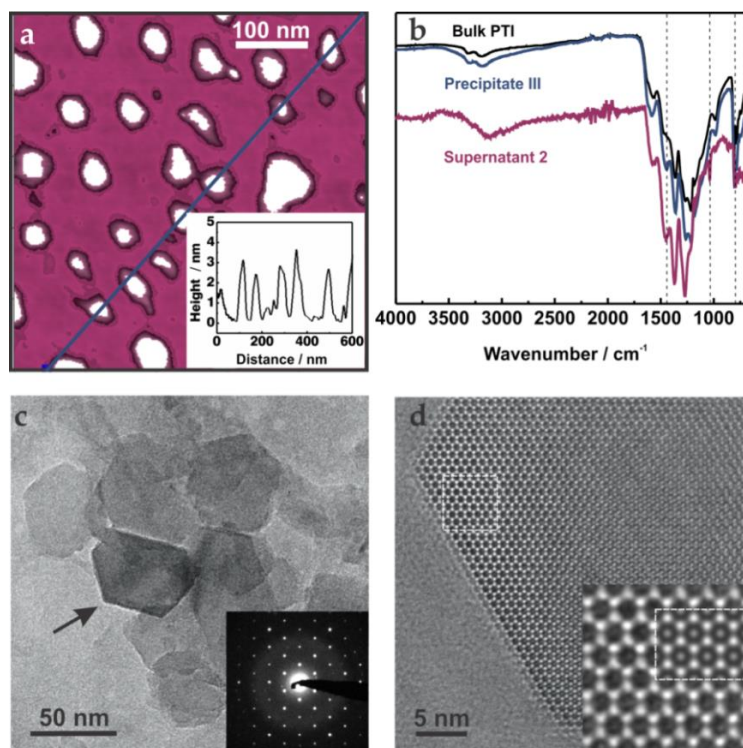


**Figure 3.9** AFM image of exfoliated PTI nanosheets deposited on a Si/SiO<sub>2</sub> wafer (a) and the corresponding height image (inset). IR spectrum of bulk PTI (black) compared to Precipitate III (blue) and Supernatant 2 (magenta) (b). TEM image of exfoliated ultrathin PTI nanosheets (c), higher magnification of a PTI nanosheet edge viewed along [001] (d) marked in (c) and simulation (JEMS;  $\Delta f = +50$  nm,  $t = 2.70$  nm; inset).

AFM results were further confirmed by TEM investigations. HRTEM measurements reveal that the hexagonal shape of the crystallites is in fact retained, and the 2D sheets are well separated and conformally spread across the substrate (Figure 3.9(c)). Selected area electron diffraction (SAED) patterns are fully consistent with the expected hexagonal symmetry of an individual PTI layer (Figure 3.9(c, inset) and Figure S12(a), 7.1 Supporting information).<sup>5b</sup>

X-ray diffraction patterns (Figure S12(b), 7.1 Supporting information) confirm that both the restacked PTI nanosheets (Precipitate III) and the precipitates from the previous steps (Precipitate I and II) show reflections which are consistent with bulk PTI,<sup>5a,b</sup> confirming that the structure of the parent bulk PTI is retained in the nanosheets. Interestingly, the presence of (*hkl*) reflections showing no obvious asymmetry or line broadening further

suggests that the same stacking pattern is adopted after centrifugation, without the occurrence of turbostratic disorder in the restacked material.

The identity of the nanosheets was further confirmed by FTIR spectroscopy (Figure 3.9(b)). The characteristic IR spectrum of the nanosheet Precipitate II is largely reminiscent of that of the bulk material,<sup>5a,b</sup> both having a band at  $810\text{ cm}^{-1}$  (triazine ring sextant out of plane bending) and a fingerprint region  $1200\text{ cm}^{-1} - 1620\text{ cm}^{-1}$  which is dominated by the same  $\nu(\text{C}-\text{NH}-\text{C})$  and  $\nu(\text{C}=\text{N})$  stretching vibrations. Nevertheless, Precipitate II shows a more highly resolved band at  $1440\text{ cm}^{-1}$  and the intensity ratio of the  $\nu(\text{C}-\text{NH}-\text{C})$  vibrations at  $1260\text{ cm}^{-1}$  and  $1210\text{ cm}^{-1}$  is slightly shifted. The IR of the nanosheet suspension (Supernatant 2, measured in solution against a water background) shows slightly broadened and shifted bands in the region between  $1000\text{ cm}^{-1}$  and  $1200\text{ cm}^{-1}$  compared to the bulk material. These changes can be attributed to the water environment of the nanosheets in Supernatant 2. The composition of the nanosheets (Precipitate III) was analyzed by elemental analysis (EA), revealing slight differences from the bulk material (Table S3, Supporting information). PTI nanosheets show decreased lithium content compared to the starting material, suggesting that lithium ions are released during the exfoliation process, possibly by  $\text{Li}^+-\text{H}^+$  exchange at the [...] basic [...] imide groups through reaction with water. The atomic C/N ratio of Precipitate II (0.62) is similar to the one in bulk PTI (0.64).

To further probe the chemical environment and bonding between the carbon and nitrogen atoms in the PTI nanosheets (Precipitate III), XPS measurements were conducted. No obvious shifts of the binding energy of C 1s and N 1s core electrons are observable, suggesting that the chemical states of both carbon and nitrogen atoms in the nanosheets (Precipitate III) are the same as in bulk PTI (Supporting Information). Two oxygen peaks are observed for Precipitate III, which are due to air (O1 at 530.8 eV) and water (532.1 eV), respectively (Figure S14, 7.1 Supporting information).<sup>18</sup> Note that the bulk material contains only the first oxygen peak (O1).

To gain more insights into the local structure of the nanosheets relative to the one of bulk PTI, we performed solid-state NMR spectroscopy with  $^{15}\text{N}$  isotope-enriched samples of Precipitates I-III and bulk PTI in comparison (Figure 3.10). While being overall similar, both  $^{13}\text{C}$  and  $^{15}\text{N}$  spectra reveal subtle differences in the relative signal intensities on going from the bulk to the restacked nanosheets. These changes are predominantly attributed to a decrease in the lithium content in the channels and the resulting higher local symmetry of carbon and nitrogen environments in the restacked samples. As the Li content does not further decrease with increasing degree of exfoliation, it is likely determined initially by the sonication process and unaffected by the subsequent centrifugation exfoliation steps. In contrast, the water content in the samples, apparent from  $^1\text{H}$  spectra (signals at 6.2 ppm and 4.6 ppm), tremendously increases from Precipitate I to III. Polarization exchange between the PTI protons and the ones of the water molecules as ascertained by  $^1\text{H}^1\text{H}$  proton driven spin diffusion spectroscopy (Figure 3.10(d) and Figure S16, 7.1 Supporting



information) is even faster than the exchange among the PTI protons. This points to a close vicinity of the nanosheets and water on a molecular scale. Assuming dense monolayers of water on the surface of the nanosheet stacks, we find that between 2 and 4 PTI layers are interspersed with two water layers, based on the relative proton signal intensities (7.1 Supporting information and Figure S15, 7.1 Supporting information). The derived height of the nanosheet stack (PTI) 2–4 corresponds well to that measured by AFM (1 nm – 2 nm). Therefore, NMR presents a viable "bulk method" to indirectly determine the thickness of nanosheet stacks.

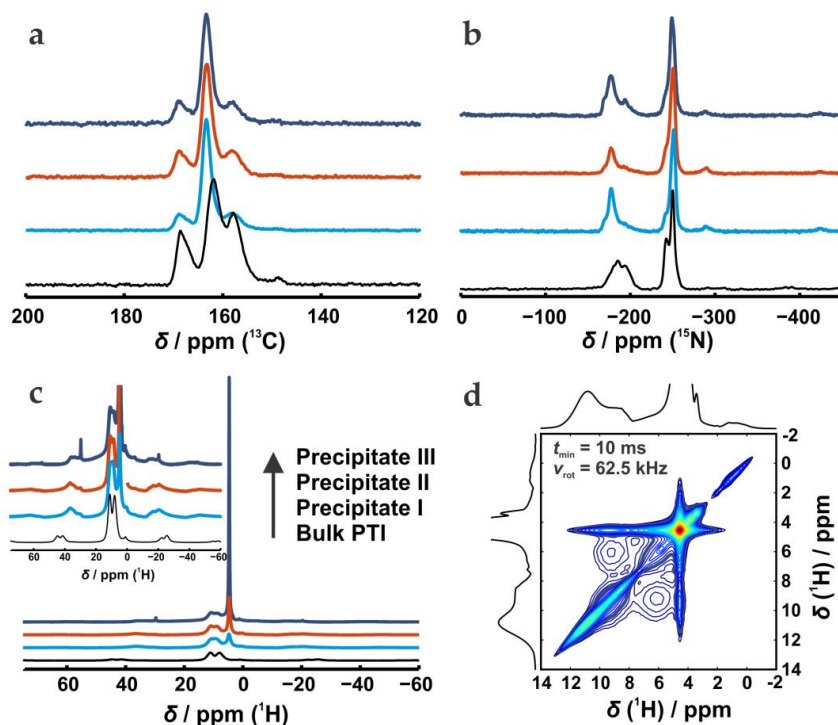


**Figure 3.10**  $^{13}\text{C}$  (a) and  $^{15}\text{N}$  (b) CP-MAS NMR spectra and  $^1\text{H}$  (c) CP-MAS NMR spectra for Precipitates I–III and bulk PTI, respectively.  $^1\text{H}$ – $^1\text{H}$  proton driven spin diffusion spectrum (d) for Precipitate III.

The brown color of the PTI nanosheet suspension indicates substantial absorption in the visible range of the spectrum, similar to bulk PTI. While the strong absorption edge just below 400 nm is likewise present in the nanosheet suspension, the broad band around 450 nm is less pronounced for Supernatant 2 (measured in water), which may be due to the absence of layer stacking or to solvation effects. Quantum confinement effects are not noticeable, since there are only minute changes in the absorption material. More insights into the electronic band structure is given by *Moewes and co-workers*, who extracted a band gap of 2.2 eV for the LiCl-intercalated material.<sup>20</sup>

Owing to their small particle size and, thus, higher exposed surface area and possibly higher number of active sites, the PTI nanosheets were tested for photocatalytic hydrogen evolution and compared to the water reduction activity of the bulk material. The photocatalytic activity of the PTI nanosheet suspension (Supernatant 2), of the bulk material as well as agglomerated PTI (Precipitate I) and partially exfoliated nanosheet fractions (Pre-



precipitate II) was measured in a water/triethanolamine (TEoA) solution (for details see 7.1 Supporting information) under visible light illumination (Figure 3.11). Under the conditions applied, bulk PTI evolves  $4.3 \mu\text{mol H}_2$  per hour. Sonication of the material for 15 h in water lowers the activity of the suspension by about 43 %. The formed agglomerates were centrifuged at 3000 rpm, redispersed and tested with regard to their photocatalytic activity, confirming the same low activity of Precipitate I compared to sonicated PTI. Precipitate II, containing partially exfoliated PTI, shows an improvement in hydrogen evolution by 28 % ( $6.4 \mu\text{mol H}_2$  per hour).

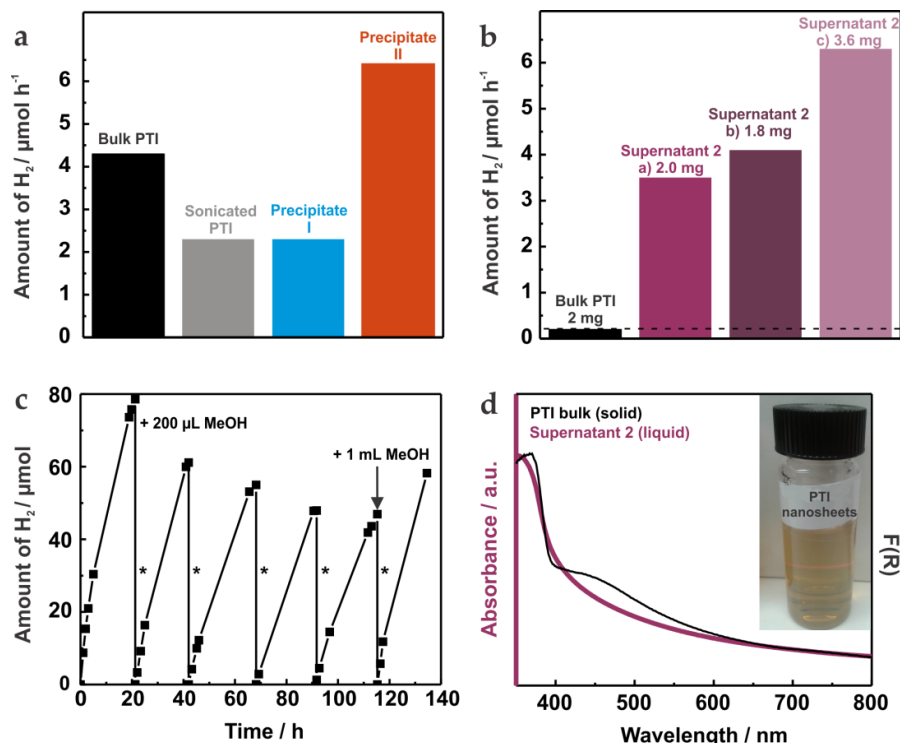


**Figure 3.11** Photocatalytic activity toward  $\text{H}_2$  production of the Pt-doped Precipitates (I and II) compared to sonicated PTI and bulk PTI (a), and of the nanosheet suspensions compared to bulk PTI (b), measured in a 10 vol% TEoA/water solution for 3 h illumination with visible light ( $> 420 \text{ nm}$ ). Cyclic stability tests of the nanosheet suspension: Supernatant 1 with methanol as electron donor (c). The reactor was purged several times (marked with an asterisk) and methanol was reinjected twice. UV-Vis spectrum of bulk PTI measured as solid in diffuse reflectance mode compared to Supernatant 2 measured as liquid in transmission mode (d).

To examine the low concentrated PTI nanosheet suspensions (Supernatant 2), 2 mg of bulk PTI was tested and compared to three different suspensions (2a, 2b and 2c) containing 2.0 mg, 1.8 mg and 3.6 mg of nanosheets, respectively. While bulk PTI shows an activity of  $0.2 \mu\text{mol H}_2$  per hour (Figure 3.11(b)), 2 mg of the PTI nanosheets (Supernatant 2a) exhibits a much higher hydrogen evolution rate, corresponding to an improvement by a factor of 18 ( $3.5 \mu\text{mol H}_2$  per hour; 1.3 % apparent quantum efficiency at 400 nm for non-optimized conditions, see ref 21) as compared to the bulk material. As expected, the more concentrated nanosheet suspension (Supernatant 2c) shows an even higher photocatalytic activity, suggesting that hydrogen evolution is not yet diffusion limited under these conditions and light harvesting is not yet impeded by scattering effects. Measurements prob-

ing whether sustained hydrogen evolution over extended periods of time is feasible were performed with Supernatant 1 and TEOA (Figure S18; 7.1 Supporting information) or methanol as electron donor (Figure 3.11(c)). While with TEOA a decrease in activity was detected, which may be due to degradation of the material under basic conditions, long-term measurements in methanol show that the PTI nanosheets are steadily evolving hydrogen for at least 130 h. Note that after the sixth cycle (after addition of methanol), the hydrogen evolution rate of the first cycle ( $6.1 \mu\text{mol H}_2$  per hour) could almost be recovered ( $5.4 \mu\text{mol H}_2$  per hour). Furthermore, a strongly wavelength-dependent hydrogen evolution rate was observed (Figure S18; 7.1 Supporting information).

### 3.2.3 Conclusion

In conclusion, triazine-based PTI nanosheets have been successfully synthesized through a simple and cost-effective aqueous exfoliation method starting with bulk PTI powder. The structure and morphology of the nanosheets was identified by complementary techniques including TEM, XRD, AFM and solid-state NMR spectroscopy, highlighting the close relationship between the parent PTI and the nanosheets. In agreement with AFM measurements revealing nanosheet thicknesses of 1 nm – 2 nm, NMR points to facile water incorporation in the restacked nanosheets, forming arrangements of 2 – 4 PTI layers interspersed with water layers. Exfoliated PTI is the first structurally well defined, crystalline 2D carbon nitride showing high activity toward photocatalytic water-splitting, which is among the highest ever observed for pristine carbon nitrides, including mesoporous "g-C<sub>3</sub>N<sub>4</sub>".<sup>9a,12a,19</sup> The photocatalytic activity of the exfoliated sample is superior by a factor of > 17 to both the non-exfoliated counterpart and melon (internal standard) and by a factor of > 8 to "g-C<sub>3</sub>N<sub>4</sub>" (calculated for 2 mg).<sup>12</sup> Our study draws on highly defined, structurally unambiguous carbon nitride nanosheets and thus paves the way for a better understanding of structure-property relationships in carbon nitrides and the factors influencing the photocatalytic activity in this promising, yet still largely ill-defined, class of photocatalysts.

### Bibliography

- (1) (a) M. R. Hoffmann, T. M. Scot, W. Choi, D. W. Bahnemann, *Chem. Rev.* **1995**, *95*, 69. (b) A. L. Linsebigler, G. Lu, J. T. Yates, *Chem. Rev.* **1995**, *95*, 735.
- (2) (a) X. Wang, K. Maeda, A. Thomas, K. Takanabe, G. Xin, J. M. Carlsson, K. Domen, M. Antonietti, *Nat. Mater.* **2009**, *8*, 76. (b) Y. Wang, X. Wang, M. Antonietti, *Angew. Chem., Int. Ed.* **2012**, *51*, 68. (c) Y. Zheng, J. Liu, J. Liang, M. Jaroniec, S. Z. Qiao, *Energy Environ. Sci.* **2012**, *5*, 6717.
- (3) K. Schwinghammer, B. Tuffy, M. B. Mesch, E. Wirnhier, C. Martineau, F. Taulelle, W. Schnick, J. Senker, B. V. Lotsch, *Angew. Chem., Int. Ed.* **2013**, *52*, 2435.
- (4) Y. Ham, K. Maeda, D. Cha, K. Takanabe, K. Domen, *Chem. Asian J.* **2013**, *8*, 218.
- (5) (a) M. J. Bojdys, J.-O. Müller, M. Antonietti, A. Thomas, *Chem. Eur. J.* **2008**, *14*, 8177. (b) E. Wirnhier, M. Döblinger, C. Gunzelmann, J. Senker, B.V. Lotsch, W. Schnick, *Chem. Eur. J.* **2011**, *17*,

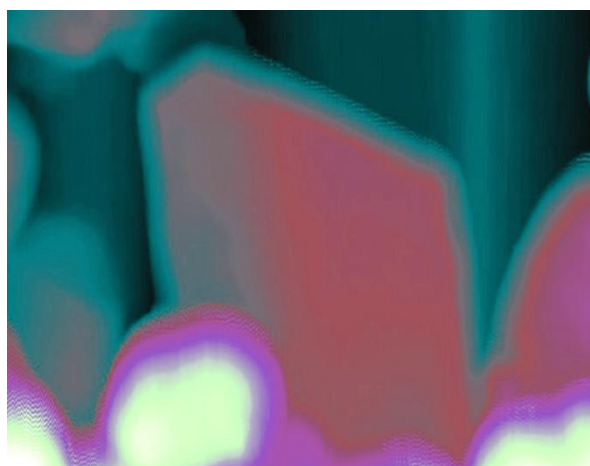
3213. (c) S. Y. Chong, J. T. A. Jones, Y. Z. Khimyak, A. I. Cooper, A. Thomas, M. Antonietti, M. J. Bojdys, *J. Mater. Chem. A* **2013**, *1*, 1102.
- (6) B. V. Lotsch, M. Döblinger, J. Sehnert, L. Seyfarth, J. Senker, O. Öckler, W. Schnick, *Chem. Eur. J.* **2007**, *13*, 4969.
- (7) (a) J. Yu, S. Wang, B. Cheng, Z. Lin, F. Huang, *Catal. Sci. Technol.* **2013**, *3*, 1782. (b) G. Liao, S. Chen, X. Quan, H. Yu, H. Zhao, *J. Mater. Chem.* **2012**, *22*, 2721. (c) X. Bai, L. Wang, R. Zong, Y. Zhu, *J. Phys. Chem. C* **2013**, *117*, 9952.
- (8) (a) Y. Wang, J. Zhang, X. Wang, M. Antonietti, H. Li, *Angew. Chem., Int. Ed.* **2010**, *49*, 3356. (b) G. Liu, P. Niu, C. Sun, S. C. Smith, Z. Chen, G. Q. Lu, H.-M. Cheng, *J. Am. Chem. Soc.* **2010**, *132*, 11642. (c) Z. Lin, X. Wang, *Angew. Chem., Int. Ed.* **2013**, *52*, 1735.
- (9) (a) J. H. Zhang, X. F. Chen, K. Takanaabe, K. Maeda, K. Domen, J. D. Epping, X. Z. Fu, M. Antonietti, X. C. Wang, *Angew. Chem., Int. Ed.* **2010**, *122*, 451. (b) J. Zhang, G. Zhang, X. Chen, S. Lin, L. Möhlmann, G. Dołęga, G. Lipner, M. Antonietti, S. Blechert, X Wang, *Angew. Chem., Int. Ed.* **2012**, *51*, 3183.
- (10) (a) Y. Wang, R. Shi, J. Lin, Y. Zhu, *Energy Environ. Sci.* **2011**, *4*, 2922. (b) Y. Zhang, T. Mori, J. Ye, M. Antonietti, *J. Am. Chem. Soc.* **2010**, *132*, 6294.
- (11) (a) B. Kiskan, J. Zhang, X. Wang, ;- Antonietti, Y. Yagci, *ACS Macro Lett.* **2012**, *1*, 546. (b) X. Wang, K. Maeda, X. Chen, K. Takanaabe, K. Domen, Y. Hou, X. Fu, M. Antonietti, *J. Am. Chem. Soc.* **2009**, *131*, 1680.
- (12) (a) S. Yang, Y. Gong, J. Zhang, L. Zhan, L. Ma, Z. Fang, R. Vajtai, X. Wang, P. M. Ajayan, *Adv. Mater.* **2013**, *25*, 2452. (b) X. Zhang, X. Xie, H. Wang, J. Zhang, B. Pan, Y. Xie, *J. Am. Chem. Soc.* **2013**, *135*, 18. (c) P. Niu, L. Zhang, G. Liu, H.-M. Cheng, *Adv. Funct. Mater.* **2012**, *22*, 4763. (d) M. J. Bojdys, N. Severin, J. P. Rabe, A. I. Cooper, A. Thomas, M. Antonietti, *Macromol. Rapid Commun.* **2013**, *34*, 850.
- (13) (a) M. Cai, D. Thorpe, D. H. Adamson, H. C. Schniepp, *J. Mater. Chem.* **2012**, *22*, 24992. (b) A. K. Geim, K. S. Novoselov, *Nat. Mater.* **2007**, *6*, 183.
- (14) V. Štengl, J. Henych, *Nanoscale* **2013**, *5*, 3387.
- (15) D. Voiry, H. Yamaguchi, J. Li, R. Silva, D. C. B. Alves, T. Fujita, M. Chen, T. Asefa, V. B. Shenoy, G. Eda, M. Chhowalla, *Nat. Mater.* **2013**, *12*, 850.
- (16) (a) Y. Ebina, N. Sakai, T. Sasaki, *J. Phys. Chem. B* **2005**, *109*, 17212. (b) S. Ida, Y. Okamoto, S. Koga, H. Hagiwara, T. Ishihara, *RSC Adv.* **2013**, *3*, 11521. (c) W. Wang, J. C. Yu, D. Xia, P. K. Wong, Y. Li, *Environ. Sci. Technol.* **2013**, *47*, 8724.
- (17) (a) J. N. Coleman, M. Lotya, A. ÓNeill, S. D. Bergin, P. J. King, U. Khan, K. Young, A. Gaucher, S. De, R. J. Smith, *et al. Science* **2011**, *331*, 568. (b) S. D. Bergin, V. Nicolosi, P. V. Streich, S. Giordani, Z. Sun, A. H. Windle, P. Ryan, N. P. P. Niraj, Z.-T. T. Wang, L. Carpenter, *et al. Adv. Mater.* **2008**, *20*, 1876. (c) Since the surface tension of water equals 72.1 mJ m<sup>-2</sup>, the surface energy of the nanosheet suspension (~102 mJ m<sup>-2</sup>) can be calculated considering the temperature and the entropy factor.<sup>17a,b</sup>
- (18) G. A. George, *Polym. Int.* **1994**, *33*, 439.
- (19) X. Chen, Y.-S. Jun, K. Takanaabe, K. Maeda, K. Domen, X. Fu, M. Antonietti, X. Wang, *Chem. Mater.* **2009**, *21*, 4093.
- (20) E. J. McDermott, E. Wirnhier, W. Schnick, K. S. Virdi, C. Scheu, Y. Kauffmann, W. D. Kaplan, E. Z. Kurmaev, A. Moewes, *J. Phys. Chem. C* **2013**, *117*, 8806.
- (21) B. J. Ohtani, *Photochem. Photobiol., C* **2010**, *11*, 157.

### 3.3 Investigations on the catalytically relevant sites of PTI

#### Cation and anion exchange of crystalline poly(triazine imide) and its effect on structural and optical properties

Katharina Schwinghammer, Maria B. Mesch, Viola Duppel, Leslie Schoop, Eamon J. McDermott, Tristan de Boer, Alexander Moewes, Jürgen Senker and Bettina V. Lotsch

*To be submitted.*



#### Abstract

The relationship between the structure and the optical and photocatalytic properties of highly crystalline PTI are investigated with respect to cation ( $\text{Li}^+ / \text{H}^+$ ) and anion ( $\text{Cl}^- / \text{Br}^-$ ) intercalation. PTI can be synthesized under ionothermal conditions by a polycondensation reaction starting from a nitrogen-rich precursor such as dicyandiamide. The choice of salt melt determines the ion intercalation into PTI and impacts both structural and optoelectronic properties of PTI. A eutectic mixture of  $\text{LiCl}/\text{KCl}$  leads to the insertion of chloride ions into the C,N-network, while synthesis in a  $\text{LiBr}/\text{KBr}$  salt melt leads to bromide intercalation. In both cases, PTI ( $P6_3cm$ , no 185) is intercalated with lithium and proton ions that are situated within the C,N-layers. The C,N-layers consist of imide-bridged triazine units which can form voids. The layers are stacked on top of each other in an ABA fashion such that every triazine unit is “sandwiched” by two inverted ones (see Figure 3.12(a,b)). The voids can form channels along the  $c$ -direction. Stirring the products ( $\text{PTI}/\text{Li}^+\text{Cl}^-$  or  $\text{PTI}/\text{Li}^+\text{Br}^-$ ) in concentrated acids such as  $\text{HCl}$ ,  $\text{HBr}$  or  $\text{HF}$  gradually induces the removal of lithium ions, accompanied by lithium-proton exchange ( $\text{PTI}/\text{H}^+\text{Cl}^-$  or  $\text{PTI}/\text{H}^+\text{Br}^-$ ). From powder X-ray diffraction analysis, the structure of  $\text{PTI}/\text{HCl}(\text{HBr})$  is similar with the starting compound. However, the removal of the lithium ions leads to a contraction of the PTI layers along  $[001]$ , and most importantly a relocation of the chloride positions from the interlayer space to within the plane of the PTI layers, accompanied by partial agglomeration. A concomitant lateral shift of the C,N-layers is possible (caused by the repulsion of

the anions) but cannot be proven. The appearance of the 011 reflection — forbidden in the parent compound — suggests a lowering in symmetry from  $P6_3cm$  (no 185) to  $P6_3/m$  (no 176). The as-synthesized PTI/HCl shows a great similarity with  $C_6N_9H_3 \cdot HCl$  reported in 2001,<sup>1</sup> which can be synthesized by a high-pressure solid-state reaction of melamine and cyanuric chloride. Although PTI/LiBr does not show photocatalytic activity, its chloride intercalated counterpart remains as a promising visible-light photocatalyst due to the stronger interplanar  $\pi$ -orbital overlap or more accessible active sites. The lithium-proton exchange of PTI/LiCl(LiBr) to PTI/HCl(HBr) induces the densification of the structure along [001] and, hence, approaching C,N-layers, however this surprisingly results in the loss of the photocatalytic properties. Only a minor blue-shift of the absorption edge is observed after protonation which cannot be the main reason for the loss in photocatalytic activity. Thus, the observed inactivity most likely arises from blocked or modified catalytically relevant sites due to protonation and sterical hindrances from the relocation of the anions. These observations emphasize the importance of the accessibility of the nitrogens as possible active sites.

### 3.3.1 Introduction

Carbon nitrides in general and melon in particular have come into focus as the first polymeric photocatalysts capable of overall water splitting since the seminal report by Wang *et al.*<sup>2</sup> in 2009. Even though melon is only moderately active compared to most inorganic photocatalysts,<sup>2</sup> its abundance, low-cost scalability, light weight and sustainability make it an attractive photocatalyst for prospective large-scale applications. Subsequent publications focused on improving the low efficiency of melon mainly by band gap engineering through doping with heteroatoms as well as organic co-polymerization to enhance light harvesting, composite formation to counteract charge recombination, and morphology control *e.g.* by enlarging its surface area.<sup>3</sup> Indeed, a couple of these modified carbon nitrides outperform their inorganic competitors. Unfortunately, the race to reach the highest photocatalytic activities among the carbon nitrides is leading to a disregard of the photocatalytic mechanism. This might also be due to the structural imperfection of melon itself. Therefore, crystalline PTI/LiCl, which has shown to be as active as amorphous melon (when TEoA is used as the electron donor),<sup>4</sup> may be the better choice to study structure property-activity relationships due to its superior long-range order. PTI ( $C_6N_9H_3$ ) is a two-dimensional polymer of imide-bridged triazine units forming six-membered ring motifs. These C,N-layers are stacked in an ABA fashion forming continuous channels along the *c*-axis.<sup>1,5-7</sup> It has been shown that these channels can be filled with lithium cations along with anions such as chloride (PTI/LiCl)<sup>5,6</sup> or bromide (PTI/LiBr)<sup>7</sup> depending on the synthesis conditions. In case of chloride and bromide intercalation, PTI crystallizes in the  $P6_3cm$  space group (no 185) with stacking distances depending on the intercalated ions (3.36 Å for chloride and 3.52 Å for bromide, respectively) (Figure 3.12(a,b)).<sup>5-7</sup> For charge-compensation, lithium ions are intercalated into the structure and found to reside within the six-membered ring motifs; Li cations can be partly exchanged by protons.<sup>8</sup> Interest-

ingly, depending on the amount of intercalated ions, the band gap and band positions and thus the photocatalytic activity of PTI can be varied. For instance, *Moewes and co-workers*<sup>8</sup> determined a band gap of 2.2 eV for PTI fully loaded with Li/Cl, and of 2.8 eV when no ions are intercalated. Further, it was suggested that the hydrogen evolution performance of PTI/LiCl may be further maximized by removing the lithium ions while maintaining full chloride loading.<sup>8</sup> This assumption serves as the basis for the work discussed here. We further show that in contrast to chloride intercalated PTI, PTI/LiBr does not exhibit any photocatalytic activity, which strengthens the hypothesis that the optical and photocatalytic properties of PTI are dependent on the intercalated ionic components as well as the stacking behavior of PTI.

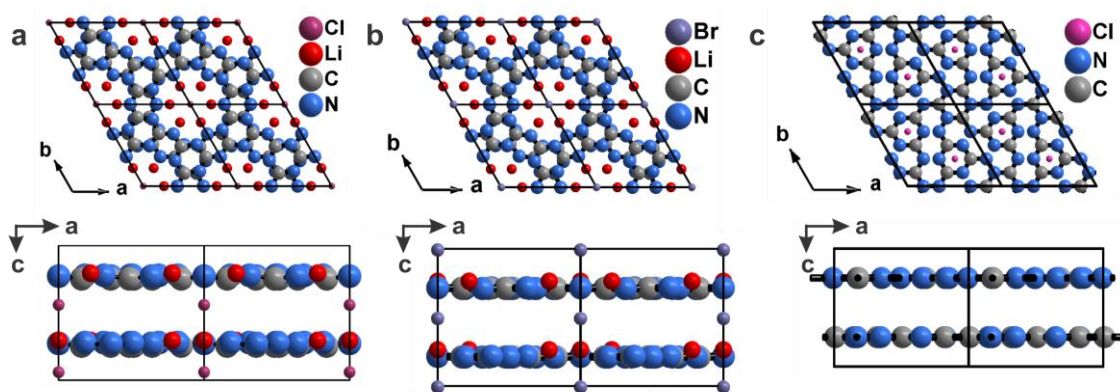


**Figure 3.12** Idealized crystal structure (without protons) of fully loaded (a) PTI/LiCl (ICSD 422088),<sup>5</sup> (b) PTI/LiBr (CCDC 902173)<sup>7</sup> and (c)  $C_6N_9H_3 \cdot HCl$ <sup>9</sup> viewed along the  $c$ -direction (two layers on top of each other) (top) and along the  $b$ -direction (bottom).

Before the publication of PTI/LiCl in 2008,<sup>6</sup> *Wolf and co-workers*<sup>9</sup> already reported on a PTI-based compound of composition  $C_6N_9H_3 \cdot HCl$ . Interestingly, this system seems to fulfill the criteria of *Moewes and co-workers* for a lithium-free but chloride-containing sample.<sup>8</sup> More precisely, *Wolf and co-workers*<sup>9</sup> synthesized this PTI-like compound by means of a high-pressure route (1.0 GPa – 1.5 GPa, at 500 °C – 550 °C).  $C_6N_9H_3 \cdot HCl$  is built up from ABA-stacked imide-bridged triazine units.<sup>9</sup> In contrast to PTI/LiCl(LiBr), the triazine units might not be stacked directly on top of each other but may be laterally shifted such that every triazine unit follows a void filled with a chloride (along the  $c$ -axis). While in PTI/LiCl(LiBr) the chlorides are localized between the C,N layers, the high-pressure leads to a chloride intercalation within the C,N-layers in the case of  $C_6N_9H_3 \cdot HCl$  and a decreased interlayer distance of 3.22 Å. The different stacking leads to a change in symmetry as the  $c$  glide plane is lost ( $P6_3/m$ , no 176) compared to  $P6_3cm$  (no 185) in PTI/LiCl(LiBr) (Figure 3.12(c)). The protons are charge-compensating the layers leading to a partial protonation of the C,N-framework. The exact protonation sites (triazine or imino nitrogen site) were not finally clarified but seem to be interesting in terms of photocatalysis and the investigation on active sites. Despite the prediction of *Moewes and co-workers*,<sup>8</sup> *McMillan and co-workers*<sup>10</sup> reported that  $C_6N_9H_3 \cdot HCl$  is photocatalytically inactive and formed no hydrogen in an aqueous methanol solution. The photocatalytic activity of PTI/HCl(HBr) in

an aqueous triethanolamine solution has not been tested yet although TEOA is easier to oxidize than methanol.

Here, we demonstrate that the photocatalytic activity of PTI depends on its ionic loading which at the same time influences the layer stacking and accessibility of catalytically relevant sites. To this end, we synthesized PTI with full chloride or bromide loading and various lithium-proton-contents by stirring PTI/LiCl(LiBr) in water (0 % HCl(HBr) and different concentrated acids ( $\leq 36$  % HCl,  $\leq 47$  % HBr and 40 % HF). Treating PTI/LiCl(LiBr) with highly concentrated acids leads to an almost lithium-free ( $< 0.1$  wt%) and highly protonated species (PTI/HCl(HBr)). Interestingly, PTI/HCl(HBr) exhibits highly ordered nitrogen environments. The removal of the lithium ions induces a contraction of the C,N-layers, a congestion of the voids with chlorides(bromides) and a protonation of possible active centers which causes a blockage of catalytically relevant sites. This leads to a loss of the photocatalytic activity. The investigation on the structure and properties of PTI related to its photocatalytic activity sheds light on catalytically relevant sites of PTI.

### 3.3.2 Results and discussion

PTI/LiCl,Br was successfully synthesized according to literature protocols<sup>5,7</sup> and then stirred in several concentrated acids (12 % – 36 % HCl, 16 % – 47 % HBr and 40 % HF) or pure water (0 % HCl and 0 % HBr) as described in the Supporting Information (see Chapter 7.1). The filtrated solids have been excessively washed with water (until neutralization of the filtrate), dried at 60 °C in air and finally characterized.

According to elemental analysis (Table 3.3), a gradual decrease in lithium content is detected for PTI/LiCl(HBr) when increasing the acid strength. The lowest lithium content is observed for the samples stirred in the strongest acids (36 % HCl and 47 % HBr). However, even after stirring and washing the samples multiple times with concentrated acids and water, traces of lithium ions ( $\geq 0.04$  wt%) remain. Apparently, parts of the removed lithium ions are exchanged by protons which are necessary for charge-compensation since the amount of intercalated counter anions (chlorine and bromine) remains nearly unchanged after acid treatment. In the case of PTI/LiCl the reported anion contents vary drastically (11.0 wt%<sup>5</sup> and 3.3 wt%).<sup>6</sup> The anion content of as-synthesized PTI/LiCl (8.2 wt%) is in the range of the literature but lower than that of  $C_6N_9H_3 \cdot HCl$  (14.5 wt%).<sup>9</sup> For PTI/LiBr a higher bromide content is detected (7.5 wt%) compared to the literature (3.8 wt%).<sup>7</sup> The harsh acidic conditions do not lead to hydrolysis and fragmentation of the C,N-network since the carbon-to-nitrogen (weight) ratios of the acid treated samples are mostly in agreement with the parent compounds. Surprisingly, the C/N value for PTI/LiCl after acid treatment is slightly reduced compared to the parent compound and seems to approach the value for  $C_6N_9H_3 \cdot HCl$ .<sup>9</sup> Most likely the concentrated acids react with carbon-rich species and purifies PTI/LiCl from amorphous carbon (implying that those species are

present in larger amounts in pristine PTI/LiCl) as reported in the case of carbon nanotubes.<sup>11</sup>

**Table 3.3** Elemental composition of the PTI/LiCl,Br samples before and after acid treatment measured in combination with elemental analysis, ICP and XPS.

sample	C [wt%]	N [wt%]	H [wt%]	Li <sup>a</sup> [wt%]	Li <sup>b</sup> [wt%]	Cl / Br <sup>c</sup> [wt%]	Cl / Br <sup>b</sup> [wt%]	rest <sup>d</sup> [wt%]	wt. C/N
<b>PTI/LiCl</b>	30.7	51.4	1.7	2.3	2.1	8.2	4.9	9.0	0.60
PTI/LiCl 0% HCl	30.7	51.4	1.7	2.3	2.0	-	4.3	9.6	0.60
PTI/LiCl 12% HCl	30.9	53.0	1.9	1.7	2.1	-	5.7	7.2	0.58
PTI/LiCl 18% HCl	30.4	52.3	2.2	1.4	1.5	-	5.6	8.1	0.58
PTI/LiCl 36% HCl	31.3	53.6	2.1	0.1	0.0	8.7	5.5	7.4	0.58
C <sub>6</sub> N <sub>9</sub> H <sub>3</sub> ·HCl	26.60	46.77	2.05			14.01			0.57
(C <sub>6</sub> N <sub>9.05</sub> H <sub>5.51</sub> Cl <sub>1.07</sub> ) <sup>9</sup>									
C <sub>6</sub> N <sub>9</sub> H <sub>3</sub> ·HCl	28.39	50.06	1.95			14.94			0.57
(C <sub>6</sub> N <sub>9.07</sub> H <sub>4.91</sub> Cl <sub>1.07</sub> ) <sup>9</sup>									
<b>PTI/LiBr</b>	31.5	46.9	2.0	1.2	-	7.47	-	-	0.67
PTI/LiBr 0% HBr	31.5	46.9	2.0	1.2	2.3	-	6.6	1.8	0.67
PTI/LiBr 16% HBr	31.6	47.2	2.1	0.4	0.6	-	7.3	11.4	0.67
PTI/LiBr 23.5% HBr	32.2	48.0	2.2	0.6	0.7	-	6.2	10.8	0.67
PTI/LiBr 47% HBr	31.6	47.1	2.1	0.1	0.0	-	6.9	12.2	0.67

<sup>a</sup> Data from ICP analysis. <sup>b</sup> Data from XPS analysis. <sup>c</sup> Data from titration. <sup>d</sup> Based on EA, ICP (Li) and XPS (Cl,Br).

More details about the elemental composition and chemical environment can be obtained by X-ray photoelectron spectroscopy (XPS) and are shown in the Supporting Information. Consistent with the ICP results, the XPS spectra show that the acid treatment leads to a removal of lithium ions as observed by the gradually vanishing lithium signals (1s) of PTI/LiCl,Br at 54.8 eV / 54.9 eV with increasing concentrations of acids used until they completely disappear (PTI/LiCl: 36% HCl and PTI/LiBr: 47% HBr) (Figure S22 and Figure S24). The removal of lithium ions by HCl treatment has also been stated by *Ham et al.*<sup>12</sup> upon performing ion exchange in PTI/LiCl with [Pt(NH<sub>3</sub>)<sub>4</sub>]<sup>2+</sup>. We further observed that the chemical environment of the anions slightly changes (Figure S22 and Figure S24). While the binding energies of Cl in PTI/LiCl are 197.7 eV (2p<sub>3/2</sub>) and 199.3 eV (2p<sub>1/2</sub>), the signals shift to lower energies when treated with 36 % HCl: 197.0 eV (2p<sub>3/2</sub>) and 198.6 eV (2p<sub>1/2</sub>), which indicates slightly weakened bonding of the chlorides and the PTI scaffold. A similar shift of the signals can be observed for the bromides in the case of protonated PTI/LiBr.

The chemical environments of the carbon as well as nitrogen atoms of PTI/LiCl and PTI/LiBr slightly change after the acid treatment (Figure S21 and Figure S23). In total, three carbon signals (1s) located at 284.6 eV, 286.2 eV and 287.6 eV can be deconvoluted for PTI/LiCl and PTI/LiBr. While the first weak signal can be attributed to typical C-C bonds from adventitious carbon which is used for calibration,<sup>13-15</sup> the two other carbon peaks arise from sp<sup>2</sup> C atoms.<sup>14,16,17</sup> Theoretically, all carbon atoms in PTI should exhibit the same chemical environment. However, the irregular lithium/proton distribution is the reason for the existence of two sp<sup>2</sup> C signals. The carbon signal at 287.6 eV shifts about 0.3 eV to higher binding energies (287.9 eV) for the sample treated with concentrated



acids. In general, the signals of PTI/LiBr are broadened and the adventitious carbon peak at 284.6 eV is more evident, suggesting a larger carbon impurity and lower crystal order compared to PTI/LiCl. With regard to the high-resolution N (1s) spectra, two signals at 398.3 eV and 399.9 eV can be identified and attributed to the  $sp^2$  N atoms of the triazine rings<sup>13,18,19</sup> and bridging nitrogen atoms<sup>13,14</sup> in  $N(H_2^+, H, HLi^+, Li)(C_3N_3)_2$ , respectively (Figure S21 and Figure S23). Both signals slightly shift to higher binding energy (398.5 eV and 400.0 eV) due to protonation.

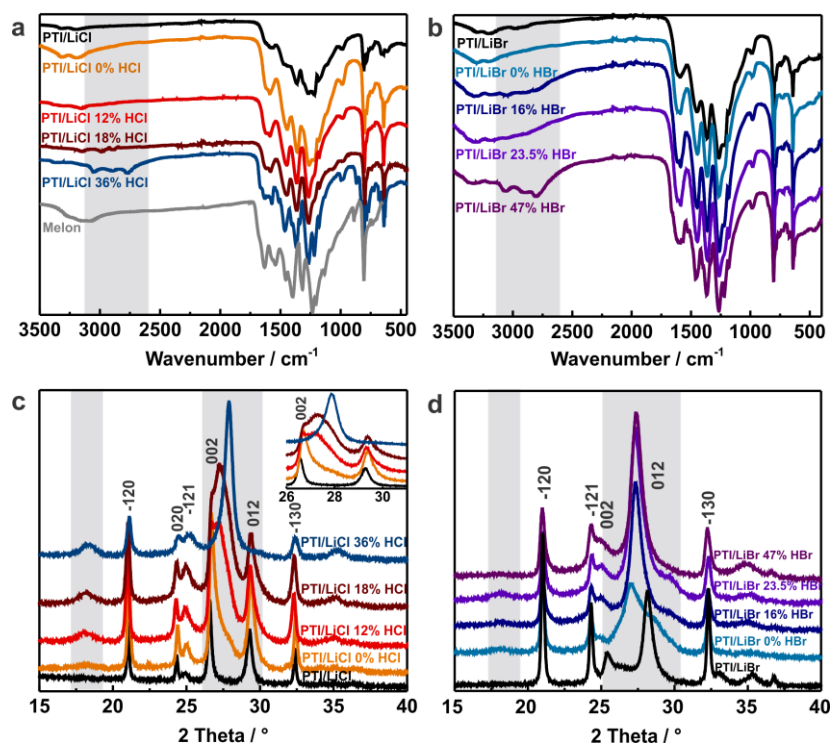


**Figure 3.13** IR spectra (top) and PXRD patterns (bottom) of PTI/LiCl (a,c) and PTI/LiBr (b,d) samples protonated with HCl or HBr solutions of different concentrations. The IR spectrum of melon is shown for comparison in (a). Regions that changed due to protonation are highlighted in grey.

The IR spectra of PTI/LiCl and PTI/LiBr are depicted in Figure 3.13(a,b). Both spectra are in agreement with the IR spectra of the literature and are nearly identical.<sup>5-7</sup> The bands at  $3300\text{ cm}^{-1}$  and  $3180\text{ cm}^{-1}$  indicate the presence of  $-NH$  groups. The sharp feature at  $805\text{ cm}^{-1}$  is attributed to the out-of-plane breathing mode of triazine units and the region from  $1200\text{ cm}^{-1}$  to  $1600\text{ cm}^{-1}$  can be assigned to the  $C=N$  stretching modes of  $C,N$  heterocycles. When protonated with concentrated acids another feature appears in the region from  $3100\text{ cm}^{-1}$  to  $2750\text{ cm}^{-1}$  due to the protonation of the  $-NH$  groups and the coordination to the anions (chloride or bromide) as also observed by *Wolf and co-workers*.<sup>1</sup> Further, the bands in the region from  $1200\text{ cm}^{-1}$  to  $1600\text{ cm}^{-1}$  appear to be more well-defined, which indicates a higher degree of local order for the protonated samples as compared to their parent compounds. While most of the PTI vibrations are unaffected, better agreement is found between the protonated samples and  $C_6N_9H_3 \cdot HCl$ <sup>9</sup> (Figure 3.14, left).

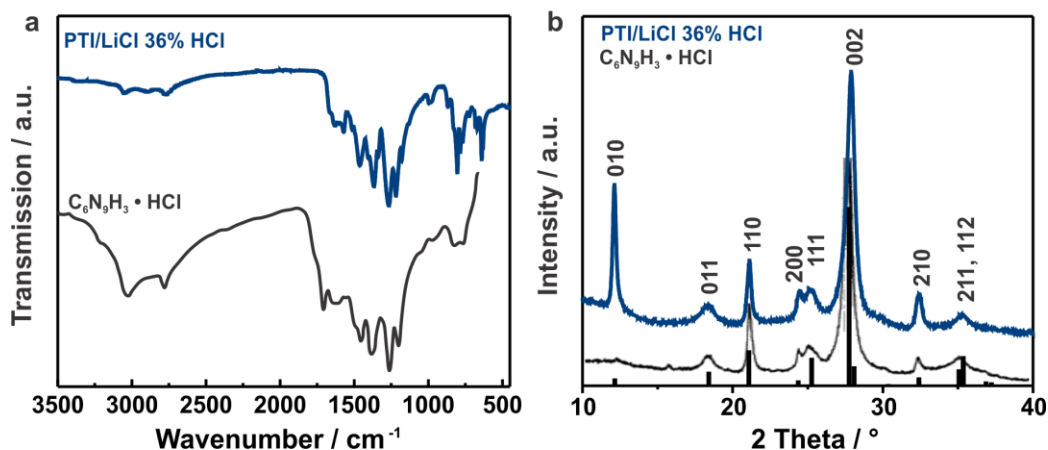


**Figure 3.14** IR spectra (a) and PXRD patterns (b) of PTI/LiCl 36% HCl as compared to  $C_6N_9H_3 \cdot HCl$  from the literature.<sup>1</sup>

The powder X-ray diffraction patterns of PTI/LiCl(LiBr) are in agreement with the literature, though less crystalline.<sup>5,7</sup> Acid treatment of PTI/LiCl(LiBr) leads to a gradual phase transformation which seems to be brought to completion when concentrated acids are used (PTI/LiCl 36% HCl and PTI/LiBr 47% HBr). The removal of the lithium ions through lithium-proton exchange leads to a decrease in layer distance of the PTI layers as indicated by the shift of the 002 stacking reflection to higher angles (Figure 3.13(c,d)). Further, loss of the  $c$  glide plane and symmetry reduction to  $P6_3/m$  (no 176) is observed since a new reflection at  $18.1^\circ 2\theta - 18.3^\circ 2\theta$  appears which can be assigned to the previously absent and forbidden 011 reflection. These changes in the PXRD pattern have already been observed by *Ham et al.*<sup>12</sup> and explained by partial delamination or decomposition of the framework but have not been further analyzed.

**Table 3.4** List of  $hkl$  and  $2\theta$  values for PTI/LiCl 36% HCl compared to PTI/LiCl and  $C_6N_9H_3 \cdot HCl$ .

PTI/LiCl (as-synthesized)		PTI/LiCl 36% HCl		$C_6N_9H_3 \cdot HCl$	
$hkl$	$2\theta / ^\circ$	$hkl$	$2\theta / ^\circ$	$hkl$	$2\theta / ^\circ$
010	12.1	010	12.1	010	12.1
		011	18.3	011	18.4
-120	21.1	110	21.1	110	21.1
020	24.4	200	24.4	200	24.3
-121	24.9	111	25.2	111	25.2
002	26.6	002	27.9	002	27.7
012	29.3				
-130	32.4	210	32.4	210	32.4

Interestingly, the PXRD pattern of PTI/LiCl 36% HCl is similar to the one of  $C_6N_9H_3 \cdot HCl$  (Figure 3.14, right and Table 3.4).<sup>1</sup> The positions of the reflections of the two compounds are identical which has additionally been confirmed by LeBail fits (see Supporting information, Figure S25). Rietveld refinements, however, was not possible due to the low quality of the powder patterns (generally, structure solution through Rietveld refinement in C,N-polymers is hampered by their relatively low crystallinity).

While a profile fit is possible, yielding lattice parameters of  $a = b = 8.50 \text{ \AA}$  and  $c = 6.44 \text{ \AA}$  for PTI/LiCl 36% HCl (Table 3.5), the intensity of the reflections of the protonated samples (especially the 010 reflection) do not agree with those reported for  $\text{C}_6\text{N}_9\text{H}_3\cdot\text{HCl}$ . A fit of the protonated PTI/LiCl samples was only possible by contracting the layer distance and more importantly by the “migration” of the anions towards the C,N-layers as reported for  $\text{C}_6\text{N}_9\text{H}_3\cdot\text{HCl}$  (Figure 3.12(c)). A lateral shift of the C,N-layers, as suggested for  $\text{C}_6\text{N}_9\text{H}_3\cdot\text{HCl}$  did not result in improved LeBail fits. The high intensity of the 010 reflection of PTI/LiCl 36% HCl could only be recovered by a hypothetical overpopulation of the chlorine content within the PTI-voids. Since the chlorine content remains unaffected after protonation, the additional electron density might arise from intercalated water within the voids.

**Table 3.5** Lattice parameters from Le Bail fits for the various PTI/LiCl (X% HCl) samples based on PTI/LiCl<sup>5</sup> and  $\text{C}_6\text{N}_9\text{H}_3\cdot\text{HCl}$ .<sup>1</sup>

samples	lattice parameter from LeBail fit based on PTI/LiCl ( $P6_3cm$ )		lattice parameters from LeBail fit based on $\text{C}_6\text{N}_9\text{H}_3\cdot\text{HCl}$ ( $P6_3/m$ )	
	$a=b$	$c$	$a=b$	$c$
original cifs	8.47	6.75	8.44	6.44
as-synthesized PTI/LiCl	8.46	6.74	8.53	6.65
PTI/LiCl 0% HCl	8.46	6.71	8.53	6.65
PTI/LiCl 12% HCl	8.51	6.70	8.50	6.58
PTI/LiCl 18% HCl	8.49	6.69	8.50	6.56
PTI/LiCl 36% HCl	8.46	6.73	8.50	6.44

We also observed this phase transformation when PTI/LiBr was stirred in other acids such as HF (40 %) or an aqueous solution of ammonium fluoride (Figure 3.15). Note that elemental analysis suggests that no fluorine has been intercalated and the bromine content remained unaffected, which is in stark contrast to previous reports.<sup>7</sup>

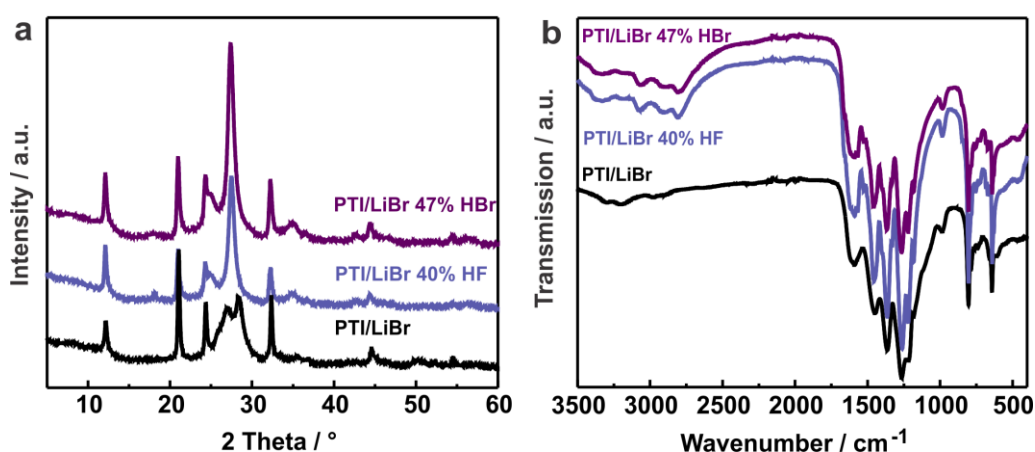


**Figure 3.15** PXRD patterns (a) and IR spectra (b) of PTI/LiBr either treated with 47% HBr or with 40% HF.

To further investigate the chemical environment of PTI/LiCl 36% HCl, we performed MAS ssNMR measurements and compared the results with PTI/LiCl and  $\text{C}_6\text{N}_9\text{H}_3\cdot\text{HCl}$

(measured under identical conditions) (Figure 3.16).  $C_6N_9H_3 \cdot HCl$  was synthesized by *E. Wirnhier* (LMU Munich) according to the procedure described in the literature.<sup>1</sup>

As already shown by elemental analysis, PTI/LiCl 36% HCl contains residual lithium ions and therefore,  $^7Li$  MAS spectra were recorded (Figure 3.16(d)). While for PTI/LiCl only one lithium environment (non-mobile lithium ion at 1 ppm with spinning sidebands, which result from quadrupolar interaction; deconvolution yields a quadrupolar coupling constant of 180 kHz and an asymmetry parameter of 0.8)<sup>20</sup> can be detected, the residual lithium ions of PTI/LiCl 36% HCl show two different lithium environments (a mobile lithium without spinning sidebands at 0 ppm and a non-mobile one at 2 ppm).

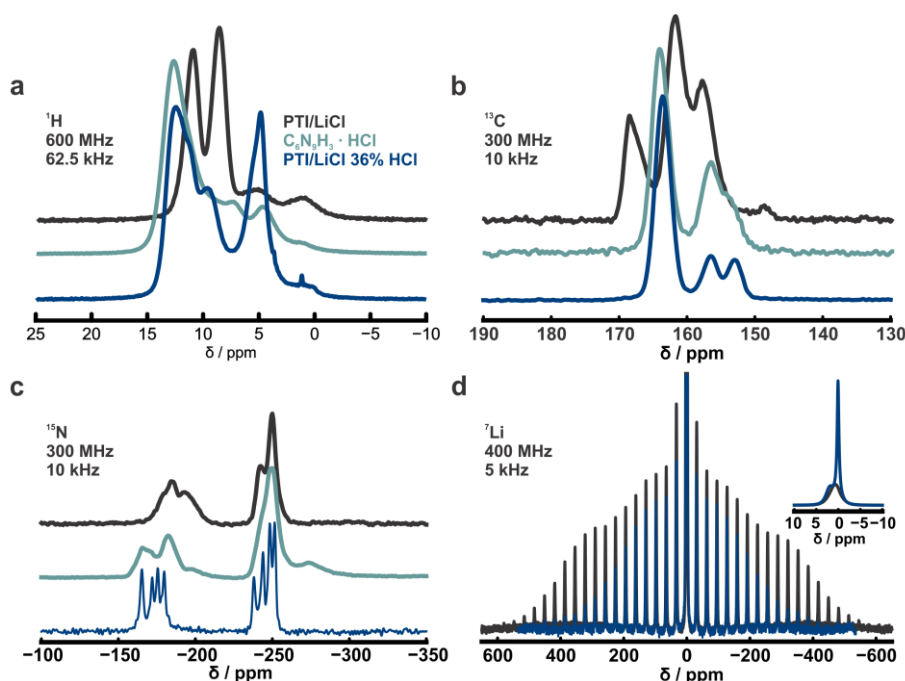


**Figure 3.16**  $^1H$  (a),  $^{13}C$  (b),  $^{15}N$  (c) and  $^7Li$  (d) CP-MAS solid-state NMR spectra of PTI/LiCl 36% HCl compared to PTI/LiCl and  $C_6N_9H_3 \cdot HCl$  (PTI/HCl) measured under identical conditions as given in the Figure. While for PTI/LiCl only one lithium signal is detected, two lithium signals can be detected in the case of PTI/LiCl 36% HCl (inset).

Additionally, high-resolution  $^1H$  measurements were conducted for all samples. Their main signals arise between 7 ppm and 15 ppm. The intensities below 6 ppm result most likely from residual water and probe background and consequently are not part of the samples. For PTI/LiCl 36% HCl this is corroborated by 2D spectra, as will be described later. The high-resolution  $^1H$  spectrum of PTI/LiCl reveals two main signals at 8 ppm and 11 ppm, whereas  $C_6N_9H_3 \cdot HCl$  has a broad signal at 12.5 ppm with a shoulder at the up-field side of the signal. The  $^1H$  spectrum of PTI/LiCl 36% HCl also has a broad signal at about 12.5 ppm with a shoulder and an additional signal at about 10 ppm. Besides the latter signal, the spectrum largely matches the one of  $C_6N_9H_3 \cdot HCl$ . To gain deeper insights into these additional features, a 2D  $^7Li$ - $^1H$  HMQC spectrum with a mixing time of 352  $\mu s$  (see Figure S29, Supporting Information) was recorded. It reveals a correlation between the lithium signals and the additional proton signals between 12.5 ppm and 9 ppm. The

intensity of these proton signals are reduced for the samples containing even less lithium. Hence, we believe that the additional signals arise from the residual lithium ions. The residual lithium ions complicate the evaluation especially of the  $^1\text{H}$  ssNMR spectra and consequently further experiments are necessary to completely remove the residual lithium ions.

The  $^{13}\text{C}$  CP–MAS ssNMR spectrum of PTI/LiCl 36% HCl reveals three signals at 163.5 ppm, 156.3 ppm and 152.9 ppm. As expected for a protonated structure, all three signals have protons nearby. This was confirmed by a 2D  $^{13}\text{C}$ – $^1\text{H}$  heteronuclear multiple bond correlation (HMQC) experiment (see Figure S28, Supporting Information), as all carbon atoms show correlation peaks with proton signals above 7 ppm. This also supports the assumption that  $^1\text{H}$  signals below 6 ppm are not part of the sample. For PTI/LiCl, the  $^{13}\text{C}$  CP–MAS ssNMR spectrum gives three overlapping signals between 153 ppm and 170 ppm. According to *Wirnhier et al.*<sup>5</sup> they are assigned to three different  $\text{C}_3\text{N}_3$ -triazine carbon signals which are non-protonated (168.0 ppm) and protonated (162.6 ppm and 157.9 ppm). Further details about the proton/lithium structure and the shift assignment are given in the PhD thesis of Maria B. Mesch (University of Bayreuth).<sup>20</sup> The spectrum of  $\text{C}_6\text{N}_9\text{H}_3\cdot\text{HCl}$  looks very similar to that of PTI/LiCl 36% HCl, revealing three signals at 164.3 ppm, 156.6 ppm and 154.0 ppm, although the latter two are less well-resolved. According to *Wolf and co-workers*,<sup>1</sup> the most prominent  $^{13}\text{C}$  signal of  $\text{C}_6\text{N}_9\text{H}_3\cdot\text{HCl}$ , at 164.3 ppm, is assigned to the non-protonated  $\text{C}_3\text{N}_3$ -triazine carbon which is in agreement with the one of PTI/LiCl 36% HCl. The signals at 156.6 ppm and 154.0 ppm arise due to partial protonation. While *Wolf and co-workers*<sup>1</sup> assumed protonation of the more basic triazine-nitrogen to be more favorable, protonation of the imide-nitrogen could not be excluded. According to *Wolf and co-workers*<sup>1</sup> the protonation of the triazine-nitrogen would lead to a 1:1:1 splitting in the  $^{13}\text{C}$  spectrum, while the protonation of the imide-nitrogen would result in two different carbon signals (2:1).<sup>1</sup> It might also be possible that both kinds of nitrogen atoms (heterocycle and imide-bridge) are partially protonated. Although the signal assignment is not clear yet, comparison of the  $^{13}\text{C}$  NMR spectral features reveals that PTI/LiCl 36% HCl is similar to  $\text{C}_6\text{N}_9\text{H}_3\cdot\text{HCl}$ .

This was further studied using  $^{15}\text{N}$  experiments. All spectra show signals in the area of tertiary nitrogen atoms (–200 ppm to –150 ppm) and signals for NH groups (–230 ppm to –260 ppm), as expected for these structures with the main difference being the resolution. The  $^{15}\text{N}$  spectrum of PTI/LiCl 36% HCl is highly interesting due to its exceptionally well-resolved  $^{15}\text{N}$  resonances, which implies a high local order of the nitrogen signals. The NH signals (–230 ppm to –253 ppm) and the signals between –160 ppm and –180 ppm are splitted into four, which are assigned to tertiary nitrogen atoms. The splittings are caused by protonation and changes in the chemical environments of the nitrogen atoms. Further, the latter signals are shifted to lower field (–160 ppm and –180 ppm) compared to PTI/LiCl (–165 ppm and –210 ppm) due to the approach of the chlorid ions, which is well in agreement with the shifts observed for  $\text{C}_6\text{N}_9\text{H}_3\cdot\text{HCl}$ . A protonation induces additional positive charges resulting in a lower core shielding.



The split signals in the  $^{13}\text{C}$  as well as  $^{15}\text{N}$  CP–MAS ssNMR spectra of PTI/LiCl 36% HCl still need to be clarified. Therefore, further investigations using neutron diffraction, 2D ssNMR experiments ( $^1\text{H}$ – $^{15}\text{N}$ ), distance measurements or direct excitation experiments are needed, preferably with  $^{15}\text{N}$ -enriched lithium-free samples.

We further performed a series of 2D and pseudo 2D experiments ( $^1\text{H}$ – $^1\text{H}$  double-quantum-single-quantum,  $^1\text{H}$ – $^{13}\text{C}$  CP build-up and  $^1\text{H}\{^7\text{Li}\}$ REDOR) which are not discussed here but added to the supplementary information for completeness (see Figure S27,28). Clearly, PTI/LiCl 36% HCl significantly differs from PTI/LiCl according to the ssNMR spectra. In general, better agreement can be observed for PTI/LiCl 36% HCl and  $\text{C}_6\text{N}_9\text{H}_3\cdot\text{HCl}$ .

We used transmission electron microscopy (TEM) to investigate the morphology changes during protonation to obtain information about possible hydrolysis and degradation during the acid treatment. TEM images of PTI/LiCl 36% HCl demonstrate the formation of regular crystallites with hexagonal symmetry (Figure 3.17(a) and Figure S42), as also observed for the parent compound. However, some of these crystallites form agglomerates along the  $c$ -axis after the acid treatment (Figure 3.17(b)). In contrast to PTI/LiCl, the PTI/LiBr crystallites seem to be corroded (frayed edges) and agglomerated even before acid treatment (Figure S31). Since the bromine-containing eutectic salt melt is more aggressive than LiCl/KCl, the resulting PTI/LiBr crystallites are damaged before the performed acid treatment.

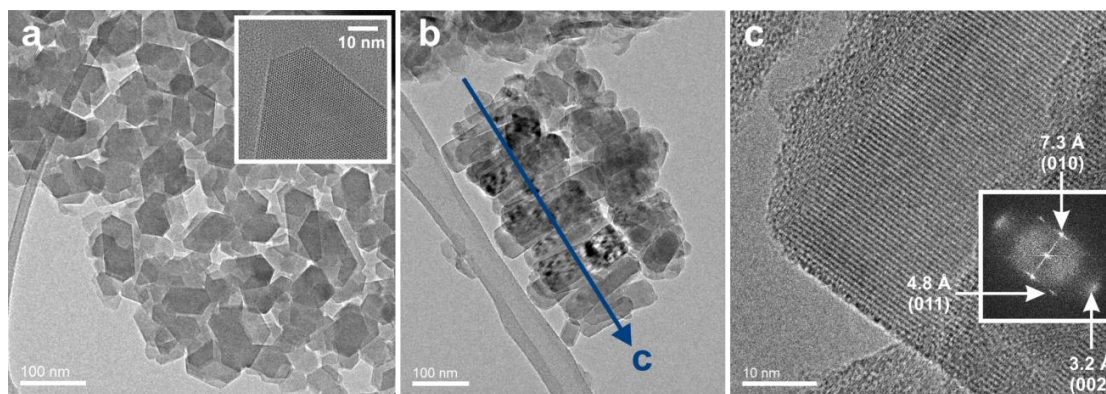


**Figure 3.17** TEM images of PTI/LiCl 36% HCl. (a) Overview of PTI crystallites spread over the TEM grid, inset shows a crystallite at higher magnification. (b) The sample contains also crystallites which are aligned along the  $c$ -axis (known from SAD). (c) FFT (inset) of a PTI crystallite shows three different reflections, namely 010 and 002 which are also found in PTI/LiCl, as well as additionally the 011 reflection which only exists in the acid treated sample.

By means of selected area diffraction (SAD) patterns and fast Fourier transforms (FFTs), the crystallites differed from the parent compound, a reduced symmetry has been noticed. The SAD patterns of PTI/LiCl 36% HCl and PTI/LiBr 47% HBr are in agreement with the PXRD patterns. Most of the reflections seen here are also visible in PTI/LiCl(LiBr) indicating that both compounds are structurally closely related (see Figure S32–34, Supporting Information). Similar to the results of the PXRDs, the stacking distances of the acid treated

samples are smaller than those of their parent compounds and an additional reflection is observed which can be assigned to the 011 reflection (Figure 3.17(c) and see Figure S30 of the Supporting Information). According to SAD simulations (Figure S34), the acid treated samples are structurally very similar to  $C_6N_9H_3 \cdot HCl$  ( $P6_3/m$ , no 176), and distinct from PTI/LiCl.

Stirring PTI/LiCl,Br in concentrated acids causes slightly optical whitening of the samples (Figure S35, Supporting Information). The UV-Vis spectra of PTI/LiCl 0% – 18% HCl are identical to that of PTI/LiCl and the literature,<sup>4</sup> showing a dominant absorption in the UV region between 300 nm and 400 nm with a sharp absorption edge at 420 nm and a very broad feature at around 450 nm (Figure 3.18(a)). This absorption is less intense after stirring the sample in 36 % HCl. In contrast to PTI/LiCl, PTI/LiBr exhibits a broad absorption up to 800 nm (Figure S36). Most likely, this optical feature (resulting in the darker color of the sample), combined with the increased carbon content determined by C/N analyses and the corroded crystallites indicates partial decomposition of the framework and the formation of amorphous carbon due to the more aggressive LiBr/KBr conditions as compared to LiCl/KCl.<sup>21</sup> Still, a small blue-shift (ca. 0.1 eV) of the absorption edge can also be observed here after acid treatment (Figure S36). A band gap of 1.8 ( $\pm 0.2$ ) eV can be extracted for PTI/LiCl by X-ray emission spectroscopy (XES), while the acid treatment leads to a widening of the band gap to up to 2.1 ( $\pm 0.2$ ) eV for PTI/LiCl 36% HCl. XES analyses have not been performed for PTI/LiBr due to its lower crystallinity as compared to PTI/LiCl and its broad and ill-defined UV-Vis absorption spectrum.

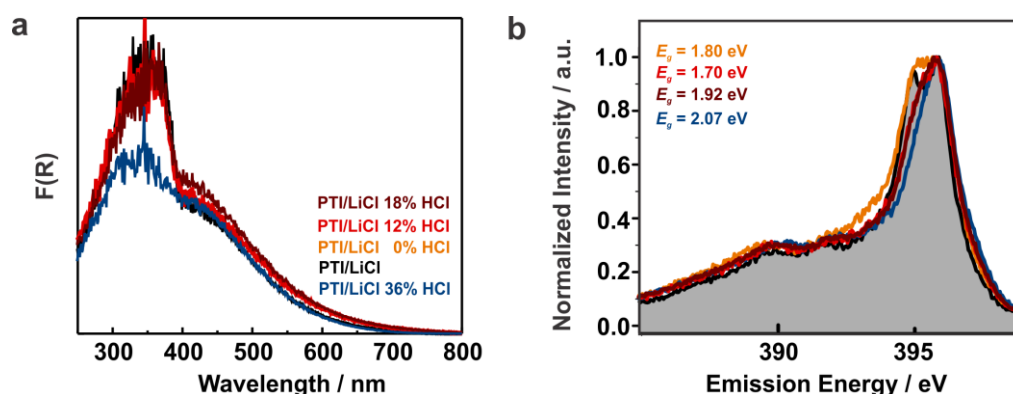


**Figure 3.18** UV-Vis (a) and XES (b) spectra of PTI/LiCl samples protonated with varied concentrated HCl solutions.

Finally, we investigated the photocatalytic activity of the PTI samples. To this end, we used platinum nanoparticles (2.2 wt%) as the co-catalyst, which were formed *in situ* by photoreduction of  $H_2PtCl_6$ , and 10 vol% of an electron donor (methanol or triethanolamine) was added. The dispersed samples (10 mg in 10 mL) were illuminated with simulated sunlight with a 420 nm cut-off mirror (see Chapter 7.1 Supporting information). While PTI/LiCl produces a significant amount of hydrogen as described in previous chapters, the activity declines for PTI/LiCl 12% through 18% HCl until it collapses for PTI/LiCl 36% HCl (Figure 3.19 and Figure S38). Similar to the results

reported for  $C_6N_9H_3 \cdot HCl$  by *McMillan and co-workers*,<sup>10</sup> the photocatalytic activity of PTI/LiCl 36% HCl was negligibly low (even when illuminated with a 250 nm – 2000 nm filter), especially when MeOH was chosen as sacrificial agent. Even though *Moewes and co-workers*<sup>8</sup> had predicted a high photocatalytic activity for lithium-free PTI/LiCl, actually the opposite has been shown to be the case for PTI/HCl here.

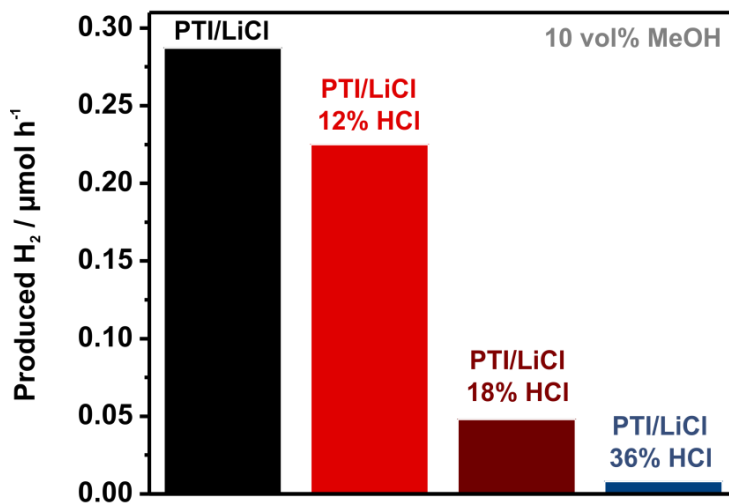


**Figure 3.19** Photocatalytic activity of 2.2 wt% Pt-modified PTI/LiCl compared to PTI/LiCl 12–36% dispersed in an aqueous 10 vol% methanol solution and illuminated with a 420 nm cut-off filter.

The photocatalytic activity of PTI/LiBr is very low even before the acid treatment, but also declines further when treated with acids (see Figure S38 and Figure S39). The gradual decrease in photocatalytic activity seems to correlate with the extraction of the lithium ions and the accompanied phase transformation from PTI/LiCl,Br to PTI/HCl,Br which had not been considered by *Moewes and co-workers*.<sup>8</sup>

For this reason, we tried to reinsert the lithium ions in PTI/LiCl 36% HCl to re-form photocatalytically active PTI/LiCl,Br. To this end, a PTI/LiCl 36% HCl sample (containing 0.19 ( $\pm 0.01$ ) wt% of lithium) was stirred in a saturated LiOH solution (alternatively, dialysis was carried out with a saturated LiCl solution) for more than one week and rinsed the obtained product in water until neutralized. According to ICP, the lithium content of PTI/LiCl 36% HCl could be increased from 0.19 wt% to 0.53 ( $\pm 0.01$ ) wt% (by stirring in LiOH solution) and to 0.58 ( $\pm 0.01$ ) wt% (by dialysis with LiCl) but did not reach the original value of 2.1 wt% (PTI/LiCl). Even though we saw an increase in the lithium content, the PXRD patterns remained unchanged, thus no phase transformation back to PTI/LiCl could be detected. While we could triple the lithium content, the photocatalytic activity only increased by about 39 %, which might be due to the irreversibly contracted layer distance and less accessible active sites of PTI (Figure S40) in the more densified structure of PTI/LiCl 36% HCl. We also reheated PTI/LiCl 36% HCl in a LiCl/KCl salt melt (under closed atmosphere) to reinsert lithium ions but the resulting products did not show any increased lithium content.



### 3.3.3 Conclusion

In conclusion, the acidic extraction of the lithium ions in PTI/LiCl(LiBr)<sup>5-7</sup> is accompanied by a lithium-proton exchange and results in an irreversible phase transformation from PTI/LiCl(LiBr) to PTI/HCl(HBr). While PTI/LiCl(LiBr) can easily be synthesized by an ionothermal procedure, high-pressure was needed for the synthesis of PTI/HCl (C<sub>6</sub>N<sub>9</sub>H<sub>3</sub>·HCl) so far.<sup>1</sup> The presence of residual lithium ions in PTI/HCl(HBr) indicates that the lithium-proton exchange has not been completed. Due to the results of X-ray and selected area diffraction, IR and XPS analysis, we conjecture that the protonated samples essentially consist of PTI/HCl(HBr). The PXRD patterns of PTI/HCl(HBr) further show reduced symmetry (space group *P6<sub>3</sub>/m*) and a reduced interdistance compared to the parent compound PTI/LiCl(LiBr). Notably, the position of the anions in PTI/HCl(HBr) has changed compared to PTI/LiCl(LiBr); Cl and Br now likely reside in the voids within the PTI layers. A lateral shift of the C,N-layers as suggested for C<sub>6</sub>N<sub>9</sub>H<sub>3</sub>·HCl may be possible but cannot be verified. Additionally, partial agglomeration of the PTI crystallites was detected by TEM. Interestingly, solid-state NMR measurements reveal an exceptionally high order in the carbon nitride backbone of PTI/HCl which will be further analyzed in the future. While the reduced layer distance in PTI/HCl(HBr) would be expected to result in improved interlayer interactions, including charge separation and transfer, as compared to PTI/LiCl(LiBr), the band gap increases for PTI/HCl(HBr) and lower photocatalytic activity has been detected. The loss in the photocatalytic activity of PTI/HCl(HBr) can be reasoned by: a) a hampered charge transfer along the stacking direction (and stacked triazines) due to a possible lateral shift of the C,N-layers,<sup>11,12</sup> b) a reduced absorption in the region of visible light due to an increased band gap and c) more significant, a reduced accessibility of the catalytically relevant sites due to the contraction of the carbon nitride layers, partial agglomeration, more packed voids and proton-poisoned nitrogen moieties which can act as anchor groups for the co-catalyst platinum. The insights obtained by studying the ionic effects on the structure-property-activity relationships in PTI in particular and organic photocatalysts in general, will be helpful for unmasking of catalytically relevant sites.

### Bibliography

- (1) Z. Zhang, K. Leinenweber, M. Bauer, L. A. J. Garvie, P. F. McMillan, G. H. Wolf, *J. Am. Chem. Soc.* **2001**, *123*, 7788.
- (2) X. Wang, K. Maeda, A. Thomas, K. Takanabe, G. Xin, J. M. Carlsson, K. Domen, M. Antonietti, *Nat. Mater.* **2009**, *8*, 76.
- (3) X. Wang, K. Maeda, X. Chen, K. Takanabe, K. Domen, Y. Hou, X. Fu, M. Antonietti, *J. Am. Chem. Soc.* **2009**, *131*, 1680.
- (4) K. Schwinghammer, B. Tuffy, M. B. Mesch, E. Wirnhier, C. Martineau, F. Taulelle, W. Schnick, J. Senker, B. V. Lotsch, *Angew. Chem. Int. Ed.* **2013**, *52*, 2435.
- (5) E. Wirnhier, M. Döblinger, D. Gunzelmann, J. Senker, B. V. Lotsch, W. Schnick, *Chem. Eur. J.* **2011**, *17*, 3213.

- (6) M. J. Bojdys, J.-O. Müller, M. Antonietti, A. Thomas, *Chem. Eur. J.* **2008**, *14*, 8177.
- (7) S. Y. Chong, J. T. A. Jones, Y. Z. Khimiyak, A. I. Cooper, A. Thomas, M. Antonietti, M. J. Bojdys, *J. Mater. Chem. A* **2013**, *1*, 1102.
- (8) E. J. McDermott, E. Wirnhier, W. Schnick, K. S. Viridi, C. Scheu, Y. Kauffmann, W. D. Kaplan, E. Z. Kurmaev, A. Moewes, *J. Phys. Chem. C* **2013**, *117*, 8806.
- (9) P. F. McMillan, V. Lees, E. Quirico, G. Montagnac, A. Sella, B. Reynard, P. Simon, E. Bailey, M. Deifallah, F. Corà, *J. Solid State Chem.* **2009**, *182*, 2670.
- (10) A. B. Jorge, D. J. Martin, M. T. S. Dhanoa, A. S. Rahman, N. Makwana, J. Tang, A. Sella, F. Corà, S. Firth, J. A. Darr, P. F. McMillan, *J. Phys. Chem. C* **2013**, *117*, 7178.
- (11) E. R. Edwards, E. F. Antunes, E. C. Botelho, M. R. Baldan, E. J. Corat, *Applied Surface Science* **2011**, *258*, 641.
- (12) Y. Ham, K. Maeda, D. Cha, K. Takane, K. Domen, *Chem. Asian J.* **2013**, *8*, 218.
- (13) S. Yang, Y. Gong, J. Zhang, L. Zhan, L. Ma, Z. Fang, R. Vajtai, X. Wang, P. M. Ajayan, *Adv. Mater.* **2013**, *25*, 2452.
- (14) M. Kim, S. Hwang, J.-S. Yu, *J. Mater. Chem.* **2007**, *17*, 1656.
- (15) A. Essafti, Y. Ijdiyaou, M. Azizan, *Sol. Energ. Mat. Sol. C* **2006**, *90*, 4.
- (16) B. Angleraud, N. Mubumbila, P. Y. Tessier, V. Fernandez, G. Turban, *Diam. Relat. Mater.* **2001**, *10*, 1142.
- (17) S. S. Roy, R. McCann, P. Papakonstantinou, P. Maguire, J. A. McLaughlin, *Thin Solid Films* **2005**, *482*, 145.
- (18) J. Xu, Y. Li, S. Peng, G. Lu, S. Li, *Phys. Chem. Chem. Phys.* **2013**, *15*, 7657.
- (19) M. Aono, S. Aizawa, N. Kitazawa, Y. Watanabe, *Thin Solid Films* **2008**, *516*, 648.
- (20) M. B. Mesch, *PhD thesis*, University of Bayreuth, **2016**.
- (21) [http://www.crct.polymtl.ca/fact/documentation/FTsalt/FTsalt\\_Figs.htm](http://www.crct.polymtl.ca/fact/documentation/FTsalt/FTsalt_Figs.htm), accessed on 21<sup>st</sup> of December **2015**.

# Chapter IV

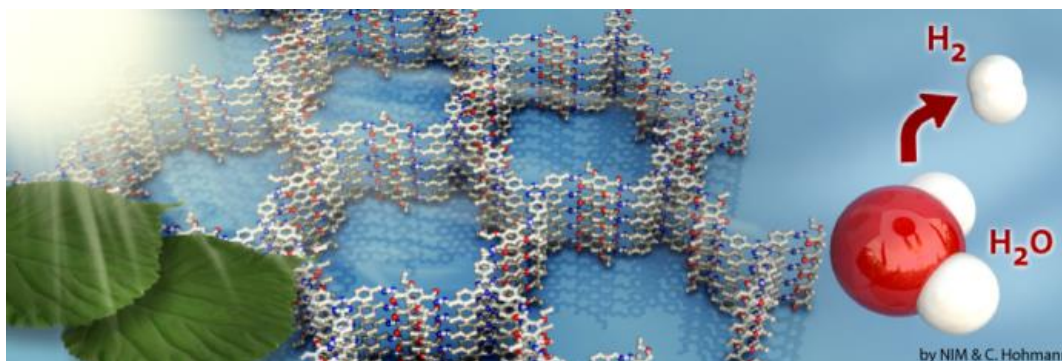
## 4 Covalent organic frameworks

### 4.1 TFPT-COF as photocatalyst

#### A hydrazone-based covalent organic framework for photocatalytic hydrogen production

Linus Stegbauer, Katharina Schwinghammer and Bettina V. Lotsch

Published in: *Chem. Sci.* **2014**, *5*, 2789–2793; DOI: 10.1039/C4SC00016A.



#### Abstract

Covalent organic frameworks (COFs) have recently emerged as a new generation of porous polymers combining molecular functionality with the robustness and structural definition of crystalline solids. Drawing on the recent development of tailor-made semiconducting COFs, we report here on a new COF capable of visible-light driven hydrogen generation in the presence of Pt as a proton reduction catalyst (PRC). The COF is based on hydrazone-linked functionalized triazine and phenyl building blocks and adopts a layered structure with a honeycomb-type lattice featuring mesopores of 3.8 nm and the highest surface area among all hydrazone-based COFs reported to date. When illuminated with visible light, the Pt-doped COF continuously produces hydrogen from water without signs of degradation. With their precise molecular organization and modular structure combined with high porosity, photoactive COFs represent well-defined model systems to study and adjust the molecular entities central to the photocatalytic process.

### 4.1.1 Introduction

The last decade has seen a continuous rise in activity revolving around the development of potent photocatalytic systems which are capable of transforming solar energy into chemical fuels.<sup>1</sup> Whilst most photocatalysts are based on inorganic semiconductors,<sup>2</sup> there are a few examples of materials composed solely of light elements.<sup>3</sup> These systems, prominently represented by carbon nitride polymers, are moderately active in hydrogen generation from water,<sup>4</sup> however their performance can be significantly enhanced by morphology tuning and structural modifications, including doping.<sup>5,6</sup> The major downside of these polymers, however, is their lack of crystallinity and generally low surface areas, which are inherently hard to control. In addition, carbon nitrides are invariably composed of heptazine or triazine units, thus offering only limited chemical variety and they are not very susceptible to systematic post-modification. A closely related class of organic polymers, dubbed covalent organic frameworks (COFs), is apt to overcome these inherent weaknesses of carbon nitrides by combining chemical versatility and modularity with potentially high crystallinity and porosity.<sup>7-11</sup> Recently, unique 2D COFs with interesting optoelectronic properties have emerged, representing ideal scaffolds for exciton separation and charge percolation within self-sorted, nanoscale phase-separated architectures. Whereas most COFs rely on the formation of water-labile boronate ester linkages,<sup>12</sup> a few other examples based on imine<sup>13-17</sup> and hydrazine<sup>18</sup> linkages have been synthesized recently. For example, the imine-based COF-LZU1 in combination with Pd has been used as catalyst in *Suzuki* couplings.<sup>19</sup> Surprisingly, after the pioneering work by *Yaghi*, hydrazone formation has not been used again for the synthesis of COFs, although hydrazones are typically much less prone to hydrolysis than imines.<sup>20</sup> This chemoselective type of bond formation between a substituted acyl hydrazine and an aldehyde is highlighted by its use in labeling modified proteins<sup>21</sup> and for drug delivery purposes.<sup>22</sup>

Although big strides towards photoactive COFs with light-harvesting and charge separation capabilities have already been made,<sup>15,23-27</sup> COFs have not yet been explored as photosensitizers in photocatalytic systems for the production of solar fuels. A first indication of the underlying potential of COFs as a photoactive material was the light-induced activation of oxygen by a squaraine-based COF reported recently by *Jiang and co-workers*.<sup>13</sup>

Herein, we report the first COF which is active in visible light induced hydrogen evolution in the presence of Pt as the proton reduction catalyst (PRC). Our hydrazone-based COF (TFPT-COF) is constructed from 1,3,5-*tris*-(4-formyl-phenyl)triazine (TFPT) and 2,5-diethoxy-terephthalohydrazide (DETH) building blocks (Figure 4.1), featuring mesopores of 3.8 nm in diameter and the highest surface area among all hydrazone-based COFs reported so far.

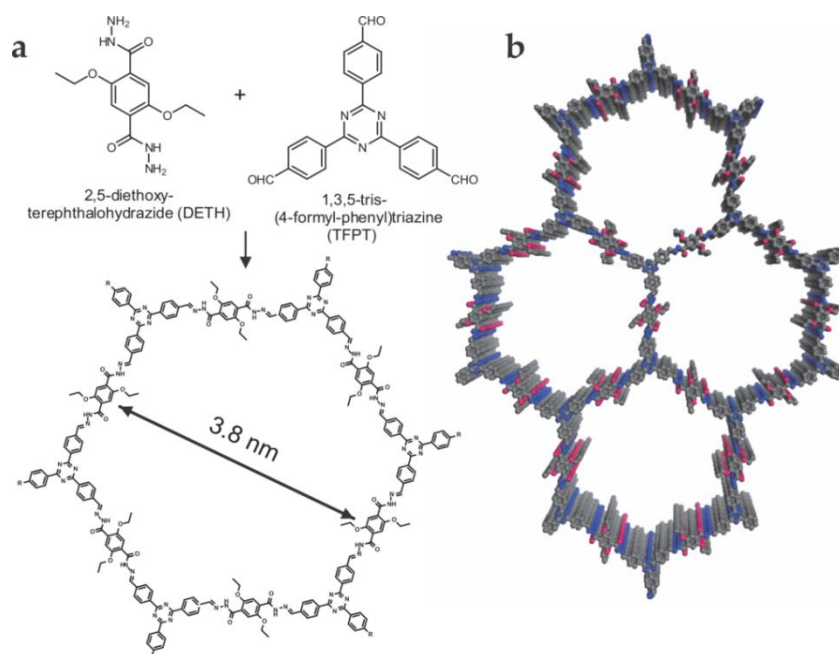


**Figure 4.1** Acetic acid catalyzed hydrazone formation furnishes a mesoporous 2D network with a honeycomb-type in plane structure. (a) Scheme showing the condensation of the two monomers to form the TFPT-COF. (b) TFPT-COF with a co-facial orientation of the aromatic building blocks, constituting a close-to eclipsed primitive hexagonal lattice (grey: carbon, blue: nitrogen, red: oxygen).

#### 4.1.2 Results and Discussion

##### TFPT-COF: Synthesis and characterization

Triazine-based molecules offer high electron mobilities, electron withdrawing character<sup>28</sup> and are hence widely used in synthetic chemistry<sup>29</sup> and optoelectronics.<sup>28</sup> TFPT has a much smaller dihedral angle between the phenyl and triazine unit ( $\sim 7.7^\circ$ ) compared to its benzene centered analogue ( $38.3^\circ$ ) (Figure S43, 7.1 Supporting information).<sup>30</sup> As a consequence, the use of TFPT should facilitate the formation of a planar COF with an extended  $\pi$ -system compared to the monomers and enhanced crystallinity. Indeed, the TFPT-COF turns out to be crystalline and at the same time stable in methanol and other solvents (Figure S57, 7.1 Supporting information).

TFPT-COF was synthesized by the acetic acid catalyzed reversible condensation of the building blocks in dioxane–mesitylene (1:2 v/v) at 120 °C in a sealed pressure vial under an argon atmosphere for 72 hours. The product was obtained as a fluffy pale-yellow nanocrystalline solid. To remove any starting material or solvent contained in the pores, TFPT-COF was centrifuged, washed with DMF and THF, soaked in DCM for 3 hours, and subsequently heated to 120 °C under a high dynamic vacuum for 12 h ( $10^{-7}$  mbar). It is worth mentioning that TFPT-COF could also be synthesized by *in situ* deprotection and subsequent condensation in a one-pot procedure (see Scheme S6, 7.1 Supporting information). Using this reaction scheme, the acetal protected TFPT is deprotected by treatment with a catalytic amount of camphorsulfonic acid in the solvent mixture. The COF formation is then started by adding the corresponding catalytic amount of sodium acetate to the reac-

tion mixture. After 72 h, we obtained a material chemically and structurally identical to TFPT-COF (Figure S44, 7.1 Supporting information). This protocol opens the door to a new variety of acetal-protected building blocks and at the same time enhances the solubility of otherwise insoluble building blocks due to the aliphatic protection group.

ATR-IR data of TFPT-COF show stretching modes in the range  $1670\text{ cm}^{-1}$  –  $1660\text{ cm}^{-1}$  and  $1201\text{ cm}^{-1}$  –  $1210\text{ cm}^{-1}$ , which are characteristic of C=N moieties. The lack of the aldehyde Fermi double resonance at  $2824\text{ cm}^{-1}$  and  $2721\text{ cm}^{-1}$ , as well as the aldehyde carbonyl stretching vibration at  $1700\text{ cm}^{-1}$  of the TFPT monomer clearly suggests the absence of any starting material. Furthermore, the triazine moiety is still present in the TFPT-COF as ascertained by the triazine semicircle stretch vibration at  $806\text{ cm}^{-1}$  (Figure S45, 7.1 Supporting information).

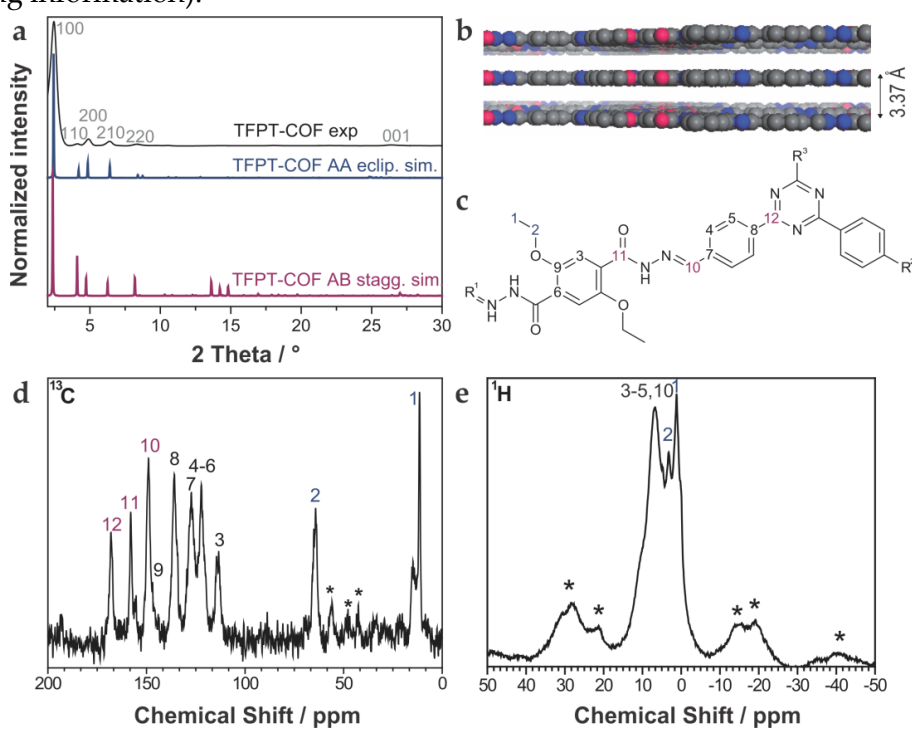


**Figure 4.2** Characterization of the TFPT-COF by PXRD and MAS solid-state NMR spectroscopy. (a) and (b) PXRD suggests a (close to) eclipsed layer stacking as confirmed by Pawley refinement of the AA-stacked structure model. (c) Assignment of  $^{13}\text{C}$  and  $^1\text{H}$  NMR data. (d)  $^{13}\text{C}$  CP-MAS NMR spectrum, asterisks mark spinning side bands. (e)  $^1\text{H}$  MAS NMR spectrum with a group of signals centered between 1 and 8 ppm; asterisks mark spinning side bands.

$^1\text{H}$  solid-state NMR MAS spectroscopy shows the presence of the ethoxy group through signals at 1.39 ppm ( $\text{CH}_3\text{-CH}_2\text{-O}$ ) and 3.29 ppm ( $\text{CH}_3\text{-CH}_2\text{-O}$ ) (Figure 4.2(e)). The aromatic region is represented by a broadened signal at 6.5 ppm. Furthermore, the  $^{13}\text{C}$  CP-MAS spectrum clearly supports the formation of a hydrazone bond corresponding to the signal at 148.9 ppm, and confirms the presence of the triazine ring (167.9 ppm) (Figure 4.2(d)). All other signals were also unambiguously assigned to the corresponding carbon atoms (Figure 4.2(c)).<sup>18</sup>

Powder X-ray diffraction (PXRD) measurements confirm the formation of a crystalline framework with metrics being consistent with the structure model shown in Figure 4.1. Comparison of the experimental data with the simulation<sup>31</sup> reveal a hexagonal structure with  $P6/m$  symmetry and an eclipsed AA layer stacking, which is in line with most COF structures reported to date (Figure 4.2(a)).<sup>7-11</sup> Nevertheless, we assume that slight offsets with respect to the ideal co-facial layer stacking have to be taken into account as recently delineated by Heine,<sup>32</sup> Dichtel and co-workers.<sup>33</sup> Subtle layer offsets which are not resolvable by XRD result in the minimization of repulsive electrostatic forces between the layers with respect to the energetically less favorable, fully eclipsed structures. Nevertheless, whether the same situation also holds true for hydrazone COFs has yet to be demonstrated.

Pawley refinement (including peak broadening) of the experimental powder pattern gave lattice parameters of  $a = b = 41.90 \text{ \AA}$  (Figure 4.2(a) and Figure S47, 7.1 Supporting information). The theoretical powder pattern of the related staggered conformation derived from the *gra net* with  $P6_3/m$  symmetry does not reproduce the observed intensity distribution and was therefore discarded (Figure 4.2(a) and Figure S50, 7.1 Supporting information). The 001 diffraction peak at  $2\theta = 26.6^\circ$  corresponds to an interlayer distance of  $3.37 \text{ \AA}$  (Figure 4.2(b)), suggesting a typical van der Waals contact between the aromatic layers. Interestingly, the presence of the ethoxy groups protruding into the pores does not notably increase the interlayer distance, thus indicating a predominantly coplanar arrangement with the plane of the honeycomb lattice.

According to the above theoretical studies and other predictions for the stacking of triazines by Gamez *et al.*,<sup>34</sup> we have also simulated a parallel displaced structure (displacement vector  $1.4 \text{ \AA}$ ) with an AA'A-type stacking sequence (Figure S51 and Figure S52, 7.1 Supporting information). As expected, the simulated PXRD is very similar to both the experimental PXRD as well as the PXRD calculated for the perfectly eclipsed structure (Figure S43, 7.1 Supporting information).

Argon sorption measurements at 87 K clearly show the formation of mesopores as indicated by a typical type IV adsorption isotherm (Figure 4.3(a)). The Brunauer–Emmett–Teller (BET) surface area was calculated to be  $1603 \text{ m}^2 \text{ g}^{-1}$  (total pore volume is  $1.03 \text{ cm}^3 \text{ g}^{-1}$ , Figure S54, 7.1 Supporting information), which is the highest measured surface area among all hydrazone COFs reported to date.<sup>13-18,35</sup> Comparing these values with those of COF-43, derived from a benzene-centered trigonal building block with the same pore size,<sup>18</sup> the surface area has more than doubled, probably as a consequence of the smaller dihedral angle of the triazine-centered TFPT and the resulting more favorable stacking interactions, or due to the more complete activation of the material. The pore size distribution (PSD) was evaluated with non-local density functional theory (NLDFT). The experimental PSD exhibits a maximum at  $3.8 \text{ nm}$ , thereby verifying the theoretical pore diameter of  $3.8 \text{ nm}$  (Figure S55, 7.1 Supporting information), which is the same pore size found by Yaghi and co-workers for their benzene-centered COF.<sup>18</sup> Transmission electron microscopy images confirm the data derived from PXRD and sorption measurements. The



hexagonal pore arrangement with pore distances of  $\approx 3.4$  nm is clearly visible, as well as the layered nanomorphology (Figure 4.3(b)).

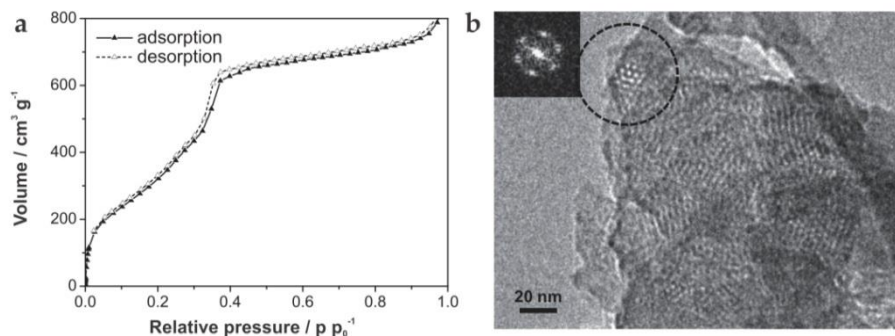


**Figure 4.3** Structural characterization of TFPT-COF by physisorption and TEM. (a) The argon-sorption isotherm shows the formation of mesopores, consistent with the predicted pore size based on the structure model. The reversible type IV isotherm (adsorption: black triangles, desorption: white triangles) gives a BET surface of  $1603 \text{ m}^2 \text{ g}^{-1}$ . (b) TEM image showing the formation of hexagonal pores.

The diffuse reflectance UV-Vis spectrum of the yellow powder exhibits an absorption edge around 400 nm (the spike at 350 nm is due to a change of the light source), with the absorption tail extending well beyond 600 nm (Figure 4.4(a)). We estimate an optical band gap of roughly 2.8 eV from the absorption edge, based on the Kubelka-Munk function (Figure S56, 7.1 Supporting information). The TFPT-COF shows a pronounced red-shift of the absorption edge by 33 nm in comparison with the individual building blocks. A similar broadened and red-shifted absorption of the COF with respect to the monomers has been found by *Jiang and co-workers* for several COF systems.<sup>13,23–27</sup> In principle, the observed HOMO-LUMO gap of the TFPT-COF is large enough to enable water splitting through band gap excitation and at the same time small enough to harvest a significant portion of the visible light spectrum.

To investigate this possibility, we studied the light-induced hydrogen evolution mediated by Pt-modified TFPT-COF in the presence of a sacrificial electron donor as the photocatalytic system under visible light irradiation. While TFPT-COF primarily acts as a photosensitizer for exciton generation, Pt functions as PRC. We previously demonstrated that the Pt-modified triazine-based carbon nitride poly(triazine imide) (PTI) shows substantial photocatalytic activity, despite its amorphous character.<sup>6</sup> Therefore, the presence of triazine moieties in the TFPT-COF, along with a moderate band gap, renders this crystalline COF an excellent candidate to study hydrogen-evolution and possible structure-property relationships.

### Photocatalytic hydrogen evolution

Hydrogen evolution was studied under standardized conditions and measured in the presence of the PRC Pt, using sodium ascorbate as sacrificial electron donor (see 7.1 Supporting information for details). In fact, TFPT-COF/Pt is a potent photocatalytic system, showing continuous and stable hydrogen production of  $230 \mu\text{mol h}^{-1} \text{ g}^{-1}$



(Figure 4.4(b) and Figure S64, 7.1 Supporting information). The total amount of hydrogen produced after 52 h (with sodium ascorbate) exceeds the total amount of hydrogen incorporated in the material (97.6  $\mu\text{mol}$ ), which adds evidence that hydrogen evolution is in fact catalytic and does not result from stoichiometric decomposition of the COF itself. Measurements in the dark (Figure S64, 7.1 Supporting information) show no hydrogen evolution, confirming that the evolution of hydrogen is a photoinduced effect. The monomer TFPT alone does not show photocatalytic activity under these conditions either. The long-time stability was tested by catalyst cycling, *i.e.* centrifugation of the reaction mixture, washing of the precipitate and addition of fresh sodium ascorbate solution. Even after three cycles the hydrogen evolution does not decrease (Figure S65, 7.1 Supporting information). Small fluctuations are due to small concentration differences of the COF/aqueous sodium ascorbate suspensions.

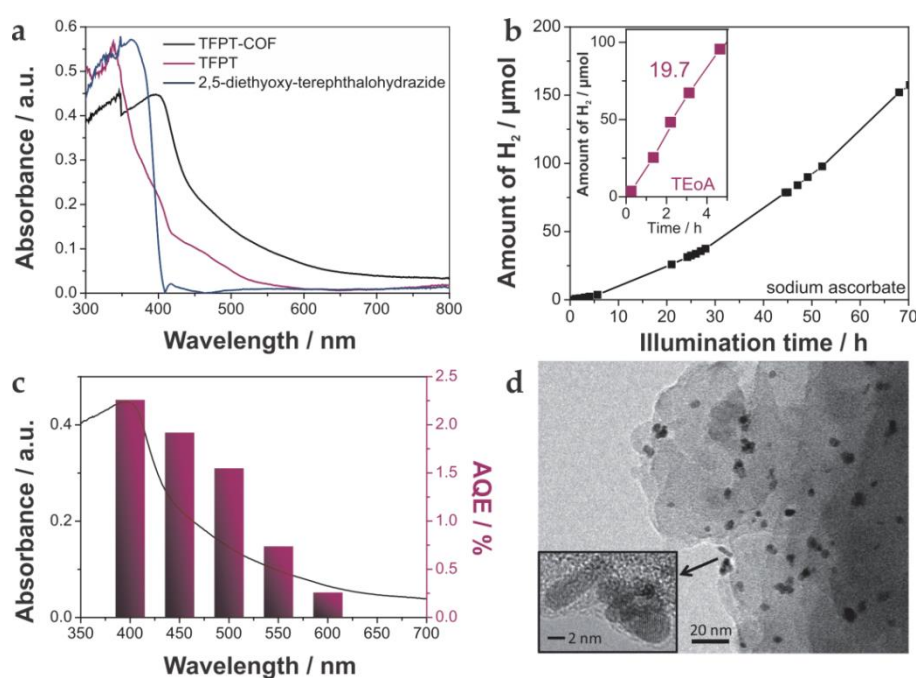


**Figure 4.4** Optical properties of the TFPT–COF and photocatalytic hydrogen evolution. (a) UV–Vis diffuse reflectance spectra of TFPT–COF (black) and its monomers (blue and purple). (b) Time course of hydrogen evolution from an aqueous sodium ascorbate solution by the Pt-modified TFPT–COF under visible light irradiation ( $\lambda \geq 420$  nm). The inset shows the hydrogen evolution rate (19.7  $\mu\text{mol h}^{-1}$ ) from 10 vol% aqueous TEOA solution over 5 h (purple). (c) Overlay of UV–Vis absorption of TFPT–COF and action spectrum of Pt-modified TFPT–COF in a 10 vol% aqueous TEOA solution using 40 nm FWHM band-pass filters. (d) TEM image of TFPT–COF/Pt after illumination for 84 h showing the formation of Pt nanoparticles (5 nm).

Using a 10 vol% aqueous triethanolamine (TEoA) solution as sacrificial donor, an even higher hydrogen evolution rate was detected, with the amount of hydrogen evolved in the first five hours being as high as 1970  $\mu\text{mol h}^{-1} \text{g}^{-1}$ , corresponding to a quantum efficiency of 2.2 %, while maximum AQEs of up to 3.9 % were obtained for individual batches (Figure 4.4(b)). However, this high rate comes along with a quicker deactivation of the photocatalytic system. By reducing the amount of TEOA (1 vol%) and adjusting the suspension to pH = 7, stable hydrogen evolution for a longer time range (24 hours) was detected.

The observed high amount of hydrogen evolved under standard basic conditions ( $1970 \mu\text{mol h}^{-1} \text{g}^{-1}$ ) suggests that TFPT-COF/Pt is superior to Pt-modified amorphous melon,  $g\text{-C}_3\text{N}_4$  (which was synthesized according to *Zhang et al.*<sup>5</sup> at  $600^\circ\text{C}$ ) and crystalline PTI ( $720 \mu\text{mol h}^{-1} \text{g}^{-1}$ ,  $840 \mu\text{mol h}^{-1} \text{g}^{-1}$  and  $864 \mu\text{mol h}^{-1} \text{g}^{-1}$ , respectively),<sup>6</sup> which were tested under similar conditions for three hours with TEOA as sacrificial donor. We also studied oxygen evolution to probe whether full water splitting is possible with the TFPT-COF. However, no  $\text{O}_2$  could be detected under the conditions used (see 7.1 Supporting information).

### Reconversion of TFPT-COF

After photocatalysis, the amorphous material was coated with dispersed Pt nanoparticles, formed *in situ* (Figure 4.4(d)). The TEM images suggest that the material loses its long-range order during photocatalysis (Figure 4.4(d)), which is supported by XRD measurements (Figure 4.5 and Figure S58, 7.1 Supporting information). This loss of long-range order has also been observed by *Dichtel and co-workers* and has been assigned to exfoliation of the COF in water.<sup>20</sup> To test this hypothesis, we carried out sorption measurements and PXRD after photocatalysis (95 h of irradiation in sodium ascorbate solution). TFPT-COF/Pt was filtered off as a greenish solid (Figure 4.5, inset picture, see 7.1 Supporting information for more images). A DCM extract of the solid catalyst did not contain any molecular material, which suggests that the as-obtained powder did not decompose and no monomers were released. At the same time, however, crystallinity was lost (Figure S58, 7.1 Supporting information) and the BET surface area was reduced to  $410 \text{ m}^2 \text{ g}^{-1}$  (Figure S60, 7.1 Supporting information). Nevertheless, we found that the amorphous product can easily be reconverted into the crystalline and porous TFPT-COF with a BET surface area of  $1185 \text{ m}^2 \text{ g}^{-1}$  (Figure 4.5 and 7.1 Supporting information) by subjecting it to the initial synthesis conditions. Further experiments revealed that the TFPT-COF loses its long-range order during sonication in water. Overall, this observation strengthens the hypothesis that the COF is exfoliated in water,<sup>20</sup> thereby losing its long-range order, while the connectivity and photoactivity is retained.

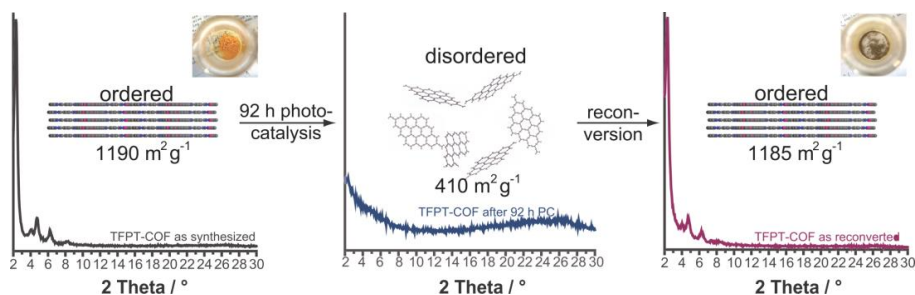


**Figure 4.5** Transformation of TFPT-COF during photocatalysis and subsequent recovery by reconversion (see 7.1 Supporting information for details). Inset photographs show color change from yellow (TFPT-COF) to green (TFPT-COF/Pt).

### 4.1.3 Conclusion

In conclusion, we have developed a new crystalline hydrazone-based TFPT-COF, which is the first COF to show photocatalytic hydrogen evolution under visible light irradiation in the presence of Pt as PRC. This framework is competitive with the best non-metal photocatalysts for hydrogen production and represents a light weight, well-ordered model system, which in principle can be readily tuned — by replacement, expansion or chemical modification of its building blocks — to further study and optimize the underlying mechanism of hydrogen evolution mediated by the framework and to enhance its light harvesting capability. The triazine moieties in the TFPT-COF, which are likewise present in the recently developed triazine-based carbon nitride photocatalytic system PTI/Pt, may point to an active role of the triazine unit in the photocatalytic process.

The development of COFs as tunable scaffolds for photocatalytic hydrogen evolution enables a general bottom-up approach toward designing tailor-made photosensitizers and photocatalysts with tunable optical and electronic properties, a goal we are currently pursuing in our lab. We expect this new application of COFs in photocatalysis to open new avenues to custom-made heterogeneous photocatalysts, and to direct and diversify the ongoing development of COFs for optoelectronic applications.

### Bibliography

- (1) X. Chen, S. Shen, L. Guo, S. S. Mao, *Chem. Rev.* **2010**, *110*, 6503.
- (2) H. Tong, S. Ouyang, Y. Bi, N. Umezawa, M. Oshikiri, J. Ye, *Adv. Mater.* **2012**, *24*, 229.
- (3) (a) S. Yanagida, A. Kabumoto, K. Mizumoto, C. Pac, K. Yoshino, *J. Chem. Soc. Chem. Commun.* **1985**, 474; (b) J. Liu, S. Wen, Y. Hou, F. Zuo, G. J. O. Beran, P. Feng, *Angew. Chem. Int. Ed.* **2013**, *52*, 3241; (c) X. Wang, K. Maeda, A. Thomas, K. Takanabe, G. Xin, J. M. Carlsson, K. Domen, M. Antonietti, *Nat. Mater.* **2009**, *8*, 76.
- (4) K. Maeda, X. Wang, Y. Nishihara, D. Lu, M. Antonietti, K. Domen, *J. Phys. Chem. C* **2009**, *113*, 4940.
- (5) J. Zhang, X. Chen, K. Takanabe, K. Maeda, K. Domen, J. D. Epping, X. Fu, M. Antonietti, X. Wang, *Angew. Chem. Int. Ed.* **2010**, *49*, 441.
- (6) K. Schwinghammer, B. Tuffy, M. B. Mesch, E. Wirnhier, C. Martineau, F. Taulelle, W. Schnick, J. Senker, B. V. Lotsch, *Angew. Chem. Int. Ed.* **2013**, *52*, 2435.
- (7) A. P. Côté, A. I. Benin, N. W. Ockwig, M. O'Keeffe, A. J. Matzger, O. M. Yaghi, *Science* **2005**, *310*, 1166.
- (8) H. M. El-Kaderi, J. R. Hunt, J. L. Mendoza-Cortes, A. P. Côté, R. E. Taylor, M. O'Keeffe, O. M. Yaghi, *Science* **2007**, *316*, 268.
- (9) A. P. Côté, H. M. El-Kaderi, H. Furukawa, J. R. Hunt, O. M. Yaghi, *J. Am. Chem. Soc.* **2007**, *129*, 12914.
- (10) S.-Y. Ding, W. Wang, *Chem. Soc. Rev.* **2013**, *42*, 548.
- (11) X. Feng, X. Ding, D. Jiang, *Chem. Soc. Rev.* **2012**, *41*, 6010.
- (12) Y. Du, K. Mao, P. Kamakoti, P. Ravikovitch, C. Paur, S. Cundy, Q. Li, D. Calabro, *Chem. Commun.* **2012**, *48*, 4606.

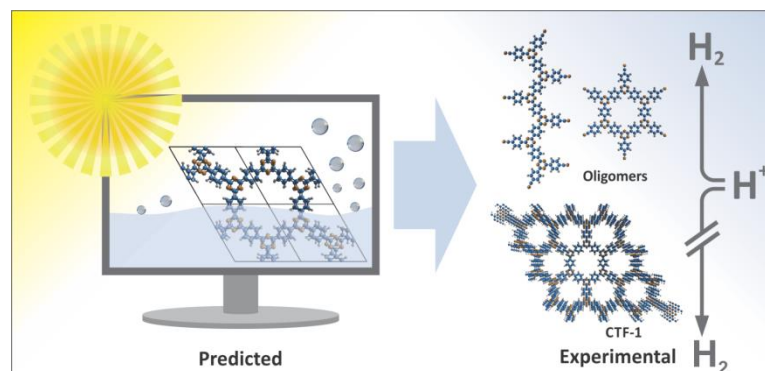
- (13) A. Nagai, X. Chen, X. Feng, X. Ding, Z. Guo, D. Jiang, *Angew. Chem. Int. Ed.* **2013**, *52*, 3770.
- (14) X. Chen, M. Addicoat, S. Irle, A. Nagai, D. Jiang, *J. Am. Chem. Soc.* **2012**, *135*, 546.
- (15) S. Wan, F. Gándara, A. Asano, H. Furukawa, A. Saeki, S. K. Dey, L. Liao, M. W. Ambrogio, Y. Y. Botros, X. Duan, S. Seki, J. F. Stoddart, O. M. Yaghi, *Chem. Mater.* **2011**, *23*, 4094.
- (16) F. J. Uribe-Romo, J. R. Hunt, H. Furukawa, C. Klöck, M. O'Keeffe, O. M. Yaghi, *J. Am. Chem. Soc.* **2009**, *131*, 4570.
- (17) M. G. Rabbani, A. K. Sekizkardes, Z. Kahveci, T. E. Reich, R. Ding, H. M. El-Kaderi, *Chem.–Eur. J.* **2013**, *19*, 3324.
- (18) F. J. Uribe-Romo, C. J. Doonan, H. Furukawa, K. Oisaki, O. M. Yaghi, *J. Am. Chem. Soc.* **2011**, *133*, 11478.
- (19) S.-Y. Ding, J. Gao, Q. Wang, Y. Zhang, W.-G. Song, C.-Y. Su, W. Wang, *J. Am. Chem. Soc.* **2011**, *133*, 19816.
- (20) D. N. Bunck, W. R. Dichtel, *J. Am. Chem. Soc.* **2013**, *135*, 14952.
- (21) T. P. King, S. W. Zhao, T. Lam, *Biochemistry* **1986**, *25*, 5774.
- (22) C. C. Lee, E. R. Gillies, M. E. Fox, S. J. Guillaudeu, J. M. J. Fréchet, E. E. Dy, F. C. Szoka, *Proc. Natl. Acad. Sci. U.S.A.* **2006**, *103*, 16649.
- (23) S. Jin, X. Ding, X. Feng, M. Supur, K. Furukawa, S. Takahashi, M. Addicoat, M. E. El-Khouly, T. Nakamura, S. Irle, S. Fukuzumi, A. Nagai, D. Jiang, *Angew. Chem. Int. Ed.* **2013**, *52*, 2017.
- (24) E. L. Spitler, W. R. Dichtel, *Nat. Chem.* **2010**, *2*, 672.
- (25) X. Ding, X. Feng, A. Saeki, S. Seki, A. Nagai, D. Jiang, *Chem. Commun.* **2012**, *48*, 8952.
- (26) X. Ding, J. Guo, X. Feng, Y. Honsho, J. Guo, S. Seki, P. Maitarad, A. Saeki, S. Nagase, D. Jiang, *Angew. Chem. Int. Ed.* **2011**, *50*, 1289.
- (27) X. Ding, L. Chen, Y. Honsho, X. Feng, O. Saengsawang, J. Guo, A. Saeki, S. Seki, S. Irle, S. Nagase, V. Parasuk, D. Jiang, *J. Am. Chem. Soc.* **2011**, *133*, 14510.
- (28) T. Ishi-i, K. Yaguma, T. Thiemann, M. Yashima, K. Ueno, S. Mataka, *Chem. Lett.* **2004**, *33*, 1244.
- (29) D. Sun, S. Ma, Y. Ke, D. J. Collins, H.-C. Zhou, *J. Am. Chem. Soc.* **2006**, *128*, 3896.
- (30) (a) Z.-S. Li, J.-X. Chen, Y.-B. Huang, G.-R. Chen, T.-Y. Lan, *Acta Crystallogr. Sect. E: Struct. Rep. Online* **2006**, *62*, 777; (b) V. Volkis, E. Nelkenbaum, A. Lisovskii, G. Hasson, R. Semiat, M. Kapon, M. Botoshansky, Y. Eishen, M. S. Eisen, *J. Am. Chem. Soc.* **2003**, *125*, 2179.
- (31) Material Studio v. 5.5.0.0, *Accelrys Software Inc.* **2011**.
- (32) B. Lukose, A. Kuc, T. Heine, *Chem.–Eur. J.* **2011**, *17*, 2388.
- (33) B. T. Koo, W. R. Dichtel, P. Clancy, *J. Mater. Chem.* **2012**, *22*, 17460.
- (34) (a) S. Grimme, *Angew. Chem. Int. Ed.* **2008**, *47*, 3430; (b) J. Antony, B. Alameddine, T. A. Jenny, S. Grimme, *J. Phys. Chem. A* **2012**, *117*, 616; (c) T. J. Mooibroek, P. Gamez, *Inorg. Chim. Acta* **2007**, *360*, 381; (d) W. Pisula, H. Tsao, D. Dudenko, D. Cho, S. Puniredd, Y. Zhao, A. Mavrinskiy, J. Shu, M. Hansen, M. Baumgarten, K. Müllen, *Polymers* **2013**, *5*, 833.
- (35) (a) S. Chandra, S. Kandambeth, B. P. Biswal, B. Lukose, S. M. Kunjir, M. Chaudhary, R. Babarao, T. Heine, R. Banerjee, *J. Am. Chem. Soc.* **2013**, *135*, 17853; (b) S. Kandambeth, D. B. Shinde, M. K. Panda, B. Lukose, T. Heine, R. Banerjee, *Angew. Chem. Int. Ed.* **2013**, *52*, 13052; (c) S. Kandambeth, A. Mallick, B. Lukose, M. V. Mane, T. Heine, R. Banerjee, *J. Am. Chem. Soc.* **2012**, *134*, 19524.

## 4.2 Oligomers of the archetype covalent-triazine framework CTF-1

### Phenyl-triazine oligomers for light-driven hydrogen evolution

Katharina Schwinghammer, Stephan Hug, Maria B. Mesch, Jürgen Senker and Bettina V. Lotsch

Published in: *Energy Environ. Sci.* **2015**, *8*, 3345–3353; DOI: 10.1039/C5EE02574E.



#### Abstract

The design of stable, yet highly tunable organic photocatalysts which orchestrate multi-step electron transfer reactions is at the heart of the newly emerging field of polymer photocatalysis. Covalent triazine frameworks such as the archetypal CTF-1 have been theorized to constitute a new class of photocatalytically active polymers for light-driven water splitting. Here, we revisit the ionothermal synthesis of CTF-1 by trimerization of 1,4-dicyanobenzene catalyzed by the Lewis acid zinc chloride and demonstrate that the microporous black polymer CTF-1 is essentially inactive for hydrogen evolution. Instead, highly photoactive phenyl-triazine oligomers (PTOs) with higher crystallinity as compared to CTF-1 are obtained by lowering the reaction temperature to 300 °C and prolonging the reaction time to > 150 hours. The low reaction temperature of the PTOs largely prevents incipient carbonization and thus results in a carbon-to-nitrogen weight ratio close to the theoretical value of 3.43. The oligomers were characterized by MALDI-TOF and quantitative solid-state NMR spectroscopy, revealing variations in size, connectivity and thus nitrile-to-triazine ratios depending on the initial precursor dilution. The most active PTO samples efficiently and stably reduce water to hydrogen with an average rate of  $1076 (\pm 278) \mu\text{mol h}^{-1} \text{g}^{-1}$  under simulated sunlight illumination, which is competitive with the best carbon nitride-based and purely organic photocatalysts. The photocatalytic activity of the PTOs is found to sensitively depend on the polymerization degree, thus suggesting a prominent role of the unreacted nitrile moieties in the photocatalytic process. Notably, PTOs even show moderate hydrogen production without the addition of any co-catalyst.

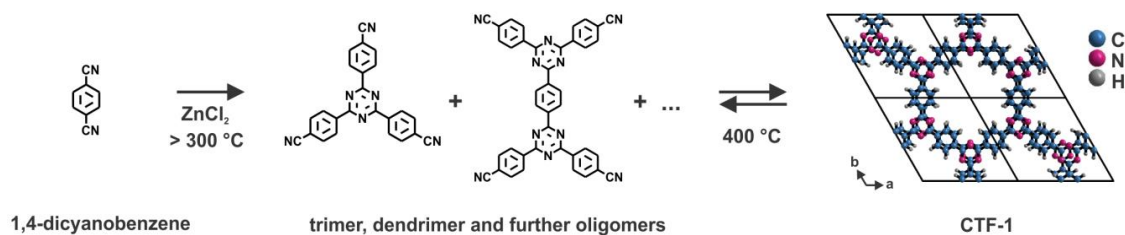
### Broader Context

The increasing demand of renewable energy resources, such as hydrogen generated by photocatalytic water reduction, necessitates the exploration of efficient, stable, non-toxic and abundant photocatalysts. While organic photocatalysts fulfil these requirements, rational catalyst design remains challenging both experimentally and computationally due to the scarcity of structure–property–activity insights, particularly in disordered polymeric systems. This case in point is illustrated by the archetype covalent triazine framework CTF-1, which was computationally predicted to satisfy the (thermodynamic) criteria for exhibiting activity for photocatalytic hydrogen evolution, but shown to be nearly inactive here. We demonstrate further that triazine-based oligomers populated with terminal nitrile groups, rather than the extended framework, are highly active photocatalysts for the hydrogen evolution reaction. The nitrile groups likely act as solubilizing agents and conduits for charge transfer between the oligomer, co-catalyst and reactants, which puts the role of functional groups embedded in the carbon nitride backbone in the spotlight. This work thus illustrates the potential of well-defined oligomeric systems as a new generation of metal-free photocatalysts and provides a guideline for the rational design of novel organic photocatalysts by molecular engineering.

#### 4.2.1 Introduction

The direct conversion of solar energy to chemical energy, exemplified by light-induced water splitting into hydrogen and oxygen, enables the sustainable generation of storable chemical fuels and is hence a green energy cycle.<sup>1</sup> However, the development of a cost-effective process for the generation of hydrogen from water has yet to be developed.<sup>1</sup> Since the discovery of water splitting on an *n*-type semiconducting TiO<sub>2</sub> electrode by *Fujishima and Honda* in 1972,<sup>2</sup> research largely focused on inorganic semiconductors that often entail costly and environmentally critical fabrication steps.<sup>3</sup> The development of carbon-based photocatalysts has become an active research field, which has produced the first promising examples of polymers,<sup>4</sup> graphite oxide,<sup>5</sup> carbon nitrides<sup>6–8</sup> and COFs<sup>9</sup> as predominantly carbon-based photocatalysts. In particular, the incorporation of triazine units into polymeric systems has been shown to correlate with efficient hydrogen evolution as the triazine nitrogen, with its free electron pair and electron poor character, may act as the active site.<sup>6,7,9–12</sup> An example of such a triazine system is the covalent triazine framework CTF-1 (see Scheme 4.1) which was first synthesized in 2008 by *Kuhn et al.*<sup>13</sup> CTF-1 is built from alternating triazine and phenyl building blocks forming a 12-membered hexagonal ring system, resulting in layers which are stacked in a close-to-eclipsed AA-type fashion.<sup>13</sup> The black colored and highly porous product is obtained from 1,4-dicyanobenzene by a trimerization reaction under inert ionothermal conditions at 400 °C for 40 hours.<sup>13</sup> However, incipient carbonization occurs due to the elevated reaction temperature, as evidenced by the larger carbon content and the dark color of the product.<sup>13</sup> In 2012, *Ren et al.*<sup>14</sup> achieved the synthesis of yellow colored and thus largely carbon-

free, but non-porous CTF-1 through a super acid-catalyzed (microwave-assisted) synthesis.



**Scheme 4.1** Reaction mechanism of CTF-1 starting from 1,4-dicyanobenzene, which leads to the formation of oligomers *via* trimerization and, ultimately, to an extended 2D CTF (right). The idealized crystal structure of fully condensed, crystalline CTF-1 is shown in an AA-type eclipsed configuration (viewed along the *c*-direction).

Such colored compounds may be capable of light-induced hydrogen evolution drawing on recent experimental and theoretical results delineating the structural and photophysical properties of CTF-1-type materials.<sup>14,15</sup> Moreover, based on first principles calculations, *Zhao and co-workers*<sup>16</sup> predicted that certain CTFs including CTF-1 should be promising visible-light photocatalysts according to the suitable band gap of CTF-1 (2.42 eV) and the position of its band potentials which are dependent on the nitrogen content of the CTFs, the number of ring systems, and the extent of  $\pi$ - $\pi$  interactions.

Here, we revisit the synthesis of CTF-1 and demonstrate that conditions circumventing the formation of amorphous carbon invariably yield low molecular weight triazine-based compounds, henceforth referred to as phenyl-triazine oligomers (PTO), with intriguing optical and electronic properties. These oligomers are studied with respect to their photocatalytic activity for hydrogen evolution and compared to the archetypal CTF-1 and the related molecular model system 2,4,6-tris(*p*-cyanophenyl)-1,3,5-triazine, henceforth referred to as “the trimer”. In contrast to black CTF-1 which shows negligible catalytic activity, the most active PTO samples exhibit an average, but non-optimized hydrogen evolution rate of 1076 ( $\pm 278$ )  $\mu\text{mol h}^{-1} \text{g}^{-1}$ . Thus, PTOs are competitive with the commonly used melon (*g*-C<sub>3</sub>N<sub>4</sub>) and other purely organic photocatalysts<sup>6-11,17-19</sup> with regards to hydrogen evolution under simulated sunlight, and long-term stability. Notably, PTOs are even active without the addition of any co-catalyst.<sup>19</sup> Their high activity and potential to act in a Pt-free environment (121  $\mu\text{mol h}^{-1} \text{g}^{-1}$ ) renders triazine-based photocatalysts and PTOs in particular promising candidates for truly abundant photocatalysts.

#### 4.2.2 Results and Discussion

CTF-1 synthesized according to literature protocols was tested for hydrogen evolution under simulated sunlight (for experimental details see below and Table S15, 7.1 Supporting information) but was found to show very low activity. We rationalize the low activity of CTF-1 with the large carbon content in the sample, as the synthesis of CTF-1 seems to be a delicate balance between incomplete polymerization resulting mostly in



oligomers, and the competitive formation and degradation of the framework yielding amorphous carbon at elevated temperatures. At the originally applied synthesis temperature of 400 °C, a large amount of carbon is formed, which may well hinder light penetration to the photocatalyst.<sup>13</sup> In addition, the thermodynamic driving force for electron transfer in the extended system may be too low to support efficient hydrogen evolution.

### Synthesis

We therefore attempted to synthesize non-carbonized CTF-1. While the synthesis of yellow colored CTF-1 according to *Ren et al.*<sup>14</sup> requires water-free conditions, we modified the original ionothermal approach,<sup>13</sup> thereby obtaining PTOs rather than the extended CTF-1 polymer. The syntheses of the PTOs were carried out in a fashion analogous to the original ionothermal synthesis using zinc chloride melts, as established by *Antonietti and co-workers*.<sup>13</sup>

**Table 4.1** Synthesis conditions used for the PTOs and the reference material CTF-1.

sample	eq. ZnCl <sub>2</sub>	synthesis temperature / °C	synthesis time <sup>a</sup> / h
PTO-300-1	1	300	168
PTO-300-2.5	2.5	300	168
PTO-300-5	5	300	168
PTO-300-10	10	300	168
PTO-300-15	15	300	168
PTO-350-1	1	350	96
PTO-350-10	10	350	96
CTF-1 <sup>b</sup>	1	400	48

<sup>a</sup> Heating at a rate of 60 °C h<sup>-1</sup> and cooling at 10 °C h<sup>-1</sup>. <sup>b</sup> Synthesized according to *Kuhn et al.*<sup>13</sup>

As already stated in that work, syntheses at temperatures below 350 °C yielded mainly soluble products after two days of reaction time. Due to the slow reaction kinetics at 350 °C we prolonged the reaction times to increase the conversion, in accordance with *van't Hoff's* law.<sup>20</sup> Indeed, reaction times of 96 h for syntheses at 350 °C and of 168 h at 300 °C led to oligomeric products which were insoluble in organic solvents (THF, acetone, ethanol, chloroform and dichloromethane), water and hot 1 M HCl. During the organic washing procedure (and later on by Soxhlet extraction) with THF, smaller oligomers and unreacted starting material were washed off (organic phase of PTO, see Figure S68 and Figure S69, 7.1 Supporting information). The detailed synthesis conditions are shown in Table 4.1. The products are identified by adding to the prefix PTO first the synthesis temperature and then the equivalents of zinc chloride with respect to 1,4-dicyanobenzene used in the synthesis.

### Characterization

First, we analyzed the crystallinity of the as-obtained materials by powder XRD measurements and compared the results with CTF-1 (Figure 4.6(a,c)). The diffraction patterns of PTO-350-1 and the as-prepared CTF-1 sample are largely reminiscent of CTF-1,<sup>13</sup> albeit



with less intense reflections. At the lower reaction temperature of 300 °C and prolonged reaction time, materials with higher crystallinity are obtained which differ from the reference and cannot simply be assigned to the precursors. While PTO-300-1 still shows similarities to the framework due to the presence of the prominent 100 reflection, the samples synthesized with a larger amount of ZnCl<sub>2</sub> (e.g. PTO-300-15) display diffraction patterns completely different from CTF-1, yet faintly resembling the trimer. We believe that the powder diffraction patterns of the PTO samples differ from the one of CTF-1 due to the formation of oligomers. These oligomers exhibit a decreased layer distance compared to CTF-1 (Table S8, 7.1 Supporting information). Furthermore, it seems that the oligomers formed at a one-to-one precursor to ZnCl<sub>2</sub> ratio (PTO-300-1) differ from the ones synthesized in an excess of zinc chloride (> 1 equivalent).

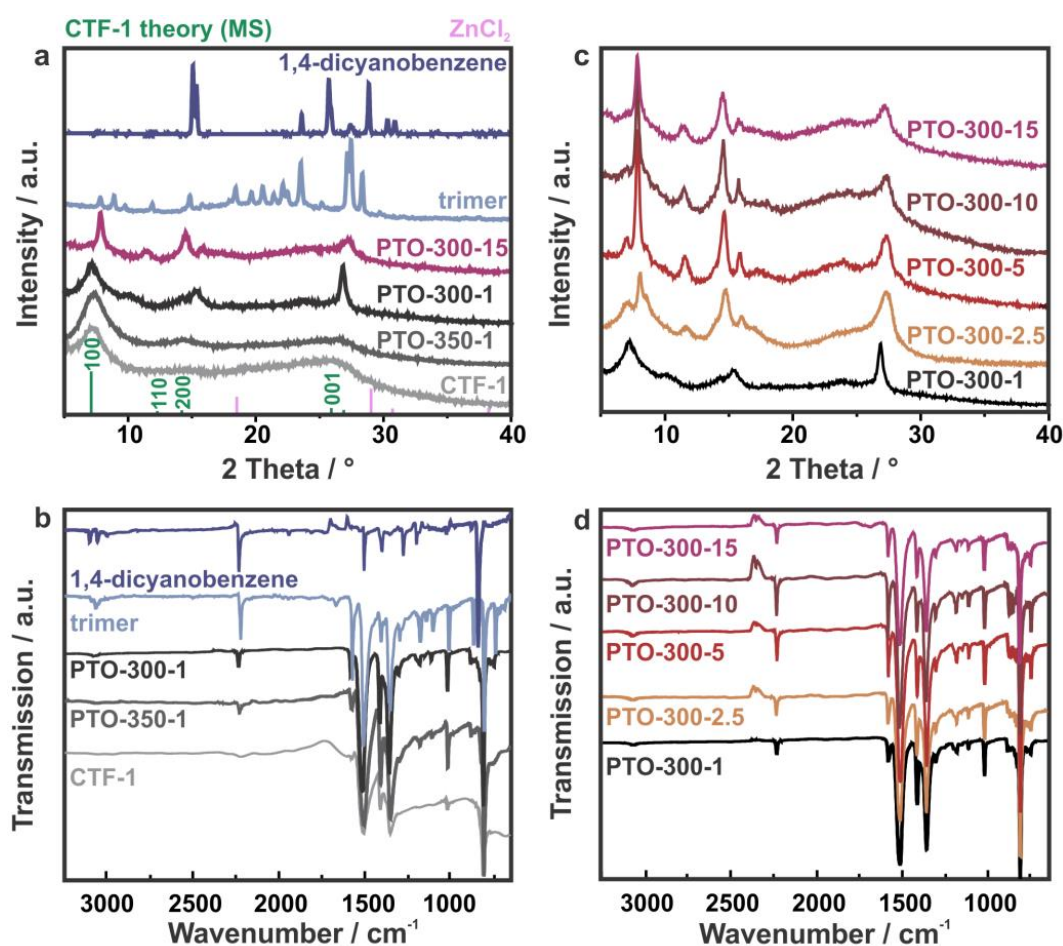


**Figure 4.6** (a) PXRD patterns and (b) IR spectra of the PTOs: PTO-350-1, PTO-300-1 and PTO-300-15 in comparison to the as-synthesized CTF-1, the trimer and 1,4-dicyanobenzene. The diffraction patterns of ZnCl<sub>2</sub> and the simulated pattern of CTF-1<sup>13</sup> are added for clarity. (c) PXRD patterns and (d) IR spectra of the PTOs synthesized at 300 °C with different amounts of ZnCl<sub>2</sub>.

We used IR spectroscopy as a tool to survey the progress of the trimerization reaction based on the characteristic IR signals of the nitrile groups of the starting material, which are expected to form triazine rings. The IR spectra are depicted in Figure 4.6(b,d). The materials synthesized between 300 °C – 350 °C show the same prominent bands as CTF-1

and the trimer. The characteristic bands for the triazine unit are found at  $1506\text{ cm}^{-1}$  (C–N stretching mode)<sup>21,22</sup> and  $1355\text{ cm}^{-1}$  (in-plane ring stretching vibrations),<sup>23,24</sup> confirming the successful formation of triazine rings under these synthesis conditions. The lower temperature clearly leads to incomplete polymerization as indicated by the additional signal at  $2227\text{ cm}^{-1}$  representing unreacted nitrile groups in the sample.

To further confirm the formation of CTF-1-like materials, we conducted elemental analysis (Table S9, 7.1 Supporting information). The elemental analysis (EA) data of the as-synthesized PTOs synthesized at  $300\text{ }^{\circ}\text{C}$  reveal values very close to the theoretical ones for CTF-1 and the ones reported by *Ren et al.*<sup>14</sup> for yellow colored CTF-1. The results are in sharp contrast to the materials synthesized above  $300\text{ }^{\circ}\text{C}$  and the ones found by *Antonietti and co-workers*<sup>13</sup> where a higher carbon content (and C/N ratio) is observed due to partial carbonization of the products.<sup>13</sup> An incipient carbonization can also be detected for the materials synthesized in an excess of zinc chloride (PTO-300-15). No statement on the extent of trimerization of the PTOs and thus the amount of unreacted nitrile groups can be made based on EA because the precursor of the synthesis (1,4-dicyanobenzene) has the same elemental composition and, hence, C/N ratio as one formula unit of CTF-1 or any intermediate oligomer.

To gain more insights into the local chemical environment in the different materials, XPS measurements were conducted (Figure S70 and Figure S71, 7.1 Supporting information). The nitrogen environments of the low temperature products (PTO-300-1 and 15) are in agreement with the as-synthesized CTF-1 sample showing a dominant N 1s peak at around  $398.9\text{ eV}$ . According to the literature,<sup>25,26</sup> this as well as the weak signal at  $400.3\text{ eV}$  observed for CTF-1 can be assigned to nitrogen atoms within the triazine units (C–N=C) as well as terminal nitrile groups. More likely, however, the signal at  $400.3\text{ eV}$  arises from pyrrolic nitrogen containing decomposition products since this signal is more prominent in the CTF-1 sample. The C 1s XPS measurements of the three samples reveal two peaks. The first signal at  $284.6\text{ eV}$  is attributed to the carbon atoms of the phenyl rings as well as adventitious carbon (C–C) which is used for calibration.<sup>27</sup> The second one appearing at around  $286.8\text{ eV}$  for CTF-1 and PTO-300-1 and at  $286.3\text{ eV}$  for PTO-300-15 is assigned to the carbon atoms in the triazine (N=C–N) and nitrile moieties (–C≡N).<sup>28</sup> The C–C carbon signal of CTF-1 is more dominant in comparison to the triazine/nitrile peak due to a higher amorphous carbon content which was already verified by elemental analysis. For the different samples, no obvious shifts of the binding energy of C 1s and N 1s core electrons are observable, suggesting that the chemical states of both carbon and nitrogen atoms in the PTOs are the same as in the more highly condensed CTF-1 sample.

The results obtained by IR and XPS were further supported by  $^{13}\text{C}$  and  $^{15}\text{N}$  ssNMR spectroscopy. The  $^{13}\text{C}$  CP–MAS ssNMR spectra of PTO-300-1, PTO-300-10 as well as CTF-1 (Figure 4.7, left) show strong signals at  $169\text{ ppm}$ ,  $138\text{ ppm}$ ,  $130\text{ ppm}$  and  $115\text{ ppm}$ . The signal at  $169\text{ ppm}$  is assigned to triazine ring carbon atoms,<sup>29</sup> while the signals at  $138\text{ ppm}$  and  $130\text{ ppm}$  correspond to the phenyl ring. The signal at  $115\text{ ppm}$  is characteristic for

nitrile groups as well as the carbon of the phenyl ring to which the nitrile groups are bound. Although it is significantly weaker in CTF-1 it indicates residual nitrile groups in all materials. The  $^{15}\text{N}$  CP-MAS ssNMR spectra of all samples (Figure 4.7, right) show only one signal at around  $-125$  ppm. From the chemical shift alone it is not possible to distinguish between the triazine unit and terminal nitrile groups, as their signals appear in the same region.<sup>30,31</sup> Note that in PTO-300-10 the carbon peaks at 130 ppm and 115 ppm as well as the nitrogen peak show a fine structure, indicating better crystallinity. This is also supported by the XRD measurements shown above.

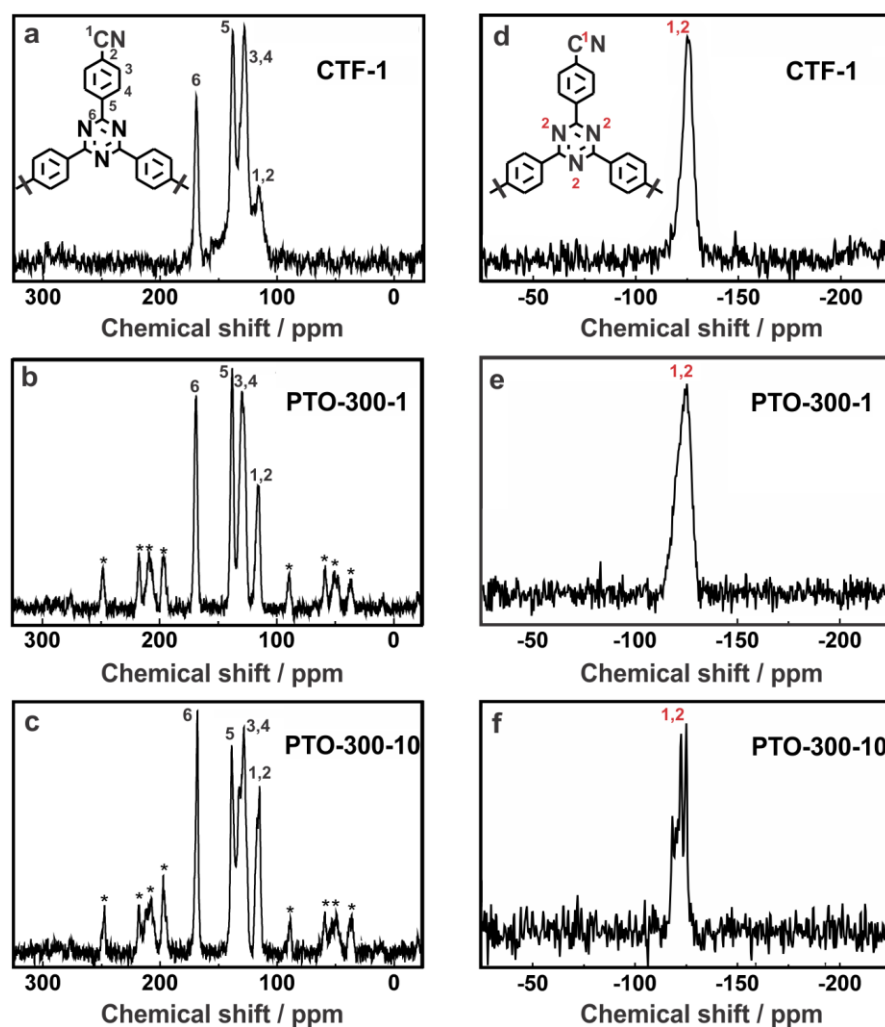


**Figure 4.7**  $^{13}\text{C}$  CP-MAS ssNMR spectra of (a) CTF-1, (b) PTO-300-1 and (c) PTO-300-10.  $^{15}\text{N}$  CP-MAS ssNMR spectra of (d) CTF-1, (e) PTO-300-1 and (f) PTO-300-10. Asterisks mark rotational spinning side bands. A contact time of 5 ms was used for all measurements and the spinning speed was set to 10 kHz (all PTO measurements), 20 kHz ( $^{13}\text{C}$  of CTF-1) and 5 kHz ( $^{15}\text{N}$  of CTF-1), respectively.

To summarize, the results from IR and ssNMR spectroscopy strongly suggest the successful formation of triazine rings already at a reaction temperature of  $300\text{ }^{\circ}\text{C}$ , while the phenyl rings are maintained. In addition, unreacted nitrile groups are found in all products, with higher relative quantities of free nitriles for the PTO samples. Whereas at  $400\text{ }^{\circ}\text{C}$

the polymerization process is almost complete, incomplete polymerization and the formation of oligomers are detected at lower temperatures.

Porosity data were calculated from argon sorption measurements and are summarized in Table S9 (7.1 Supporting information). According to *Kuhn et al.*<sup>13</sup> CTF-1 displays a relatively high surface area (SA) of  $791 \text{ m}^2 \text{ g}^{-1}$  due to microporosity, which is confirmed by sorption measurements of our CTF-1 sample ( $610 \text{ m}^2 \text{ g}^{-1}$ ). In contrast, the PTOs synthesized below  $400 \text{ }^\circ\text{C}$  show significantly lower values in the range of  $6 \text{ m}^2 \text{ g}^{-1} - 116 \text{ m}^2 \text{ g}^{-1}$ , suggesting that either no distinct continuous 1D pore system is formed or pore blocking occurs. Similarly low surface areas ( $2 \text{ m}^2 \text{ g}^{-1} - 4 \text{ m}^2 \text{ g}^{-1}$ ) were reported by *Ren et al.*<sup>14</sup> for their yellow colored CTF-1s synthesized by a super acid-catalyzed (microwave-assisted) procedure. The surface areas of PTO-300 samples are slightly increased compared to the ones synthesized at  $350 \text{ }^\circ\text{C}$ , whereas a higher salt concentration ( $> 1 \text{ eq.}$ ) leads to lower surface areas irrespective of how much excess of salt melt was used.

### Estimation of the degree of polymerization

While the chemical environments of the PTOs are similar to CTF-1 based on IR, ssNMR and XPS, appreciable differences between the samples are discernible, even in PXRD and EA. We assumed that these differences result from different degrees of polymerization and, hence, nitrile content of the PTOs synthesized at  $300 \text{ }^\circ\text{C}$  compared to CTF-1 and PTO-350. Therefore, MALDI-TOF measurements were performed with PTO-300-1 and PTO-300-15 to further analyze the molecular sizes of the synthesized PTOs (Figure S72,73, 7.1 Supporting information). No mass signal was detected for the starting material 1,4-dicyanobenzene ( $m/z = 128$ ) and the polymer CTF-1 itself. For the PTOs, multiples of masses of 1,4-dicyanobenzene ( $n \times 128$  for  $n = 0, 1, 2, 3, \dots$ ) are expected since the polymerization up to CTF-1 proceeds without the formation of side products. Taking into account the rules of the trimerization reaction—three nitrile groups forming one triazine unit—fragments of 1,4-dicyanobenzene triplets (trimers) with a mass of  $384 \text{ m/z}$  should be observable. Furthermore, the formation of chains or dendrimers (of the trimer units) leads to  $(3 + 2n)$  multiples of the mass of 1,4-dicyanobenzene (Figure 4.8(b), Table S11,12, 7.1 Supporting information). A ring closure would lead to  $(12 + 7n)$  multiples of the 1,4-dicyanobenzene mass (Figure 4.8(b) and Table S13, 7.1 Supporting information). In contrast to CTF-1, we obtained signals in the mass spectra for the PTO samples (Table S10 and Figure S71,72, 7.1 Supporting information) which, in principle, already suggests that the molecular sizes of the PTOs are smaller than CTF-1 and more susceptible to ablation by ionization. The recorded mass spectra of PTO-300-1 and PTO-300-15 differ from each other in that they show small fragments ( $m/z \leq 12 \times 128$ ) for the sample synthesized with a high zinc chloride content (PTO-300-15) and additionally larger ones ( $m/z > 12 \times 128$ ) for the PTO synthesized with a 1:1 precursor ratio (PTO-300-1). For both samples, multiples of odd numbers up to 11 of the masses of 1,4-dicyanobenzene were found which can be assigned to chain fragments or small dendrimers (Table S10,12, 7.1 Supporting information). Additionally, a signal at 12 times the mass of 1,4-dicyanobenzene was recorded which

likely represents a 12-membered ring (Figure 4.8(b), Table S10,13, 7.1 Supporting information).

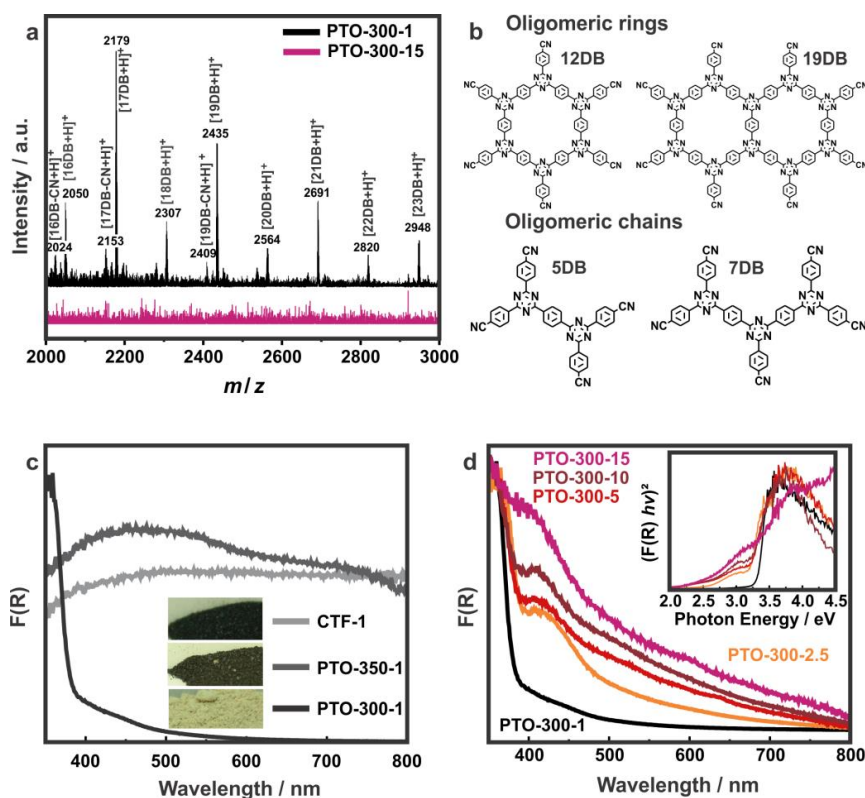


**Figure 4.8** (a) MALDI-TOF spectra of PTO-300-1 compared to PTO-300-15, measured in positive mode and in the mass range of 2000–3000. For both PTO materials signals have been detected in the mass spectra below the mass range of 2000. DB represents the mass of the precursor 1,4-dicyanobenzene ( $m/z = 128$ ). (b) Examples of possible ring and chain-like oligomers with their calculated masses. (c) UV-Vis spectra and product color (inset) of the PTO samples synthesized at different temperatures compared to CTF-1. (d) UV-Vis spectra of the PTO samples synthesized at 300 °C with different precursor ratios from low (bottom) to high  $\text{ZnCl}_2$  content (top) and their corresponding Tauc plots (inset).

In the case of PTO-300-1, the mass spectra also show larger fragments of 16 – 23 multiples of 1,4-dicyanobenzene due to longer chains, larger dendrimers and double ring systems (Figure 4.8(a), Table S10–13, 7.1 Supporting information). It seems that the amount of zinc chloride is crucial for the obtained molecular size of the oligomers as well as the type of oligomeric fragments formed. A high dilution of the starting material leads to smaller, chain-like oligomers (*e.g.* PTO-300-15) with very low porosities and more favorable stacking interactions (see below and Table S9, 7.1 Supporting information). In contrast, higher concentration of 1,4-dicyanobenzene (PTO-300-1) favors the formation of larger oligomers featuring higher porosities due to the formation of ring-systems (see Table S9, 7.1 Supporting information). The polymerization degree of the PTO samples was also roughly estimated by means of IR spectroscopy. To this end, we relate the IR signal intensities and integrals of the nitrile ( $2227\text{ cm}^{-1}$ ) and triazine bands ( $1355\text{ cm}^{-1}$ ) and compare them with those of the trimer and CTF-1 (Figure 4.6(c,d) and Table S11,14, 7.1 Supporting information). In the case of CTF-1, almost no nitrile signal is visible in the IR spectrum,

which indicates a near-zero nitrile-to-triazine ratio due to the largely complete conversion to the trimerized product. On the contrary, the highest nitrile-to-triazine ratio is obtained for the trimer itself (see Table S11,12, 7.1 Supporting information). The PTO samples invariably yielded lower nitrile-to-triazine ratios compared to the trimer. This is consistent with the assumption that the polymerization proceeded further than the trimer in the case of the PTO samples. More precisely, a relatively high nitrile-to-triazine ratio was calculated for PTOs-300 synthesized with large zinc chloride contents (e.g. PTO-300-15), which can only be explained by the formation of short chains or small dendrimers (Table S11,12, 7.1 Supporting information). PTO-300-1 samples reveal lower ratios caused by ring closure or larger dendrimers (Table S11,13, 7.1 Supporting information). To get a more quantitative picture of the degree of polymerization,  $^{13}\text{C}$  one pulse ssNMR spectra of PTO-300-1 and PTO-300-10 were recorded (Figure S76, 7.1 Supporting information). As already described in a previous section the signals for the triazine units and the nitrile groups are well resolved (169 ppm for triazine as well as 120 ppm – 110 ppm for nitrile groups and the benzene carbons to which the nitrile groups are bound). Using the integrals of the signals, the nitrile-to-triazine ratio can be calculated. Due to the significantly longer spin-lattice relaxation of the triazine carbons compared to the other carbon species the chosen measurement conditions lead to a slight underestimation of around 5 % for the intensity of the triazine signal (for further details see the 7.1 Supporting information). The calculated ratio for the PTO-300-10 sample is 0.46, suggesting a mixture of trimers (0.50) and short chains or small dendrimers (< 0.50). For PTO-300-1 it is much lower (0.21) pointing towards a higher degree of polymerization. Therefore, the formation of dendrimers or ring structures is favored under these conditions. This is well in line with the IR and MALDI-TOF data.

### Optical properties

Interestingly, the materials showed different colors compared to the samples synthesized at 400 °C (black), as depicted in Figure 4.8(c). While the samples synthesized at 350 °C are still rather dark and their color is independent of the amount of  $\text{ZnCl}_2$  used, the synthesis at 300 °C leads to products with yellow (PTO-300-1) or green-greyish complexion (PTO-300-15). The colors of the PTOs differ also from those of the starting materials and the trimer (colorless), which again suggests the formation of oligomeric products.

UV-Vis spectra were recorded in order to evaluate the absorption characteristics of the materials as a function of their polymerization state (Figure 4.8(c,d)). When comparing the samples synthesized at different temperatures, a strong absorption in the UV region (350 nm) is observed for the PTO samples synthesized at 300 °C, with a sharp absorption edge around 370 nm (3.2 eV – 3.3 eV, assuming a direct band gap), as well as a weak and broad absorption in the visible light range. According to *Butchosa et al.*<sup>15</sup> these strong absorptions in the UV are caused by  $\pi \rightarrow \pi^*$  and  $n \rightarrow \pi^*$  excitations, resulting from absorptions within isolated molecular units and oligomer stacking, respectively. The long sloping wavelength tail extending beyond 700 nm in the samples synthesized at higher

salt contents (Figure 4.8(d)) likely occurs due to enhanced absorption caused by incipient carbonization. Likewise, the materials synthesized at elevated temperatures ( $> 300\text{ }^{\circ}\text{C}$ ) show broad absorption in the whole visible region with no distinct absorption edge, which is expected judging from their dark sample color (Figure 4.8(c)). Note, however, that theoretical calculations suggested a band gap of 2.42 eV for CTF-1.<sup>16</sup> When comparing the UV–Vis spectra of the PTO samples synthesized at  $300\text{ }^{\circ}\text{C}$  but with different zinc chloride concentrations (Figure 4.8(d)), a second absorption around 410 nm arises, which increases relative to the UV absorption and slightly red-shifts for the materials when synthesized in an excess of salt melt ( $> 1$  eq.). This feature may be associated with a reduced interlayer distance for the PTO-300 samples obtained with increasing salt content (Table S8, 7.1 Supporting information), or with more pronounced torsional angles in the otherwise planar systems as suggested by *Butchosa et al.*<sup>15</sup> However, due to the sloping background caused by incipient carbonization,<sup>7</sup> it is not possible to reliably extract the intensity of this absorption or the position of the absorption edge.

### Photocatalytic hydrogen evolution

Since triazine-based organic semiconductors have been reported to reduce water to hydrogen under visible light irradiation, we reasoned that the incorporation of triazine units into organic frameworks may be a viable strategy to rationally design efficient organic photocatalysts.<sup>12</sup> The high chemical and thermal stabilities of the CTFs, together with the suitable optical properties based on theoretical calculations and our experimental findings, should render CTFs suitable photocatalysts for the water-splitting reaction.<sup>16</sup> Platinum-loaded (2.2 wt%) CTF-1 itself ( $0.02\text{ }\mu\text{mol h}^{-1}$ ) and the PTO-350 samples ( $0.45\text{ }\mu\text{mol h}^{-1}$ ) showed only negligible activity in a buffered (pH 7) aqueous triethanolamine (TEoA) solution when illuminated with simulated sunlight. These low activities may be explained by the large carbon content in the samples which results from incipient carbonization, or by a mismatch in energy levels. The excess of carbon absorbs a significant portion of the light which then cannot penetrate deeply into the photocatalyst. The low crystallinity of the materials may also hinder the photocatalytic process in that the light-induced charge carriers quickly recombine at traps rather than being able to diffuse to the surface of the material. In contrast, the samples synthesized below  $350\text{ }^{\circ}\text{C}$  (PTO-300) exhibit a stable and high hydrogen evolution rate for over 100 hours under the conditions described above (Figure 4.9(a,b) and Figure S82, 7.1 Supporting information, right). The most active PTO-300 materials were found to produce  $10.8 (\pm 2.8)\text{ }\mu\text{mol h}^{-1}$  hydrogen on average when illuminated with simulated sunlight. The action spectrum of the PTO-300 samples suggest that the highest hydrogen contribution arises from wavelengths with an energy of  $400 (\pm 20)\text{ nm}$ , revealing average estimated apparent quantum efficiencies of  $5.5 (\pm 1.1)\%$  (Figure 4.9(c)). Activities above 450 nm are negligible due to the weaker absorption in this wavelength range. In several cases, not only a constant hydrogen evolution rate was observed but even an increase in activity over time (*e.g.* Figure S78, 7.1 Supporting information), likely due to the gradually improved wettability of the oligomers and, hence, dispersion. We have analyzed the recovered photocatalyst after operating for over



tens of hours and can exclude hydrolysis or any photodegradation of the catalyst (Figure S87,89, 7.1 Supporting information). An additional vibration band at  $1771\text{ cm}^{-1}$  is observed in the IR spectrum for the photocatalysts treated in a phosphate buffer (Figure S87, 7.1 Supporting information, right) which can be explained by possible phosphate coordination. No hydrolysis products are observed in the  $^{13}\text{C}$  CP MAS ssNMR spectra (Figure S89, 7.1 Supporting information).

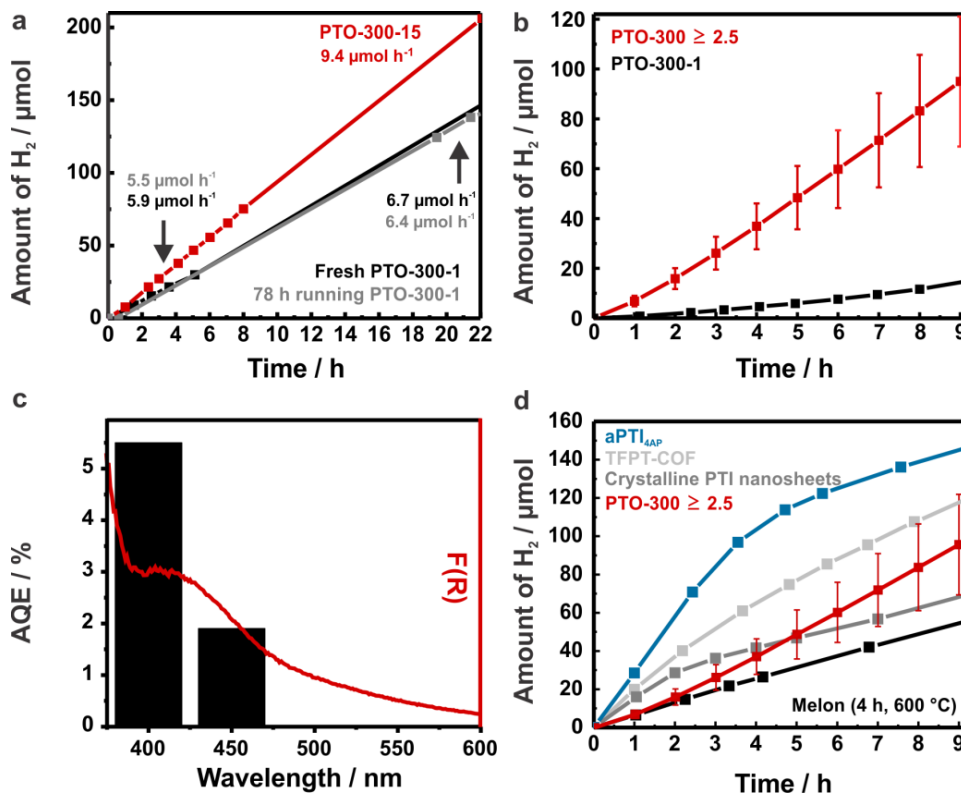


**Figure 4.9** (a) Stability test of 10 mg Pt-modified PTO-300-15 and PTO-300-1 in 10 vol% buffered (pH 7, 0.5 M, phosphate buffer) TEOA solution under irradiation with simulated sunlight (for PTO-300-15, red) and UV-Vis light ( $\geq 250\text{ nm}$  for PTO-300-1). Stable hydrogen evolution for over 100 h (PTO-300-1) shown as two slopes: the black slope represents a fresh PTO-300-1 suspension within the first 20 h and the grey represents the same suspension after 78 h of photocatalysis, demonstrating stable  $\text{H}_2$  evolution for at least 100 h. (b) Average  $\text{H}_2$  evolution rate of Pt-modified PTO-300 $\geq 2.5$  with standard deviation, compared to PTO-300-1. (c) Action spectrum of Pt-PTO-300-5 dispersed in a buffered (pH 7, 0.5 M, phosphate buffer) 10 vol% TEOA solution (measured with a 40 nm FWHM band pass filter), overlaid on the UV-Vis spectrum of the photocatalyst. (d) Reproducible hydrogen evolution rate of Pt-PTO-300 $\geq 2.5$  and of the best performing sample (Pt-PTO-300-2.5) in comparison with literature photocatalysts used as internal standards under identical reactor and illumination conditions (230 mL reactor volume, top-irradiation, equal irradiation surface and intensity  $380\text{ mW cm}^{-2}$ ), as well as dispersion volume (10 mL of 10 vol% TEOA solution), 10 mg (2 mg for PTI nanosheets) Pt-modified photocatalyst (2.2 wt% Pt) under reported conditions.

A factor significantly influencing the variation of activity in the series of PTOs is the ratio of precursor to  $\text{ZnCl}_2$  in the syntheses at  $300\text{ }^\circ\text{C}$ . Higher activities are observed for PTO-300 samples for which an excess of zinc chloride was used in the synthesis ( $> 1\text{ eq.}$ ) (Figure 4.9(b)). In line with our previous observations described above, the large zinc chloride content leads to the formation of smaller oligomers, whereas a low zinc chloride envi-



ronment favors the formation of larger PTO fragments which are photocatalytically less active (Figure 4.9(b)). Similar observations have recently been reported for carbon nitriles,<sup>32</sup> where oligomers of melon showed an increased photocatalytic activity compared to the polymer. Furthermore, the activity of these oligomers depended on their size such that smaller oligomers of melon showed a higher activity compared to the larger ones.<sup>32</sup> We believe that the increased activity of the smaller oligomers compared to their larger relatives or the polymer might be associated with the amount of terminal groups. The terminal groups in the PTO samples are nitrile moieties which appear in larger quantities for the samples synthesized in excess of zinc chloride. A large nitrile content favors hydrogen bonding and thus, leads to a better dispersion of the photocatalyst during the photocatalytic experiment. Furthermore, it is expected that platinum, which is used as a co-catalyst, preferably coordinates to the terminal nitrile groups and thus promotes improved charge transfer.<sup>33</sup> Another possibility is that the nitrile groups can be considered as active sites themselves, as the photocatalytic activity scales roughly with the relative amount of nitrile groups in the sample. Note, however, that we do not observe a linear correlation between the observed activity and the excess of zinc chloride used. Nevertheless, the interplay between triazines and nitriles or, in other words, a reasonably large conjugated backbone, is decisive since a certain amount of triazines is needed to exhibit a photocatalytic response. For instance, the trimer ( $0.08 \mu\text{mol h}^{-1}$ ) showed only minor activity even with UV-Vis ( $\geq 250 \text{ nm}$ ) illumination (Figure S79, 7.1 Supporting information). Note that we observe quite significant batch-to-batch variations in the samples with ZnCl<sub>2</sub>-to-precursor ratios of  $> 1$  (Table S17 and Figure S86, 7.1 Supporting information), which we attribute to the dilution and low diffusion of the precursor during the ionothermal reaction at  $300 \text{ }^\circ\text{C}$ , and the resulting variations in the oligomer size, indicating that the synthesis is not yet fully optimized. For example, next to average hydrogen evolution rates around  $10 \mu\text{mol h}^{-1}$ , lower ( $3.4 \mu\text{mol h}^{-1}$ ) and higher hydrogen evolution rates of  $30.3 \mu\text{mol h}^{-1}$  were observed, the latter with an estimated apparent quantum efficiency of up to  $9.9 (\pm 2.0) \%$ . A fine-tuning of the synthesis parameters and the deliberate introduction of additional nitrile groups may therefore further improve the photocatalytic activity of these phenyl-triazine oligomers.

Another important aspect for gauging the intrinsic photocatalytic activities of the samples is to relate them to their specific surface areas, which may correlate with the number of exposed active sites. In this case, however, the PTOs with smaller surface areas showed significantly improved activity and we can therefore exclude surface area effects as dominant factors for the photocatalytic performance (Table S15, 7.1 Supporting information).

Further, the question arises as to whether residual zinc chloride is present as an impurity or quantitatively incorporated into the system and as such may influence the photocatalytic activity of the PTOs. *Thomas and co-workers*<sup>34</sup> reported on possible Zn<sup>2+</sup> incorporation in CTFs during the synthesis of CTF-0 (derived from 1,3,5-tricyanobenzene) when synthesized in the presence of large zinc chloride quantities. Minor amounts of Zn<sup>2+</sup> ions

within the structure might act as “dopants” as reported previously for carbon nitrides.<sup>35</sup> However, this zinc doping procedure (stirring melon in an acidic ethanol zinc chloride solution) most likely leads to an increased amount of nitrile groups from de-polymerization and opening of the triazine rings as seen from the IR spectra. It is therefore doubtful whether the Zn-doping or the formation of nitriles was the reason for the improved activity of the carbon nitrides.<sup>35</sup> Here, the presence of zinc chloride in the PTO is  $\leq 0.1$  wt% as established by ICP-AES analysis (Table S9, 7.1 Supporting information). As we cannot completely exclude that minute amounts of impurities may be the reason for the different activities of PTOs-300, we performed two different control experiments. Firstly, zinc chloride (5 mg, 10 mg and 17 mg) was added to a standardized PTO-300 suspension for photocatalysis, which resulted in a long-term decrease in activity presumably caused by chlorine poisoning of the platinum nanoparticles (Figure S80, 7.1 Supporting information, left). Secondly, a PTO-300 sample was excessively washed with 0.1 M ethylenediaminetetraacetic acid (EDTA), which acts as a complexing agent for zinc ions (Table S16, 7.1 Supporting information), and compared the activities before and after EDTA treatment. Here again, no change in activity was detected after washing (Figure S80, 7.1 Supporting information, left), which implies that  $\text{Zn}^{2+}$  doping is probably not the reason for the activity differences.

We therefore hypothesize that besides the different nitrile content variations in activity within the oligomers primarily arise from the different optical properties (more well-defined absorption in the visible, see Figure 4.8(d)) as well as more favorable carrier dynamics. The latter may be most facile for oligomers with shorter lengths and smaller interlayer distances, which leads to stronger  $\pi$ -orbital overlap and hence more efficient extraction of the charge carriers at the interfaces. This is supported by the significantly enhanced dispersibility of the smaller oligomers with a higher degree of nitrile moieties.

In addition, several control experiments were performed to ensure that the evolution of hydrogen is indeed photocatalytic and not due to chemical reactions with the catalyst. Most fundamentally, the absence of light resulted in no activity, proving the hydrogen evolution to be photo-induced. Secondly, the activity of the photocatalyst was tested without the addition of the proton reduction catalyst platinum. In fact, unmodified PTO-300 also showed a moderate, yet significant hydrogen evolution rate (PTO-300-15:  $1.21 \mu\text{mol h}^{-1}$  or  $121 \mu\text{mol h}^{-1} \text{g}^{-1}$ ; PTO-300-1:  $0.53 \mu\text{mol h}^{-1}$  or  $53 \mu\text{mol h}^{-1} \text{g}^{-1}$ ), which indicates that PTO-300 acts as an actual photocatalyst rather than just a photosensitizer (Figure S81, 7.1 Supporting information). Surprisingly, PTO-300 ( $121 \mu\text{mol h}^{-1} \text{g}^{-1}$ ) significantly outperforms other co-catalyst-free light element photocatalysts (*e.g.* melon:  $1 \mu\text{mol h}^{-1} \text{g}^{-1}$  –  $40 \mu\text{mol h}^{-1} \text{g}^{-1}$ ,<sup>8</sup> msp-g- $\text{C}_3\text{N}_4$ :  $2 \mu\text{mol h}^{-1} \text{g}^{-1}$ ,<sup>17</sup>  $\text{B}_{4.3}\text{C}$ :  $14.5 \mu\text{mol h}^{-1} \text{g}^{-1}$ ,<sup>19</sup> and PTI:  $0 \mu\text{mol h}^{-1} \text{g}^{-1}$ ).<sup>6,7,10</sup> Yet, this modest activity is significantly increased and stabilized by platinum deposition. The absence of an electron donor resulted in negligible activity ( $0.01 \mu\text{mol h}^{-1}$ ) which underlines the importance of a sacrificial donor in the system to avoid recombination of the generated charge carriers and to enhance the driving force for

hole collection as compared to the oxidation of pure water. The highest activities were observed when Pt-modified PTO-300 was suspended in an aqueous TEOA solution. However, other electron donors such as oxalic acid and EDTA also led to sustained hydrogen evolution (Figure S82, 7.1 Supporting information).

We also tested PTOs-300 doped with 3 wt%  $\text{Co}_3\text{O}_4$  nanoparticles and silver nitrate as sacrificial agents for water oxidation. However, no oxygen was detected (within the detection limit), even though triazine-based materials have been predicted to be oxygen evolution catalysts due to their suitable HOMO potential.<sup>16</sup>

PTO-300 synthesized from diluted zinc chloride melt is competitive (average rate of  $1076 \mu\text{mol h}^{-1} \text{g}^{-1}$ , maximum rate of  $3030 \mu\text{mol h}^{-1} \text{g}^{-1}$ ) with highly condensed heptazine- and triazine-based carbon nitride photocatalysts, such as melon (*e.g.* msp- $g\text{-C}_3\text{N}_4$ :  $1490 \mu\text{mol h}^{-1} \text{g}^{-1}$  or  $g\text{-C}_3\text{N}_4$  doped with barbituric acid:  $294 \mu\text{mol h}^{-1} \text{g}^{-1}$ ),<sup>17,36</sup> crystalline PTI nanosheets ( $1750 \mu\text{mol h}^{-1} \text{g}^{-1}$ ),<sup>10</sup> 4AP doped amorphous PTI ( $4907 \mu\text{mol h}^{-1} \text{g}^{-1}$ ),<sup>7</sup> TFPT-COF ( $1970 \mu\text{mol h}^{-1} \text{g}^{-1}$ )<sup>9</sup> and boron carbide ( $\text{B}_{4.3}\text{C}$ :  $31 \mu\text{mol h}^{-1} \text{g}^{-1}$ ).<sup>19</sup> As differing measurement set-ups (light-sources, intensities, irradiation type *e.g.* inner *vs* top-irradiation) may give different results for the same photocatalyst in different laboratories we compare PTO-300 with four of the above reported photocatalysts measured under identical instrumental conditions, namely melon ( $g\text{-C}_3\text{N}_4$ ) synthesized from dicyandiamide for 4 hours at  $600 \text{ }^\circ\text{C}$ ,<sup>8a</sup> crystalline PTI/LiCl nanosheet suspension,<sup>10</sup> 16 % 4-AP doped amorphous PTI<sup>7</sup> and TFPT-COF<sup>9</sup> (Figure 4.9(d)). While PTO-300-1 ( $1.5 \mu\text{mol h}^{-1}$ ) is less active than melon ( $6.4 \mu\text{mol h}^{-1}$ ), PTOs-300 synthesized in an excess of zinc chloride ( $10.8 (\pm 2.8) \mu\text{mol h}^{-1}$ ) are superior to melon and rival TFPT-COF ( $15.5 \mu\text{mol h}^{-1}$ ). Whereas some photocatalysts tested here (TFPT-COF and (amorphous doped) PTI) exhibit a significant decrease in their hydrogen evolution rate over time within an aqueous TEOA solution, PTO-300 shows long term stability.

### 4.2.3 Conclusions

We have demonstrated that a lower reaction temperature during ionothermal CTF-1 synthesis gives rise to oligomers of CTF-1 which differ in their length and connectivity. These oligomers are highly efficient hydrogen evolution photocatalysts which show an average hydrogen evolution rate of  $10.8 (\pm 2.8) \mu\text{mol h}^{-1}$  (10 mg photocatalyst) with simulated sunlight, whereas hardly any activity was observed for the CTF-1 polymer. We hypothesize that the suspicious absence of activity in CTF-1 is due to a reduced thermodynamic driving force for hydrogen evolution or to the incipient carbonization at its synthesis temperature of  $400 \text{ }^\circ\text{C}$ , where light absorption by carbon prevents photon absorption by the framework, thus rendering hydrogen evolution unfeasible. For the triazine-based oligomers obtained at different precursor/zinc chloride ratios, distinct crystallinity, surface area, nitrile content as well as variations in activity were observed. Specifically, PTOs synthesized with an excess of zinc chloride ( $> 1$  equivalent relative to the precursor) dis-

play higher crystallinity, a reduced layer distance, smaller surface areas, lower hydrophobicity, smaller fragment sizes and a larger amount of terminal nitrile groups. These features were found to contribute to substantially improved photocatalytic activity compared to PTOs obtained with 1:1 precursor/zinc chloride ratio. Since the observed activity enhancement likely correlates with an increased amount of nitrile moieties and improved  $\pi$ -stacking of the oligomers, we believe that by controlling the polymerization progress, we can significantly enhance the charge transfer kinetics, which still is the limiting factor in organic photocatalysts. Finally, the oligomers show the highest activity observed for metal-free organic photocatalysts in the absence of any co-catalyst, thus boding well for the development of earth-abundant organic photocatalysts by controlled polymerization reactions and molecular engineering.<sup>6–10,17–19</sup>

## Bibliography

- (1) X. Chen, S. Shen, L. Guo, S. S. Mao, *Chem. Rev.* **2010**, *110*, 6503.
- (2) A. Fujishima, K. Honda, *Nature* **1972**, *238*, 37.
- (3) H. Tong, S. Ouyang, Y. Bi, N. Umezawa, M. Oshikiri, J. Ye, *Adv. Mater.* **2012**, *24*, 229.
- (4) S. Yanagida, A. Kabumoto, K. Mizumoto, C. Pac, K. Yoshino, *J. Chem. Soc., Chem. Commun.* **1985**, *8*, 474.
- (5) T.-F. Yeh, J.-M. Syu, C. Cheng, T.-H. Chang, H. Teng, *Adv. Funct. Mater.* **2010**, *20*, 2255.
- (6) Y. Ham, K. Maeda, D. Cha, K. Takanabe, K. Domen, *Chem. – Asian J.* **2013**, *8*, 218.
- (7) K. Schwinghammer, B. Tuffy, M. B. Mesch, E. Wirmhier, C. Martineau, F. Taulelle, W. Schnick, J. Senker, B. V. Lotsch, *Angew. Chem., Int. Ed.* **2013**, *52*, 2435.
- (8) (a) X. Wang, K. Maeda, A. Thomas, K. Takanabe, G. Xin, J. M. Carlsson, K. Domen, M. Antonietti, *Nat. Mater.* **2009**, *8*, 76; (b) L. Seyfarth, J. Seyfarth, B. V. Lotsch, W. Schnick, J. Senker, *Phys. Chem. Chem. Phys.* **2010**, *12*, 2227.
- (9) L. Stegbauer, K. Schwinghammer, B. V. Lotsch, *Chem. Sci.* **2014**, *5*, 2789.
- (10) K. Schwinghammer, M. B. Mesch, V. Duppel, C. Ziegler, J. Senker, B. V. Lotsch, *J. Am. Chem. Soc.* **2014**, *136*, 1730.
- (11) M. K. Bhunia, K. Yamauchi, K. Takanabe, *Angew. Chem., Int. Ed.* **2014**, *53*, 11011.
- (12) Y. Wang, X. Wang, M. Antonietti, *Angew. Chem., Int. Ed.* **2012**, *51*, 68.
- (13) P. Kuhn, M. Antonietti, A. Thomas, *Angew. Chem., Int. Ed.* **2008**, *47*, 3450.
- (14) S. Ren, M. J. Bojdys, R. Dawson, A. Laybourn, Y. Z. Khimyak, D. J. Adams, A. I. Cooper, *Adv. Mater.* **2012**, *24*, 2357.
- (15) C. Butchosa, T. O. McDonald, A. I. Cooper, D. J. Adams, M. A. Zwijnenburg, *J. Phys. Chem. C* **2014**, *118*, 4314.
- (16) X. Jiang, P. Wang, J. Zhao, *J. Mater. Chem. A* **2015**, *3*, 7750.
- (17) X. Wang, K. Maeda, X. Chen, K. Takanabe, K. Domen, Y. Hou, X. Fu, M. Antonietti, *J. Am. Chem. Soc.* **2009**, *131*, 168.
- (18) J. Liu, Y. Liu, N. Liu, Y. Han, X. Zhang, H. Huang, Y. Lifshitz, S.-T. Lee, J. Zhong, Z. Kang, *Science* **2015**, *347*, 970.

- (19) J. Liu, X. Wen, Y. Hou, F. Zuo, G. J. O. Beran, P. Feng, *Angew. Chem., Int. Ed.* **2013**, *52*, 3241.
- (20) J. H. van't Hoff, *Die Gesetze des chemischen Gleichgewichtes für den verdünnten, gasförmigen oder gelösten Zustand*, Engelmann, Leipzig, 2<sup>nd</sup> ed **1915**, p. 105.
- (21) M. J. Bojdys, J. Jeromenok, A. Thomas, M. Antonietti, *Adv. Mater.* **2010**, *22*, 2202.
- (22) V. G. Manecke, D. Wöhrle, *Makromol. Chem.* **1968**, *120*, 176.
- (23) P. Kuhn, A. Thomas, M. Antonietti, *Macromolecules* **2009**, *42*, 319.
- (24) M. R. Liebl, J. Senker, *Chem. Mater.* **2013**, *25*, 970.
- (25) W. J. Gammon, O. Kraft, A. C. Reilly, B. C. Holloway, *Carbon* **2003**, *41*, 1917.
- (26) G. Beamson, D. Briggs, *High Resolution XPS of Organic Polymers*, the Scienta ESCA300 Database, **1992**.
- (27) J. A. Taylor, G. M. Lancaster, J. W. Rabalais, *Appl. Surf. Sci.* **1978**, *1*, 503.
- (28) (a) S. Yang, Y. Gong, J. Zhang, L. Zhan, L. Ma, Z. Fang, R. Vajtai, X. Wang, P. M. Ajayan, *Adv. Mater.* **2013**, *25*, 2452; (b) M. Barber, J. A. Connor, M. F. Guest, I. H. Hillier, M. Schwarz, M. Stacey, *J. Chem. Soc., Faraday Trans. 2* **1973**, *69*, 551; (c) B. A. Sexton, N. R. Avery, *Surf. Sci.* **1983**, *129*, 21.
- (29) B. Jürgens, E. Irran, J. Senker, P. Kroll, H. Müller, W. Schnick, *J. Am. Chem. Soc.* **2003**, *125*, 10288.
- (30) S. Hug, M. Tauchert, S. Li, U. E. Pachmayr, B. V. Lotsch, *J. Mater. Chem.* **2012**, *22*, 13956.
- (31) E. T. Haupt, D. Leibfritz, *Spectrochim. Acta, Part A* **1989**, *45*, 119.
- (32) V. W. Lau, M. B. Mesch, V. Duppel, V. Blum, J. Senker, B. V. Lotsch, *J. Am. Chem. Soc.* **2015**, *137*, 1064.
- (33) (a) B. Y. Kukushkin, *Platinum Met. Rev.* **1998**, *42*, 106 ; (b) V. W. Lau, I. Moudrakovski, T. Botari, S. Weinburger, M. B. Mesch, V. Duppel, J. Senker, V. Blum, B. V. Lotsch **2015**, *submitted*.
- (34) P. Katekomol, J. Roeser, M. J. Bojdys, J. Weber, A. Thomas, *Chem. Mater.* **2013**, *25*, 1542.
- (35) B. Yue, Q. Li, H. Iwai, T. Kako, J. Ye, *Sci. Technol. Adv. Mater.* **2011**, *12*, 034401.
- (36) J. Zhang, X. Chen, K. Takanabe, K. Maeda, K. Domen, J. D. Epping, X. Fu, M. Antonietti, X. Wang, *Angew. Chem., Int. Ed.* **2010**, *49*, 441.



# Chapter V

## 5 Summary

### 5.1 PTI/LiCl as a new triazine-based 2D carbon nitride photocatalyst & enhancement of its photocatalytic activity

#### PTI/LiCl as a new triazine-based 2D photocatalyst

(Chapter 3.1, published in *Angew. Chem. Int. Ed.* **2013**, 52, 2435)

For four years, heptazine-based “melon” was the only carbon nitride which had been used as photocatalyst for light-induced water splitting. In Chapter 3.1 a new photocatalytically active carbon nitride, PTI/LiCl, has been introduced, which in contrast to melon exclusively consists of triazine building blocks (Figure 5.1).

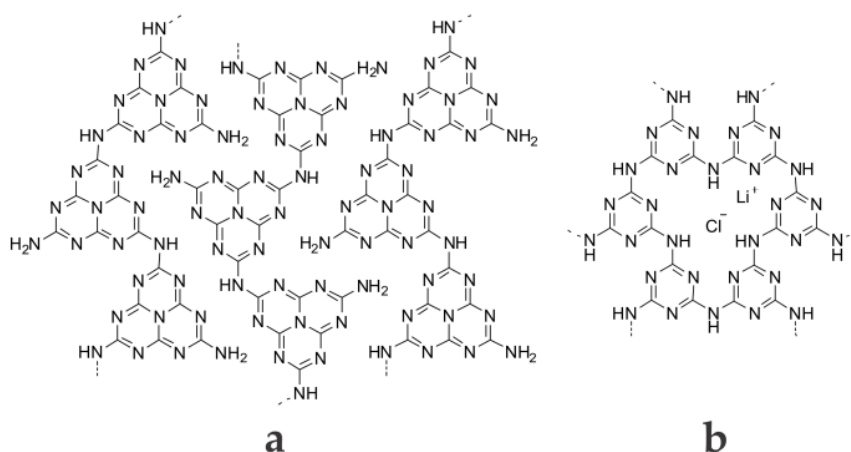


**Figure 5.1** Idealized structures of heptazine-based melon (often called *g*-C<sub>3</sub>N<sub>4</sub>) (a) and triazine-based PTI/LiCl (b).

According to the measurements presented in Chapter 3.1, the activity of crystalline PTI/LiCl is competitive with that of heptazine-based amorphous melon. In addition, its high crystallinity makes PTI/LiCl an excellent candidate for the elucidation of the photocatalytic mechanism which until now has not been completely clarified. As already known from heptazine-based photocatalysts, we found that the photocatalytic activities of PTI/LiCl and related systems largely depend on the reaction conditions at which they have been synthesized (such as reaction temperature, time, atmosphere and choice of

precursors) and the testing conditions (*e.g.* amount and choice of sacrificial agents, co-catalysts, as well as illumination conditions).

### Enhancing the photocatalytic activity of PTI/LiCl

(Chapter 3.1, published in *Angew. Chem. Int. Ed.* 2013, 52, 2435 and Chapter 3.2, published in *J. Am Chem. Soc.* 2014, 136, 1730)

Akin to melon, the moderate photocatalytic activity of crystalline PTI/LiCl can be improved by engineering its optoelectronic properties, morphology and surface properties which is discussed in Chapter 3.1 and 3.2. In Chapter 3.1, it is shown that PTI/LiCl synthesized in argon and ambient atmosphere has an increased surface area and more defects (*e.g.* terminal nitrile groups, incomplete polymerization and oxygen defects) as well as higher photocatalytic activity compared to crystalline PTI/LiCl, which has been synthesized under autogeneous ammonia pressure. Like crystalline PTI/LiCl, the amorphous version is composed of triazine units as verified by solid-state (ss) cross-polarization polarization-inversion (CPPI) NMR measurements (Figure 5.3(c,d)).

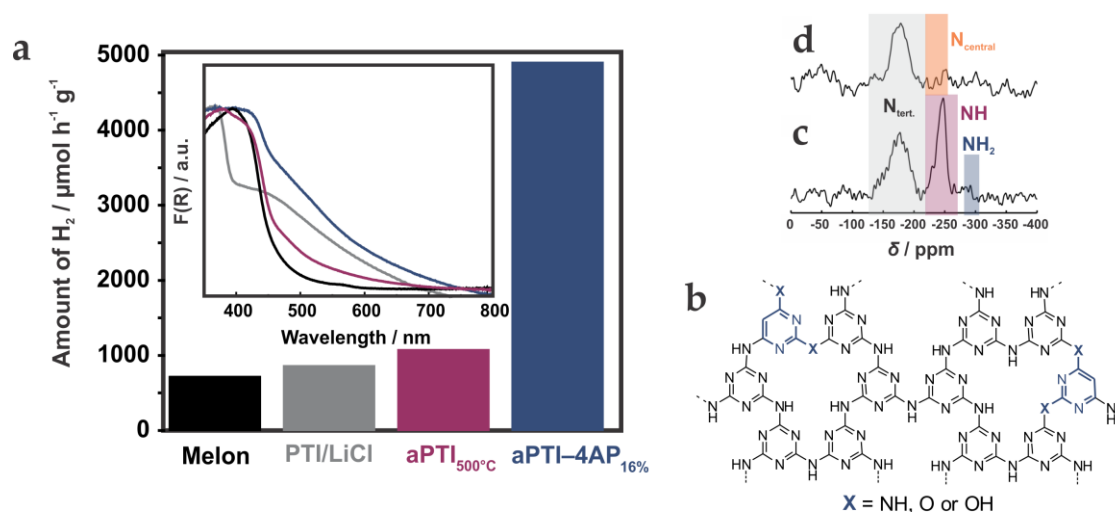


**Figure 5.3** (a) Enhancement of the photocatalytic activity towards light-induced hydrogen evolution of PTI co-polymerized with 4AP (b; idealized structure) as compared to melon, crystalline and amorphous PTI, and UV-Vis absorption spectra (inset). (c)  $^{15}\text{N}$  CP-MAS ssNMR spectrum (10 kHz) and (d)  $^{15}\text{N}$  CPPI-MAS spectrum (6 kHz with an inversion time of 400  $\mu\text{s}$ ) of 4AP-doped PTI suggesting a triazine-based structure due to the missing central heptazine nitrogen and signals of amino groups.

By a co-polymerization reaction between the PTI/LiCl precursor dicyandiamide and an organic “dopant” (4-amino-2,6-dihydroxypyrimidine (4AP)), amorphous PTI-like materials with increased carbon and oxygen content have been synthesized (Figure 5.3(b)). Optimization of the reaction conditions led to materials with improved optical properties and about six times higher photocatalytic activities as compared to crystalline PTI/LiCl (Figure 5.3(a)). The enhanced activity of the 4AP-doped PTI co-polymers compared to the undoped samples can be attributed to surface area effects and improved visible light harvesting properties. We further suppose that position of the LUMO level is more suitable



for water reduction and allows enhanced photocatalytic activity. Further, we demonstrate that doping with other pyrimidine-based organic molecules (such as 2-amino-4,6-dihydroxypyrimidine (2AP), 2,4,6-triaminopyrimidine (TAP) and barbituric acid (BA)) also results in photocatalytically active materials with higher activities than the native (*i.e.* undoped) PTI (see Chapter 3.1.4).

In Chapter 3.2 we have shown that the exfoliation of crystalline PTI/LiCl through a simple sonication procedure in water leads to PTI crystallites 1 nm – 2 nm in height with lateral sizes of less than 100 nm which are structurally closely related to their mother compound (Figure 5.4(b,d)). While the C/N connectivity and the chlorine content of the PTI nanosheets are essentially identical with the ones of the bulk material, the PTI nanosheets contain less lithium ions (Figure 5.4(a,inset)). A  $^1\text{H}$ - $^1\text{H}$  proton driven spin diffusion spectrum of the exfoliated PTI nanosheets further supports the formation of few-layer PTI stacks and implies a strong interaction between protons of the PTI nanosheets with water physisorbed on the PTI surface (Figure 5.4(c)). We believe that the increased surface area and thus, facile access to catalytically relevant sites on the nanosheets, as well as the strong substrate-PTI interactions are likely the reasons for the improved photocatalytic activity of exfoliated PTI compared to bulk crystalline PTI/LiCl (Figure 5.4(a)).

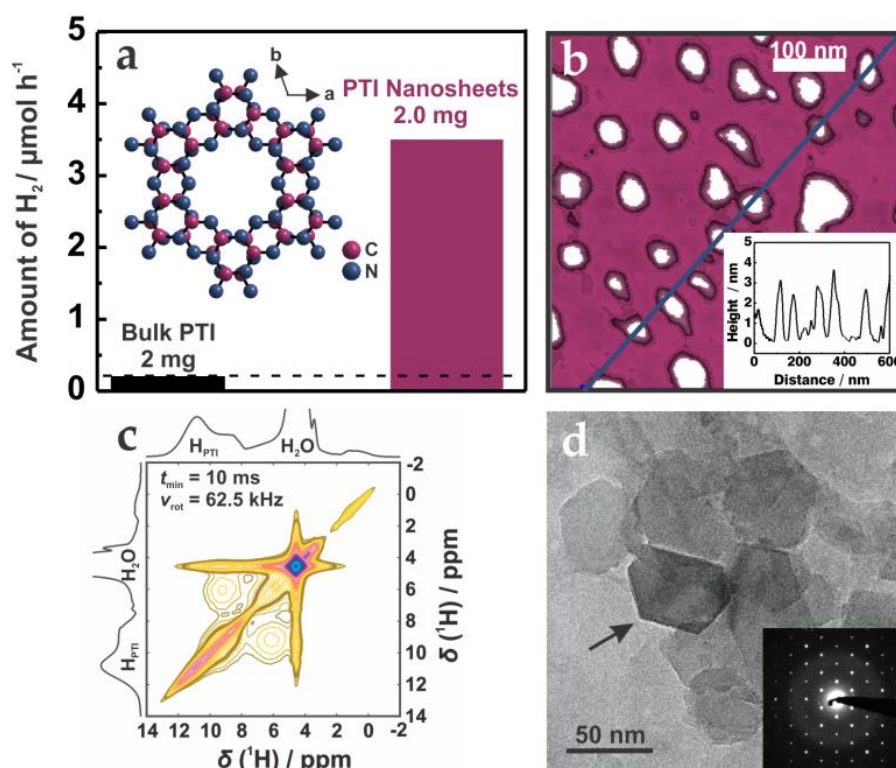


**Figure 5.4** (a) Visible light hydrogen evolution rate of exfoliated, crystalline PTI/LiCl compared to bulk PTI. The inset shows the idealized structure (without ion loading) of PTI (view along the  $c$ -axis). (b) AFM image of PTI crystallites on a silicon substrate and the corresponding height profile (inset). (c)  $^1\text{H}$ - $^1\text{H}$  proton driven spin diffusion NMR spectrum of restacked PTI nanosheets displays significant polarization exchange between the protons of PTI and the surrounding water shell of the PTI crystallites. (d) TEM micrograph of the PTI crystallites viewed along [001]; corresponding SAD pattern (inset).

## Investigations on the catalytically relevant sites of PTI/LiCl,Br

(To be submitted, Chapter 3.3)

In Chapter 3.3 we further show that the photocatalytic activity of crystalline PTI largely depends on its ionic loading which in turn, impacts its stacking behavior and hence, the accessibility of its catalytically relevant sites. While Li/Cl-intercalated PTI has shown to be photocatalytically active, the exchange of the chloride anions with bromides leads to inactivity, which is likely due to an increased interlayer stacking and, hence, decreased  $\pi$ -orbital overlap. We partially exchanged the lithium ions with protons through washing the materials with concentrated acids. Reducing the lithium content (in PTI/LiCl and PTI/LiBr) entailed a structural change which was recognized by a decrease in layer distance, a change of the anion positions (to within the C,N layers) and a reduction in symmetry (Figure 5.2(a–c)).

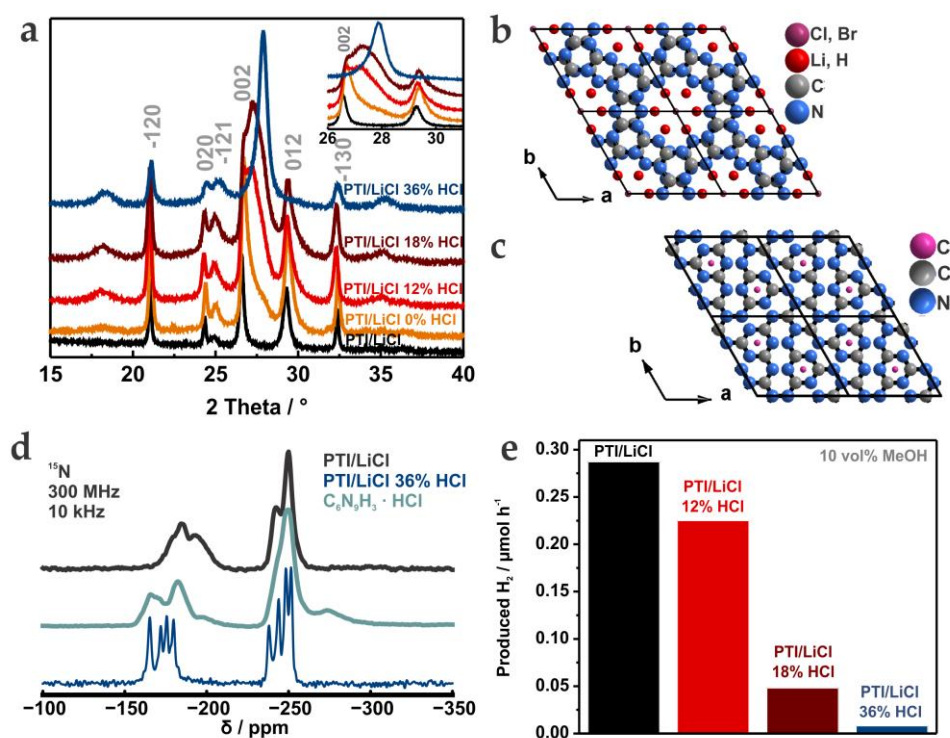


**Figure 5.2** (a) PXRD patterns of PTI/LiCl treated with concentrated acids compared to PTI/LiCl. The series of PXRD patterns depicts the change in structure and symmetry during protonation. (b) Crystal structure of PTI/LiCl,Br. (c) Model crystal structure of PTI/LiCl,Br treated with concentrated acids on the basis of  $C_6N_9H_3 \cdot HCl$  (proposed due to the similarities of both compounds). (d)  $^{15}N$  ssNMR spectra of the different PTI systems, showing the high local order for PTI/LiCl after acid treatment (PTI/LiCl 36% HCl). (e) Hydrogen evolution rates of PTI/LiCl before (black) and after acid treatment at different concentrations (in 10 vol% MeOH,  $\geq 420$  nm).

Although an increase in photocatalytic activity due to an improved  $\pi$ -orbital overlap could have been expected, the lithium-depleted materials showed only marginal hydrogen evolution (Figure 5.2(e)). This may be attributed to a lateral shift of the C,N-layers after acid treatment, which might hamper charge transfer perpendicular to the layers.<sup>1,2</sup> More likely though, protonation blocks catalytically relevant sites, thus impeding efficient

interaction with the co-catalyst, the substrate (water/protons) or the sacrificial electron donor. The exceptionally high local order of PTI/HCl (apparent especially in  $^{15}\text{N}$  ssNMR measurements, Figure 5.2(d)) renders these materials excellent candidates for in-depth investigations of their structure – property – photocatalytic activity relationship.

## 5.2 Rational design of a photocatalytically active COF

(Chapter 4.1, published in *Chem. Sci.* **2014**, *5*, 2789)

Carbon nitrides are powerful candidates for light-element photocatalysts, due to their easy, scalable and low-cost synthesis. Only a few other light-weight photocatalysts are known to date, such as  $\alpha$ -sulfur,<sup>3</sup> red phosphorus,<sup>4</sup>  $\beta$ -rhombohedral boron,<sup>5</sup> boron carbides,<sup>6</sup> ternary BCN nanosheets,<sup>7</sup> polypyridines,<sup>8,9</sup> polyphenylene,<sup>10</sup> as well as benzene-pyrene co-polymers.<sup>11</sup> Chapter 4.1 presents a new class of organic photocatalysts, the covalent organic frameworks (COFs). COFs consist of two or three different subunits which potentially offer several benefits for the rational design of non-metal photocatalysts (*e.g.* related to charge transfer, charge stabilization, co-catalyst anchor groups or light harvesting). The COF shown here, called TFPT-COF, provides a water stable hydrazone-linkage, a charge stabilizing and electron withdrawing triazine unit, an extended delocalized  $\pi$ -electronic system, and thus absorption in the visible range as well as a high surface area due to its inherently porous nature (Figure 5.5(a)). The TFPT-COF exhibits a hexagonal structure with a  $P6/m$  symmetry forming pores of 3.8 nm in diameter and a close-to-eclipsed AA layer stacking of 3.4 Å. Its optical band gap of roughly 2.8 nm is, in principle, large enough to enable water splitting.

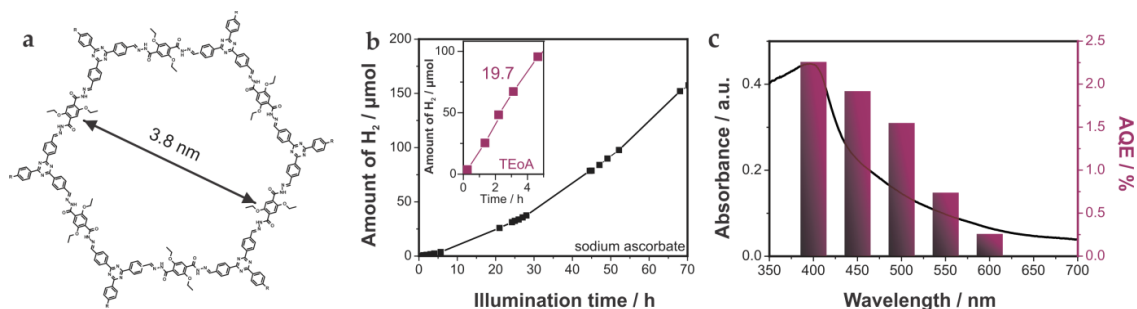


**Figure 5.5** (a) Idealized structure of the TFPT-COF showing with the estimated theoretical pore diameter. (b) Hydrogen evolution rates of Pt-TFPT-COF in an aqueous sodium ascorbate and TEoA (inset) solution. (c) Action spectrum of Pt-TFPT-COF in 10 vol% TEoA solution using 40 nm FWHM band-pass filters.

The photocatalytic hydrogen evolution experiments with platinum as co-catalyst and a suitable electron donor (triethanolamine or sodium ascorbic acid) show that the TFPT-COF is able to sustainably reduce water to hydrogen (Figure 5.5(b,c)). Further, we noticed a reversible loss in the long-range order of the COF during photocatalysis, which may indicate *in situ* exfoliation, as crystallinity could be re-introduced when subjecting the COF to its original synthesis conditions. The presented COF is one of the first examples for

a bottom-up approach toward designing heterogeneous photocatalysts based on a molecular building block approach.

### 5.3 Polymerization degree & photocatalytic activity illustrated on CTF-1

(Chapter 4.2, published in *Energy Environ. Sci.* **2015**, *8*, 3345)

Even if a material should be thermodynamically capable to photocatalytically split water, other factors such as kinetics and solvation effects can thwart its actual activity. This is illustrated in Chapter 4.2 for the archetypal covalent triazine framework CTF-1. CTF-1 has been theorized to be a suitable photocatalyst for light-driven water splitting due to its HOMO-LUMO gap of 2.42 eV and its adequate band positions relative to the hydrogen reduction and water oxidation potential, respectively. Compared to other covalent organic frameworks, CTF-1 can be easily synthesized through a trimerization reaction of 1,4-dicyanobenzene catalyzed by the Lewis acid  $\text{ZnCl}_2$ . However, we found that the necessary high temperature of 400 °C initializes partial decomposition of the triazine-based framework and carbonization, recognized by the black color of the resulting product and its higher than expected carbon content. We show that the reduction of the reaction temperature to 300 °C leads to the formation of oligomeric fragments rather than an ideal extended framework. The resulting phenyl-triazine oligomers (PTOs) have the same elemental composition as the framework, as well as identical IR, XPS, and ssNMR signatures, except additional signals for the unreacted nitriles (Figure 5.5(b)).

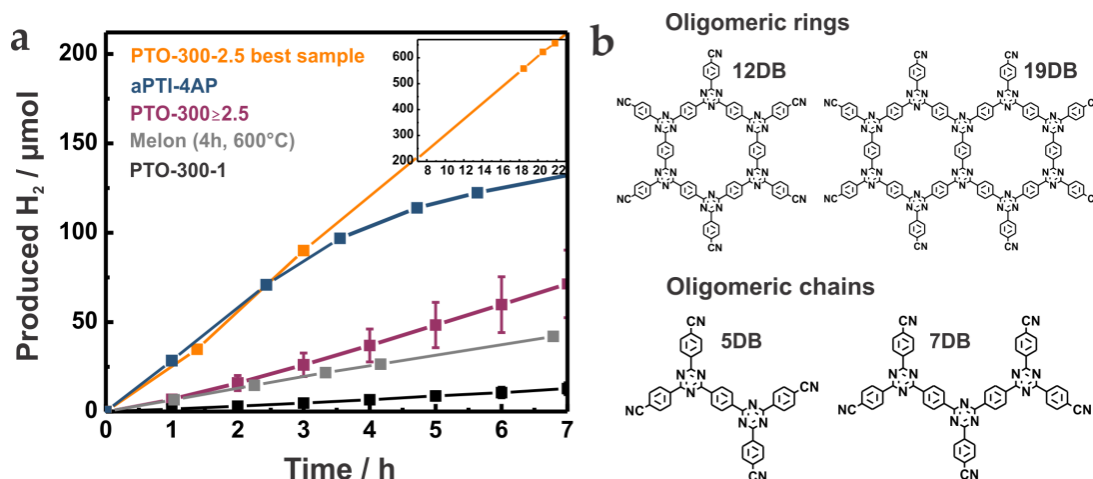


**Figure 5.6** (a) Average photocatalytic hydrogen evolution rates ( $\lambda \geq 420$  nm) of the as-synthesized Pt-phenyl-triazine-oligomers (PTO) synthesized in 1:1 precursor-to- $\text{ZnCl}_2$  ratio (PTO-300-1) and excess of  $\text{ZnCl}_2$  (PTO-300 $\geq$ 2.5) compared to the PTO sample with the highest  $\text{H}_2$  evolution rate (PTO-300-2.5 best sample), Pt-4AP co-polymerized PTI and Pt-melon measured in pH 7 (0.5 M, phosphate buffer) 10 vol% TEOA solution. (b) Examples of oligomeric fragments (rings and chains) of  $n$ -times the mass of the precursor 1,4-dicyanobenzene (DB) detected by MALDI-TOF of the PTO-300 samples.

We noticed that the intensity of the nitrile signals varied with the amount of  $\text{ZnCl}_2$  used relative to the precursor. With the help of quantitative ssNMR and IR spectroscopy in

combination with MALDI-TOF experiments, we could estimate the polymerization degree and connectivity of the oligomers. The oligomers show masses of up to 23 times the mass of the trimer. Oligomers synthesized in a 1:1 precursor-to-ZnCl<sub>2</sub> ratio (PTO-300-1) seem to be larger compared to the ones synthesized in excess of ZnCl<sub>2</sub> and to form ring-like structures, thus featuring fewer unreacted nitrile termini and higher BET surface areas. The performed photocatalytic experiments show very low activities for the polymer CTF-1 and the trimer, whereas the PTOs produce significant amounts of hydrogen (Figure 5.5(a)). The oligomers synthesized in excess of ZnCl<sub>2</sub> are clearly more active than PTO-300-1, which can be explained by their higher crystallinity, reduced layer distance, lower hydrophobicity, smaller fragment sizes and hence larger amount of terminal nitrile groups. Finally, the oligomers show the highest activity observed for metal-free organic photocatalysts in the absence of any co-catalyst, thus boding well for the development of earth-abundant oligomeric photocatalysts by controlled polymerization reactions and molecular engineering.

## Bibliography

- (1) C. Merschjann, T. Tyborski, S. Orthmann, F. Yang, K. Schwarzburg, M. Lublow, M. C. Lux-Steiner, T. Schedel-Niedrig, *Phys. Rev. B* **2013**, *87*, 205204.
- (2) C. Merschjann, S. Tschierlei, T. Tyborski, K. Kailasam, S. Orthmann, D. Hollmann, T. Schedel-Niedrig, A. Thomas, S. Lochbrunner, *Adv. Mater.* **2015**, *27*, 7993.
- (3) G. Liu, P. Niu, L. Yin, H.-M. Cheng, *J. Am. Chem. Soc.* **2012**, *134*, 9070.
- (4) F. Wang, W. K. H. Ng, J. C. Yu, H. Zhu, C. Li, L. Zhang, Z. Liu, Q. Li, *Appl. Catal. B* **2012**, *111–112*, 409.
- (5) G. Liu, L.-C. Yin, P. Niu, W. Jiao, H.-M. Cheng, *Angew. Chem. Int. Ed.* **2013**, *52*, 6242.
- (6) J. Liu, S. Wen, Y. Hou, F. Zuo, G. J. O. Beran, P. Feng, *Angew. Chem. Int. Ed.* **2013**, *52*, 3241.
- (7) C. Huang, C. Chen, M. Zhang, L. Lin, X. Ye, S. Lin, M. Antonietti, X. Wang, *Nat. Commun.* **2015**, *6*.
- (8) S. Matsuoka, T. Kohzuki, Y. Kuwana, A. Nakamura, S. Yanagida, *J. Chem. Soc. Perkin Trans.* **1992**, *2*, 679.
- (9) T. Maruyama, T. Yamamoto, *J. Phys. Chem. B* **1997**, *101*, 3806.
- (10) S. Yanagida, A. Kabumoto, K. Mizumoto, C. Pac, K. Yoshino, *J. Chem. Soc., Chem. Commun.* **1985**, 474.
- (11) R. S. Sprick, J.-X. Jiang, B. Bonillo, S. Ren, T. Ratvijitvech, P. Guiglion, M. A. Zwijnenburg, D. J. Adams, A. I. Cooper, *J. Am. Chem. Soc.* **2015**, *137*, 3265.



# Chapter VI

## 6 Conclusion and Outlook

The worldwide growing energy demands, the depletion of precious forest and fossil resources and the progressing pollution of the earth's atmosphere enforce a drastic change in the energy economy. The combustion of high-density green energy carriers such as hydrogen is one approach to conserve our environment. In this context, particular attention has been given in the development of environmentally benign routes for the generation of hydrogen. Photocatalytic water splitting emerged as a potential industrially applicable approach for the renewable production of hydrogen. However, for an efficient conversion of sunlight suitable photocatalysts are necessary. The commonly used photocatalysts are inorganic semiconductors which often suffer from insufficient light harvesting or contain partially toxic or scarce metals. Current research is driven by the discovery and further development of organic photocatalysts for light-induced water splitting. The benefits of organic polymers over inorganic materials are their low-cost large-scale synthesis, easily tunable band gap, absorption in the wavelength range of visible light and light-weight character. This idea dates back to the early 1980s and 1990s when phenylene- and pyridine-polymers have firstly been revealed as organic photocatalysts.<sup>1,2</sup> Only since the introduction of carbon nitrides as photocatalysts in 2009,<sup>3</sup> the race for organic photoactive materials for solar fuels production started since this material class offers a platform for a multitude of modifications on the molecular level. Until 2013, only ill-defined melon-type samples were investigated for photocatalysis which belong to the category of heptazine-based carbon nitrides. The question has been raised and answered in this thesis whether the lesser known but crystalline triazine-based carbon nitride called poly(triazine imide) PTI/LiCl<sup>4,5</sup> might be an attractive photocatalyst as well.

In 2013, we<sup>6</sup> and others<sup>7</sup> have shown that crystalline PTI/LiCl is indeed able to reduce water to hydrogen with the help of visible light. In Chapter 3.1 of this work, the applicability of PTI/LiCl as a photocatalyst has been demonstrated. More precisely, under identical photocatalytic conditions, PTI/LiCl can compete with the amorphous melon reference published in 2009.<sup>3,6</sup> This illustrates that both building blocks, heptazines and triazines, are suitable photoactive components which opens up more possibilities for the design of efficient photocatalysts.



Furthermore, PTI/LiCl is the first crystalline system that has been shown to be photocatalytically active. Its 2D character and high crystallinity makes PTI/LiCl an interesting material for further photocatalysis research since a minimum of defects simplifies the investigation of the structure-property relationships and the factors influencing the photocatalytic activity. In this regard, HCl-treated PTI/LiCl, which is presented in Chapter 3.3 and that demonstrates an even higher degree of order, would be an even better candidate for detailed research. In the case of melon, *Merschjann and colleagues*<sup>8</sup> have shown that light illumination leads to the formation of singlet excitons which are highly confined to the heptazine units and which are transported along the stacking direction. It would be interesting to investigate whether PTI follows the same charge transfer mechanism and whether the triazines differ from the heptazines towards charge carrier dynamics. In this regard, time-resolved photoluminescence and scanning tunneling microscopy (STM) measurements on highly crystalline PTI samples would give further insights on the carrier distribution in the framework and the time-scale at which the processes occur.

Chapter 3.1 shows that the photocatalytic activity of PTI/LiCl is largely dependent on the applied synthesis conditions. Similar to melon, some amorphous PTI samples are demonstrated here to be even more active than their crystalline versions.<sup>6</sup> In classical catalysis, imperfections in the crystal structures are causing charge recombination. In contrast, irregularities of the carbon nitride scaffold can be even beneficial for photocatalysis depending on the nature of “defects”. In order to optimize the organic photocatalysts, it is important to figure out what kind of defects are beneficial and which are detrimental. We show that the defects in the form of point defects through the insertion of heteroatoms (Chapter 2.1.4) or additional carbon and oxygen atoms (Chapter 3.1) result in carbon nitrides with higher photocatalytic activity. This can be rationalized by the adjustment of the band potentials of carbon nitrides with regards to the potentials for the water splitting reaction. Furthermore, the band gap of a photocatalyst directly influences its light harvesting properties and hence, its photocatalytic activity. This point is illustrated in Chapter 3.1 for PTI/LiCl. Here, we demonstrate that co-polymerization of PTI with several pyrimidine-based molecules lead to a five to six-fold higher photocatalytic activity compared to non-doped PTI which could be attributed to band gap engineering.<sup>6</sup>

Defects in organic polymers can also arise due to incomplete polymerization reactions. Recent findings of *Lau and colleagues*<sup>9</sup> and the ones discussed in Chapter 4.2 on covalent triazine frameworks (CTFs)<sup>10</sup> point out that organic polymers with a lower degree of polymerization are significantly more active towards water reduction than the ones which are more highly polymerized. The degree of polymerization has an influence on the type and number of residual terminal sites which in turn have an effect on the dispersibility of the photocatalyst and, moreover, the adhesion of the co-catalyst and sacrificial agents on the photocatalyst's surface. Since it has been discussed that carbon nitrides mostly suffer from low charge carrier dynamics,<sup>11</sup> the attachment of the reactants on the photocatalyst's surface seems to be a key aspect. This also includes the adhesion of water itself. In Chapter



3.2, we demonstrate that the 2D material PTI/LiCl can be exfoliated in 1 nm – 2 nm high PTI crystallites which are two orders of magnitude more active than bulk PTI/LiCl.<sup>12</sup> This could be attributed to a) an improved access to the active centers due to an increased surface area and b) to a stronger interaction of the protons of PTI with the ones of water. The improved adhesion of the water molecules on the platinum-decorated PTI surface supports a quicker charge transfer of the excited electrons from the photocatalyst to the platinum surface where the actual proton reduction takes place. *Lau and colleagues*<sup>13</sup> demonstrated that terminations such as –NH–ethyl, –N–C≡N, –urea, –COOH and –OH/K groups, which can coordinate well with the co-catalyst (in this case platinum), result in photocatalytically active carbon nitrides, whereas terminal sites which cause steric repulsion (e.g. –phthalimide, –toluene and –N(–ethyl)<sub>2</sub>) lead to inactivity. However, further investigation on the role of the terminal sites and their interaction with the co-catalyst are still required and should be tackled in the future.

The rapidly increasing number of published papers over the past years (see Figure 6.1) supports our beliefs that the photocatalytic activity of carbon nitrides is not yet exhausted. Highly active carbon nitrides can be synthesized by following the compiled experiences from former researchers which are summarized in Chapter 2.1.4.

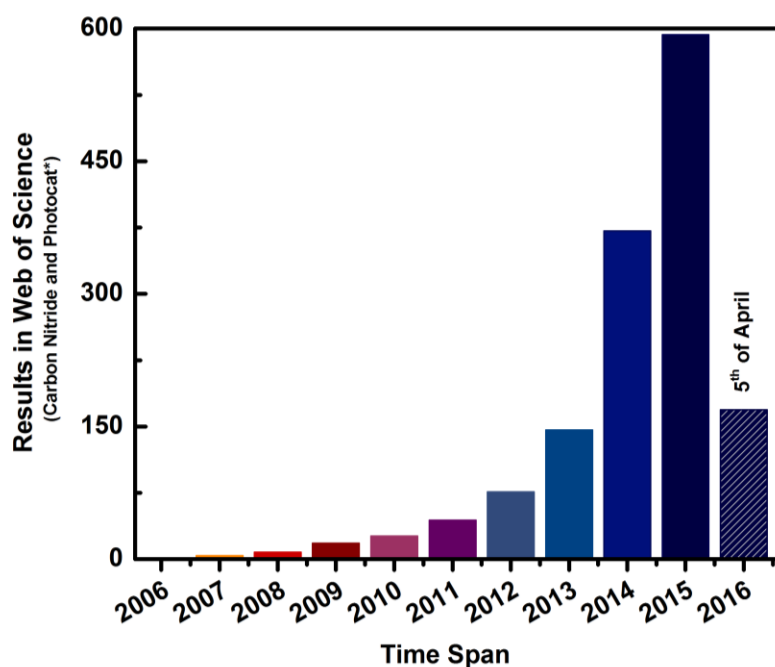


**Figure 6.1** Number of results for the combined terms “carbon nitride” and “photocat\*” in Web of Science™ Database for several time spans.

The photoactive components of carbon nitrides are their electron-deficient and fairly electron-delocalized triazine and heptazine cores which are assumed to benefit charge stabilization. The stacking of these ring systems leads to overlapping  $\pi$ -orbitals which allow energy transfer along the stacking direction.<sup>8</sup> These key criteria can be found also in other 2D organic systems. In Chapter 4, we show that two of those systems from the category of covalent organic frameworks (COFs) are indeed photocatalytically active towards

water reduction. In detail, we present a water-stable hydrazone-based 1,3,5-*tris*-(4-formylphenyl)triazine (TFPT)-COF<sup>14</sup> (Chapter 4.1) and phenyl-triazine-oligomers (PTOs) derived from the archetypal CTF-1 (Chapter 4.2).<sup>10</sup> Their hydrogen evolution rates rival the ones of the common carbon nitrides. Since their efficiencies are still far from industrial targets, our results can be considered as initial steps and pave the way towards the application of organic photocatalysts in large-scale hydrogen generation. While carbon nitrides are restricted to be composed either of heptazine or triazines, COFs offer a platform of possible subunits with varying properties which can be assembled into frameworks with interesting optoelectronic properties. Important attributes for photocatalysis such as strong light harvesting properties, charge stabilization, rapid charge carrier dynamics and the combination of water oxidation and reduction centers can be coupled here. More importantly, the COF skeleton exhibits great opportunities for post-synthetic modification, for instance co-catalyst coupling.<sup>15</sup> In addition, some of these COFs, when porous, are theoretically capable of storing the evolved gases which remedies the problem of hydrogen storage or gas separation. The pores can be further used as templates for the incorporation and homogenous distribution of co-catalysts.<sup>16,17</sup>

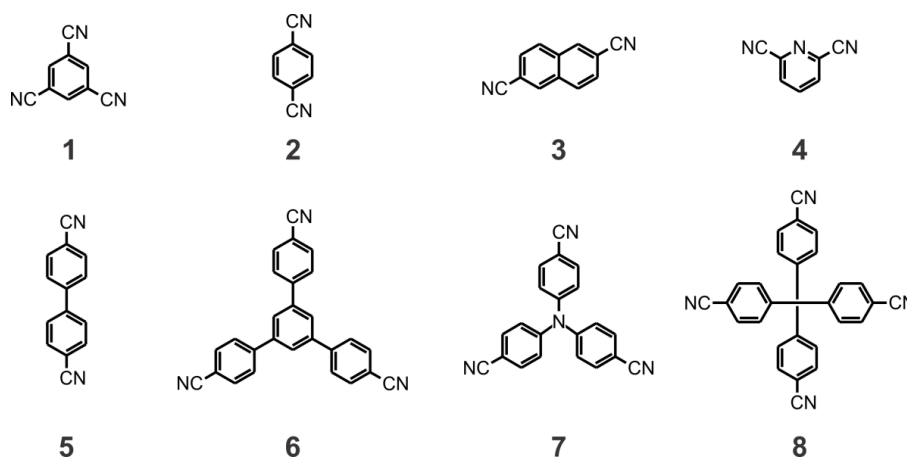


**Figure 6.2** The illustrated molecules can be trimerized to triazine-based oligomers or CTFs with interesting absorption properties for photocatalysis: 1,3,5-tricyanobenzene (CTF-0) (1), 1,4-dicyanobenzene (CTF-1) (2), 2,6-dicyanonaphthalene (CTF-2) (3), 2,6-dicyanopyridine (4), 4,4'-dicyanobiphenyl (5), 1,3,5-*tris*(4-cyanophenyl)benzene (6), *tris*-(4-cyanophenyl)amine (7) and tetrakis(4-cyanophenyl)methane (8).

A plethora of other COFs might be photocatalytically active. For instance, *Zhao and co-workers*<sup>18</sup> theorized CTF-0<sup>19</sup> (derived from 1; see Figure 6.2) and CTF-2<sup>20</sup> (derived from 3) to be potential photocatalysts due to their suitable band potentials. CTFs derived from 3<sup>21</sup> and 4–8<sup>22</sup> demonstrate interesting absorption properties and should be tested in the future. In analogy to the presented CTF-1 (derived from 2) oligomers (Chapter 4.2), oligomers of 2D heptazine-based frameworks (*e.g.* HBF-1, HBF-2 and HBF-3; Figure 6.3) might be interesting to explore for their photocatalytic activity. Similar to CTF-1, the published HBFs<sup>23</sup> have been synthesized at high temperatures which most likely induces a degradation of the framework and is currently the reason for the dark colors of the products.

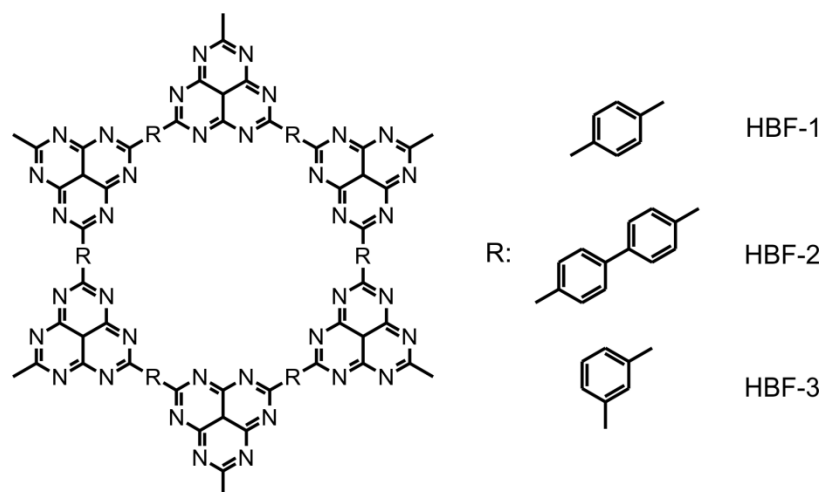


**Figure 6.3** Heptazine-based frameworks with three different aromatic spacers (R) resulting in HBF-1, HBF-2 and HBF-3.

Next to the photocatalytic water reduction, the organic photocatalysts mentioned above might be able to catalyze other important processes such as the conversion of the greenhouse gas carbon dioxide into valuable hydrocarbon products.<sup>24,25</sup> However, the reduction from CO<sub>2</sub> to useful fuels represents a major challenge even with inorganic photocatalysts since transfer of multiple electrons and protons are required. The formation of methane and methanol is thermodynamically favorable but kinetic hindrance leads to the formation of mostly carbon monoxide, formaldehyde and formic acid.<sup>26</sup> Moreover, CO<sub>2</sub> reduction competes with the reduction of water resulting in the evolution of hydrogen. Hence, great scepticism<sup>27</sup> arose (mostly due to missing isotope labelling experiments) when *Mao et al.*<sup>28</sup> claimed that non-modified urea-melon can photocatalytically convert CO<sub>2</sub> to methanol and ethanol (AQE = 0.18%) without the addition of a noble metal cocatalyst. We have high hopes that by terminal site engineering organic polymers can be applied for CO<sub>2</sub> reduction in the future.

Looking forward, organic polymers are well placed to provide multifaceted solutions for the environmental challenges we face, which can be accomplished by the reduction of anthropogenic CO<sub>2</sub> and the replacement of fossil fuels with photogenerated hydrogen.

## Bibliography

- (1) S. Yanagida, A. Kabumoto, K. Mizumoto, C. Pac, K. Yoshino, *J. Chem. Soc., Chem. Commun.* **1985**, 474.
- (2) S. Matsuoka, T. Kohzuki, Y. Kuwana, A. Nakamura, S. Yanagida, *J. Chem. Soc. Perkin Trans.* **1992**, 2, 679.
- (3) X. Wang, K. Maeda, A. Thomas, K. Takanabe, G. Xin, J. M. Carlsson, K. Domen, M. Antonietti, *Nat. Mater.* **2009**, 8, 76.
- (4) E. Wirnhier, M. Döblinger, D. Gunzelmann, J. Senker, B. V. Lotsch, W. Schnick, *Chem. Eur. J.* **2011**, 17, 3213.
- (5) M. J. Bojdys, J.-O. Müller, M. Antonietti, A. Thomas, *Chem. Eur. J.* **2008**, 14, 8177.

- (6) K. Schwinghammer, B. Tuffy, M. B. Mesch, E. Wirnhier, C. Martineau, F. Taulelle, W. Schnick, J. Senker, B. V. Lotsch, *Angew. Chem. Int. Ed.* **2013**, *52*, 2435.
- (7) Y. Ham, K. Maeda, D. Cha, K. Takanabe, K. Domen, *Chem. Asian J.* **2013**, *8*, 218.
- (8) C. Merschjann, T. Tyborski, S. Orthmann, F. Yang, K. Schwarzburg, M. Lublow, M. C. Lux-Steiner, T. Schedel-Niedrig, *Phys. Rev. B* **2013**, *87*, 205204.
- (9) V. W.-h. Lau, M. B. Mesch, V. Duppel, V. Blum, J. Senker, B. V. Lotsch, *J. Am. Chem. Soc.* **2015**, *137*, 1064.
- (10) K. Schwinghammer, S. Hug, M. B. Mesch, J. Senker, B. V. Lotsch, *Energy Environ. Sci.* **2015**, *8*, 3345.
- (11) M. N. Huda, J. A. Turner, *J. Appl. Phys.* **2010**, *107*, 123703.
- (12) K. Schwinghammer, M. B. Mesch, V. Duppel, C. Ziegler, J. Senker, B. V. Lotsch, *J. Am. Chem. Soc.* **2014**, *136*, 1730.
- (13) V. W. Lau, I. Moudrakovski, T. Botari, S. Weinburger, M. B. Mesch, V. Duppel, J. Senker, V. Blum, B. V. Lotsch, **2015**, submitted.
- (14) L. Stegbauer, K. Schwinghammer, B. V. Lotsch, *Chem. Sci.* **2014**, *5*, 2789.
- (15) K. Sakaushi, M. Antonietti, *Acc. Chem. Res.* **2015**, *48*, 1591.
- (16) X. Chen, F. Yuan, Q. Gu, X. Yu, *J. Mater. Chem. A* **2013**, *1*, 11705.
- (17) P. Pachfule, M. K. Panda, S. Kandambeth, S. M. Shivaprasad, D. D. Diaz, R. Banerjee, *J. Mater. Chem. A* **2014**, *2*, 7944.
- (18) X. Jiang, P. Wang, J. Zhao, *J. Mater. Chem. A* **2015**, *3*, 7750.
- (19) P. Katekomol, J. Roeser, M. Bojdys, J. Weber, A. Thomas, *Chem. Mater.* **2013**, *25*, 1542.
- (20) M. J. Bojdys, J. Jeromenok, A. Thomas, M. Antonietti, *Adv. Mater.* **2010**, *22*, 2202.
- (21) R. Palkovits, M. Antonietti, P. Kuhn, A. Thomas, F. Schüth, *Angew. Chem. Int. Ed.* **2009**, *48*, 6909.
- (22) S. Ren, M. J. Bojdys, R. Dawson, A. Laybourn, Y. Z. Khimyak, D. J. Adams, A. I. Cooper, *Adv. Mater.* **2012**, *24*, 2357.
- (23) M. J. Bojdys, S. A. Wohlgemuth, A. Thomas, M. Antonietti, *Macromolecules* **2010**, *43*, 6639.
- (24) J. Graham, N. Hammer, *Handbook of Climate Change Mitigation*, Chen, W.-Y., Seiner, J., Suzuki, T., Lackner, M., Eds.; Springer US: **2012**, 1755.
- (25) J. Mao, K. Li, T. Peng, *Catal. Sci. Technol.* **2013**, *3*, 2481.
- (26) K. Li, X. An, K. H. Park, M. Khraisheh, J. Tang, *Catal. Today* **2014**, *224*, 3.
- (27) K. Maeda, K. Sekizawa, O. Ishitani, *Chem. Commun.* **2013**, *49*, 10127.
- (28) J. Mao, T. Peng, X. Zhang, K. Li, L. Ye, L. Zan, *Catal. Sci. Technol.* **2013**, *3*, 1253.

# Chapter VII

## 7 Appendix

### 7.1 Supporting information

#### 7.1.1 Supporting information of Chapter 3.1

##### **Experimental section**

##### *Photocatalysis*

1 mg mL<sup>-1</sup> aqueous suspension of carbon nitride catalyst were prepared and dispersed with an ultrasonic bath for 30 min. Triethanolamine (TEoA) was used as a sacrificial electron donor and H<sub>2</sub>PtCl<sub>6</sub> (8 wt% in H<sub>2</sub>O) was used as the Pt co-catalyst precursor which was photo-reduced during the reaction. Suspensions with 10 vol% TEoA and 6 μL H<sub>2</sub>PtCl<sub>6</sub> (2.3 wt% Pt) were illuminated in 24 mL glass vials in an argon atmosphere with PTFE/Teflon septa. Samples were side-illuminated with a 300 W Xenon lamp with a water filter and dichroic mirror blocking wavelengths < 420 nm. The evolved gas was measured by gas chromatography with an online injection system and using a thermal conductivity detector with argon as carrier gas.

##### *Syntheses*

Crystalline PTI/LiCl according to *Wirnhier et al.*<sup>S1,S2</sup> Dicyandiamide (0.20 g, 2.38 mmol) and a eutectic mixture of lithium chloride (59.2 mol%, 0.90 g, 21.33 mmol) and potassium chloride (40.8 mol%, 1.01 g, 14.70 mmol) were ground together in a glovebox. The reaction mixture was transferred into a dried thick-walled silica glass tube (ø<sub>ext.</sub> 15 mm, ø<sub>int.</sub> 11 mm). The tube was placed in a vertical tube furnace and heated under atmospheric argon pressure at 6 °C min<sup>-1</sup> to 400 °C. This temperature was held for 12 h and afterwards the sample was cooled to room temperature at 20 °C min<sup>-1</sup>. After this procedure, the tube was evacuated and sealed at a length of 120 mm. In a second step the ampule was placed in a vertical tube furnace and heated at 1 °C min<sup>-1</sup> to 600 °C at which the sample was held for 24 h. After cooling down to room temperature the ampule was broken and the sample was isolated and washed with boiling water to remove residual salt. The resulting material PTI/LiCl was obtained as a brown powder (80 mg, 50 %). Synthesis of amorphous PTI (aPTI) using a modified procedure reported by *Wirnhier et al.*<sup>S1,S2</sup> Dicyandiamide (1.00 g, 11.90 mmol) and a eutectic mixture of lithium chloride (59.2 mol%, 2.26 g, 53.56 mmol) and potassium chloride (40.8 mol%, 2.74 g, 39.88 mmol) were ground together in a glovebox. The reaction mixture was transferred in open porcelain crucibles which were heated either in an argon-purged tube or muffle furnace at 12 °C min<sup>-1</sup> to 400 °C – 600 °C. The temperature was held for 6 h and afterwards the samples were cooled down to room temperature. The samples were isolated and washed with boiling water to remove residual salts. The resulting materials yielded beige (0.70 g, 88 %) to yellow

colored powders (0.30 g, 38 %). Yields in percentage are based on crystalline PTI and can be considered as an approximate value. Synthesis of doped amorphous PTI using a modified procedure reported by *Wirnhier et al.*<sup>51,52</sup> Dicyandiamide (0.50 g, 5.95 mmol), a eutectic mixture of lithium chloride (59.2 mol%) and potassium chloride (40.8 mol%) and 4AP as doping agent (2, 8, 16, 32 or 64 %) were ground and transferred in open porcelain crucibles, which were heated in a muffle furnace at 12 °C min<sup>-1</sup> to 400 °C – 600 °C for 6 hours. The syntheses yielded yellow (0.30 g, 75 %) to dark orange colored products (0.16 g, 40 %). Yields in percentage are based on crystalline PTI and can be considered as an approximate value. Synthesis of raw melon according to *Sattler et al.*<sup>53</sup> A porcelain crucible was loaded with melamine (20 g) and covered with a porcelain lid. The crucible was placed in a muffle furnace and maintained at 490 °C for 4 days. The product was ground to a powder and homogenized after the first day. Synthesis of “g-C<sub>3</sub>N<sub>4</sub>” according to *Zhang et al.*<sup>54</sup> A porcelain crucible was loaded with dicyandiamide and heated in a muffle furnace at 600 °C for 4 hours. The synthesis yielded a yellow colored powder.

### Methods

X-ray powder diffraction experiments were carried out [for 20 min] on a Huber G670 diffractometer in Guinier geometry using Ge(111)-monochromatized Cu-K<sub>α1</sub>-radiation ( $\lambda = 1.54051 \text{ \AA}$ ). The specimen was ground in a mortar and evenly spread between two chemplexfoils (Breitlänger GmbH). FTIR spectra were recorded on a Perkin Elmer Spektrum BX II spectrometer with an attenuated total reflectance unit. The <sup>13</sup>C and <sup>15</sup>N MAS NMR spectra were recorded at ambient temperature on an Avance 500 solid-state NMR spectrometer (Bruker) with an external magnetic field of 11.7 T, operating at frequencies of 500.1 MHz, 125.7 MHz and 50.7 MHz for <sup>1</sup>H, <sup>13</sup>C and <sup>15</sup>N, respectively. The sample was contained in a 4 mm ZrO<sub>2</sub> rotor which was mounted in a standard double resonance MAS probe (Bruker). The <sup>13</sup>C and <sup>15</sup>N chemical shifts were referenced relative to TMS and nitromethane. The <sup>1</sup>H<sup>15</sup>N and <sup>1</sup>H<sup>13</sup>C cross-polarization (CP) MAS spectra were recorded at a spinning speed of 10 kHz using a ramped-amplitude (RAMP) CP pulse on <sup>1</sup>H, centered on the  $n = +1$  Hartmann-Hahn condition, with a nutation frequency  $\omega_{\text{nut}}$  of 55 kHz (<sup>15</sup>N) and 40 kHz (<sup>13</sup>C). During a contact time of 7 ms the <sup>1</sup>H RF field was linearly varied about 20 %. The <sup>15</sup>N cross polarization combined with polarization inversion (CPPI) NMR spectrum was recorded at a spinning frequency of 6 kHz using a contact time of 7 ms and an inversion time of 400  $\mu\text{s}$ . Constant amplitude CP pulses were applied on <sup>15</sup>N ( $\nu_{\text{nut}} = 55 \text{ kHz}$ ) and <sup>1</sup>H ( $\nu_{\text{nut}} = 50 \text{ kHz}$ ). In all <sup>15</sup>N NMR experiments, a flip-back (FB)<sup>55</sup> pulse was applied on <sup>1</sup>H after the acquisition of the FID, so that the recycle delay becomes less dependent of the <sup>1</sup>H T<sub>1</sub> relaxation time. <sup>1</sup>H continuous wave (CW) decoupling (*ca* 70 kHz RF field) was applied during the acquisition of the <sup>15</sup>N signal. The recycle delay was set to 1.5 s. About 47500 and 121000 transients were accumulated for the CP and CPPI experiments, respectively. Optical diffuse reflectance spectra were collected at room temperature with a UV–VIS diffuse reflectance spectrometer (Varian, Cary 500). Powders were prepared between two quartz discs at the edge of the integrating sphere with BaSO<sub>4</sub> as the optical standard. Absorption spectra were calculated from the reflectance data with the Kubelka-Munk function. HRTEM was performed with a Philips CM 30 ST microscope (LaB<sub>6</sub> cathode, 300 kV, CS = 1.15 mm). Images were recorded with a CCD camera (Gatan) and Digital Micrograph 3.6.1 (Gatan) was used as evaluation software. Chemical analyses (EDX) were performed with a Si/Li detector (Thermo Fisher, Noran System Seven). Nitrogen adsorption measurements were performed at 77 K with an Autosorb iQ instrument (Quantachrome Instruments, Boynton Beach, Florida, USA). Samples were outgassed in vacuum at 300 °C for 12 h. For BET calculations pressure ranges were chosen with the help of the BET Assistant in the ASiQwin software (version 2.0). In accordance

with the ISO recommendations multipoint BET tags equal or below the maximum in  $V \cdot (1 - p/p_0)^{-1}$  were chosen. The quantum efficiency was calculated according to  $AQE \% = (2 \times H)/P \times 100/1$ , where  $H$  = number of evolved  $H_2$  molecules and  $P$  = incident number of photons on the sample. The incident light was measured with a thermopile power meter with a constant efficiency response across the visible spectrum. The action spectrum was measured with 40 nm FWHM light filters (Thor labs) and with the same incident light and filter transmission efficiency for each filter. Elemental analysis of the elements C, H, N and S is accomplished by high temperature digestion coupled with dynamic gas components separation. The samples are burned explosively at 1150 °C in a highly oxygenated helium atmosphere. The combustion products are  $CO_2$ ,  $H_2O$ ,  $H_2$ ,  $NO$ ,  $NO_2$ ,  $SO_2$  and  $SO_3$ . The detection of the gases is done by a thermal conductivity measurement cell. The accuracy is 0.30 %. Measurements were done on an Elementar vario EL. The determination of oxygen was done under inert conditions at high temperature (1200 °C – 1400 °C).

### Figures and tables

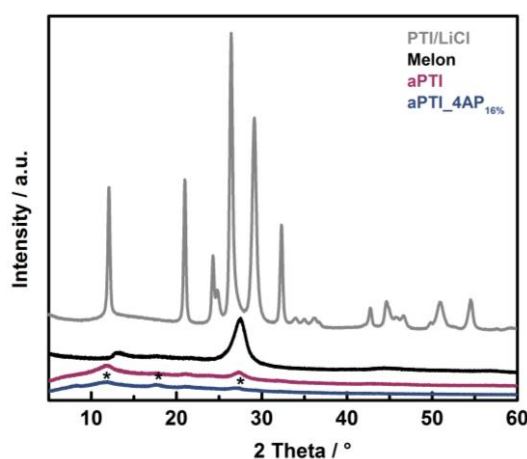


**Figure S1** PXRD patterns of aPTI-4AP<sub>16%</sub> synthesized at 550 °C, compared to crystalline PTI/LiCl, aPTI<sub>500 °C</sub> and melon. The reflections marked with an asterisk are assigned to artifacts caused by the plastic sample holder.

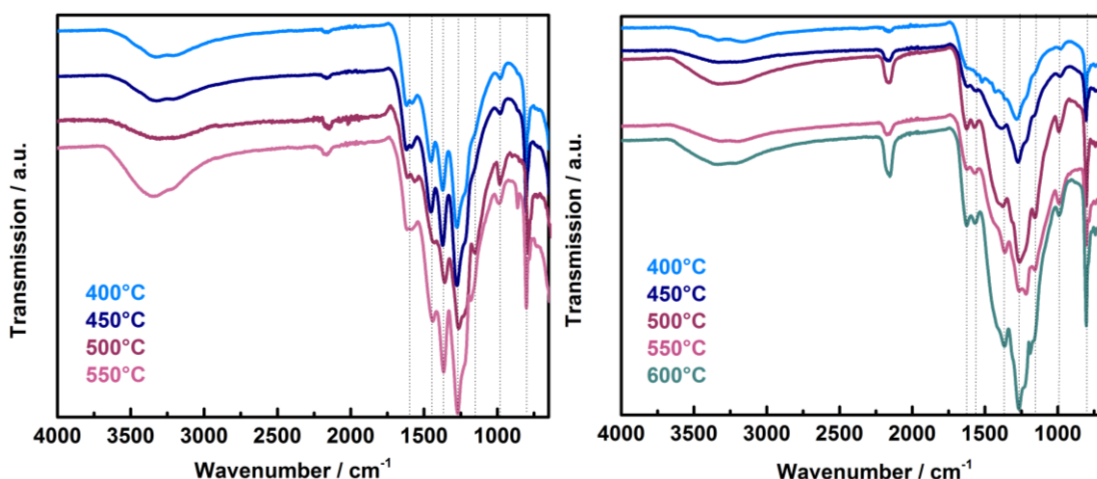


**Figure S2** FTIR spectra of aPTI synthesized at 400 °C – 600 °C in air (left) and inert atmosphere (right).

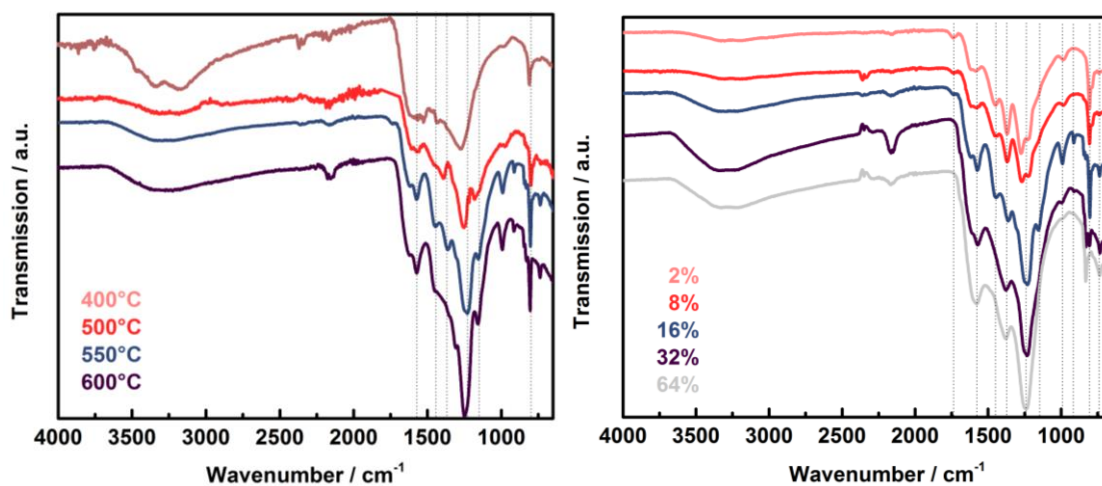


**Figure S3** FTIR spectra of aPTI-4AP<sub>16%</sub> synthesized at 400 °C – 600 °C (left) and aPTI-4AP<sub>2-64%</sub> synthesized at 550 °C (right).

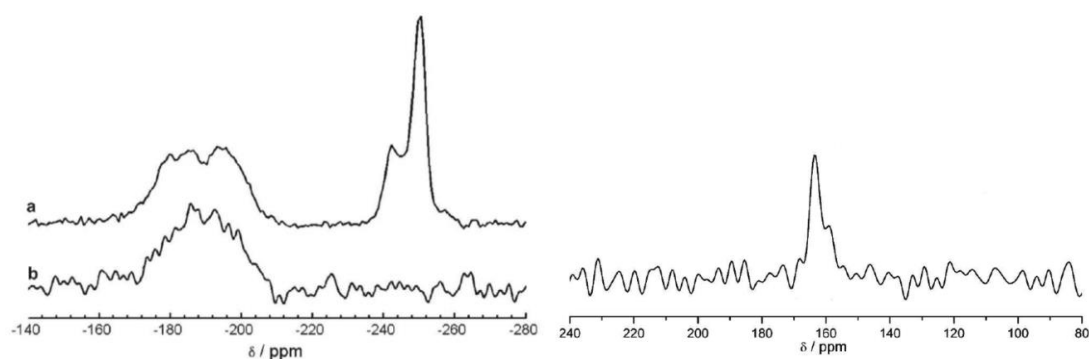


**Figure S4** <sup>15</sup>N CP-MAS NMR spectrum (a) of PTI/LiCl and a <sup>15</sup>N CPPI experiment (b) with attenuation of NH<sub>x</sub> signals (left). <sup>13</sup>C CP-MAS NMR spectra recorded with 0.5 ms contact time (right).

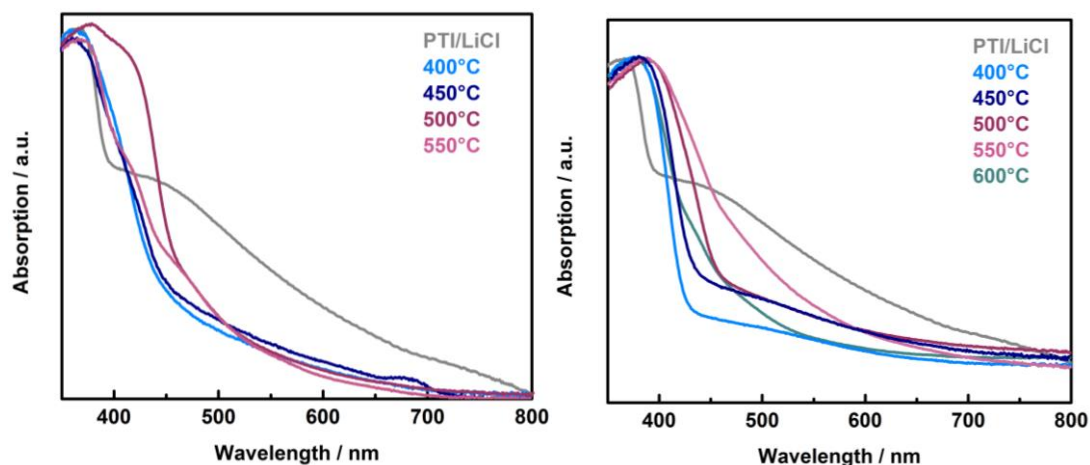


**Figure S5** UV-Vis absorption spectra of aPTI synthesized at 400 °C – 600 °C in air (left) and inert atmosphere (right) compared to crystalline of PTI/LiCl detected in diffuse reflectance mode.



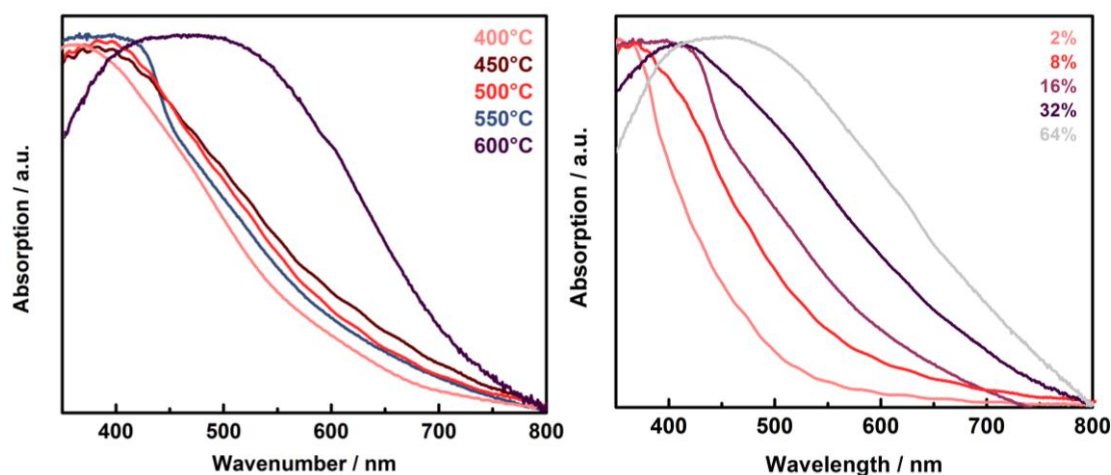


**Figure S6** UV-Vis absorption spectra of aPTI-4AP<sub>2-64%</sub> synthesized at 550 °C (left) and of aPTI-4AP<sub>16%</sub> synthesized at 400 °C – 600 °C (right) detected in diffuse reflectance mode.

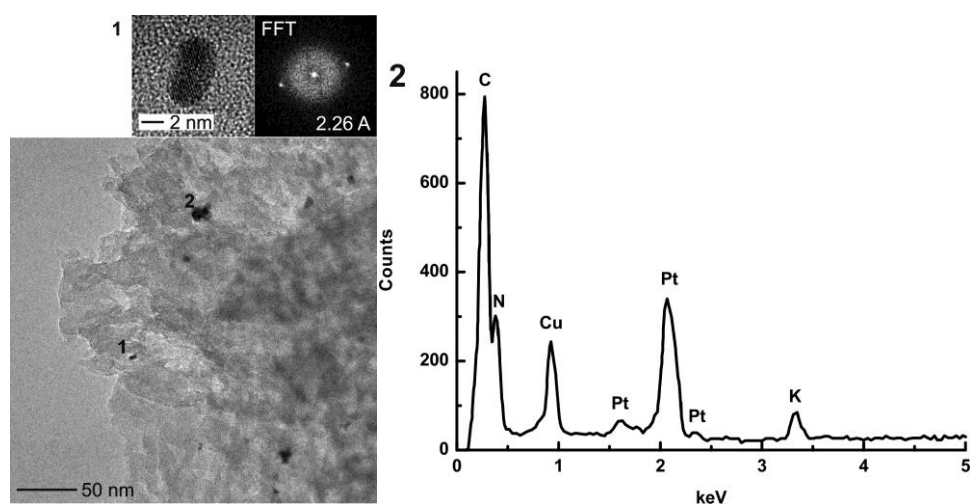


**Figure S7** A typical image of 2.3 wt% Pt-loaded aPTI-4AP after illumination for 3 h under visible light ( $\lambda \geq 420$  nm), at higher magnification (top left) and its corresponding FFT (top right) (1). The lattice planes correspond to elemental platinum. The EDX spectrum of sample location 2 is shown in (2).

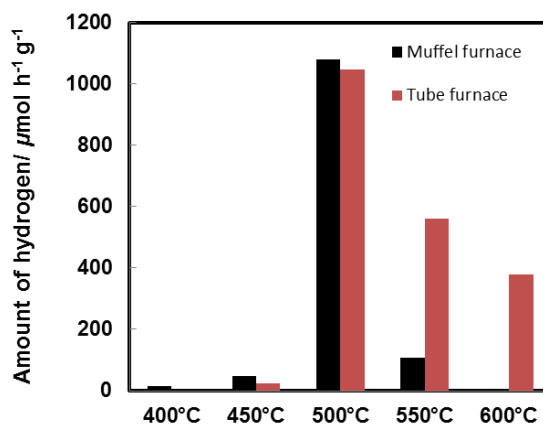


**Figure S8** Photocatalytic activity of aPTI synthesized at 400 °C – 600 °C in air (muffel furnace) and argon atmosphere (tube furnace). Synthesis of aPTI at elevated reaction temperatures (550 °C – 600 °C) under inert atmosphere resulted in better photocatalytic activity of CNs than in air. On the other hand, synthesis at lower temperatures (400 °C – 500 °C) in air resulted in marginally better photocatalytic activity compared to inert atmosphere conditions.

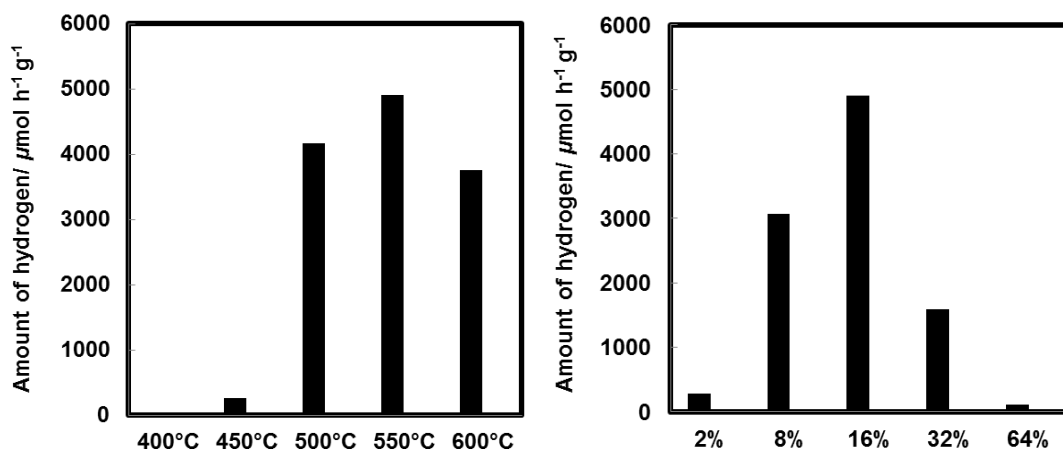


**Figure S9** Photocatalytic activity towards hydrogen production of aPTI-4AP<sub>16%</sub> synthesized at 400 °C – 600 °C (left) and of aPTI-4AP<sub>2-64%</sub> synthesized at 550 °C (right).

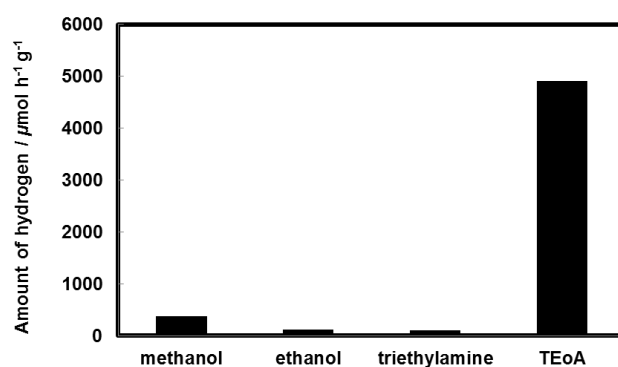


**Figure S10** Steady rate of hydrogen production from water containing various electron donors (methanol, ethanol, trimethylamine and triethanolamine TEoA; 10 vol%) under visible light ( $\lambda \geq 420$  nm) by 2.3 wt% Pt-loaded aPTI-4AP<sub>16%</sub>.

**Table S1** Elemental analysis of aPTI synthesized air or inert atmosphere (Ar) at 400 °C – 600 °C compared to PTI/LiCl and melon.

sample	atmosphere	temperature [°C]	C [wt%]	N [wt%]	H [wt%]	C/N/H	C/N
PTI/LiCl	Ar/vacuum	600	29.6	50.4	1.3	C <sub>3.0</sub> N <sub>4.4</sub> H <sub>1.6</sub>	0.68
melon	air	490	33.2	62.7	1.8	C <sub>3.0</sub> N <sub>4.9</sub> H <sub>1.9</sub>	0.62
aPTI <sub>400°C</sub>	air	400	26.9	46.6	2.8	C <sub>3.0</sub> N <sub>4.5</sub> H <sub>3.7</sub>	0.67
aPTI <sub>450°C</sub>	air	450	27.1	46.6	3.0	C <sub>3.0</sub> N <sub>4.4</sub> H <sub>4.0</sub>	0.68
aPTI <sub>500°C</sub>	air	500	24.7	41.9	2.5	C <sub>3.0</sub> N <sub>4.4</sub> H <sub>3.6</sub>	0.69
aPTI <sub>550°C</sub>	air	550	22.0	36.6	2.8	C <sub>3.0</sub> N <sub>4.3</sub> H <sub>4.6</sub>	0.70
aPTI <sub>400°C</sub>	Ar	400	27.9	50.8	3.2	C <sub>3.0</sub> N <sub>4.7</sub> H <sub>4.1</sub>	0.64
aPTI <sub>450°C</sub>	Ar	450	21.6	36.5	2.6	C <sub>3.0</sub> N <sub>4.3</sub> H <sub>4.3</sub>	0.69
aPTI <sub>500°C</sub>	Ar	500	25.9	43.8	2.4	C <sub>3.0</sub> N <sub>4.4</sub> H <sub>3.3</sub>	0.69
aPTI <sub>550°C</sub>	Ar	550	26.5	45.3	2.0	C <sub>3.0</sub> N <sub>4.4</sub> H <sub>2.7</sub>	0.68
aPTI <sub>600°C</sub>	Ar	600	26.8	45.4	2.1	C <sub>3.0</sub> N <sub>4.4</sub> H <sub>2.8</sub>	0.69

**Table S2** Elemental analysis of aPTI-4AP synthesized at 400 °C – 600 °C compared to PTI/LiCl and melon.

sample	temperature [°C]	4AP [%]	C [wt%]	N [wt%]	H [wt%]	C/N/H	C/N
PTI/LiCl	600	0	29.6	50.4	1.3	C <sub>3.0</sub> N <sub>4.4</sub> H <sub>1.6</sub>	0.68
melon	490	0	33.2	62.7	1.8	C <sub>3.0</sub> N <sub>4.9</sub> H <sub>1.9</sub>	0.62
aPTI-4AP <sub>16%</sub>	400	16	28.7	46.7	2.6	C <sub>3.0</sub> N <sub>4.2</sub> H <sub>3.2</sub>	0.72
aPTI-4AP <sub>16%</sub>	450	16	30.3	47.4	2.5	C <sub>3.0</sub> N <sub>4.0</sub> H <sub>3.0</sub>	0.74
aPTI-4AP <sub>16%</sub>	500	16	29.8	46.3	2.4	C <sub>3.0</sub> N <sub>4.0</sub> H <sub>2.9</sub>	0.75
aPTI-4AP <sub>16%</sub>	550	16	30.5	43.5	2.6	C <sub>3.0</sub> N <sub>3.7</sub> H <sub>3.1</sub>	0.82
aPTI-4AP <sub>16%</sub> *	550	16	30.1	42.2	2.9	C <sub>3.0</sub> N <sub>3.6</sub> H <sub>3.5</sub>	0.83
aPTI-4AP <sub>2%</sub>	550	2	29.2	49.0	2.4	C <sub>3.0</sub> N <sub>4.3</sub> H <sub>2.9</sub>	0.69
aPTI-4AP <sub>8%</sub>	550	8	29.8	48.3	2.3	C <sub>3.0</sub> N <sub>4.2</sub> H <sub>2.8</sub>	0.72
aPTI-4AP <sub>16%</sub>	550	16	30.5	43.5	2.6	C <sub>3.0</sub> N <sub>3.7</sub> H <sub>3.1</sub>	0.82
aPTI-4AP <sub>32%</sub>	550	32	28.2	35.9	2.7	C <sub>3.0</sub> N <sub>3.3</sub> H <sub>3.4</sub>	0.92
aPTI-4AP <sub>64%</sub>	550	64	35.5	36.8	2.6	C <sub>3.0</sub> N <sub>2.7</sub> H <sub>2.6</sub>	1.13

\* After illumination for 15 hours.

### Further co-polymerization reactions

#### Synthesis

Synthesis of doped amorphous PTI followed a modified procedure reported by *Wirnhier et al.*<sup>51,52</sup> First dicyandiamide (500.0 mg, 5.95 mmol) was mixed with the dopant: 72.0 mg 4AP (16%), 72.0 mg 2AP (16%), 70.9 mg TAP (16%), 72.5 mg BA (16%) or 95 mg melamine (16%). Then five times the weight of a eutectic mixture of lithium chloride (59.2 mol%) and potassium chloride (40.8 mol%) was added, excessively ground and transferred in a quartz glass vessel. This mixture was heated in an argon purged furnace at 12 °C min<sup>-1</sup> to 550 °C for 6 hours. After cooling down to room temperature (20 °C min<sup>-1</sup>) the samples were ground and reheated under the conditions described before to achieve a homogenous polycondensation. After cooling to ambient temperature, the samples were extensively washed (at least three times) with boiling water to remove the salt residues and then dried at 60 °C. The syntheses yielded orange colored products.

#### Doping calculations

The term “doping degree of 16 %” might be not obvious. Therefore, the calculation of the doping level is described as follows. Firstly, the carbon content is calculated for 500 mg of precursor (dicyandiamide) based on its molecular mass ( $M = 84.08 \text{ g mol}^{-1}$ ), which results in 142.9 mg or 28.6 % carbon content. This amount of DCDA-derived carbon (142.9 mg) corresponds to 84.0 % of the total carbon content within the reaction while, 16 % of the residual carbon derives from the dopant. This 16.0 % carbon content derived from the dopant yields a carbon mass of 27.2 mg. 4AP ( $M = 127.1 \text{ g mol}^{-1}$ ) has a carbon content of 378.0 mg or 37.8 %. Thus, 72.0 mg 4AP is needed to achieve 16.0 % carbon doping when 500.0 mg dicyandiamide is used. To simplify further experiments (see also L. Moser’s bachelor thesis)<sup>56</sup> these 16.0 % carbon doping is identical to 14.4 wt% 4AP doping just based on the initial weight of 500.0 mg dicyandiamide. Since 2AP has the same molar mass as 4AP, the calculations are identical. BA ( $M = 128.1 \text{ g mol}^{-1}$ ) has a total carbon content of 375.1 mg or 37.5 %. Thus, 72.5 mg BA is needed. TAP ( $M = 125.1 \text{ g mol}^{-1}$ ) has a total carbon content of 384.0 mg or 38.4 %. Thus, 70.9 mg TAP is needed. Melamine ( $M = 126.1 \text{ g mol}^{-1}$ ) has a total carbon content of 285.7 mg or 28.6 %. Thus, 95.2 mg melamine is needed.

*Photocatalysis*

1 mg mL<sup>-1</sup> aqueous solutions of carbon nitride catalyst were prepared and dispersed with an ultrasonic bath for 30 min. Triethanolamine (TEoA) was used as sacrificial electron donor and H<sub>2</sub>PtCl<sub>6</sub> (8 wt% in H<sub>2</sub>O) was used as the Pt co-catalyst precursor which was photo-reduced during the reaction. Suspensions with 10 vol% TEoA and 6 μL H<sub>2</sub>PtCl<sub>6</sub> (2.3 wt% Pt) were illuminated in 24 mL glass vials in an argon atmosphere with PTFE septa. Samples were side-illuminated with a 300 W Xenon lamp with a water filter and dichroic mirror blocking wavelengths < 420 nm. The evolved gases were measured by gas chromatography with an online injection system and using a thermal conductivity detector with argon as carrier gas.

**Bibliography**

(S1) E. Wirnhier, M. Döblinger, D. Gunzelmann, J. Senker, B. V. Lotsch, W. Schnick, *Chem. Eur. J.* **2011**, *17*, 3213.

(S2) M. J. Bojdys, J.-O. Müller, M. Antonietti, A. Thomas, *Chem. Eur. J.* **2008**, *14*, 8177.

(S3) A. Sattler, *PhD thesis*, University of Munich, **2010**.

(S4) J. Zhang, X. Chen, K. Takanebe, K. Maeda, K. Domen, J. D. Epping, X. Fu, M. Antonietti, X. Wang, *Angew. Chem. Int. Ed.* **2010**, *49*, 441.

(S5) (a) J. Tegenfeldt, U. Haerberlen, *J. Magn. Reson.* **1979**, *36*, 453-57; (b) K. Saito, C. Martineau, G. Fink, F. Taulelle, *SolidState Nucl. Mag.* **2011**, *40*, 66.

(S6) L. Moser, *Bachelor thesis*, University of Munich, **2015**.

(S6) B. Tuffy, *PhD thesis*, University of Munich, **2016**.

## 7.1.2 Supporting information of Chapter 3.2

### Experimental section

#### *Syntheses*

Crystalline PTI/LiCl according to *Wirnhier et al.*<sup>51</sup> Dicyandiamide (0.20 g, 2.38 mmol, Acros) and a eutectic mixture of lithium chloride (59.2 mol%, 0.90 g, 21.33 mmol, Roth) and potassium chloride (40.8 mol%, 1.01 g, 14.70 mmol, Roth) were ground together in a glovebox. The reaction mixture was transferred into a dried thick-walled silica glass tube ( $\varnothing_{\text{ext.}}$  13 mm,  $\varnothing_{\text{int.}}$  10 mm). The tube was placed in a horizontal tube furnace and heated under atmospheric argon pressure at  $6\text{ }^{\circ}\text{C min}^{-1}$  to  $400\text{ }^{\circ}\text{C}$ . This temperature was held for 12 h and afterwards the sample was cooled to room temperature at  $20\text{ }^{\circ}\text{C min}^{-1}$ . After this procedure, the tube was evacuated and sealed at a length of 120 mm. In a second step the ampule was placed in a vertical tube furnace and heated at  $1\text{ }^{\circ}\text{C min}^{-1}$  to  $600\text{ }^{\circ}\text{C}$  at which the sample was held for 24 h. After cooling down to room temperature the ampule was opened and the sample was isolated and washed with boiling water to remove residual salt. The resulting material PTI/LiCl was obtained as a brown powder (80 mg, 50 %).  $^{15}\text{N}$ -enriched PTI was synthesized according to the procedure described above using  $^{15}\text{N}$ -enriched dicyandiamide (Sigma-Aldrich). Synthesis of a PTI nanosheet suspension. 40 mg of bulk PTI/LiCl were dispersed in 20 mL of water. The ice-cooled suspension was sonicated for 15 h in an ultrasonic bath with an amplitude of 30 %. The final suspension was centrifuged first at 3000 rpm and then at 5000 rpm to obtain the brown-colored PTI nanosheet suspension with a concentration of  $\sim 0.2\text{ mg mL}^{-1}$ . DLS measurements, which theoretically give an idea about the hydrodynamic diameter of a spherical particle, resulted in an equivalent spherical diameter of 123 nm (98 %). Non-exfoliated PTI shows a hydrodynamic diameter of 936 nm (100 %).

#### *Methods*

For sonication a Sonorex Digital DK 102 P of Bandelin with an ultrasonic frequency of 35 kHz and an ultrasonic power of 480 W was used. For centrifugation a bench top centrifuge Sigma 3–30K, with a maximum speed of 30000 rpm was used. The centrifugation speeds 3000 rpm, 5000 rpm and 25000 rpm correspond to 795 RCF, 2208 RCF and 55201 RCF, respectively. PXRD experiments were carried out with Cu- $K\alpha_1$ -radiation ( $\lambda = 1.54051\text{ \AA}$ ) on a Bruker D8 Advance diffractometer with a Ge(111)-monochromator and a Dectris Mythen detector. The specimen was ground in a mortar and evenly spread by dispersing it with ethanol on a silicon carrier. Le Bail fits were performed with the Fullprof software suite. Peak shapes were modeled with the Thompson-Cox-Hastings pseudo-Voigt profile convoluted with axial divergence asymmetry. Due to the 2D nature of the compounds it was necessary to additionally account for selective peak broadening of the (00l) reflections. FTIR spectra were recorded on a Perkin Elmer Spectrum Two spectrometer with an attenuated total reflectance unit. Optical diffuse reflectance spectra of the solids were collected at room temperature with a UV–Vis–NIR diffuse reflectance spectrometer (Agilent Technologies, Cary 5000) at a photometric range of 175 nm – 3300 nm. Powders were prepared in a sample carrier with a quartz glass window at the edge of the integrating sphere with  $\text{BaSO}_4$  as the optical standard. Kubelka–Munk spectra were calculated from the reflectance data. Atomic force microscopy (AFM) measurements were performed on a diluted suspension of nanosheets allowed to dry on a silicon substrate, using an Asylum MFP3D Stand Alone AFM (Asylum Research, Santa Barbara, CA) using a Si micro cantilever (300 Hz resonant frequency and  $26.1\text{ N m}^{-1}$  spring constant) operated in tapping mode. HRTEM was performed with a Philips CM 30 ST microscope (LaB<sub>6</sub> cathode, 300 kV, CS = 1.15 mm). Images were recorded with a CCD camera (Gatan) and

Digital Micrograph 3.6.1 (Gatan) was used as evaluation software. Chemical analyses (EDX) were performed with a Si/Li detector (Thermo Fisher, Noran System Seven). Elemental analysis of the elements C, H, N and S is accomplished by high temperature digestion coupled with dynamic gas components separation. The samples are burnt explosively at 1150 °C in a highly oxygenated helium atmosphere. The combustion products (CO<sub>2</sub>, H<sub>2</sub>O, H<sub>2</sub>, NO, NO<sub>2</sub>, etc) are detected by a thermal conductivity measurement cell. The accuracy is 0.30%. Measurements were done on an Elementar vario EL. The <sup>1</sup>H, <sup>13</sup>C and <sup>15</sup>N MAS–NMR spectra of <sup>15</sup>N-enriched Precipitate I–III were recorded at ambient temperature on an AvanceIII HD 600 solid-state NMR spectrometer (Bruker) with an external magnetic field of 14.1 T, operating at frequencies of 600.1 MHz, 150.9 MHz and 60.8 MHz for <sup>1</sup>H, <sup>13</sup>C and <sup>15</sup>N, respectively. Additionally, the MAS–NMR spectra of the <sup>15</sup>N-enriched bulk material were collected at ambient temperature on an Avance 300 solid-state NMR spectrometer (Bruker) with an external magnetic field of 7.0 T, operating at frequencies of 300.1 MHz, 75.5 MHz and 30.4 MHz for <sup>1</sup>H, <sup>13</sup>C and <sup>15</sup>N, respectively. The samples were contained either in 1.3 mm, 1.9 mm or 4 mm ZrO<sub>2</sub> rotors which were mounted in standard triple resonance MAS probes (Bruker). The spinning speed was set to 62.5 kHz (1.3 mm), 15 kHz (1.9 mm) and 10 kHz (4 mm), respectively. The <sup>1</sup>H spectra were recorded using one pulse and Hahn-echo experiments with a RF field of 125 and 83 kHz. The <sup>1</sup>H<sup>15</sup>N cross-polarization (CP) MAS spectra were collected using a conventional sequence and contact times between 8 and 10 ms. The <sup>1</sup>H<sup>13</sup>C cross-polarization (CP) MAS spectra were acquired with a ramped-amplitude (RAMP) CP sequence. During a contact time of 8 and 4 ms the <sup>1</sup>H RF field was linearly varied about 50 %. During acquisition proton decoupling was carried out using SPINAL64 between 60 kHz and 100 kHz. The recycle delay for all the spectra was set to 3 s and the spectra were referenced relative to TMS (<sup>1</sup>H, <sup>13</sup>C) and nitromethane (<sup>15</sup>N). <sup>1</sup>H<sup>1</sup>H 2D exchange experiments were conducted in a 1.3 mm ZrO<sub>2</sub> rotor on an Avance III HD 600 Bruker spectrometer using a NOESY-type three pulse experiment at a spinning speed of 62.5 kHz. Under these conditions the polarization takes place by proton-driven spin-diffusion. Spectra with mixing times of 10 ms and 200 ms were recorded. Dynamic Light Scattering measurements were performed with a Malvern Zetasizer Nano ZS with a maximum diameter size range of 0.3 nm to 10 μm and a molecular weight range of 342 Da to 2 × 10<sup>7</sup> Da. For the setting of the pH of the nanosheet suspension a Mettler Toledo Seven Compact Labor-pH-meter was used with a five point calibration system. Photocatalysis: For testing the photocatalytic activity of the precipitates compared to bulk PTI and sonicated PTI, 10 mg of the carbon nitride catalysts were dispersed in 9 mL water and sonicated for 30 min. In case of the PTI nanosheet suspensions, 9 mL of the nanosheet suspensions (containing 2.0, 1.8 and 3.6 mg of PTI nanosheets) were directly used and compared to 2 mg of bulk PTI dispersed in 9 mL of water, which was sonicated for 30 min. Triethanolamine (TEOA, 1 mL, Roth) was used as a sacrificial electron donor and H<sub>2</sub>PtCl<sub>6</sub> (8 wt% in H<sub>2</sub>O, Sigma-Aldrich) was used as the Pt co-catalyst precursor which was photo-reduced during the reaction (~ 2.2 wt% Pt). The suspensions were illuminated in 24 mL glass vials in an argon atmosphere with PTFE/Teflon septa. The vials were purged with argon to remove any dissolved gases in the suspension. Samples were side-illuminated for 3 h with a 300 W xenon lamp with a water filter and dichroic mirror blocking wavelengths < 420 nm while stirring. For stability measurements the 9 mL of the PTI nanosheet suspension was filled in a 230 mL quartz glass reactor with a PTFE/Teflon septum under argon atmosphere. A sacrificial electron donor (1 mL) of either triethanolamine or methanol and the H<sub>2</sub>PtCl<sub>6</sub> solution (~ 2.2 wt% Pt) was added. The flask was evacuated and purged with argon. The sample was simultaneously top-illuminated (top surface = 15.5 cm<sup>2</sup>) and cooled with a water jacket under the conditions described above. For wavelength-

specific measurements, the full spectrum of the xenon lamp coupled with a band-pass filter (400 nm, 450 nm, 500 nm, 550 nm or 600 nm; bandwidth  $\pm 20$  nm) was used. The headspace of the reactor was periodically sampled with an online injection system and the gas components were quantified by gas chromatography using a thermal conductivity detector with argon as carrier gas.

## Results and discussion

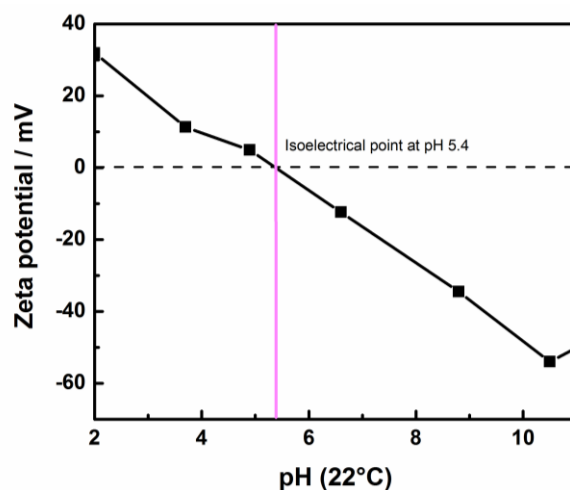


**Figure S11** pH-dependent zeta potential measurements of Supernatant 2. The isoelectric point (IP) is at pH 5.4. Below pH 5.4 the nanosheets are positively charged, above the IP the nanosheets are negatively charged.

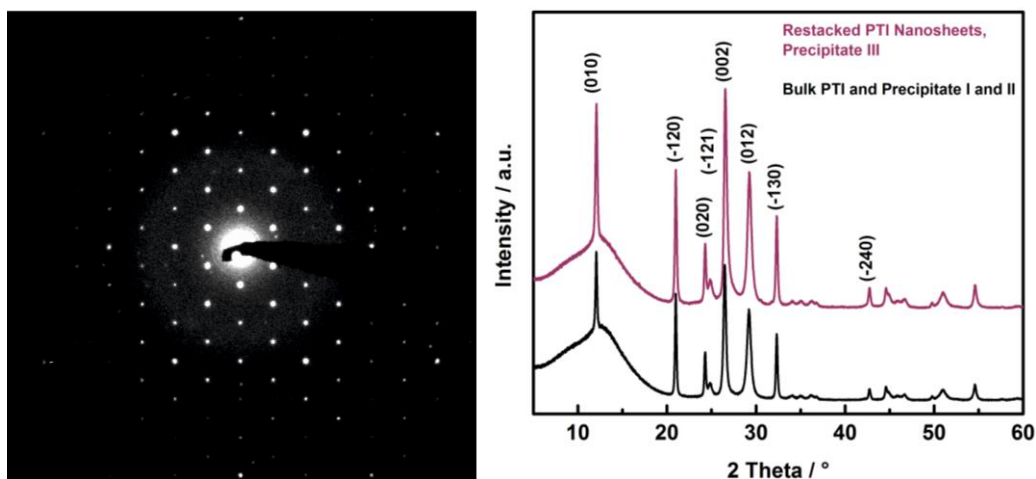


**Figure S12** Electron diffraction pattern along [001] of a PTI nanosheet (a), shown in Figure 3.9. The pattern is in agreement with the literature.<sup>51</sup> Powder X-ray diffraction patterns of bulk PTI compared to the restacked PTI nanosheets (Precipitate III, b). The broad amorphous halo around  $12^\circ 2\theta$  is caused by the sample carrier.

**Table S3** Elemental analysis of bulk PTI compared to the restacked PTI nanosheets (Precipitate III).

sample	C [wt%]	N [wt%]	H [wt%]	Li [wt%]
bulk PTI/LiCl	30.7	47.7	1.5	4.1
precipitate III	30.4	48.9	1.9	2.5

## XPS measurements

The high-resolution N 1s spectra of both bulk PTI and Precipitate III were deconvoluted into two Gaussian-Lorentzian peaks at binding energies of 398.2/398.2 eV (N1 for bulk/III) and 399.8/399.7 eV (N2 for bulk/III) (Figure S13(b)). For both materials, the dominant N1 is attributed to the  $sp^2$  N atoms of the triazine rings,<sup>S2,3</sup> while the smaller signal N2 is assigned to bridging N atoms in  $NH(C_3N_3)_2 / LiN(C_3N_3)_2$ .<sup>S2,4</sup> For bulk PTI and Precipitate III three different carbon atoms were found: 284.5/284.5 eV (C1), 286.2/285.9 eV (C2) and 287.7/287.6 eV (C3) (Figure S13(a)). C1 is assigned to adventitious carbon (especially graphitic C=C and grease),<sup>S2,4,5</sup> while C3 and C2 originate from  $sp^2$  C atoms bonded to N inside the triazine ring.<sup>S4,6</sup> The chemical environment of the chlorine atoms is unchanged for the exfoliated material (Figure S14): Both bulk and Precipitate III show one type of chlorine species (Cl1 at 197.7 eV ( $2p_{3/2}$ ) and Cl2 at 199.4 eV ( $2p_{1/2}$ )).

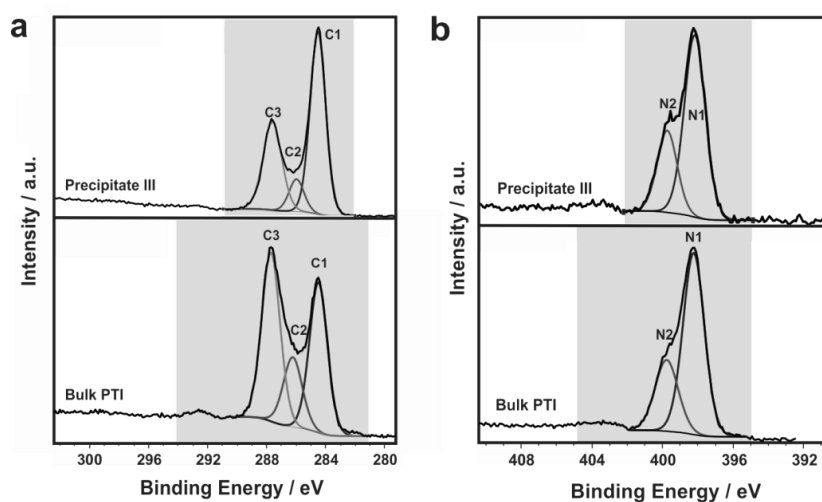


**Figure S13** XPS spectra of C 1s (a) and N 1s (b) of bulk PTI compared to the PTI nanosheets (Precipitate III).

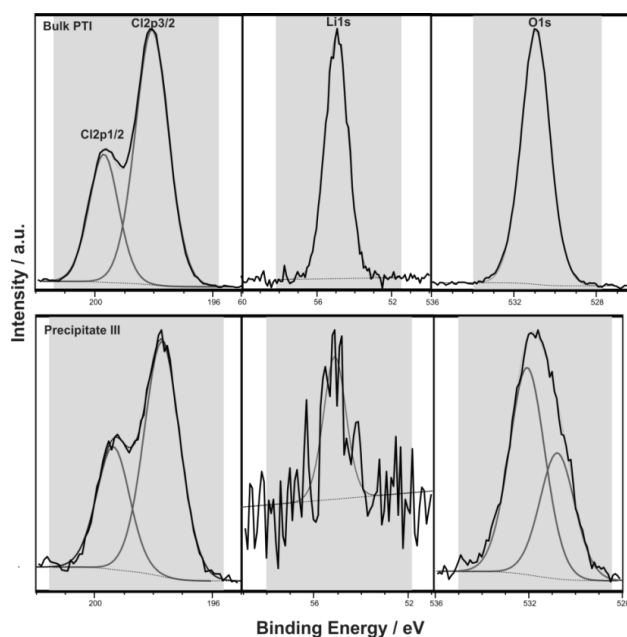


**Figure S14** XPS spectra of Cl 2p, Li 1s and O 1s of (top) bulk PTI compared to (bottom) PTI nanosheets (Precipitate III).



*Calculation of the water content*

Due to their negative zeta potential the PTI nanosheets or stacks of nanosheets carry a water shell in the suspension. Assuming that only the first hydration sphere is bonded strongly enough to be restacked together with the PTI nanosheets during the centrifugation process, the Precipitates I–III will consist of alternating PTI stacks separated by two monolayers of water. In this scenario the ratio of the PTI protons (signals at 8.9 ppm and 10.8 ppm of Figure S15) and the water protons (peaks at 4.6 ppm and 6.2 ppm of Figure S15) might be used to estimate the mean number of PTI layers sandwiched by a water shell. Since the surface density of a monolayer of water for a PTI surface is unknown, we extrapolate from results of DFT and MD calculations<sup>S7,8</sup> for different uncharged surfaces. The lowest surface water density was found on MgO (001) surfaces, where the area per water molecule amounts to 17.8 Å<sup>2</sup>.<sup>S7</sup> In contrast, on (100) silica surfaces, the highest surface density of 13.0 Å<sup>2</sup> was derived.<sup>S7</sup> For a PTI monolayer two protons occupy a unit cell with a surface area of 64.18 Å<sup>2</sup>. Taking into account a bottom and a top water monolayer for each PTI stack, the ratio of PTI protons ( $H_{\text{PTI}}$ ) to water protons ( $H_{\text{water}}$ ) was calculated as a function of the number of stacked PTI layers (Table S4).

**Table S4** Ratio between PTI protons ( $H_{\text{PTI}}$ ) and water protons ( $H_{\text{water}}$ ). Calculation based on the monolayer water density for MgO (column 1) and silica (column 2).

N° of PTI layers	$H_{\text{PTI}} : H_{\text{water(MgO)}}$	$H_{\text{PTI}} : H_{\text{water(silica)}}$
1	1 : 7.2	1 : 9.9
2	1 : 3.6	1 : 4.9
3	1 : 2.4	1 : 3.3
4	1 : 1.8	1 : 2.5
5	1 : 1.4	1 : 2.0

The deconvolution of a high-resolution <sup>1</sup>H MAS spectrum at ultrafast spinning (Figure S15, Figure S16 and Table S5) leads to  $H_{\text{PTI}} : H_{\text{water}} = 1:2.8$ . The two signals at 8.9 ppm and 10.8 ppm represent the typical resonances for the PTI protons and are independent of the water content (compare Figure and ref. 6). The resonances for the two peaks at 4.6 ppm and 6.2 ppm are typical for water, and they increase from Precipitate I to III and are in close vicinity to the PTI protons as proven by the <sup>1</sup>H<sup>1</sup>H spin-diffusion exchange spectra (Figure and Figure S16). We thus take both resonances as a measure for the relative amount of adsorbed water molecules. The residual signals at 1.0 ppm, 3.5 ppm and 3.9 ppm (Figure S15) do not exchange with the resonances for neither the PTI nor the water protons and are thus considered as small impurities. Within the limit of our model, for the lower water coverage of 17.8 Å<sup>2</sup> per H<sub>2</sub>O molecule the “nanosheet” consists, on average, of 2 to 3 PTI layers, whereas for the higher water surface density (13.0 Å<sup>2</sup> per H<sub>2</sub>O molecule) a mean value between 3 to 4 layers is derived. This amounts to a mean number of PTI layers  $N = 3(1)$ .

**Table S5** Relevant parameters for the deconvolution of the high-resolution  $^1\text{H}$  MAS spectrum for Precipitate III at ultrafast spinning ( $\nu_{\text{rot}} = 62.5$  kHz). The resonances were refined with pseudo-Voigt profiles.\*

$\delta_{\text{iso}}$ [ppm]	FWHH	G/L ratio <sup>a</sup>	intensity
1.0	2.0	0.4	0.16
3.5	0.5	0.0	0.12
3.9	0.5	0.5	0.14
4.6	0.23	0.0	5.1
6.2	2.0	0.9	0.63
8.9	2.1	0.7	1.0
10.8	2.0	0.6	1.0

\* With a value 0 the resonance is described by a Lorentzian. For the other limit 1 the peak is refined by a Gaussian profile.

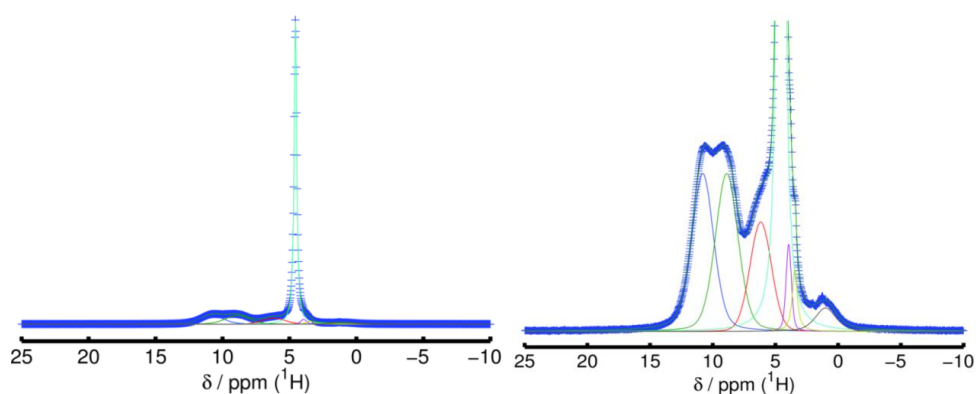


**Figure S15** High-resolution  $^1\text{H}$  MAS spectrum for Precipitate III at ultrafast spinning ( $\nu_{\text{rot}} = 62.5$  kHz), together with the deconvolution using pseudo-Voigt profiles (compare also Table S5).

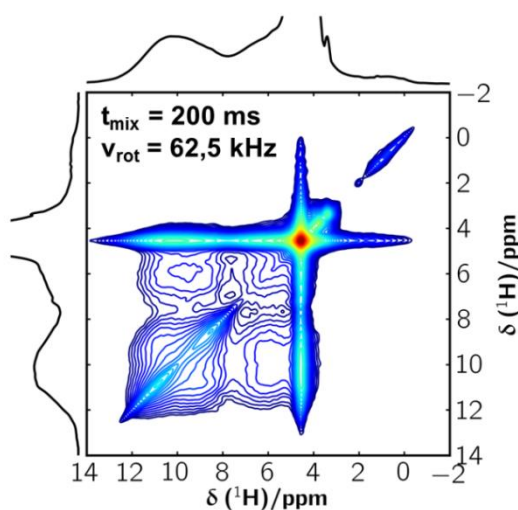


**Figure S16**  $^1\text{H}^1\text{H}$  proton driven spin diffusion spectrum for Precipitate III with a mixing time of 200 ms.

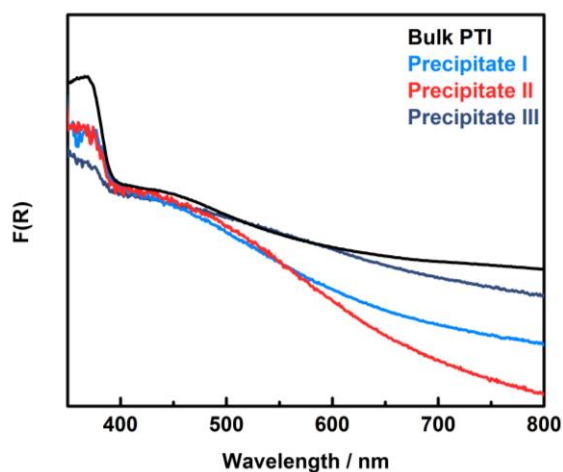


**Figure S17** UV-Vis F(R) spectrum of bulk PTI compared to the Precipitates I, II and III.

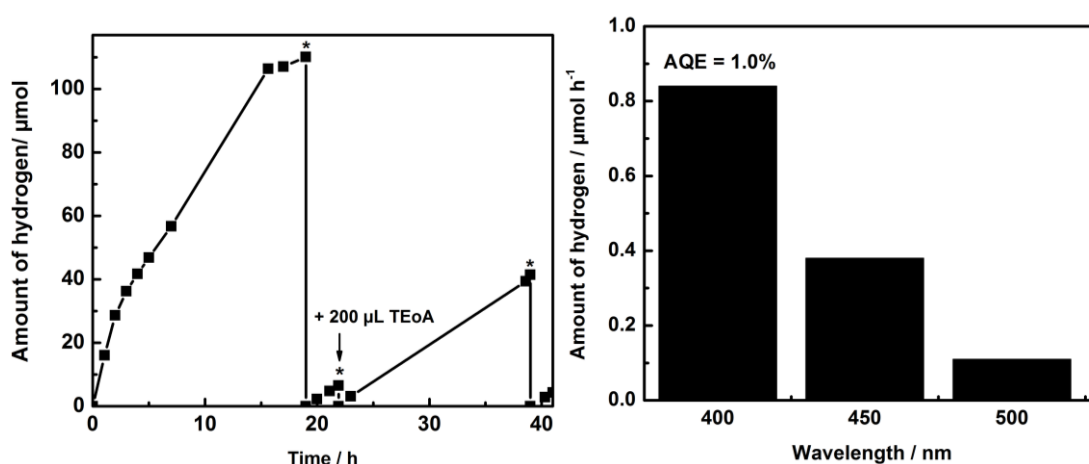


**Figure S18** Long-term measurements of the PTI nanosheets (Supernatant 2) with TEOA as electron donor. The reactor was purged in moments marked with an asterisk (left). Action spectrum of PTI nanosheets (Supernatant 2) using 40 nm FWHM band-pass filters in a 10 vol% TEOA/water solution (right).

### Control experiments

*Bulk PTI sonicated for 30 min.*

As a control experiment, bulk PTI was sonicated for 30 min in water ( $2.0 \text{ mg mL}^{-1}$ ) for dispersion and centrifuged at 5000 rpm (Supernatant,  $<0.1 \text{ mg mL}^{-1}$ ). Another reactor containing 30 min sonicated bulk PTI in water ( $1.0 \text{ mg mL}^{-1}$ ) was prepared and its photocatalytic activity was tested compared to the supernatant. The supernatant was characterized by TEM and AFM. Its concentration was very low and the suspension was only stable for several hours, in accordance with the low zeta potential of  $-24.4 \text{ mV}$  (measured at a pH of 7.2). There was no photocatalytic improvement of the supernatant compared to the 30 min sonicated, uncentrifuged bulk PTI with similar concentration. Characterization showed that bulk PTI was not sufficiently exfoliated within 30 min of sonication (Figure S19). The thickness of the obtained material was rather increased (TEM, AFM and DLS) compared to the dispersions sonicated for longer times (15 h) and the suspension contained agglomerates (320 nm in diameter for 87.4 % of the crystallites compared to 123 nm for 98 % of the

nanosheets of Supernatant 2). TEM measurements show that the shape of the crystallites of the suspension sonicated for 30 min are rather rounded, whereas longer sonication with separation steps apparently leads to smaller and less aggregated crystallites with an edged shape which were homogeneously dispersed on the TEM grid. The AFM image (Figure S19(c)) shows that sonication for 30 min yields essentially no exfoliated material. We find only one nanoparticle on a Si/SiO<sub>2</sub> wafer at a scan area of 5 × 5 μm for the PTI suspension (supernatant) sonicated for 30 min and centrifuged at 5000 rpm.

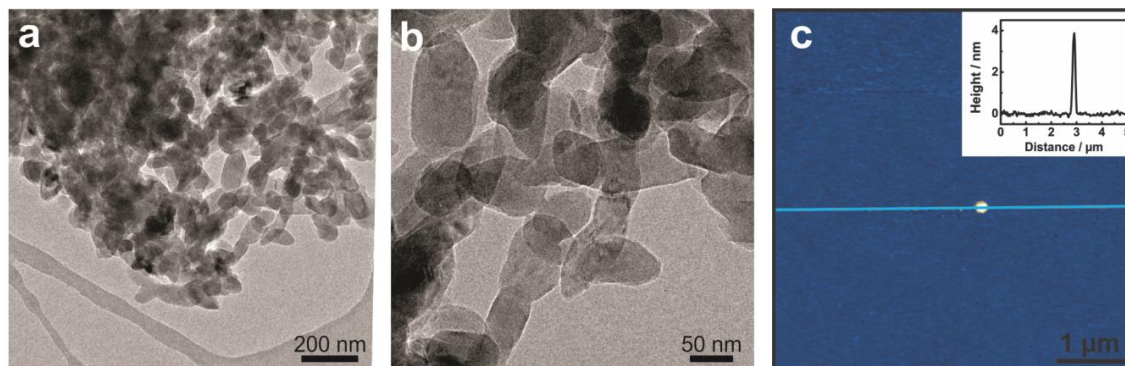


**Figure S19** TEM measurements of bulk PTI sonicated for 30 min (and centrifuged at 5000 rpm) demonstrate agglomerates (a) and enlarged crystallites (b). The AFM image shows one PTI particle (very low concentration) found on the Si/SiO<sub>2</sub> wafer on a scan area of 5 × 5 μm, after centrifuging the PTI suspension sonicated for 30 min (c).

#### *LiCl/LiOH activation*

Since we observed a loss in the lithium amount from bulk PTI (4.1 wt%) compared to Precipitate III (2.5 wt%), we tested the amount of lithium in Supernatant 3 to be about 10.7 mg L<sup>-1</sup> (0.096 mg in 9 mL; corresponding to 0.6 mg LiOH monohydrate or LiCl). To exclude any lithium hydroxide / lithium chloride “activation” of the PTI nanosheet suspension (Supernatant 2), we performed further control experiments. Three reactors of 10 mg bulk PTI containing additionally 0.6 mg, 1.0 mg or 3.0 mg of lithium hydroxide monohydrate and two reactors containing additionally 2.0 mg or 6.0 mg lithium chloride, respectively, were prepared and their photocatalytic activity (10 mL 10 vol% TEoA solution; 2.3 wt% Pt) was tested compared to pristine bulk PTI. We also compared Supernatant 2 to the same PTI nanosheet suspension which was washed several times with water toward their water reduction ability. The addition of lithium hydroxide leads to a decrease in photocatalytic activity, which may arise from an increase in pH (11.3 *vs* 10.5 for the pristine material). The addition of lithium chloride only leads to a decrease in activity when large amounts are used. Otherwise no difference is detected. The washed PTI nanosheet suspension (Supernatant 2 washed) shows a slightly decreased hydrogen evolution rate compared to the unwashed (LiOH added) suspension within the batch-to-batch error (~15 %), which might be due to loss of material during the washing procedure.

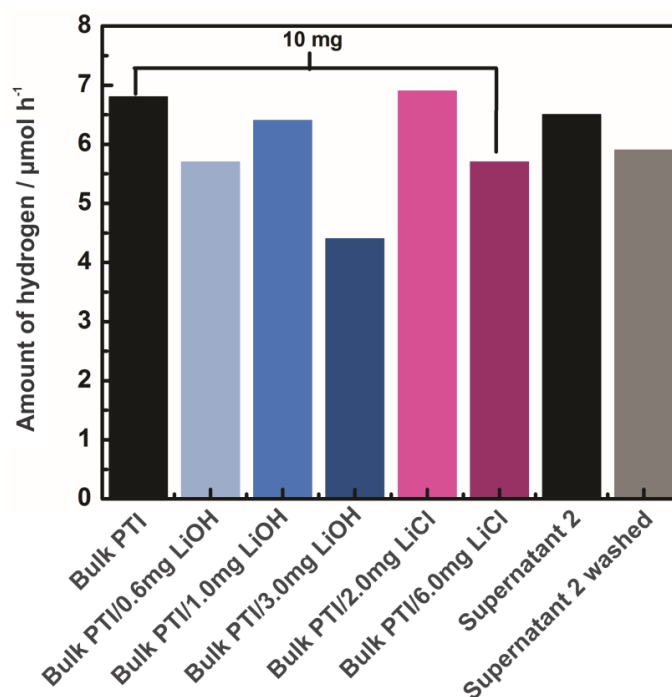


**Figure S20** Photocatalytic activity of bulk PTI compared to LiCl and LiOH monohydrate contaminated bulk PTI samples (10 mg of photocatalyst, 10 vol% TEoA, 2.3 wt% Pt) and of Supernatant 2 ( $\sim 0.2 \text{ mg mL}^{-1}$ ) compared to washed Supernatant 2 ( $<0.2 \text{ mg mL}^{-1}$ ).

### Bibliography

- (S1) (a) E. Wirnhier, M. Döblinger, D. Gunzelmann, J.; Senker, B. V. Lotsch, W. Schnick, *Chem. Eur. J.* **2011**, *17*, 3213. (b) M. J. Bojdys, J.-O. Müller, M. Antonietti, A. Thomas, *Chem. Eur. J.* **2008**, *14*, 8177.
- (S2) X. Yang, Y. Gong, J. Zhang, L. Zhan, L. Ma, Z. Fang, R. Vajtai, X. Wang, P. M. Ajayan, *Adv. Mater.* **2013**, *25*, 2452.
- (S3) (a) J. Xu, Y. Li, S. Peng, G. Lu, S. Li, *Phys. Chem. Chem. Phys.* **2013**, *15*, 7657. (b) M. Aono, S. Aizawa, N. Kitazawa, Y. Watanabe, *Thin Solid Films* **2008**, *516*, 648.
- (S4) M. Kim, S. Hwang, J.-S.; Yu, *J. Mater. Chem.* **2007**, *17*, 1656.
- (S5) (a) A. Essafti, Y. Ijdiyaou, M. Azizan, *Sol. Energ. Mat. Sol. C* **2006**, *90*, 4. (b) W. F. S. J. F. Moulder, P. E. Sobol, K. D. Bomben, Handbook X-ray Photoelectron Spectroscopy. In *Physical Electronics*, Eden Prairie, MN, USA, **1995**.
- (S6) (a) B. Angleraud, N. Mubumbila, P. Y. Tessier, V. Fernandez, G. Turban, *Diam. Relat. Mater.* **2001**, *10*, 1142. (b) S. S. Roy, R. McCann, P. Papakonstantinou, P. Maguire, J. A. McLaughlin, *Thin Solid Films* **2005**, *482*, 145.
- (S7) R. Włodarczyk, M. Sierka, K. Kwapien, J. Sauer, E. Carrasco, A. Aumer, J. F. Gomes, M. Sterrer, H.-J. Freund, *J. Phys. Chem. C* **2011**, *115*, 6764.
- (S8) J. Yang, S. Meng, L. F. Xu, E. G. Wang, *Phys. Rev. Lett.* **2004**, *92*, 146102-1-4.

### 7.1.3 Supporting information of Chapter 3.3

#### Experimental details

##### *Syntheses*

Synthesis of PTI/LiCl,Br.<sup>S1,S2</sup> All manipulations were done under argon in a glove box. Dicyandiamide (2 g, 23.8 mmol) and a eutectic mixture of either lithium chloride (59.2 mol%, 4.52 g, 107.0 mmol) and potassium chloride (40.8 mol%, 5.48 g, 73.5 mmol) (PTI/LiCl) or lithium bromide (58.7 mol%, 5.20 g, 59.9 mmol) and potassium bromide (41.3 mol%, 4.80 g, 40.3 mmol) (PTI/LiBr) were finely ground. The reaction mixture was transferred into a quartz glass vessel and placed in a horizontal tube furnace. The starting materials were heated under atmospheric argon pressure at 6 °C min<sup>-1</sup> to 400 °C and held at this temperature for 12 h. Then the sample was cooled down to room temperature at 20 °C min<sup>-1</sup>, finely ground and 2 g were transferred into a quartz ampule, which was sealed after evacuation at a length of 120 mm ( $\varnothing_{\text{ext.}}$  15 mm,  $\varnothing_{\text{int.}}$  11 mm). The ampule was placed in a slightly tilted horizontal tube furnace and heated at 6 °C min<sup>-1</sup> to 580 °C, at which temperature the sample was held for 24 h. After cooling down to room temperature (6 °C min<sup>-1</sup>), the ampule was carefully broken, and the sample was isolated and washed several times with boiling water to remove residual salt. The resulting material was dried at 100 °C to yield PTI/LiCl(LiBr) as a brown powder (150 mg – 200 mg, 38 % – 50 %). We further tried to synthesize PTI/LiF by analogy to PTI/LiCl(LiBr). To this end, we mixed small amounts of dicyandiamide (100 mg, 1.2 mmol) with a eutectic mixture of lithium fluoride and potassium fluoride and filled the mixture in a platinum vessel. After precondensation under argon flow, the reaction mixture within the platinum vessel was transferred and vacuum sealed in a large and thick-walled quartz ampule. Heating the ampule to over 500 °C lead to an explosion of the ampule since the fluorine corrodes the quartz ampule.

Lithium-proton exchange. PTI/LiCl (50 mg) was stirred in 20 mL of an aqueous 0 %, 12 %, 18 %, or 36 % HCl and PTI/LiBr (50 mg) was stirred in an aqueous 0 %, 16 %, 23.5 %, or 47 % HBr solution for one day. The obtained products were carefully and excessively washed with water until the washing fluid was pH neutral. The products (50 mg) were dried at 100 °C. The samples were labelled according to the concentration of acid used: PTI/X% HY (Y=Cl, Br). We also extended the duration of the acid treatment (with 36 % HCl and 47% HBr) to one week and heated the solution and refreshed the acid solution several times (>5), but the final products did not change with regards to their IR spectra and PXRD patterns. In the case of PTI/LiBr, an acid treatment with 40 % HF and an ammonium fluoride solution (8 M) at 60 °C for 48 h according to the literature<sup>S2</sup> was performed, but yielded the same product as PTI/LiBr 47% HBr. No fluorine was intercalated.

##### *Instruments*

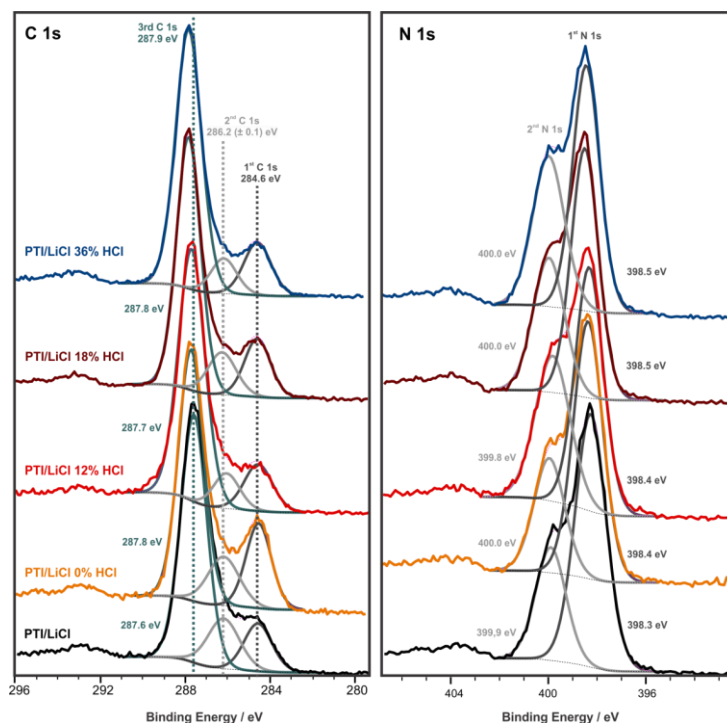
For PXRD, FTIR, UV-Vis, TEM, XPS, ICP and elemental analysis measurements: see the supplementary information of Chapter 4.2. XES and XANES measurements have been performed by T. de Boer (University of Saskatchewan, Saskatoon) and analyzed by E. McDermott (Institute of Materials Chemistry, TU Wien) as described elsewhere.<sup>S3</sup> The photoluminescence (PL) spectra were measured using a Fluorolog-3 FL 3-22 (Horiba Scientific) spectrometer with a Xenon lamp as light source. The emission spectra were measured between 280 nm and 800 nm. The sample was excited at 380 nm using a 430 nm cut-off filter to protect the detector. AFM measurements were performed with a Veeco CP II system. The AFM images were analyzed with the Gwyddion software. NMR: All spectra were referenced relative to TMS (<sup>1</sup>H, <sup>13</sup>C), nitromethane (<sup>15</sup>N) and a 1 M LiCl solution

( $^7\text{Li}$ ).  $^{13}\text{C}$  and  $^{15}\text{N}$  cross-polarization (CP) MAS-NMR spectra were recorded at ambient temperature on an AvanceII 300 or an AvanceIII HD 400 solid-state NMR spectrometer (Bruker) with an external magnetic field of 7.1 T or 9.4 T, respectively. The operating frequencies are 300.1 MHz/400.1 MHz, 75.4 MHz/100.6 MHz and 30.4 MHz/40.6 MHz for  $^1\text{H}$ ,  $^{13}\text{C}$  and  $^{15}\text{N}$ , respectively. The samples were contained in 4 mm  $\text{ZrO}_2$  rotors, which were mounted in a standard triple or double resonance MAS probe (Bruker) and the spinning speed was set to 10 kHz. For CP measurements a CP sequence with a ramped-amplitude (RAMP) contact pulse<sup>55,56</sup> on  $^1\text{H}$  (the RF field was linearly varied about 50 %) and contact times between 4 and 12 ms were applied. During the acquisition, broadband proton decoupling was carried out using SPINAL-64<sup>57</sup> with a nutation frequency of about 70 kHz. The recycle delay was chosen between 1 s and 4 s.  $^7\text{Li}$  MAS-NMR spectra and the  $^1\text{H}$ - $^{13}\text{C}$  CP build-up were conducted at ambient temperature on an AvanceIII HD 400 solid-state NMR spectrometer (Bruker) with an external magnetic field of 9.4 T, operating at frequencies of 400.1 MHz, 100.6 MHz and 155.5 MHz for  $^1\text{H}$ ,  $^{13}\text{C}$  and  $^7\text{Li}$ , respectively. The samples were contained in 4 mm  $\text{ZrO}_2$  rotors, which were mounted in a standard double resonance MAS probe (Bruker) and the spinning speed was set to 5 kHz ( $^7\text{Li}$ ) and 12.5 kHz (CP build-up), respectively. The  $^7\text{Li}$  spectra were measured using a standard one-pulse experiment with full relaxation between the scans (recycle delay 10 s for PTI/LiCl 36% HCl and 60 s for PTI/LiCl). For the  $^1\text{H}$ - $^{13}\text{C}$  CP build-up, a square contact pulse with variable duration (1  $\mu\text{s}$  – 15 ms) was used. The RF field of  $^1\text{H}$  was experimentally adjusted to the +1 Hartmann-Hahn condition<sup>58</sup> using Adamantane. During acquisition proton decoupling was carried out using SPINAL-64<sup>57</sup> with a nutation frequency of about 70 kHz. The recycle delay was set to 1 s.  $^1\text{H}$  1D and 2D MAS-NMR spectra were recorded at ambient temperature on an AvanceIII HD 600 solid-state NMR spectrometer (Bruker) with an external magnetic field of 14.1 T, operating at frequencies of 600.1 MHz, 150.9 MHz and 233.2 MHz for  $^1\text{H}$ ,  $^{13}\text{C}$  and  $^7\text{Li}$  respectively. The samples were contained in 1.3 mm  $\text{ZrO}_2$  rotors, which were mounted in a standard triple resonance MAS probe (Bruker) and the spinning speed was set to 62.5 kHz. 1D measurements were carried out using a conventional Hahn-echo experiment.  $^{13}\text{C}$ - $^1\text{H}$ - and  $^7\text{Li}$ - $^1\text{H}$ - HETCOR spectra were recorded using a D-HMQC pulse sequence.<sup>59</sup> To transfer polarization between the nuclei the supercycled symmetry based SR4<sub>i</sub><sup>2</sup> sequence was applied.<sup>510</sup> As the quadrupole moment of  $^7\text{Li}$  is quite small (< 200 kHz), strong 90° pulses (RF field ~230 kHz) were used to excite the whole spectrum. For both spectra, the  $t_1$  evolution was rotor synchronized using a dwell time of 128  $\mu\text{s}$ . For the  $^{13}\text{C}$ - $^1\text{H}$ -spectrum a recoupling time of 448  $\mu\text{s}$  was chosen and for the  $^1\text{H}$ - $^7\text{Li}$  HETCOR the recoupling time was set to 352  $\mu\text{s}$ . The 2D  $^1\text{H}$ - $^1\text{H}$  double-quantum-single-quantum (DQ-SQ) correlation spectra were recorded using a rotor-synchronized symmetry based R-sequence<sup>510,511</sup> R12<sub>2</sub><sup>59</sup> in a excitation-reconversion- $\pi/2$ -acquisition Scheme. The R-block was implemented using 180° pulses and the phase cycling was performed with the conventional 16-fold phase cycle to select the required coherence pathway  $0 \pm 2 0 -1$ . Recoupling times of 32  $\mu\text{s}$ , 96  $\mu\text{s}$  and 224  $\mu\text{s}$  were chosen. The powerlevel for the R-sequence was optimised on the sample directly. The  $^1\text{H}\{-^7\text{Li}\}$  Rotational-Echo Double-Resonance (REDOR) curves were measured using a conventional REDOR sequence.<sup>513</sup> Due to fast spinning, which was necessary to get resolution, and the therefore short  $\tau_{\text{rot}}$  (16  $\mu\text{s}$ ), the  $^7\text{Li}$  180° pulses have to be shorter than 1.6  $\mu\text{s}$  in order to reach the goal of the pulse occupying less than 10 % of  $\tau_{\text{rot}}$ . Due to experimental limits only a 180 pulse of 2.2  $\mu\text{s}$  could be used, therefore making quantitative analysis complicated. Photocatalysis The photocatalyst (10 mg) was dispersed in water (9 mL) (when MeOH was used as electron donor) or phosphate buffer (0.5 M, pH 7) (in the case of TEOA) in a 230 mL quartz glass reactor with a PTFE/Teflon septum. Then 1 mL of MeOH or TEOA and 6  $\mu\text{L}$   $\text{H}_2\text{PtCl}_6$  (8 wt% in  $\text{H}_2\text{O}$ ) (2.2 wt% Pt) was added. The reac-

tor was evacuated and purged with argon. Then the reactor was simultaneously top-illuminated (top surface = 15.5 cm<sup>2</sup>) with a 300 W Xenon lamp with a water filter and dichroic mirror blocking wavelengths < 420 nm and cooled with a water jacket. The evolved gas was measured by gas chromatography with an online injection system and using a thermal conductivity detector with argon as carrier gas.

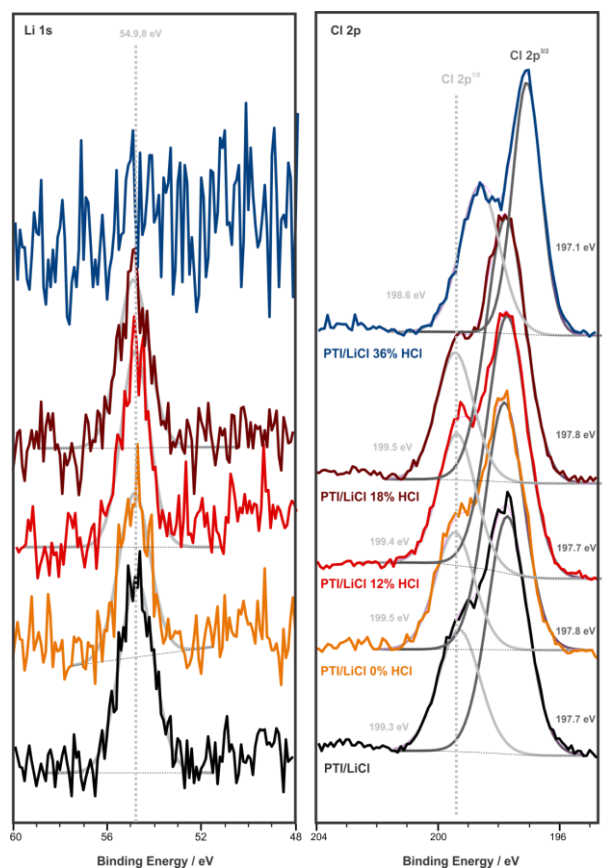
## Figures and tables

### XPS spectroscopy

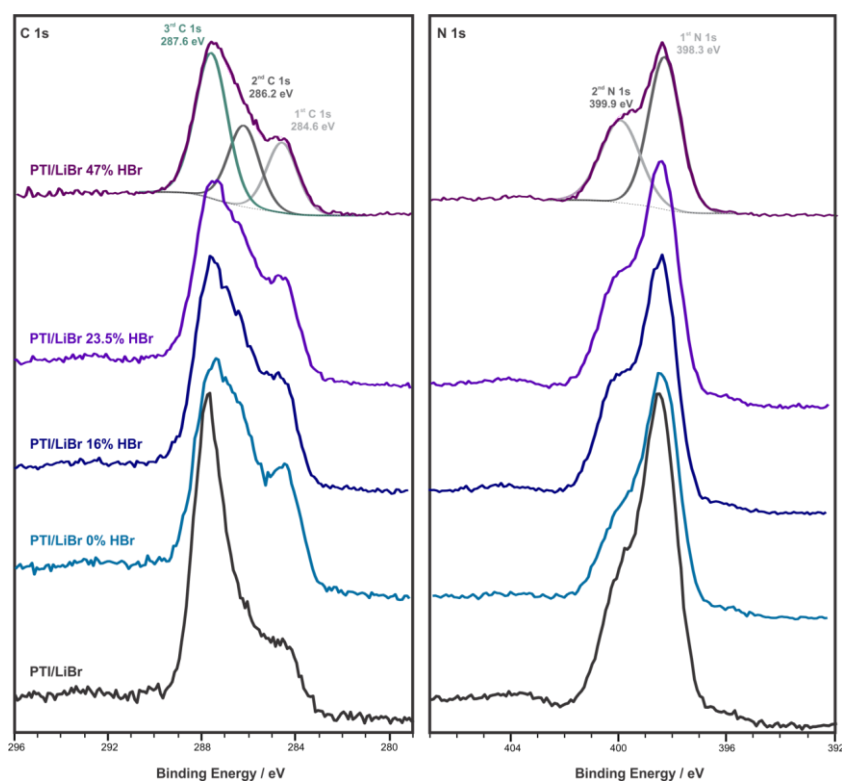


**Figure S21** C 1s (left) and N 1s XPS spectra (right) of PTI/LiCl (black), PTI/LiCl stirred in water (orange) and PTI/LiCl treated with 12 % (red), 18 % (wine red) and 36 % (blue) concentrated HCl solutions.

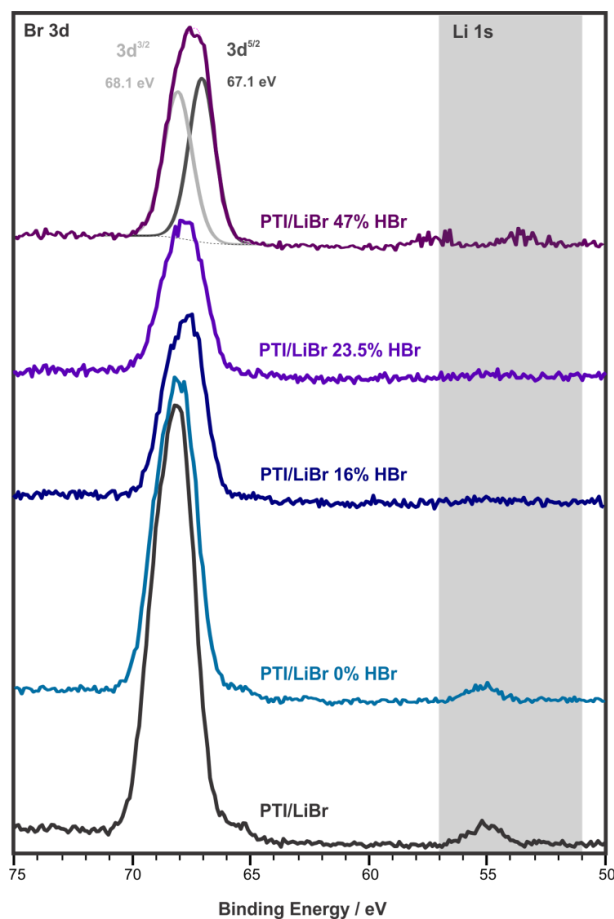




**Figure S22** Li 1s (left) and Cl 2p XPS spectra (right) of PTI/LiCl (black), PTI/LiCl stirred in water (orange) and PTI/LiCl treated with 12 % (red), 18 % (wine red) and 36 % (blue) concentrated HCl solutions.

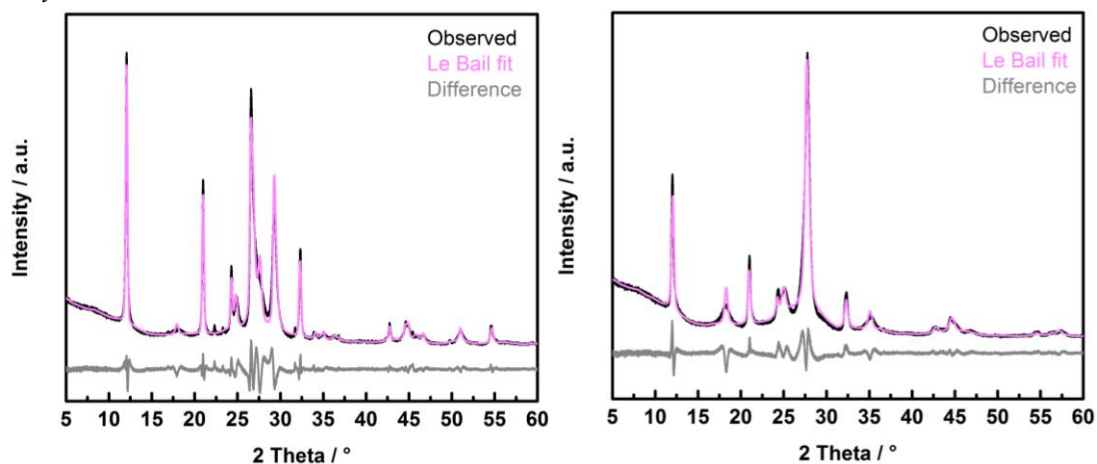


**Figure S23** C 1s (left) and N 1s XPS spectra (right) of PTI/LiBr (black), PTI/LiBr stirred in water (fair blue) and PTI/LiBr treated with 16 % (dark blue), 23.5 % (violet) and 47 % (purple) concentrated HBr solutions.



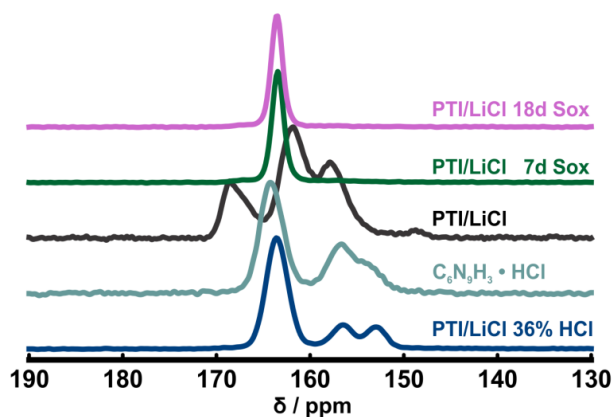
**Figure S24** Li 1s (grey region) and Br 3d XPS spectra of PTI/LiBr (black), PTI/LiBr stirred in water (fair blue) and PTI/LiBr treated with 16 % (dark blue), 23.5 % (violet) and 47 % (purple) concentrated HBr solutions.

### LeBail fits

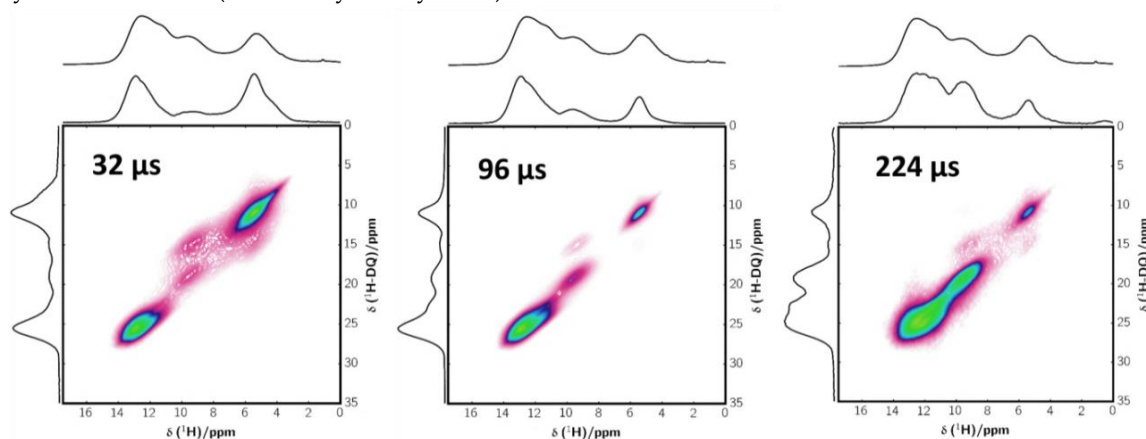


**Figure S25** LeBail fits of PTI/LiCl on the basis of PTI/LiCl (left) compared to the LeBails fit of PTI/LiCl 36% HCl on the basis of  $C_6N_9H_3 \cdot HCl$ .<sup>S15</sup> In both cases a reasonable fit could be achieved using 100 % of the fitted phase. For extracted lattice parameters see Table 3.5 of the main manuscript.

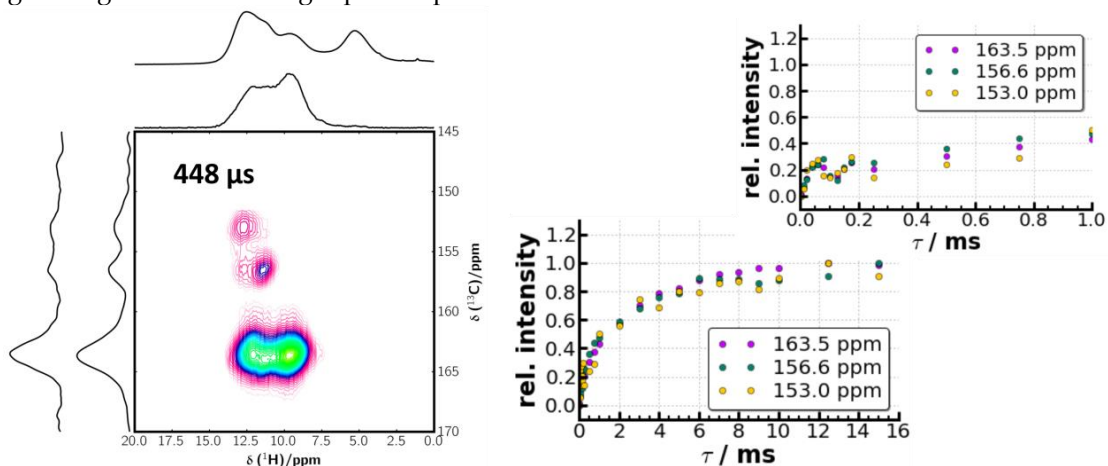
## NMR spectroscopy



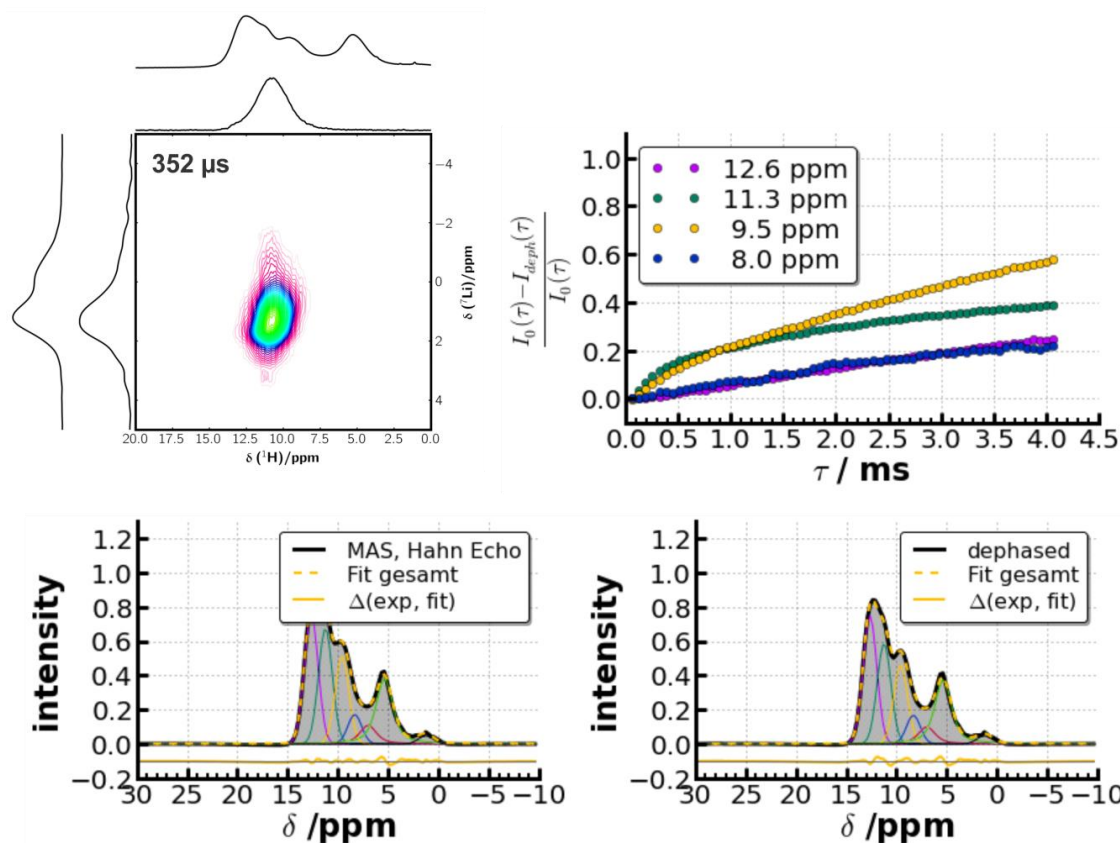
**Figure S26**  $^{13}\text{C}$  CP-MAS ssNMR spectra (300 MHz, 10 kHz) of PTI/LiCl 36% HCl compared to PTI/LiCl,  $\text{C}_6\text{N}_9\text{H}_3 \cdot \text{HCl}$  and PTI/LiCl which was Soxhlet-extracted for 7 and 18 days and measured by D. Gunzelmann (University of Bayreuth).



**Figure S27** 2D  $^1\text{H}$ - $^1\text{H}$  DS-SQ ssNMR spectra of PTI/LiCl 36% HCl detected at different mixing times (32  $\mu\text{s}$ , 96  $\mu\text{s}$  and 224  $\mu\text{s}$ ). Short mixing times visualize short proton-proton distances and long mixing times detect larger proton-proton distances.

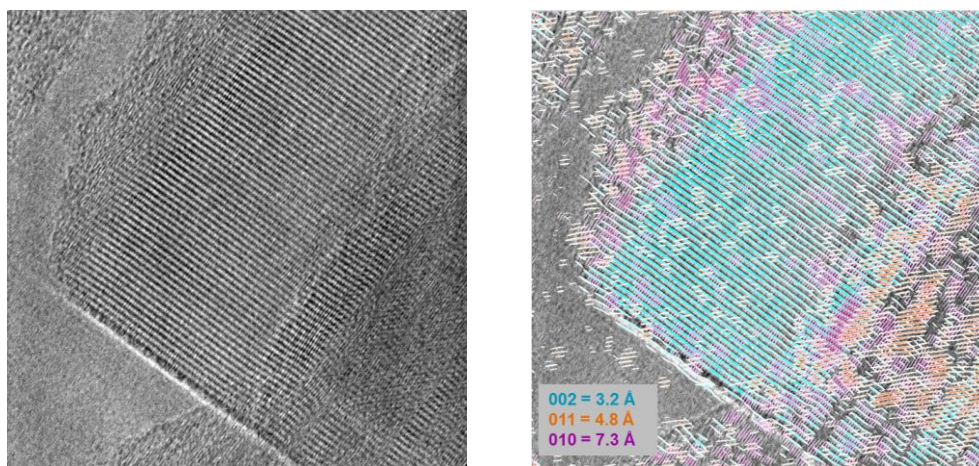


**Figure S28**  $^{13}\text{C}$ - $^1\text{H}$  HMQC ssNMR spectrum (after 448  $\mu\text{s}$  of mixing time) of PTI/LiCl 36% HCl (left) and the  $^1\text{H}$ - $^{13}\text{C}$  CP build-up curves (right) showing no major differences of the proton environment of the different  $^{13}\text{C}$  signals. The oscillation at the beginning of the CP build-up (top right) arises due to at least one dominating short distance, which for PTI/LiCl was assigned to the C-NH group with a  $^1\text{H}$ - $^{13}\text{C}$  distance of approximately 2 Å.<sup>514</sup> A quantitative evaluation of the curves is difficult, as the spinning was 10 kHz and therefore only residual dipolar couplings are observed.



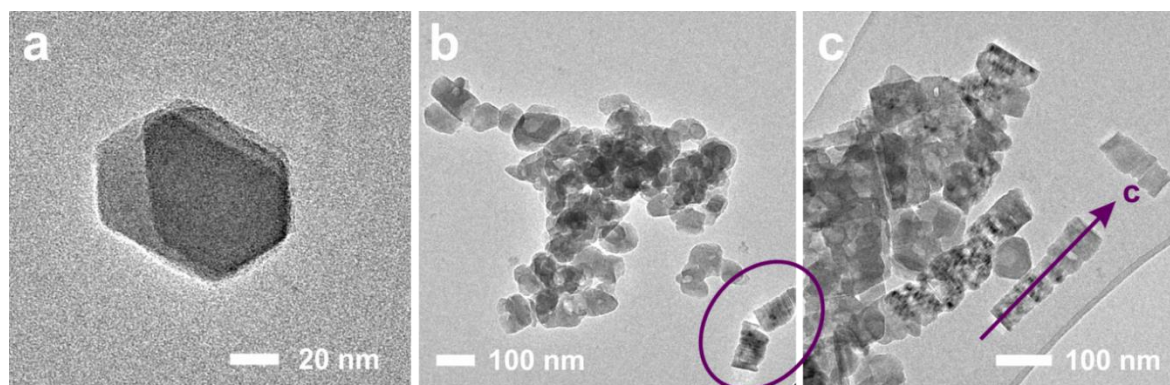
**Figure S 29** Top:  ${}^7\text{Li}$ - ${}^1\text{H}$  HMQC ssNMR spectrum of PTI/LiCl 36 % HCl detected at a mixing time of  $352 \mu\text{s}$  (left) and  ${}^1\text{H}\{{}^7\text{Li}\}$  REDOR ssNMR measurements of the same sample (right). Both are showing a closer lithium distance to the  ${}^1\text{H}$  signals appearing at 11.3 ppm and 9.5 ppm. As a spinning speed of 62.5 kHz was needed to achieve resolution, the  ${}^7\text{Li}$  pulse was too long to allow quantitative analysis (for further details see Experimental Details). Bottom: Deconvoluted  ${}^1\text{H}\{{}^7\text{Li}\}$  REDOR ssNMR spectra of PTI/LiCl 36% HCl: reference spectrum (left) and dephased spectrum (right).

TEM

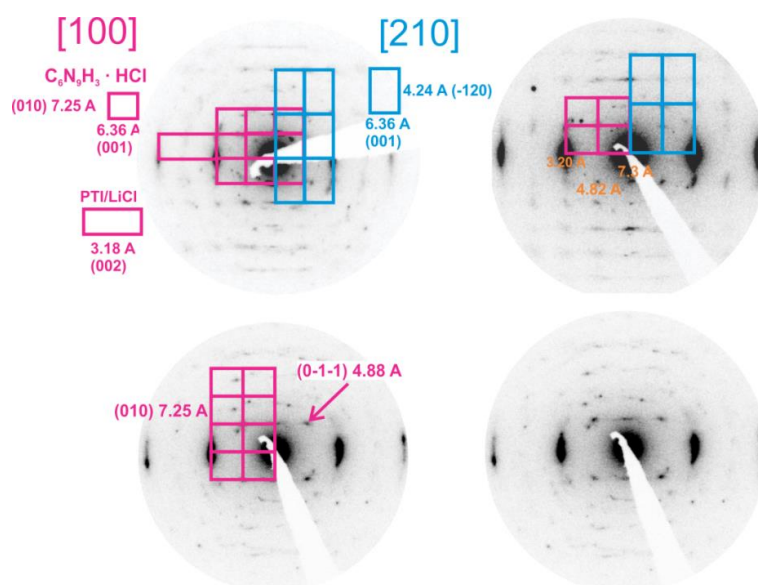


**Figure S30** TEM micrograph of PTI/LiCl 36% HCl. Different colors are given for different  $d$ -spacings in the right image to investigate the origin of the now visible characteristic 011 reflection of PTI/LiCl 36% HCl (and  $\text{C}_6\text{N}_9\text{H}_3 \cdot \text{HCl}$ ). As reported for  $\text{C}_6\text{N}_9\text{H}_3 \cdot \text{HCl}$ , an absence of the 001 and 003 reflections are observed.

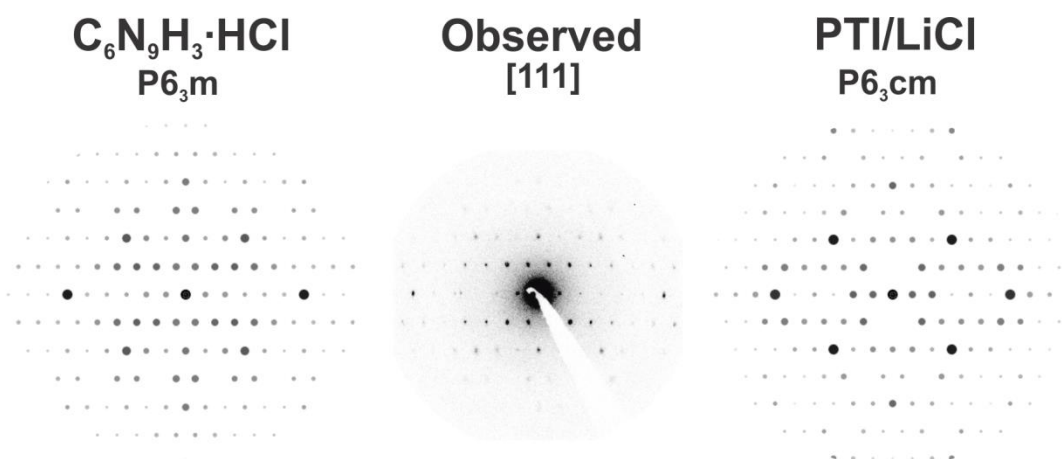




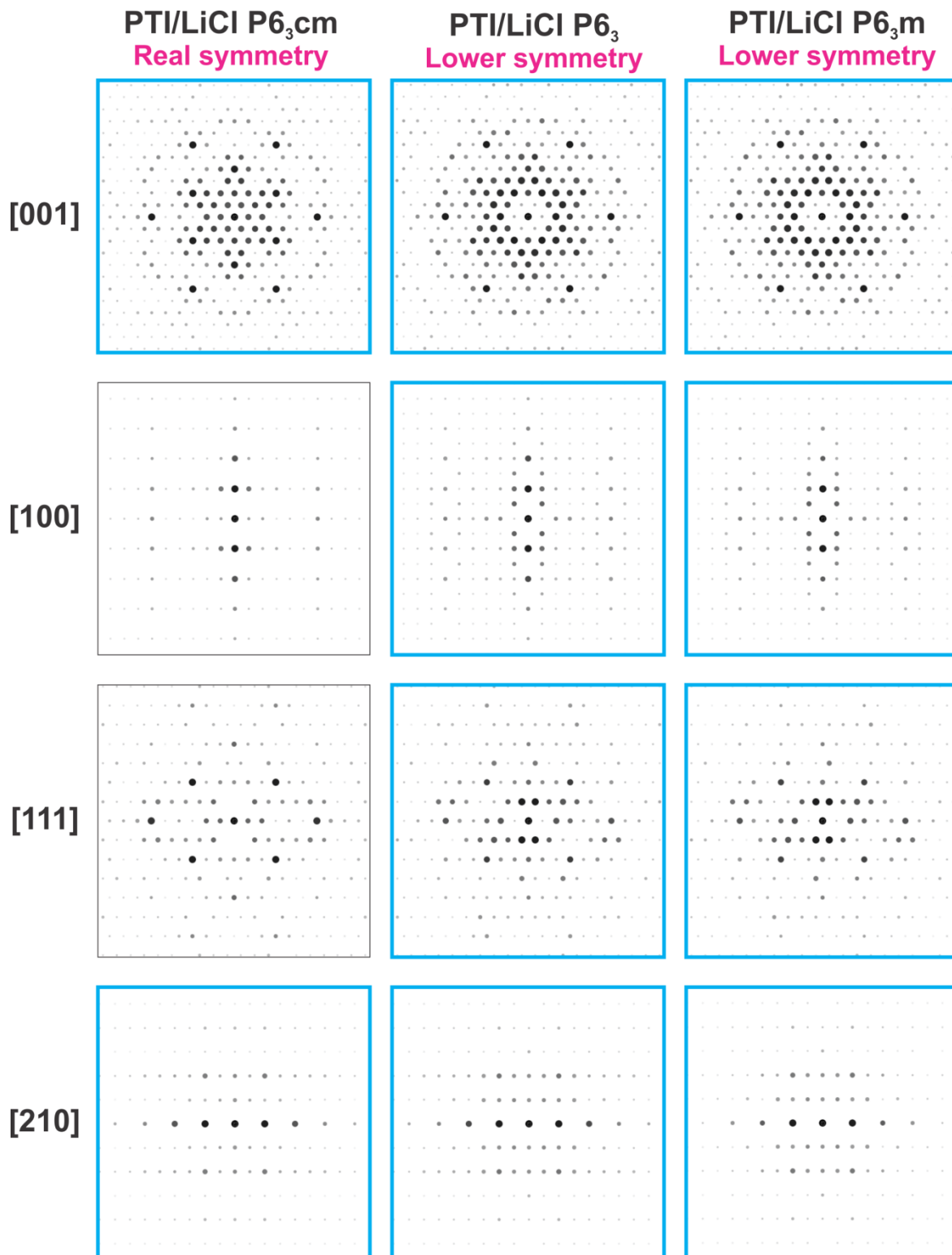
**Figure S31** TEM images of crystalline PTI/LiBr before the acid treatment: (a) High-magnification image of the crystallites, (b) overview with dispersed and agglomerated (purple cycle) regions and (c) agglomerate formation along the *c*-axis.



**Figure S32** Top: Complicated SAD patterns of PTI/LiCl 36% HCl arise from two different overlapping orientations along [100] and [210]. The observed SAD patterns can be assigned to both structures: PTI/LiCl and  $C_6N_9H_3 \cdot HCl$ . Bottom: This SAD patterns show the appearance of the 011 reflection.



**Figure S33** SAD pattern of PTI/LiCl 36% HCl viewed along [111] (middle), next to the simulated patterns of  $C_6N_9H_3 \cdot HCl$  (left) and PTI/LiCl (right). The observed pattern agrees with the pattern of  $C_6N_9H_3 \cdot HCl$ .



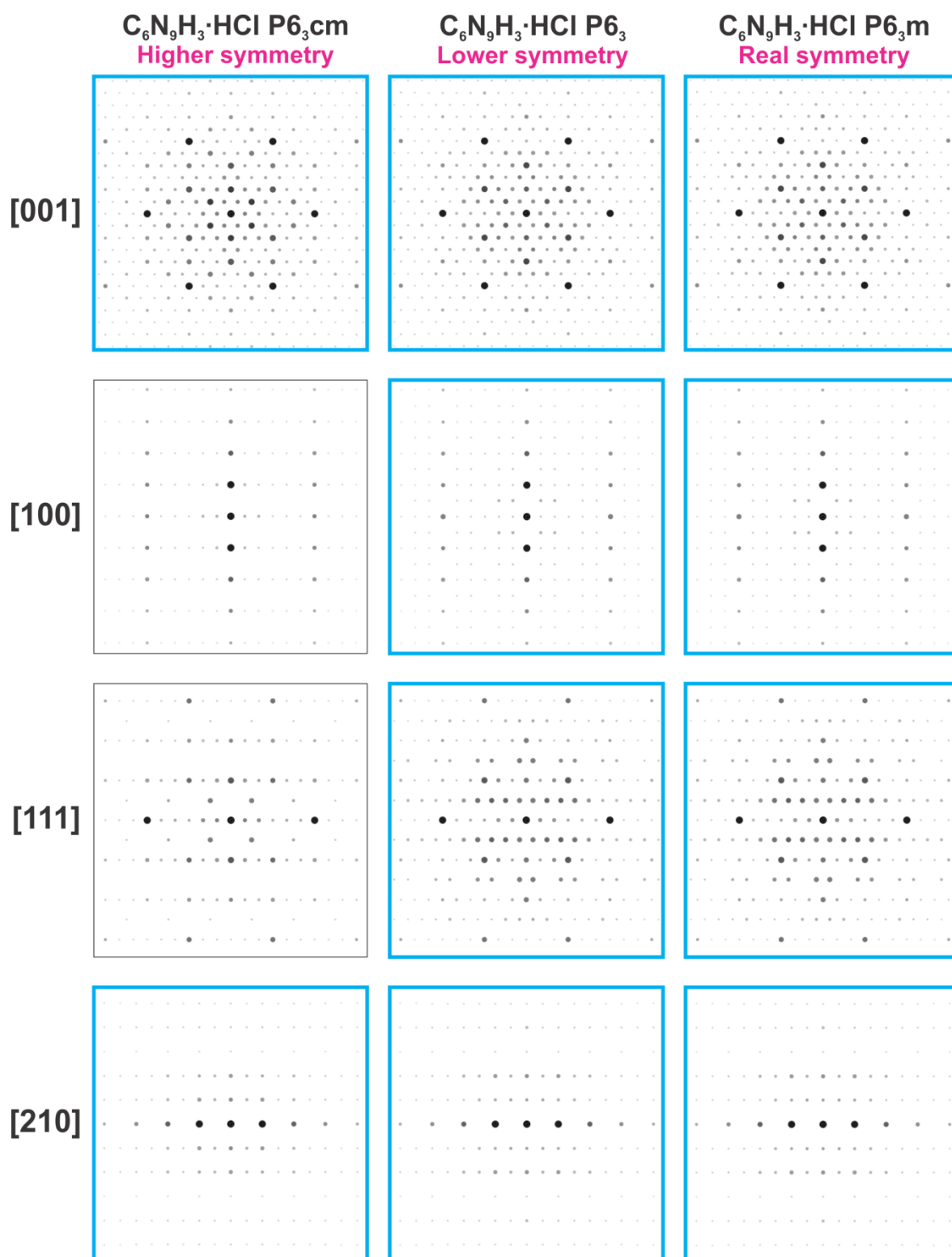


**Figure S34** Simulated patterns of PTI/LiCl (top) and  $C_6N_9H_3 \cdot HCl$  (bottom) using their real symmetry and in lower/higher symmetries viewed along different directions. Only along the [100] and [111] direction the two compounds differ from each other (with regard to their reflection positions). The observed pattern of PTI/LiCl 36% HCl matches (blue boxes) with the ones using a  $P6_3$  or  $P6_3/m$  symmetry of PTI/LiCl and  $C_6N_9H_3 \cdot HCl$ .

## UV-Vis measurements

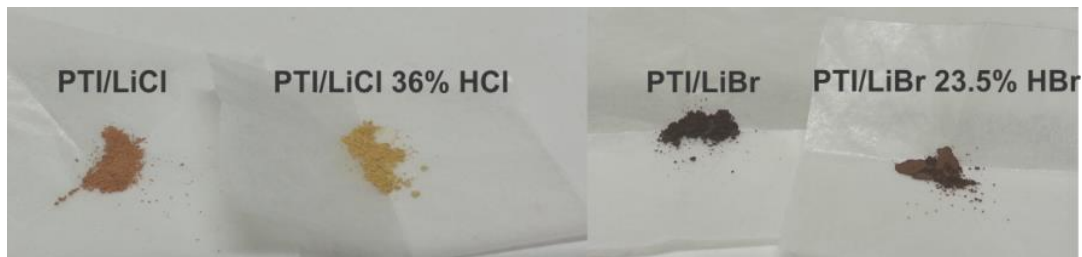


**Figure S35** Comparison of the colors of the samples: PTI/LiCl vs PTI/LiCl 36% HCl and PTI/LiBr vs PTI/LiBr 23.5% HBr (from left to right).

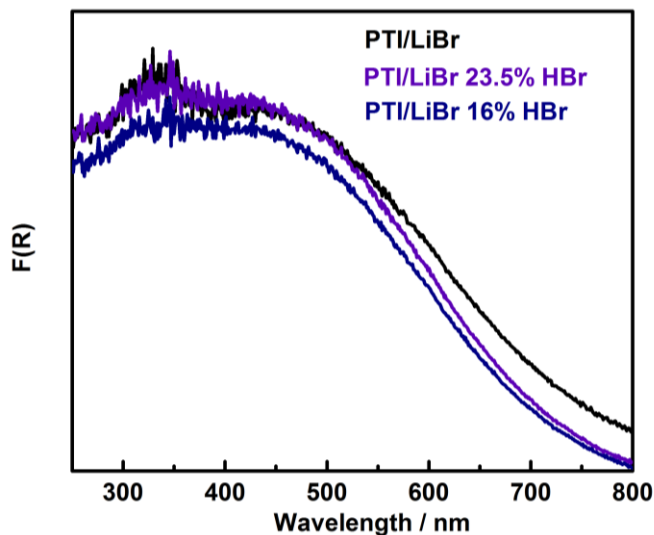


**Figure S36** UV-Vis measurements of PTI/LiBr before and after acid treatment with HBr.

## Photoluminescence measurements

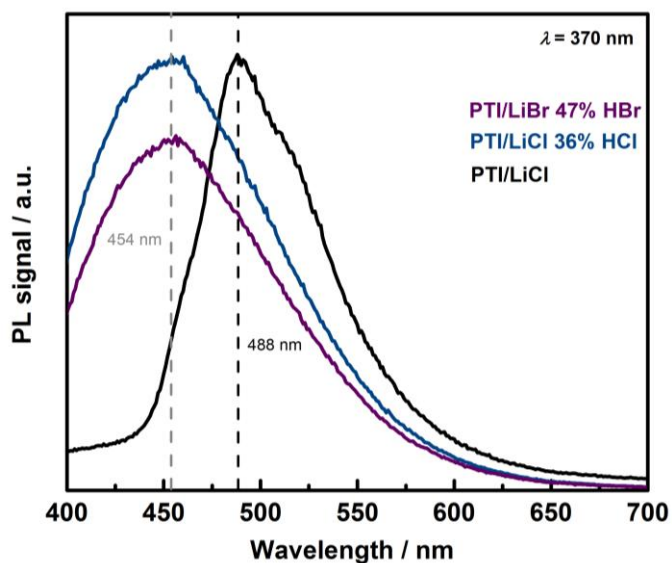


**Figure S37** PL measurements of PTI/LiCl compared to PTI/LiCl,Br stirred in concentrated acids (PTI/LiCl 36% HCl and PTI/LiBr 47% HBr).



## Photocatalytic measurements

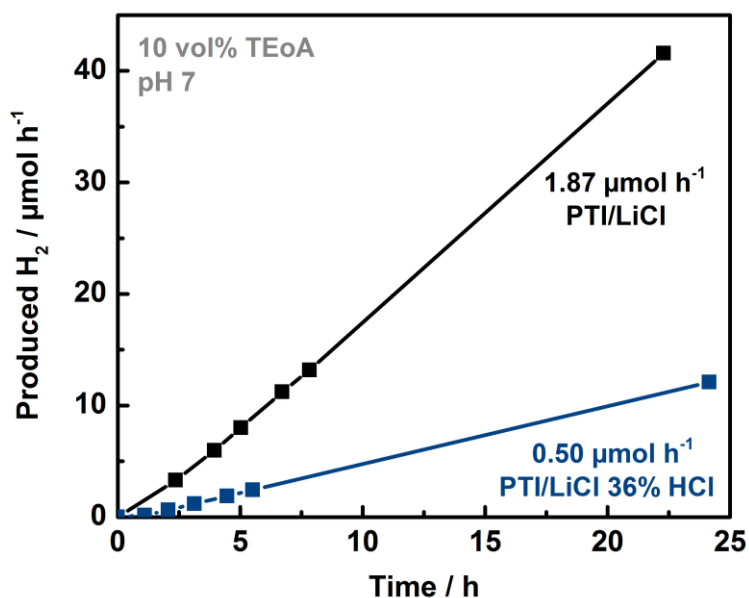


**Figure S38** Photocatalytic activity (420 nm cut-off filter) of 2.2 wt% Pt-modified PTI/LiCl before (black) and after stirring the sample in 36 % HCl solution (blue). 10 vol% triethanolamine (TEoA) has been used as electron donor in a 0.5 M phosphate buffered (pH 7) aqueous solution.

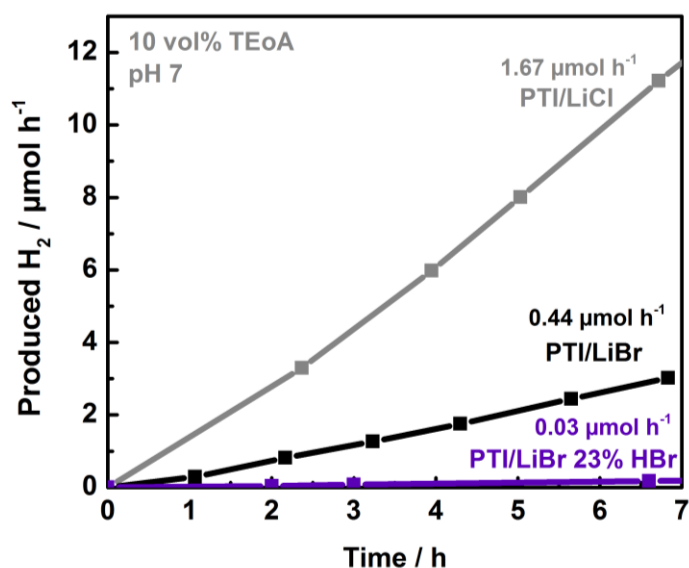


**Figure S39** Photocatalytic activity (420 nm cut-off filter) of 2.2 wt% Pt-modified PTI/LiBr before (black) and after stirring the sample in 23.5 % HBr solution (violet) compared to PTI/LiCl (grey). 10 vol% triethanolamine (TEoA) has been used as electron donor in a 0.5 M phosphate buffered (pH 7) aqueous solution.

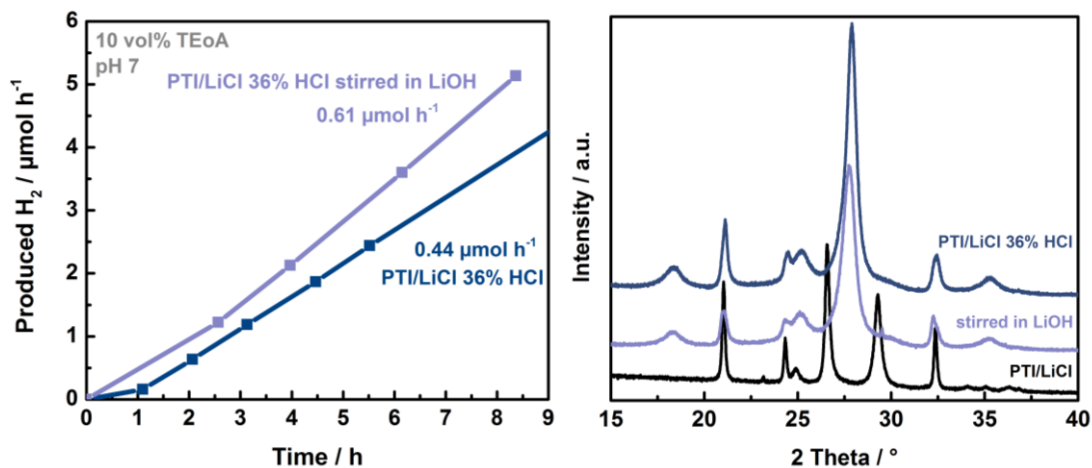


**Figure S40** (Left) Photocatalytic activity (420 nm cut-off filter) of 2.2 wt% Pt-modified PTI/LiCl 36 % HCl before (blue) and after stirring the sample in a saturated LiOH solution (pigeon blue). 10 vol% triethanolamine (TEoA) has been used as electron donor in a 0.5 M phosphate buffered (pH 7) aqueous solution. The corresponding PXRD patterns are displayed compared to the one of PTI/LiCl (right).

#### Exfoliation of PTI/LiCl 36% HCl

Exfoliation procedure according to *Schwinghammer et al.*<sup>54</sup>

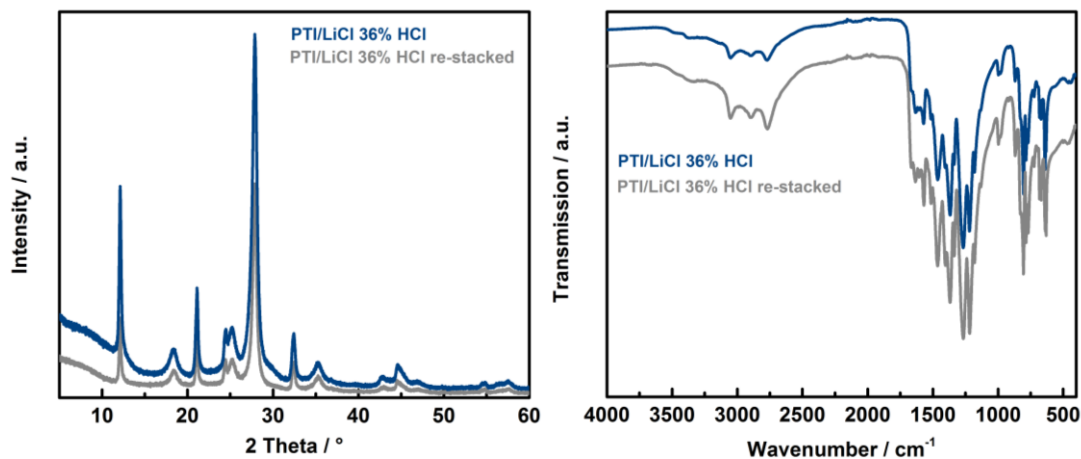


**Figure S41** PXRD pattern (left) and IR spectrum (right) of PTI/LiCl 36 % HCl is identical to the exfoliated (and re-stacked) PTI/LiCl 36% HCl sample.

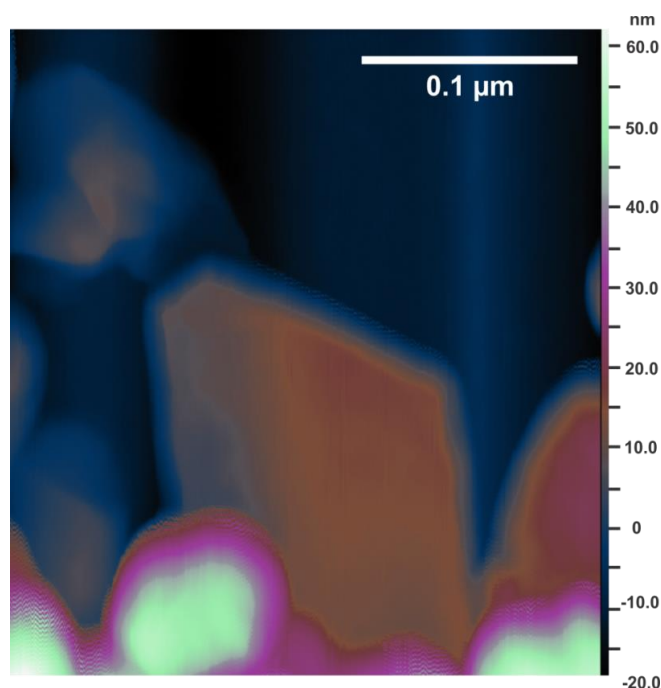


**Figure S42** AFM image of the re-stacked “exfoliated” PTI/LiCl 36% HCl sample on a SiO<sub>2</sub>/Si wafer. Rarely, few-layers of PTI/LiCl 36 % HCl have been detected, mostly multi-layer stacks were observed. Even here, the sharp edges of the hexagonal crystal are visible.

### Bibliography

- (S1) (a) E. Wirnhier, M. Döblinger, D. Gunzelmann, J. Senker, B. V. Lotsch, W. Schnick, *Chem. Eur. J.* **2011**, *17*, 3213. (b) M. J. Bojdys, J.-O. Müller, M. Antonietti, A. Thomas, *Chem. Eur. J.* **2008**, *14*, 8177.
- (S2) S. Y. Chong, J. T. A. Jones, Y. Z. Khimiyak, A. I. Coomper, A. Thomas, M. Antonietti, M. J. Bojdys, *J. Mater. Chem. A* **2013**, *1*, 1102.
- (S3) E. J. McDermott, E. Wirnhier, W. Schnick, K. S. Viridi, C. Scheu, Y. Kauffmann, W. D. Kaplan, E. Z. Kurmaev, A. Moewes, *J. Phys. Chem. C* **2013**, *117*, 8806.
- (S4) K. Schwinghammer, M. B. Mesch, V. Duppel, C. Ziegler, J. Senker, B. V. Lotsch, *J. Am. Chem. Soc.* **2014**, *136*, 1730.
- (S5) A. Pines, M. G. Gibby, J. S. Waugh, *J. Chem. Phys.* **1973**, *59*, 569.
- (S6) G. Metz, X. Wu, S. O. Smith, *J. Magn. Reson. Ser. A* **1994**, *110*, 219.
- (S7) B. M. Fung, A. K. Khitrin, K. Ermolaev, *J. Magn. Reson.* **2000**, *142*, 97.
- (S8) R. S. Hartmann, E. L. Hahn, *Phys. Rev.* **1962**, *128*, 2042.
- (S9) Z. Gan, *J. Magn. Reson.* **2007**, *184*, 39.
- (S10) A. Brinkmann, A. P. M. Kentgens, *J. Am. Chem. Soc.* **2006**, *128*, 14758.
- (S11) M. H. Levitt, *Encycl. NMR* **2002**, *9*, 165.
- (S12) P. E. Kristiansen, D. J. Mitchell, J. N. S. Evans, *J. Magn. Reson.* **2002**, *157*, 253.
- (S13) T. Gullion, *Concepts Magn. Reson.* **1998**, *10*, 277.
- (S14) M. B. Mesch, *PhD thesis*, University of Bayreuth, **2016**.
- (S15) Z. Zhang, K. Leinenweber, M. Bauer, L. A. J. Garvie, P. F. McMillan, G. H. Wolf, *J. Am. Chem. Soc.* **2001**, *123*, 7788.

## 7.1.4 Supporting information of Chapter 4.1

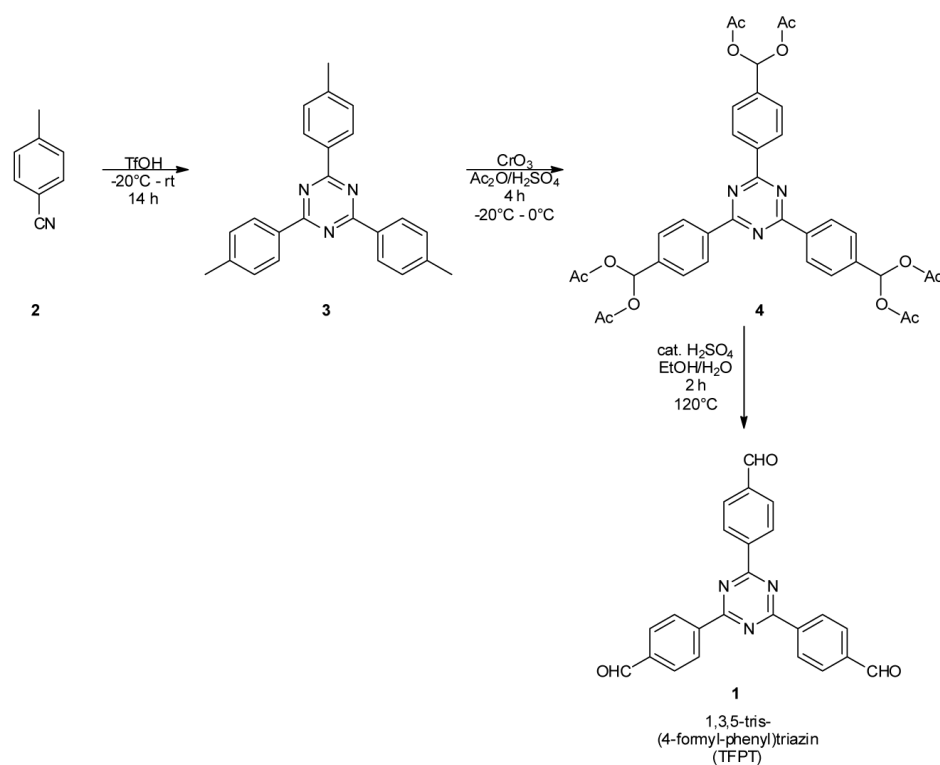
### Materials and instruments

#### *Instruments*

All reagents were purchased from commercial sources and used without further purification. The starter 2,5-diethoxy-terephthalohydrazide<sup>51</sup> was prepared according to ref. 18, the NMR data being consistent with those given in the literature. The synthesis of the second starting material TFPT<sup>52</sup> is described below. IR spectra were recorded on a Perkin Elmer Spektrum BX II FT-IR equipped with an ATR unit (Smith Detection Dura-Sample IIR diamond). The spectra were background-corrected. The <sup>13</sup>C and <sup>15</sup>N MAS NMR spectra were recorded at ambient temperature on a Bruker Avance 500 solid-state NMR spectrometer, operating at frequencies of 500.1 MHz, 125.7 MHz and 50.7 MHz for <sup>1</sup>H, <sup>13</sup>C and <sup>15</sup>N, respectively. The sample was contained in a 4 mm ZrO<sub>2</sub> rotor (Bruker) which was mounted in a standard double resonance MAS probe. The <sup>13</sup>C and <sup>15</sup>N chemical shifts were referenced relative to TMS and nitromethane, respectively. The <sup>1</sup>H-<sup>15</sup>N and <sup>1</sup>H-<sup>13</sup>C cross-polarization (CP) MAS spectra were recorded at a spinning speed of 10 kHz using a ramped-amplitude (RAMP) CP pulse on <sup>1</sup>H, centered on the  $n = +1$  Hartmann-Hahn condition, with a nutation frequency  $\nu_{\text{nut}}$  of 55 kHz (<sup>15</sup>N) and 40 kHz (<sup>13</sup>C). During a contact time of 7 ms the <sup>1</sup>H radio frequency field was linearly varied about 20 %.

UV-Vis optical diffuse reflectance spectra were collected at room temperature with a Varian Carry 500 UV-Vis diffuse reflectance spectrometer. Powders were prepared between two quartz discs at the edge of the integrating sphere with BaSO<sub>4</sub> as the optical standard. Absorption spectra were calculated from the reflectance data with the Kubelka-Munk function. Argon sorption measurements were performed at 87 K with a Quantachrome Instrument Autosorb iQ. Samples of 20 mg were preheated in vacuum at 120 °C for 12 h. For BET calculations pressure ranges were chosen between 0.20–0.34 p/p<sub>0</sub>. The pore size distribution was calculated from Ar adsorption isotherms by non-local density functional theory (NLDFT) using the “Ar-zeolite/silica cylindrical pores at 87 K” kernel (applicable pore diameters 3.5 Å – 1000 Å) for argon data as implemented in the AUTOSORB data reduction software. PXRD data were collected using a Bruker D8-advance diffractometer in reflectance Bragg-Brentano geometry employing Cu filtered CuK $\alpha$ -monochromator focused radiation (1.54059 Å) at 1600 W (40 kV, 40 mA) power and equipped with a Lynx Eye detector (fitted at 0.2 mm radiation entrance slit). Samples were mounted on Ge (111) sample holders after dispersing the powders with ethanol and letting the slurry dry to form a conformal film on the holder. The samples were measured with a 2 $\theta$ -scan from 2° to 30° as a continuous scan with 3046 steps and 5 s/step (acquisition time 4 h 47 min 45 s). Transmission electron microscopy data were obtained with a Philips CM30/ST microscope with LaB<sub>6</sub> cathode, at an acceleration voltage of 300 kV. The powder was dispersed in *n*-Butanol. One drop of the suspension was placed on a holey carbon/copper grid. Scanning electron microscopy images were obtained with a Zeiss Merlin at 1.5 kV. The TEM grids were deposited onto a sticky carbon surface.

## Synthetic procedures



**Scheme S1** Synthesis of 1,3,5-*tris*-(4-formyl-phenyl)triazine (TFPT) (**1**) by a three-step modified literature procedure.<sup>53</sup>

### 1,3,5-*tris*-(4-methyl-phenyl)triazine (**3**)

*p*-tolunitrile (**2**) (98 %, Sigma Aldrich) was liquefied by putting the storage vessel in a 60 °C drying oven for 30 min. To a 25 ml round-bottom Schlenk flask with stir bar 5.0 ml (8.24 g, 53.8 mmol, 2.15 eq) of triflic acid (AlfaAesar, 98 %) were added and cooled to -20 °C in a dewar with salt/ice bath (1:3 v/v) under stirring. By syringe 3.1 mL (2.99 g, 25.0 mmol, 1.0 eq) of **2** were added dropwise with help of a syringe pump over 1 h. The solution turned into slurry solid over time and was left for 24 h. The cake was scratched off and transferred in ice water under stirring. This solution was neutralized with 4 mL – 5 mL 25 % ammonia. The off-white precipitate was filtered off, washed with acetone (3 x 5 mL) and dried in vacuum to yield the title compound **3** (2.56 g, 7.29 mmol, 88 %). <sup>13</sup>C and <sup>1</sup>H NMR data were consistent with the literature.

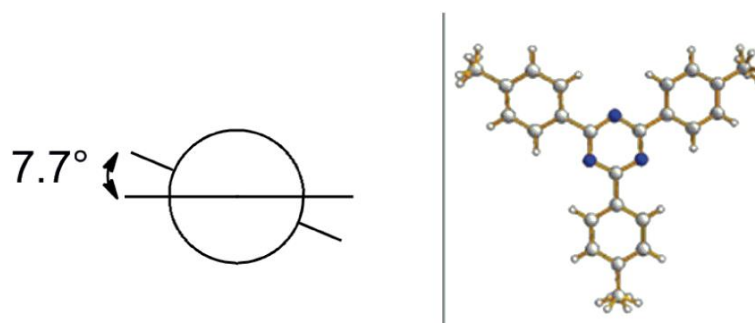
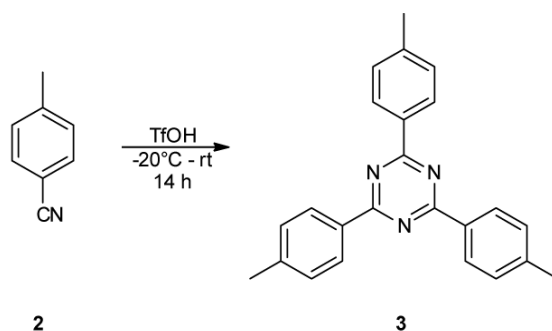


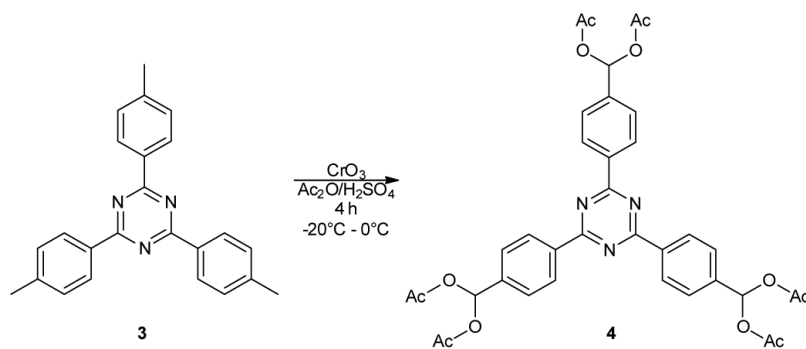
**Figure S43** Molecular structure of 1,3,5-*tris*-(4-methylphenyl)triazine. Newman projection on the single bond connecting triazine and phenyl ring (left) and structure derived from crystal data (right).<sup>53</sup>



**Scheme S2** Synthesis of 1,3,5-*tris*-(4-methyl-phenyl)triazine (3) by super-acid catalyzed trimerization of *p*-tolunitrile (2) according to a literature procedure.<sup>S2</sup>

**[4,4',4''-(1,3,5-Triazine-2,4,6-triyl)tris(4,1-phenylene)]-tris(methanetriyl)hexaacetate (4)**

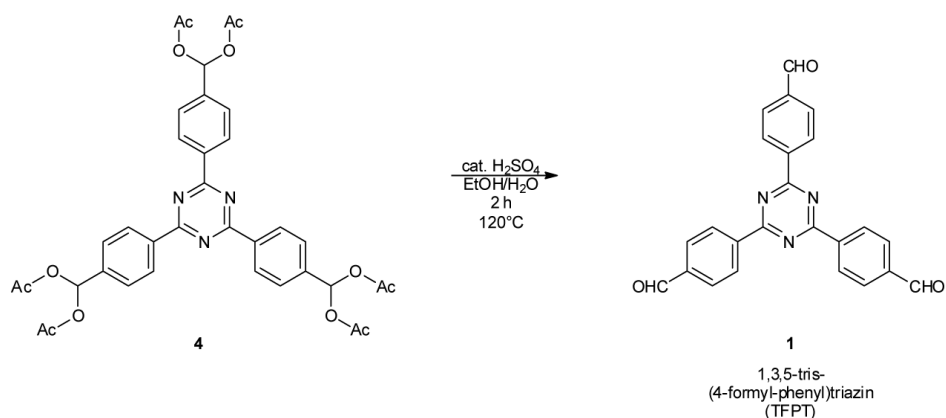
To a 25 ml round-bottom flask with stir bar and rubber septum 100 mg (0.285 mmol, 1.0 eq) of 3 and 1.00 mL of acetic anhydride were added and cooled down to  $-20^\circ\text{C}$  in a salt/ice bath. After addition of 0.2 ml 98% sulfuric acid, to the yellowish solution was added dropwise by syringe a solution of chromium(VI)oxide (250 mg, 92.6 mmol, 325 eq) in 1.25 mL acetic anhydride over a period of 3.5 h under stirring. The temperature was kept below  $0^\circ\text{C}$ . The greenish solution was stirred for another hour and then added dropwise to 12.5 mL stirred ice water. The yellowish precipitate was filtered off, washed with dest. water (3 x 3 mL) until neutral and dried in vacuum. The subsequent further purification by column chromatography (50:1 DCM/EtOAc) on silica gel yielded the title compound 4 (75 mg, 0.107 mmol, 38 %).  $^{13}\text{C}$  and  $^1\text{H}$  NMR data were consistent with the literature.



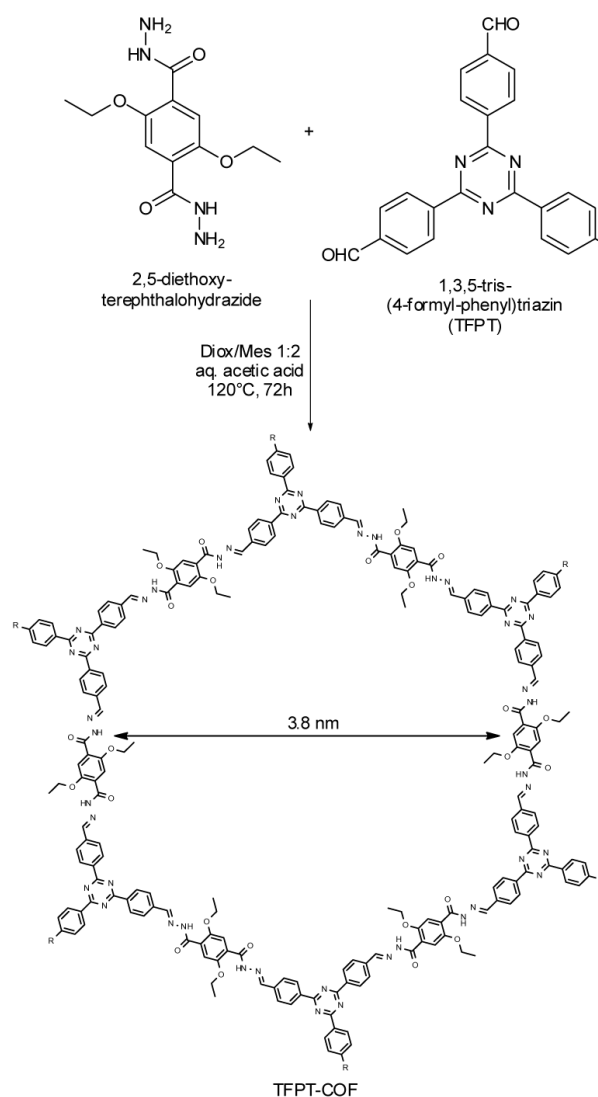
**Scheme S3** Synthesis of [4,4',4''-(1,3,5-triazine-2,4,6-triyl)tris(4,1-phenylene)]-tris(methanetriyl)hexaacetate (3) by threefold benzylic oxidation of 3 by  $\text{CrO}_3$  based on a modified literature procedure.<sup>S2</sup>

**1,3,5-tris-(4-formyl-phenyl)triazine (TFPT) (1)**

98 % sulfuric acid (0.53 mL, 14.7 eq) was added to a stirred suspension of compound 4 (460 mg, 0.66 mmol, 1.0 eq) in 5.25 mL of dest. water and 4.20 mL of ethanol in a Biotage® 20 mL microwave vial. The vial was sealed and the resulting mixture was heated under microwave irradiation to  $120^\circ\text{C}$  under stirring for 3 h. The resulting off-white precipitate was filtered, washed with water and dried under vacuum to yield title compound 1 (230 mg, 0.59 mmol, 89 %).  $^1\text{H}$  NMR data were consistent with the literature.



**Scheme S4** Synthesis of 1,3,5-*tris*-(4-formyl-phenyl)triazin (TFPT) (**1**) by a microwave-assisted acid catalyzed deprotection based on a modified literature procedure.<sup>S2</sup>



**Scheme S5** Synthesis of TFPT-COF by acid catalyzed hydrazone formation.

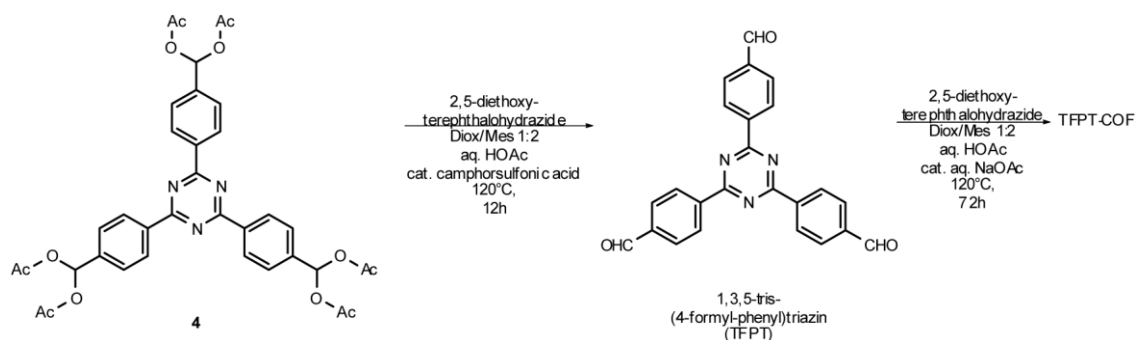
### TFPT-COF

To a Biotage® 5 mL microwave vial 17.7 mg (0.044 mmol, 2.0 eq.) of TFPT (**1**) and a stir bar was added. Then 18.6 mg (0.066 mmol, 3.0 eq) of 2,5-diethoxy-terephthalohydrazide was added and the vial was temporarily sealed with a rubber septum. Subsequently, the vial was flushed three times in argon/vacuum cycles. To the mixture 0.66 mL of mesitylene and 0.33 mL of 1,4-dioxane

were added and again degassed three times in argon/vacuum cycles. In one shot 100  $\mu\text{L}$  aqueous 6 M acetic acid was added, the vial was sealed and heated in a stirred oil bath with 120  $^{\circ}\text{C}$  (preheated) on a heating stirrer for 72 h. After slow cooling to room temperature the vial was opened and the whole mixture was centrifuged (3 x 15 min, 20000 rpm) while being washed with DMF (1 x 7 mL) and THF (2 x 7 mL). The resulting yellow precipitate was transferred to a storage vial with DCM, dried at room temperature, then in vacuum and characterized by powder X-ray diffraction.

Alternative workup: The vial was opened and the slurry suspension was transferred by a polyethylene pipette to a Büchner funnel and filtered. The filter cake was scratched off and transferred to an Erlenmeyer flask, washed with DMF (1 x 10 mL) and THF (2 x 10 mL) and again filtered off.

IR (FT, ATR): 3277 (*w*), 2966 (*w*), 2888 (*w*), 1674 (*s*), 1567 (*m*), 1515 (*s*), 1415 (*m*), 1356 (*s*), 1203 (*vs*), 1145 (*m*), 806 (*s*)  $\text{cm}^{-1}$ . For elemental analysis the COF was wrapped in filter paper and then washed with THF in a microwave oven with THF (100  $^{\circ}\text{C}$ , 3 x 20 mL). Then the COF was activated in high-vacuum for 12 h at 120  $^{\circ}\text{C}$  at  $10^{-7}$  mbar and kept under an inert atmosphere until elemental analysis was performed. Anal. calcd. for  $(\text{C}_{84}\text{H}_{74}\text{N}_{18}\text{O}_{12})_n$ : C, 66.04; H, 4.88; N, 16.50. Found: C, 64.17; H, 4.96; N, 15.48.



**Scheme S6** Synthesis of TFPT-COF by acid catalyzed *in situ* deprotection and subsequent hydrazone formation, carried out in one reaction vessel.

#### TFPT-COF from protected TFPT ([4,4',4''-(1,3,5-Triazine-2,4,6-triyl)tris(4,1-phenylene)]-tris(methane-triyl)hexaacetate (4))

To a Biotage® 5 mL microwave vial 30.8 mg (0.044 mmol, 2.0 eq) of **4** and a stir bar was added. Then 18.6 mg (0.066 mmol, 3.0 eq.) of 2,5-diethoxy-terephthalohydrazide was added and the vial was temporarily sealed with a rubber septum. Subsequently, the vial was flushed three times in argon/vacuum cycles. To the mixture 0.66 mL of mesitylene and 0.23 mL of 1,4-dioxane were added and again degassed three times in argon/vacuum cycles. In one shot 100  $\mu\text{L}$  aqueous 6 M acetic acid was added. To this vial, 0.10 mL ( $c = 20 \text{ mg mL}^{-1}$ , 0.008 mmol, 0.38 eq) of a solution of *rac*-camphorsulfonic acid in 1,4-dioxane was added, the vial was sealed and heated in a stirred oil bath with 120  $^{\circ}\text{C}$  (preheated) on a heating stirrer for 12 h. After cooling to room temperature, to the vial was added 0.02 mL ( $c = 35 \text{ mg mL}^{-1}$ , 0.008 mmol, 0.38 eq) of an aqueous solution of sodium acetate by a micro syringe. The vial was then reheated again on the preheated oil bath for 72 h at 120  $^{\circ}\text{C}$ . After slow cooling to room temperature the vial was opened and the whole mixture was centrifuged (3 x 15 min, 20000 rpm) while being washed with DMF (1 x 7 mL) and THF (2 x 7 mL). The resulting yellow precipitate was transferred to a storage vial with DCM, dried at room temperature, then in vacuum and characterized by powder X-ray diffraction.



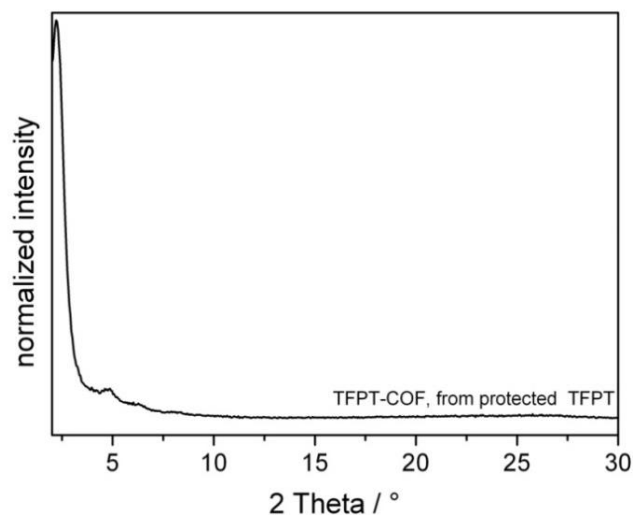


Figure S44 PXRD of the TFPT-COF from protected TFPT.

#### TFPT-COF reconverted after sonication in water/photocatalysis

To a Biotage® 5 mL microwave vial 20 mg of amorphous TFPT-COF and a stir bar were added. The vial was temporarily sealed with a rubber septum. Subsequently, the vial was flushed three times in argon/vacuum cycles. To the mixture 0.66 mL of mesitylene and 0.33 mL of 1,4-dioxane were added and again degassed three times in argon/vacuum cycles. In one shot 100  $\mu$ L aqueous 6 M acetic acid was added. The vial was sealed and heated in a stirred oil bath with 120 °C (preheated) on a heating stirrer for 72 h. After slow cooling to room temperature the vial was opened and the whole mixture was centrifuged (3 x 15 min, 20000 rpm) while being washed with DMF (1 x 7 mL) and THF (2 x 7 mL). The resulting yellow precipitate was transferred to a storage vial with DCM, dried at room temperature, then in vacuum and characterized by powder X-ray diffraction and BET surface area determination.

#### Results and discussion

##### FT-IR spectra

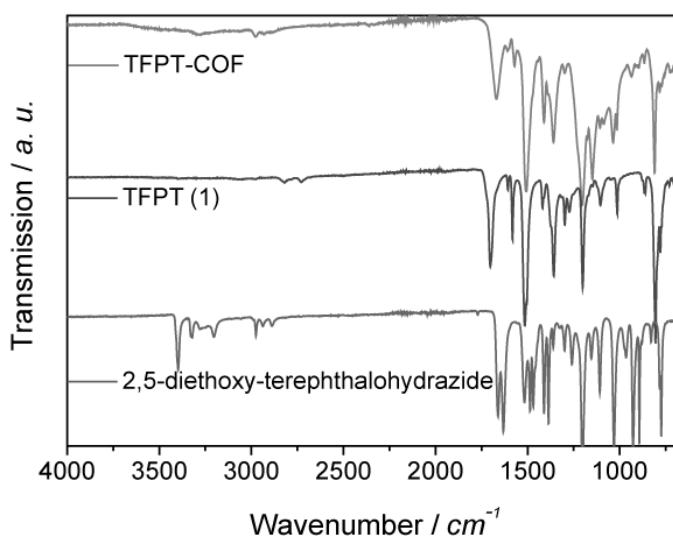


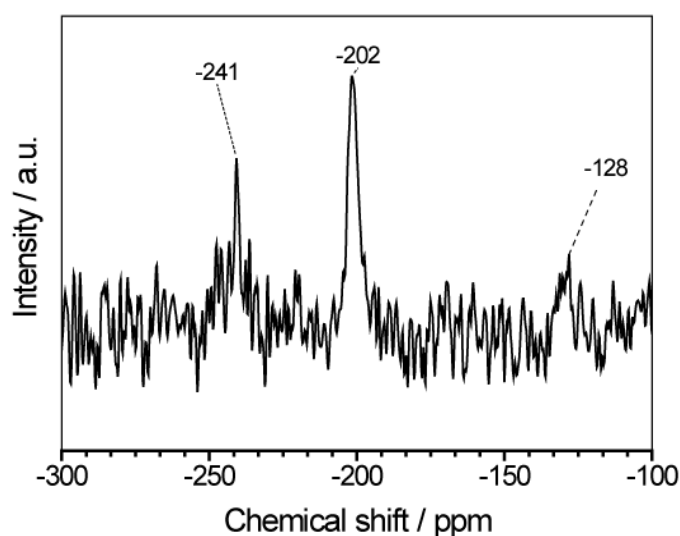
Figure S45 Stack plot FT-IR spectra of TFPT-COF and starting materials.

**Table S6** IR assignments for TFPT (purple), DETH (blue) and TFPT-COF (black).

wavenumber [cm <sup>-1</sup> ]	band Assignment
2824, 2721	fermi double peak, aldehyde C-H (specific)
> 3200	N-H stretching
1700	aldehyde C=O stretching
1632, 1660, 1670-1660, 1201	C=O stretching, C=N
806, 806	triazine ring breath

*CP-MAS NMR measurements*

The <sup>15</sup>N CP-MAS NMR spectrum exhibits a peak at -241 ppm, which we assign to the tertiary nitrogen of the hydrazone moiety, the peak at -202 ppm to the hydrazine secondary nitrogen, and the peak at -128 ppm to the nitrogen of the triazine ring.

**Figure S46** <sup>15</sup>N CP-MAS spectrum of TFPT-COF.*Powder X-ray diffraction data and structure simulation*

Molecular modeling of the COF was carried out using the Materials Studio (5.5) suite of programs by Accelrys. The unit cell was defined by two TFPT molecules bonded *via* six hydrazone linkages to 2,5-diethoxy-terephthalohydrazide. The initial structure was geometry optimized using the MS Forcite molecular dynamics module (Universal force fields, Ewald summations), and the resultant distance between opposite formyl carbon atoms in the structure was used as the *a* and *b* lattice parameters (initially 43 Å) of the hexagonal unit cell with *P6/m* symmetry (*bmn* net). The interlayer spacing *c* was chosen as 3.37 Å according to the 001 stacking reflection of the powder at  $2\theta = 26.6^\circ$ , and the crystal structure was geometry optimized using Forcite (resulting in  $a = b = 43.164$  Å).

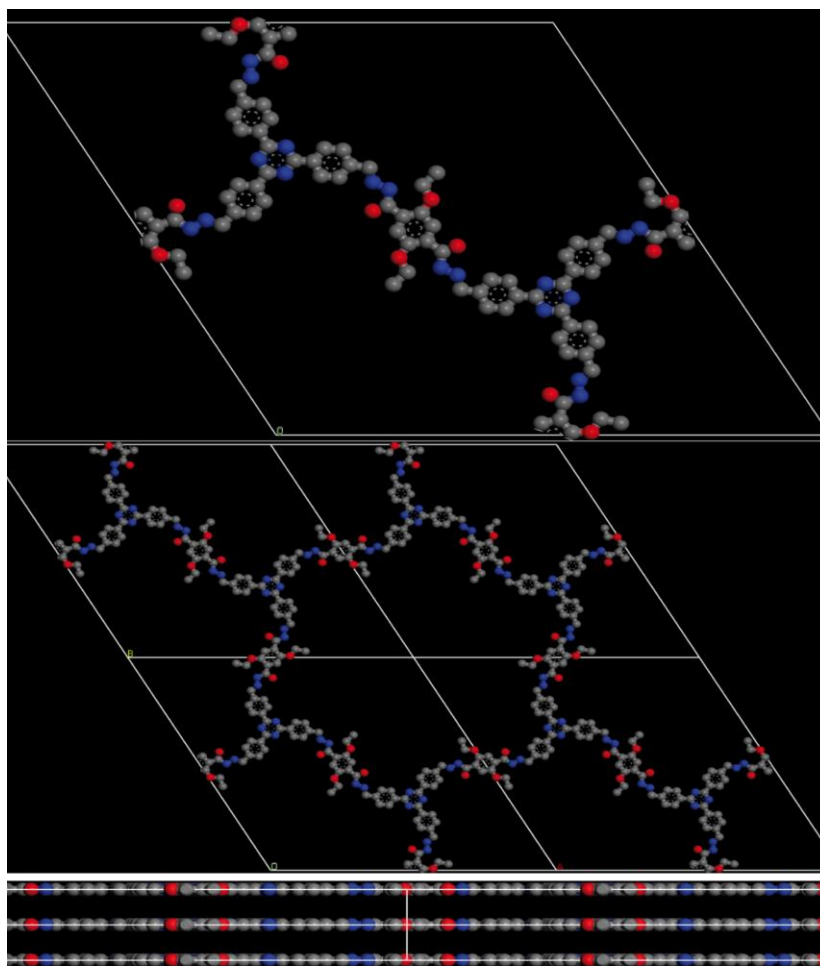


**Figure S47** Simulation of the unit cell content calculated in an eclipsed arrangement: top view onto the  $ab$ -plane and view perpendicular to the  $c$ -axis.

The MS Reflex Plus module was then used to calculate the PXRD pattern, which matched the experimentally observed pattern closely in both the positions and intensity of the reflections. The observed diffraction pattern was subjected to Pawley refinement wherein reflection profile and line shape parameters were refined using the crystallite size broadening (one size was extracted from the exp. PXRD with the help of the Scherrer equation  $\rightarrow$  crystal size:  $c = 35$  nm, kept fixed) and background in the 20<sup>th</sup> polynomial order. The refinement was applied to the calculated lattice, producing the refined PXRD profile with lattice parameters  $a = b = 41.895$  Å and  $c = 3.37$  Å.  $wRp$  and  $Rp$  values converged to 3.30 % and 6.73 %, respectively. The resulting refined crystallite size (149 nm in each lateral direction) is in reasonable agreement with the SEM and TEM data. Overlay of the observed and refined profiles shows good correlation (Figure S48).

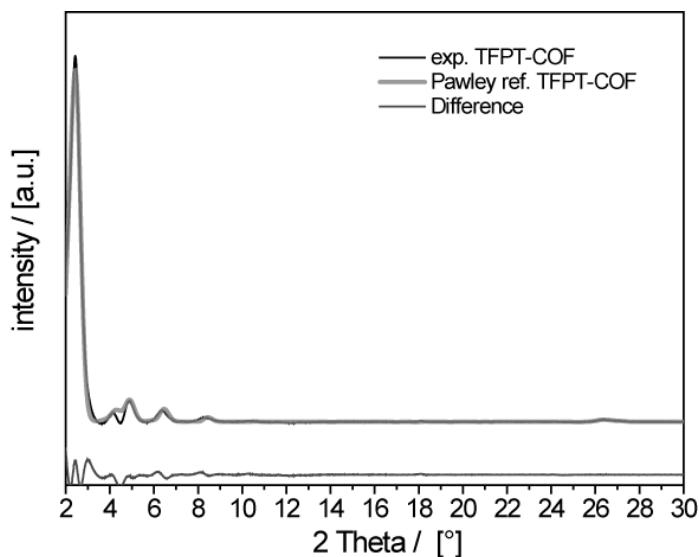


**Figure S48** Experimental powder pattern and Pawley refined pattern based on  $P6/m$  symmetry.

**Table S7** Atom coordinates of optimized  $P6/m$  structure.

atom	Ox.	Wyck.	atomic parameters		
			x/a	y/b	z/c
C1		6j	4.46484	0.49326	0
C2		6j	4.46961	0.46288	0
C3		6j	4.50666	0.46983	0
C7		6j	4.47874	0.55594	0
O8		6j	4.56434	0.57050	0
C10		6j	4.43337	0.39480	0
C11		6j	4.39330	0.36475	0
O14		6j	4.44518	0.54253	0
N15		6j	4.50051	0.59501	0
N19		6j	4.52013	0.38747	0
C21		6j	4.49094	0.64722	0
C23		6j	4.53965	0.34528	0
C25		6j	4.46512	0.69023	0
C26		6j	4.43386	0.69438	0
C27		6j	4.39837	0.66301	0
C28		6j	4.39415	0.62805	0
C29		6j	4.42460	0.62405	0
C30		6j	4.36484	0.66515	0
N31		6j	4.36636	0.69806	0

Even lower  $wRp$  and  $Rp$  values (1.94 % and 3.94 %) could be achieved by lowering the symmetry to  $P1$  (Figure S49) but keeping the angles  $\alpha$ ,  $\beta$  and  $\gamma = 90^\circ$ ,  $90^\circ$  and  $120^\circ$ . The resulting lattice parameters  $a$  and  $b$  were = 42.055 Å and 45.074 Å.

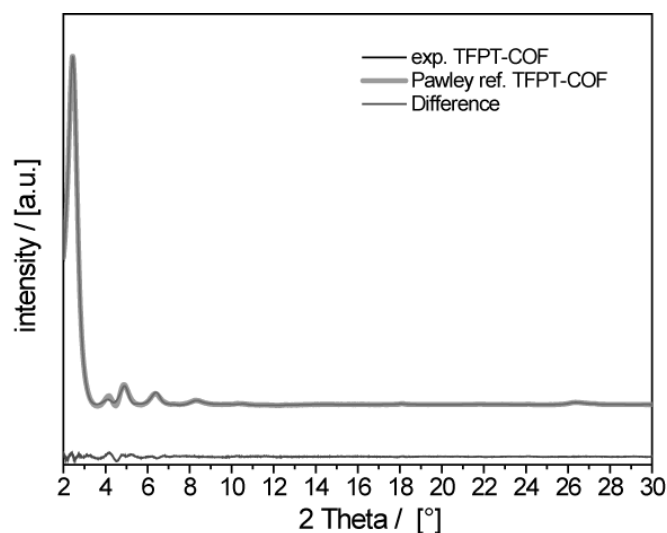


**Figure S49** Experimental powder pattern and Pawley refined pattern based on  $P1$  symmetry.

An alternative staggered COF arrangement was examined wherein  $P6_3/m$  symmetry was used (*gra* net). Comparison of the calculated PXRD pattern with the observed pattern shows less agreement with the experimental data (see Figure 4.2), thus ruling out this type of packing arrangement.

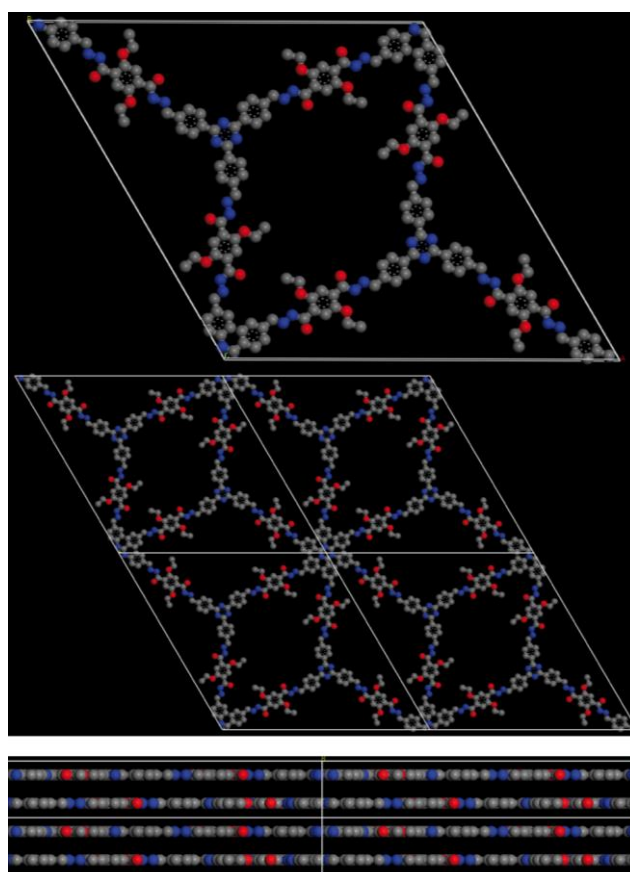


**Figure S50** Simulation of the crystal structure with staggered arrangement of adjacent layers: Top view onto the  $ab$ -plane and view perpendicular to the  $c$ -axis showing the doubled stacking period due to the staggered AB layer arrangement.

In a recent theoretical study on boronate COFs, *Dichtel et al.* (ref. 42) and *Heine* (ref. 41) pointed out that two adjacent layers in a COF are not expected to be aligned in a perfectly eclipsed manner, but shifted between  $\approx 1.3 \text{ \AA} - 1.8 \text{ \AA}$  in any direction parallel to the layer (parallel displacement). We

therefore simulated (using the software package Material Studio) an AA'A-structure of TFPT-COF where adjacent layers are offset by 1.4 Å, such that each partly positively charged carbon atom of triazine is situated beneath a partly negatively charged triazine nitrogen atom, which was found to be a likely structure for triazine units. The structure was simulated in *P1* symmetry with lattice parameters  $a = b = 42.16$  Å and  $c = 6.74$  Å ( $c$  axis doubled due to symmetry reasons).

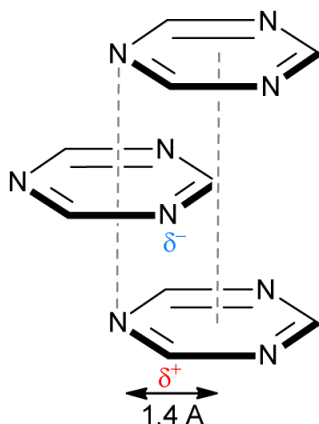


**Figure S51** Shift (parallel displacement) in a zig-zag manner to minimize electrostatic repulsion between adjacent layers.

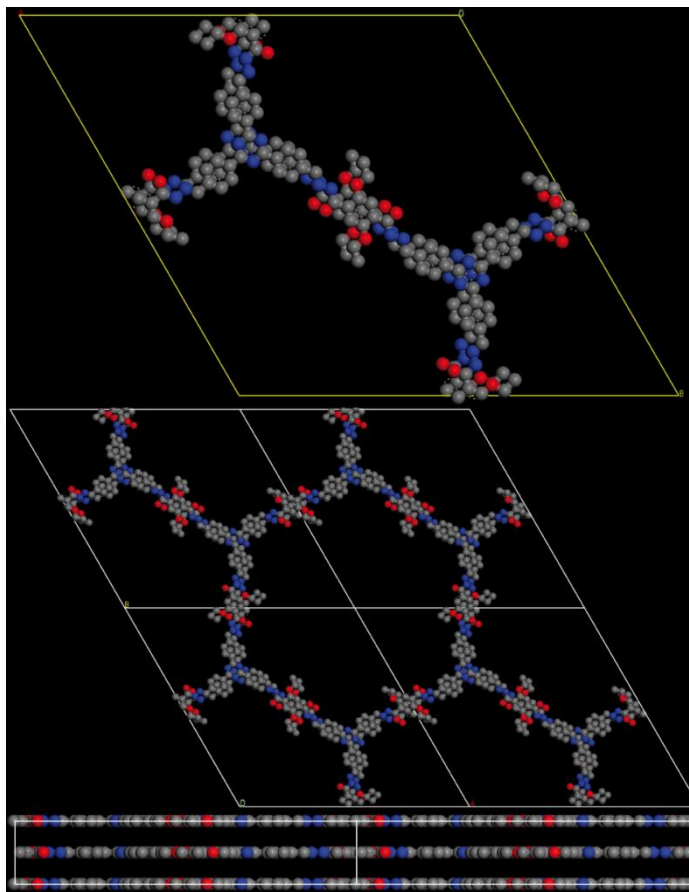


**Figure S52** Simulation of the unit cell content calculated in an eclipsed arrangement with 1.4 Å offset and zig-zag-arrangement of the layers: View onto the  $ab$ -plane (top) and view perpendicular to the  $c$ -axis (bottom).

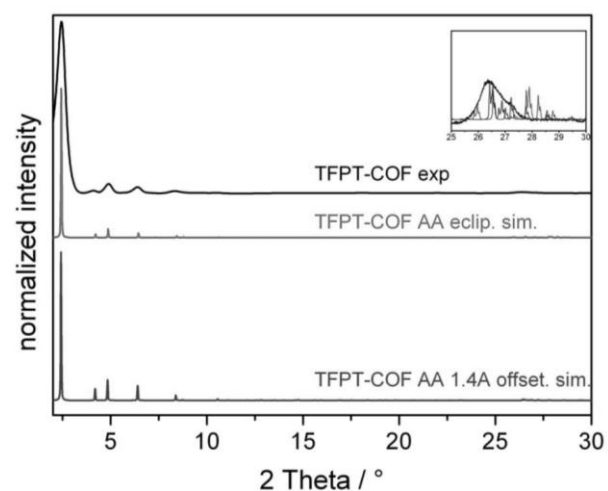


**Figure S53** Experimental powder pattern, simulated PXRD of perfectly eclipsed TFPT-COF and simulated PXRD of TFPT-COF with 1.4 Å parallel layer displacements.

*Sorption measurements and pore size distribution*

The Brunauer-Emmett-Teller (BET) surface area was calculated to be 1603 m<sup>2</sup> g<sup>-1</sup> (linear extrapolation between 0.20–0.32 p/p<sub>0</sub>).

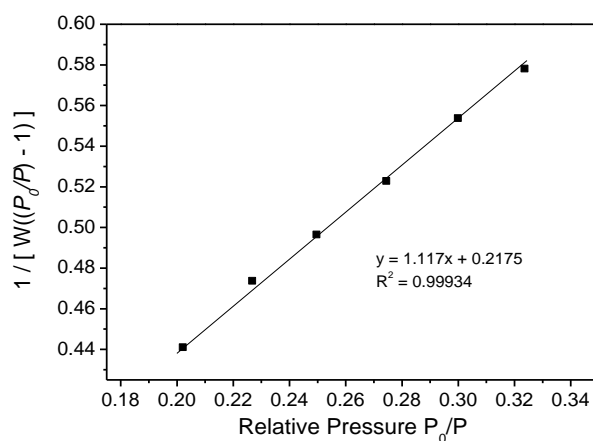


**Figure S54** Linear BET plot of TFPT-COF as obtained from Ar adsorption data at 87 K.

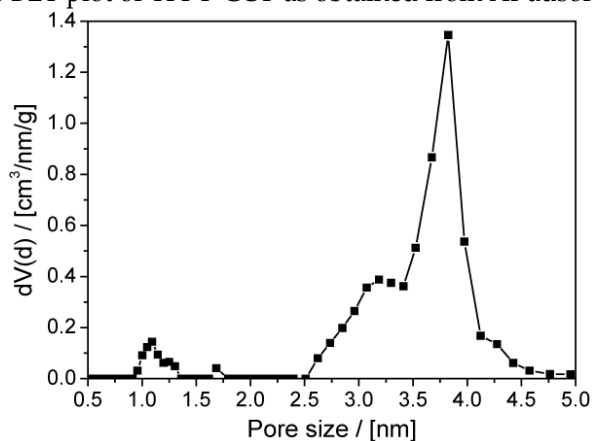


**Figure S55** Pore size distribution calculated based on NLDFT using the “Ar-zeolite/silica cylindrical pores at 87 K kernel”.

Plot of the Kubelka-Munk function

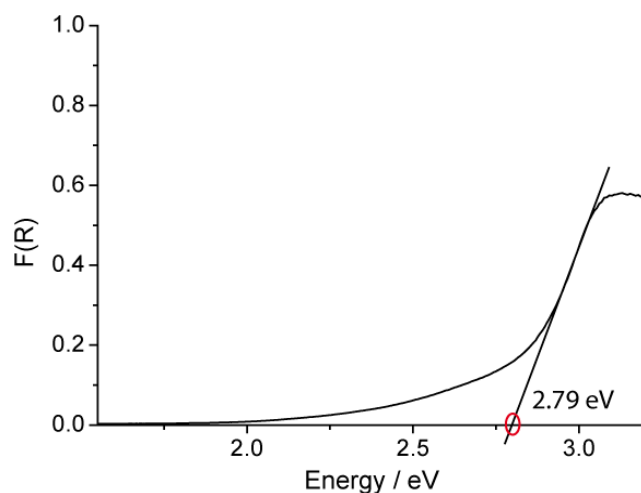


**Figure S56** Plot of Kubelka-Munk function used for band gap extraction.

*Stability of the TFPT-COF in organic solvents and water*

Stability in different organic solvents (DCM, DMF and MeOH) has been tested by soaking TFPT-COF (5 mg) in the corresponding solvent for 3 h at room temperature. A PXRD was recorded after filtration and drying in vacuum overnight.

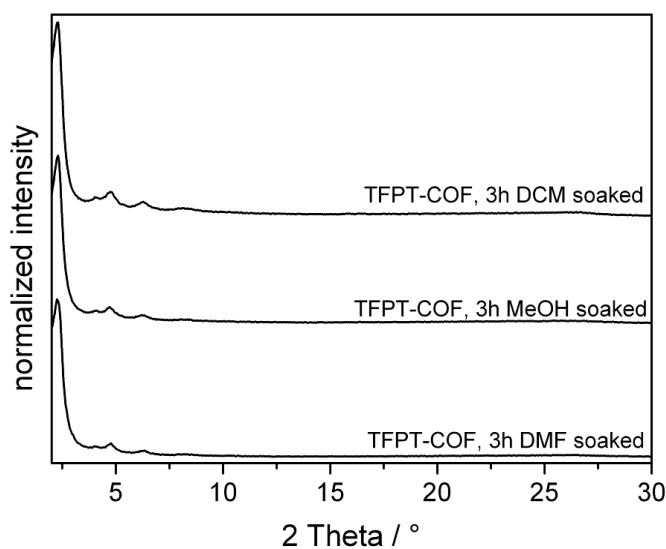


**Figure S57** PXRD measurements showing the retention of crystallinity after treatment with different solvents.

*Reconversion of TFPT-COF after photocatalysis*

20 mg of crystalline TFPT-COF (BET surface area =  $1190 \text{ m}^2 \text{ g}^{-1}$ ) was used for photocatalytic hydrogen production as described below. After irradiation with visible light for 95 h the TFPT-COF/Pt was filtered off as a green and amorphous solid (Figure S63) and washed with water, DMF ( $2 \times 7 \text{ mL}$ ) and THF ( $2 \times 7 \text{ mL}$ ). The organic filtrates were checked for any formed monomers (*e.g.* TFPT or DETH), but no traces of monomeric species were detected. The TFPT-COF/Pt has lost its crystallinity after photocatalysis as shown in Figure S58, and has a BET surface area of  $410 \text{ m}^2 \text{ g}^{-1}$  (Figure S60). The vacuum-dried powder can be reconverted (see section B) to recover crystalline TFPT-COF with its original PXRD pattern (Figure S58) and a high BET surface area of  $1184 \text{ m}^2 \text{ g}^{-1}$  (Figure S60) (yield: 14 mg, 70 %) by resubjecting it to the initial synthesis conditions. An Ar sorp-



tion isotherm of TFPT-COF/Pt<sub>reconv.</sub> was recorded and is shown in Figure S61. The corresponding pore size distribution is depicted in Figure S62, having a maximum at 3.7 nm. Further experiments revealed that the TFPT-COF has already lost its long-range order after sonication in water (Figure S58). However, the FT-IR spectrum shows the characteristic bands of the polymer (C=N at 1603 cm<sup>-2</sup>), while no additional peaks appear and no bands corresponding to the TFPT or DETH monomers are observed (Figure S59). The vacuum-dried powder can also be reconverted (see section B) to recover TFPT-COF with its original PXRD pattern (Figure S58).

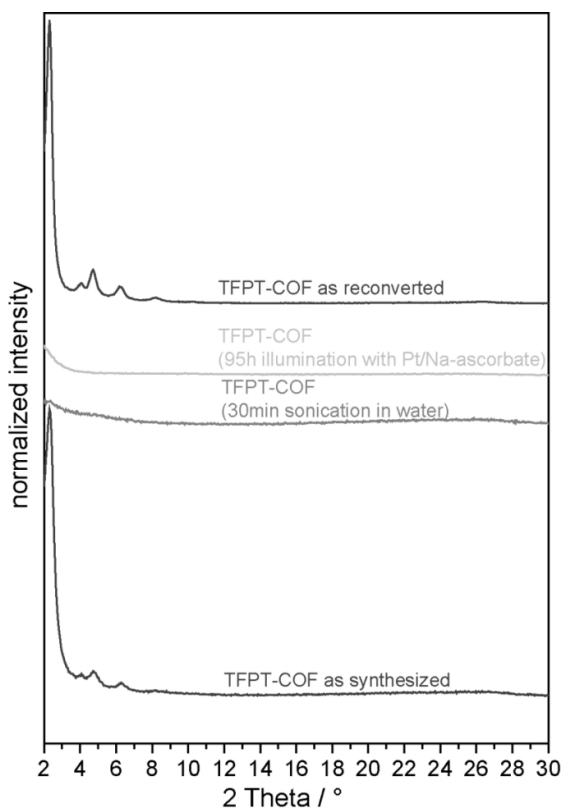


**Figure S58** PXRD patterns of TFPT-COF, showing loss of crystallinity after water exposure and photocatalysis. The crystalline TFPT-COF can be obtained by reversion by subjecting it to the initial crystallization conditions.

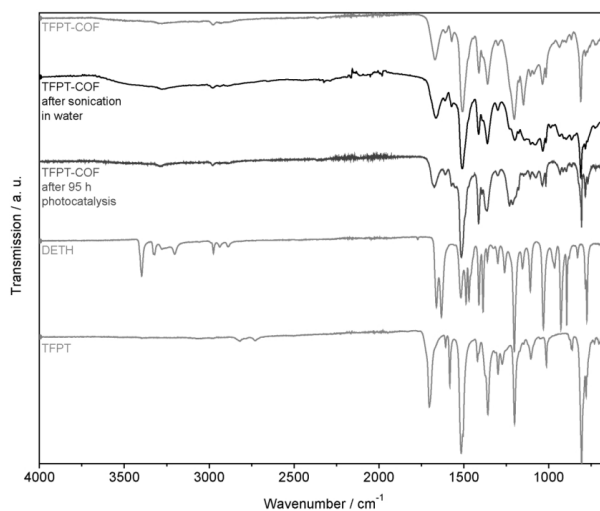


**Figure S59** FT-IR spectra showing the vibrational patterns of TFPT-COF before and after water exposure/photocatalysis.

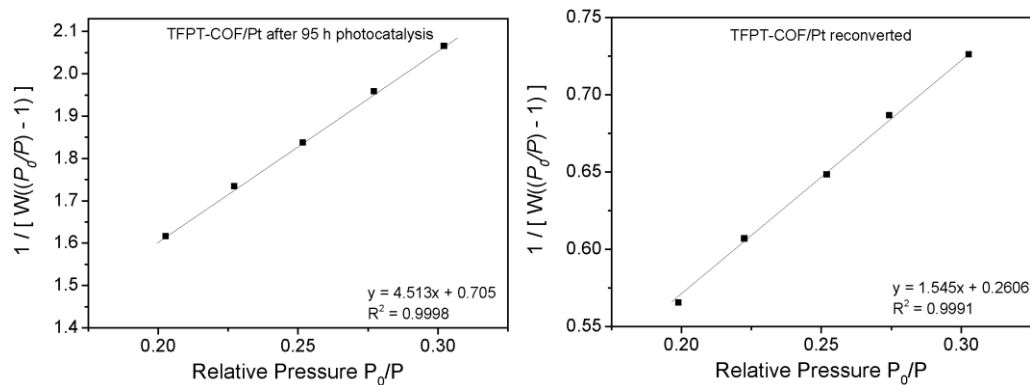


**Figure S60** Linear BET plot of TFPT-COF/Pt after 95 h photocatalysis and TFPT-COF/Pt (reconverted) as obtained from Ar adsorption data at 87 K.

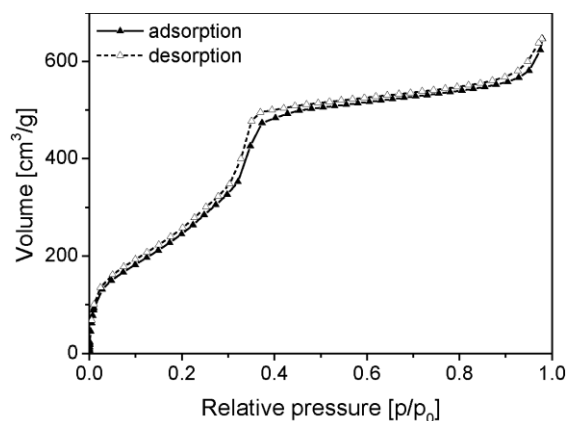


**Figure S61** Ar sorption isotherm recorded at 87 K.

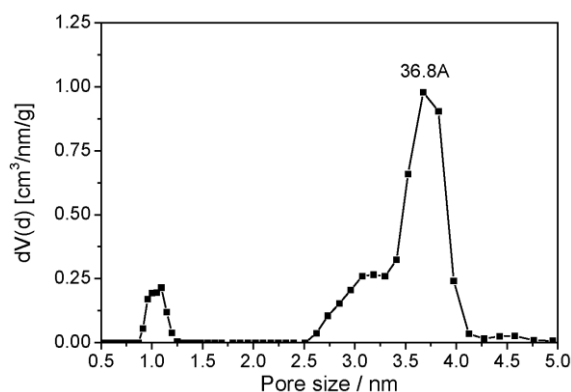


**Figure S62** Pore size distribution of TFPT/Pt after reconversion calculated based on NLDFT using the "Ar-zeolite/silica cylindrical pores at 87 K" kernel.



**Figure S63** Photographs showing TFPT-COF as-synthesized (left, yellow) and TFPT-COF/Pt after reconversion (right, green). TFPT-COF/Pt before reconversion is green, as well.

*Photocatalysis*

For long-time hydrogen evolution experiments in triethanolamine, the TFPT-COF catalyst (4 mg) was suspended in water (9 mL) and dispersed in an ultrasonic bath for 30 min. The sacrificial electron donor (1 mL) triethanolamine (TEoA, Alfa Aesar) and  $\text{H}_2\text{PtCl}_6$  (2.4  $\mu\text{L}$  of 8 wt% in  $\text{H}_2\text{O}$ , Sigma-Aldrich,  $\approx 2.2$  wt% Pt) as precursor for the *in situ* formation of the Pt co-catalyst was added. For long-time hydrogen evolution experiments in sodium ascorbate, the TFPT-COF catalyst (10 mg) was suspended in water (10 mL) and dispersed in an ultrasonic bath for 30 min. Sodium ascorbate as sacrificial electron donor (100 mg) (Sigma-Aldrich,  $\geq 98$  %) and  $\text{H}_2\text{PtCl}_6$  (6.0  $\mu\text{L}$  of 8 wt% in  $\text{H}_2\text{O}$ , Sigma-Aldrich,  $\approx 2.2$  wt% Pt) was added. The induction time and concomitant delay in hydrogen evolution observed in the first cycle is caused by the initial formation of Pt nanoparticles (induction time). The first cycle represents the first three hours of the long-term measurement—the induction time period—where Pt nanoparticles are formed by the photoreduction of  $\text{H}_2\text{PtCl}_6$ . For each cycle the photocatalyst (Pt-doped COF) was separated from its suspension (for the photocatalytic measurements) by centrifugation and was washed several times with water. The dried photocatalyst was redispersed with a fresh sodium ascorbate solution (10 mL of water and 100 mg of sodium ascorbate) and illuminated for 3 hours ( $<420$  nm) for each cycle. For visible light and UV experiments the suspensions were illuminated at a distance of 26 cm from the light source in a 230 mL quartz glass reactor with a PTFE septum under argon atmosphere. The flask was evacuated and purged with argon to remove any dissolved gases in the solution. Samples were simultaneously top-illuminated (top surface = 15.5  $\text{cm}^2$ ) with a 300 W Xenon lamp with a water filter and dichroic mirror blocking wavelengths  $<420$  nm for visible light measurements while stirring. For the action spectra, the full spectrum of the Xenon lamp coupled with a band-pass filter (400 nm, 450 nm, 500 nm, 550 nm or 600 nm; bandwidth  $\pm 20$  nm) and an 1.5 AM filter was used. Here, an aqueous triethanolamine suspension with 10 mg of Pt-doped catalyst was illuminated for three hours and the concentration of evolved hydrogen was determined by gas chromatography. The intensity of the light was measured for each wavelength, enabling the conversion of produced hydrogen values into quantum efficiencies. For oxygen evolution measurements photodeposition of  $\text{IrO}_2$  nanoparticles as oxygen-evolving co-catalyst was carried out before the photocatalytic reaction following a literature procedure.<sup>54,5</sup> To this end, 40 mg of the catalyst was dispersed in a reactant solution containing  $\text{K}_2[\text{IrCl}_6]$  (1.8 mg,  $\approx 2$  wt%, Alfa Aesar) and 40 mL of a 5 mM aqueous  $\text{KNO}_3$  solution. The suspension was irradiated as described above for 2 h using the full spectrum of the Xenon lamp. The TFPT-COF catalyst loaded with the co-catalyst was isolated from the aqueous  $\text{KNO}_3$  solution, washed several times with water, and then dried at 100 °C in a stream of argon. The  $\text{IrO}_2$ -loaded catalyst (10 mg) was dispersed in water or a phosphate buffer solution (10 mL, 0.1 M, pH = 11 or pH = 7).  $\text{Na}_2\text{S}_2\text{O}_8$  (110 mg, Sigma-Aldrich) or  $\text{AgNO}_3$  (16 mg) was added as electron acceptor. The headspace of the reactor was periodically sampled with an online injection system and the gas components were quantified by gas chromatography (thermal conductivity detector, argon as carrier gas). The quantum efficiency of the photocatalysts, under irradiation with the band-pass filter  $500 \pm 20$  nm, was determined as follows. The power of the incident light was measured with a thermo power sensor (Thorlabs) to be 14  $\text{mW cm}^{-2}$ , which is equivalent to a photon flux of 701  $\mu\text{mol h}^{-1}$ . Quantum efficiency was calculated using the equation:  $\text{AQE} = 2 \cdot [\text{H}_2]/I$  where  $I$  is the photon flux in  $\mu\text{mol h}^{-1}$  and  $[\text{H}_2]$  is the average rate of  $\text{H}_2$  evolution in  $\mu\text{mol h}^{-1}$ .

## Stability of TFPT-COF during photocatalysis

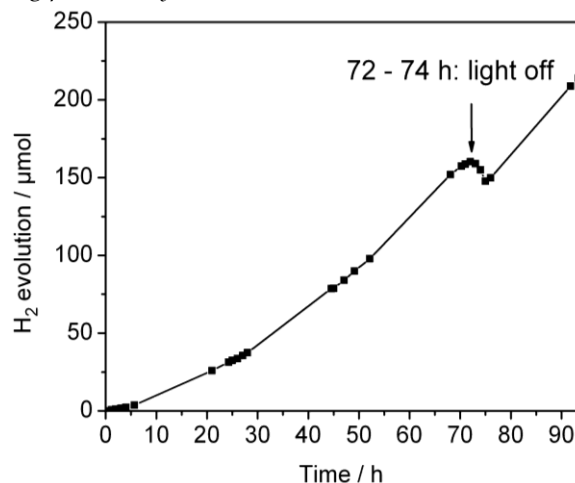


**Figure S64** Stability measurements of TFPT-COF for 95 h with ascorbate as sacrificial donor. Between the 72<sup>th</sup> and 74<sup>th</sup> hour the light source was turned off to show no hydrogen evolution in the dark (the amount of hydrogen concentration decreased during these hours due to the fact that sampling was performed, *i.e.* removing sample volume during detection).

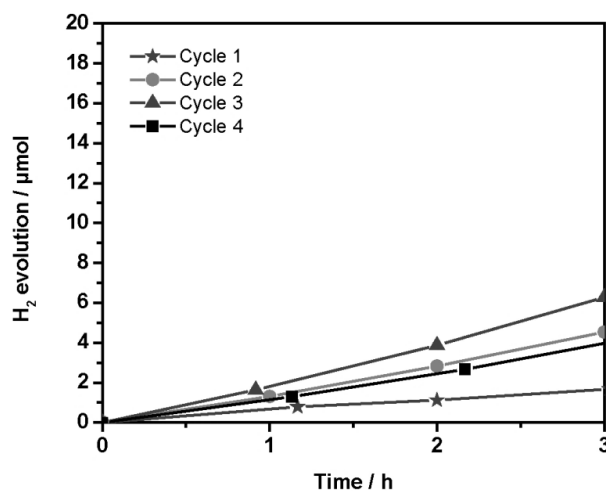


**Figure S65** Cycle measurements of TFPT-COF/Pt with sodium ascorbate as sacrificial donor. The first cycle (Cycle 1) corresponds to the first three hours of the long-term stability measurements (95 h) and shows decreased rates due to formation of Pt nanoparticles (induction period). The other cycles were carried out after centrifugation of the photocatalyst, washing with water and resuspending it in a fresh aqueous sodium ascorbate solution.

## Bibliography

- (S1) F. J. Uribe-Romo, C. J. Doonan, H. Furukawa, K. Oisaki, O. M. Yaghi, *J. Am. Chem. Soc.* **2011**, *133*, 11478.
- (S2) S.-H. Li, H.-P. Huang, S.-Y. Yu, X.-P. Li, *Chin. J. Chem.* **2006**, *24*, 1225.
- (S3) V. Volkis, E. Nelkenbaum, A. Lisovskii, G. Hasson, R. Semiat, M. Kapon, M. Botoshansky, Y. Eishen, M. S. Eisen, *J. Am. Chem. Soc.* **2003**, *125*, 2179.
- (S4) T. Ikeda, A. Tsuda, N. Aratani, A. Osuka, *Chem. Lett.* **2006**, *35*, 946.
- (S5) E. M. Sabio, R. L. Chamousis, N. D. Browning, F. E. Osterloh, *J. Phys. Chem. C.* **2012**, *116*, 3161.

### 7.1.5 Supporting information of Chapter 4.2

#### Experimental section

##### Methods

Argon adsorption/desorption measurements were performed at 87 K with an Autosorb-iQ surface analyzer (Quantachrome Instruments, USA). Samples were outgassed in vacuum at 120 °C for 6–12 h to remove all guests. For BET calculations pressure ranges of the Ar isotherms were chosen with the help of the BET Assistant in the ASiQwin software. In accordance with the ISO recommendations multipoint BET tags equal or below the maximum in  $V \cdot (1 - P/P_0)$  were chosen. IR spectroscopy measurements were carried out on a Perkin Elmer Spektrum BX II (Perkin Elmer, USA) with an attenuated total reflectance unit. PXRD was measured on a BRUKER D8 Avance (Bruker AXS, USA) in Bragg-Brentano geometry with a Cu-K $\alpha_1$ -radiation ( $\lambda = 1.54051$  Å). Elemental analysis (EA) was carried out with an Elementarvario EL (Elementar Analysensysteme, Germany). EDX was carried out on a JEOL JSM-6500F electron microscope (JEOL, Japan) with a field emission source equipped with an EDX detector (model 7418, Oxford Instruments, UK) and a Tescan Vega TS 5130MM electron microscope equipped with a Si/Li EDX detector (Oxford Instruments, UK). Inductively coupled plasma atomic emission spectroscopy (ICP-AES) was carried with a pressure digestion system by Berghof, a plasma created on a Vista Pro ICP-AES spectrometer, an Echelle-Polychromator by Fa. Varian Darmstadt and a photomultiplier.  $^{13}\text{C}$  MAS ssNMR spectra were recorded at ambient temperature on a BRUKER DSX Avance 500 FT and a BRUKER AvanceIII HD 400 NMR spectrometer (Bruker Biospin, Germany) with external magnetic fields of 11.8 T and 9.4 T, respectively. The operating frequencies are 500.1 MHz and 125.7 MHz and 400.1 MHz and 100.6 MHz for  $^1\text{H}$  and  $^{13}\text{C}$ , respectively, and the spectra were referenced relative to TMS. The samples were contained in 4 or 3.2 mm  $\text{ZrO}_2$  rotors and mounted in standard triple resonance BRUKER MAS probes. The spinning speed was set to 10 kHz or 20 kHz (for the photocatalyst after photocatalysis, CTF-1 and quantitative  $^{13}\text{C}$  measurements). During acquisition of the spectra  $^1\text{H}$  decoupling (approx. 70 kHz RF field) was applied using a SPINAL64 sequence. For  $^1\text{H}^{13}\text{C}$  ramp-amplitude (RAMP) cross-polarization (CP) MAS spectra a contact time of 5 ms and a  $90^\circ$  puls length of 2.50  $\mu\text{s}$  on  $^1\text{H}$  was set. The quantitative  $^{13}\text{C}$  measurements were recorded using a single pulse (SP) experiment. The recycle delay was varied between 60 and 6000 s for PTO-300-10, to get an idea about the T1. For the final measurements a recycle delay of 6000 s was used and 64 scans were executed. The background signal was recorded using a recycle delay of 0.5 s to make sure that only the background signal is relaxed and gives a signal. This signal was subtracted from the spectrum.  $^1\text{H}^{15}\text{N}$  CP-MAS ssNMR spectra were measured at ambient temperature on a BRUKER AvanceIII HD 400 NMR (PTO-300-1 und -10) and a BRUKER AvanceII 300 (CTF-1) NMR spectrometer with external magnetic fields of 9.4 T and 7.1 T, respectively. The operating frequencies are 400.1 MHz and 40.6 MHz and 300.1 MHz and 30.4 MHz for  $^1\text{H}$  and  $^{15}\text{N}$ , respectively. The samples were contained in 4 or 7 mm  $\text{ZrO}_2$  rotors which were mounted in standard double or triple resonance BRUKER MAS probes. The spinning speed was set to 10 or 5 kHz and the chemical shifts were referenced relative to nitromethane. During acquisition of the spectra  $^1\text{H}$  decoupling (approx. 70 kHz RF field) was applied using a SPINAL64 sequence. The spectra were recorded using a RAMP CP pulse on  $^1\text{H}$  with a nutation frequency  $\nu_{\text{nut}}$  of 40 kHz and 45 kHz on  $^{15}\text{N}$ , respectively. During a contact time of 5 ms the  $^1\text{H}$  RF field was linearly varied about 50%. The recycle delay was set to 2 s and 1.5 s. About 120000 and 40000 transients were accumulated for the CP experiments, respectively. For XPS, samples were pressed onto indium foil and the spectra were collected on an Axis Ultra (KRATOS Analytical, Manchester) X-ray photoelectron spectrometer with charge neutralization. The spectra

were processed using the software OriginPro 8.5.1 and fitted with the Gaussian function. The spectra were referenced to the adventitious carbon 1s peak at 284.600 eV. Binding energies were compared with the NIST Standard Reference Database 30 (Version 4.1) unless otherwise specified. Matrix-assisted laser deposition/ionization-time of flight (MALDI-TOF) was performed on a Shimadzu Axima Resonance mass spectrometer. Calibration was carried out using neat fullerene and using CsI ground with *trans*-2-[3-(4-*tert*-butylphenyl)-2-methyl-2-propenyldiene] malononitrile as the matrix. Each sample was ground with dithranol ( $m/z = 227$ ) as the matrix and deposited on a steel sample holder. The spectra were collected in raster mode and the laser power was progressively increased until a suitable signal-to-noise ratio was achieved. The presented spectra are averaged from 100 profiles. Optical diffuse reflectance spectra of the solids were collected at room temperature with a UV-Vis-NIR diffuse reflectance spectrometer Cary 5000 (Agilent Technologies, USA) at a photometric range of 250 nm–800 nm. Powders were prepared in a sample carrier with a quartz glass window at the edge of the integrating sphere with BaSO<sub>4</sub> as the optical standard. Kubelka-Munk spectra were calculated from the reflectance data. TEM was performed with a Philips CM 30 ST microscope (LaB<sub>6</sub> cathode, 300 kV, CS = 1.15 mm). Images were recorded with a CCD camera (Gatan) and Digital Micrograph 3.6.1 (Gatan) was used as evaluation software. Hydrogen evolution experiments in UV and simulated sunlight were carried out in a continuously cooled 230 mL quartz glass reactor (see Figure S66) with a PTFE septum under argon atmosphere. The catalyst (10 mg) was suspended in a 0.5 M pH 7 phosphate buffer solution (9 mL), triethanolamine (TEoA) was used as the sacrificial electron donor (1 mL), and H<sub>2</sub>PtCl<sub>6</sub> (6 μL of 8 wt% in H<sub>2</sub>O, ≈ 2.2 wt% Pt, Figure S90) was added as precursor for the *in situ* formation of the Pt co-catalyst while stirring. Buffered water conditions lead to higher activities and a more stable hydrogen evolution rate than using non-buffered water (Figure S83). The flask was evacuated and purged with argon to remove any dissolved gases in the suspension. Samples were simultaneously top-illuminated (top surface = 15.5 cm<sup>2</sup>) at a distance of 22 cm with a 300 W Xenon lamp with a water filter and dichroic mirror (Newport Oriel) blocking most of the wavelengths < 420 nm for simulated sunlight (spectral profile see Figure S67) and < 250 nm for UV-Vis measurements, which amounts to a light intensity of about 380 mW cm<sup>-2</sup> for the simulated sunlight and 510 mW cm<sup>-2</sup> for the ≥ 250 nm measurements on the surface of the sample.

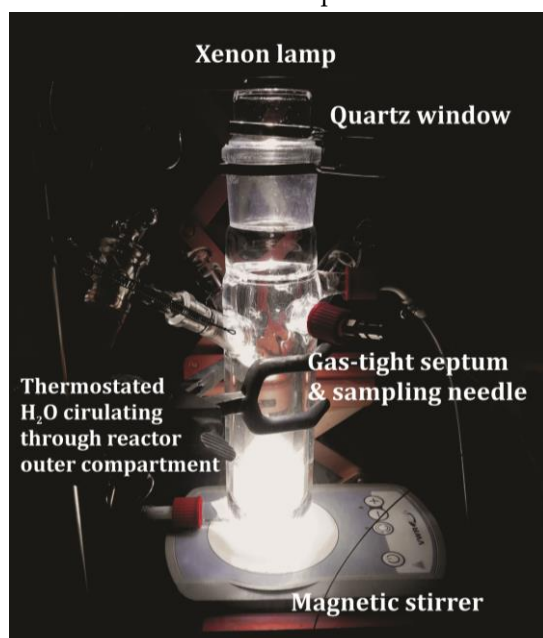


**Figure S66** Reactor set-up used for evaluating photocatalysts for hydrogen evolution.

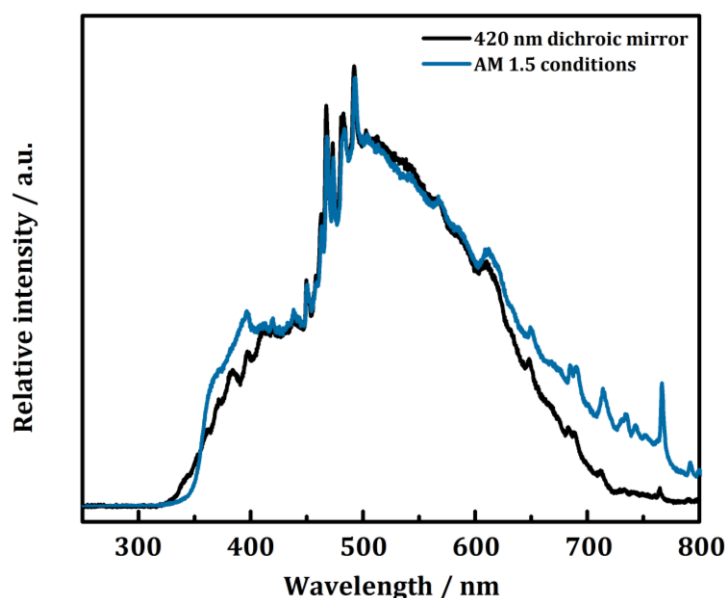


**Figure S67** Light intensity profile of the Xe lamp using the  $\geq 420$  nm dichroic mirror (simulated sunlight) compared to the AM 1.5 filter (filter and mirror purchased from Newport Oriel). Spectra were recorded with an Ocean Optics USB4000-XR1-ES spectrometer.

The headspace of the reactor was periodically sampled with an online injection system and the gas components were quantified by gas chromatography (thermal conductivity detector, argon as carrier gas). A high hydrophobicity of the CTF-1 and PTO samples was noticed at the beginning which was reduced during the photocatalytic experiment due to a better dispersion of the photocatalyst. Interestingly, the hydrogen evolution rates of the PTO-300s ( $> 1$  eq  $\text{ZnCl}_2$ ) illuminated with simulated sunlight were just slightly lower than for the samples illuminated with  $\geq 250$  nm. Apparent quantum efficiency calculations were estimated according to  $\text{AQE \%} = (2 \times H) / P \times 100 / 1$ , where  $H$  = number of evolved hydrogen molecules and  $P$  = incident number of photons on the sample. The incident light was measured with a thermopile power meter with a constant efficiency response across the visible spectrum. Wavelength specific hydrogen evolution experiments were carried out in a 30 mL glass vial also in an argon atmosphere with PTFE/Teflon septa. The samples were top-illuminated for four hours with a full spectrum mirror ( $\geq 250$  nm) and additional 40 nm FWHM light filters (400 nm, 450 nm, 500 nm, 550 nm or 600 nm) (Thor labs). The irradiation area was  $3.6 \text{ cm}^2$ . The hydrogen evolution rates were normalized with respect to irradiation intensity on the sample surface of  $14 \text{ mW cm}^{-2}$ . For the internal comparison with other organic photocatalysts (melon, PTI nanosheets and TFPT-COF), reported conditions for these materials were chosen which means using water instead of the buffered solution. Four different PTO-300 samples were also tested under AM 1.5 conditions ( $100 \text{ mW cm}^{-2}$ ) which is shown in Figure S85.

#### *Materials and syntheses*

All reactions were carried out under an argon atmosphere in flame-dried glassware. 1,4-Dicyanobenzene (98 %), DMF (99.8 %) and 1,5-bis(diphenylphosphino)pentane (97 %) were obtained from Acros Organics. Anhydrous zinc chloride (99.995 %, 25 mg product sealed in an ampule), 4-bromobenzonitrile (99 %) and  $\text{Pd}(\text{PPh}_3)_4$  (99 %) were purchased from Sigma-Aldrich. Triflic acid and zinc cyanide (98 %) were received from Alfa Aesar (98 %) and used without further purifications.

Synthesis of photoactive phenyl-triazine oligomers (PTO). In a typical CTF synthesis<sup>51</sup> a Duran ampule (1.5 x 12 cm) was charged with finely ground 1,4-dicyanobenzene (500 mg, 3.90 mmol) and ZnCl<sub>2</sub> (1-15 equivalents, see Table 5) within a glove box. The ampule was flame sealed under vacuum and was subjected in a tube oven to temperatures between 300 °C – 350 °C for 168 h – 96 h (see Table 5). After cooling to ambient temperature, the ampule was opened and its content ground thoroughly. An inhomogeneous temperature zone in addition to a high zinc chloride content yielded colorless, fiber-like crystals (which are not discussed here). The crude product was stirred in H<sub>2</sub>O (75 mL) for 1 h, filtered, and washed with 1 M HCl (2 x 75 mL). The mixture was then stirred at 90 °C in 1 M HCl (75 mL) overnight, filtered, and subsequently washed with 1 M HCl (3 x 75 mL), H<sub>2</sub>O (12 x 75 mL), THF (2 x 75 mL), and dichloromethane (1 x 75 mL). Finally, the powder was dried overnight in a desiccator.

Synthesis of CTF-1.<sup>51</sup> Similar to the synthesis described above, CTF-1 was obtained starting with 1,4-dicyanobenzene (500 mg, 3.90 mmol) under ZnCl<sub>2</sub> (1 equivalent) conditions at a reaction temperature of 400 °C for 46 hours.

Synthesis of 2,4,6-tris(*p*-bromophenyl)-1,3,5-triazine. This compound was prepared as per a modified literature procedure.<sup>52</sup> To a 15 ml Schlenk tube under argon, triflic acid (4.0 ml, 6.7 g, 44.6 mmol) was added and cooled to 0 °C. To this, 4-bromobenzonitrile (1.5 g, 8.2 mmol) was added in portions and the solution was continued to stir for an hour at 0 °C and then 16 hours at room temperature. The workup was done by pouring the reaction mixture in 100 mL ice cold water and neutralizing the resulting suspension with 25% ammonia solution. The precipitate was filtered off, washed with water (2 x 10 mL), acetone (3 x 5 mL) and dried in vacuum to afford the title compound as off-white solid (1.4 g, 94 %). <sup>1</sup>H NMR (CDCl<sub>3</sub>, 300 MHz): δ ppm 8.59 (d, *J* = 8.4 Hz, 6H), 7.72 (d, *J* = 8.4 Hz, 6H). <sup>13</sup>C NMR (CDCl<sub>3</sub>, 75 MHz): δ ppm 171.37, 135.07, 132.10, 130.55, 127.88.

Synthesis of 2,4,6-tris(*p*-cyanophenyl)-1,3,5-triazine (Trimer). In a microwave vial charged with DMF (10.0 mL), a stream of argon was bubbled for 30 min. To this was then added 2,4,6-tris(*p*-bromophenyl)-1,3,5-triazine (200 mg, 0.37 mmol), Zn(CN)<sub>2</sub> (67 mg, 0.57 mmol), Pd(PPh<sub>3</sub>)<sub>4</sub> (25 mg, 0.022 mmol), and 1,5-bis(diphenylphosphino)pentane (10 mg, 0.022 mmol). The vial was sealed and the contents were heated in a microwave for 20 min at 150 °C. The resulting suspension was poured into water (100 mL) and then filtered, washed with water (20 mL x 2), saturated sodium bicarbonate solution (10 mL x 2) and methanol (20 mL x 2) to obtain the crude product that was purified by flash chromatography (CHCl<sub>3</sub>) to obtain 2,4,6-tris(*p*-cyanophenyl)-1,3,5-triazine (Trimer) (120 mg, 85 %) as colorless solid. <sup>1</sup>H NMR 300 MHz (C<sub>2</sub>D<sub>2</sub>Cl<sub>4</sub>; 70 °C): δ 8.87 (d, *J* = 8.3 Hz, 6H), 7.93 (d, *J* = 8.3 Hz, 6H). <sup>13</sup>C NMR 75 MHz (C<sub>2</sub>D<sub>2</sub>Cl<sub>4</sub>; 70 °C): δ 170.90, 139.14, 132.46, 129.39, 118.09, 116.30. MS (MALDI): *m/z*: 384.4.

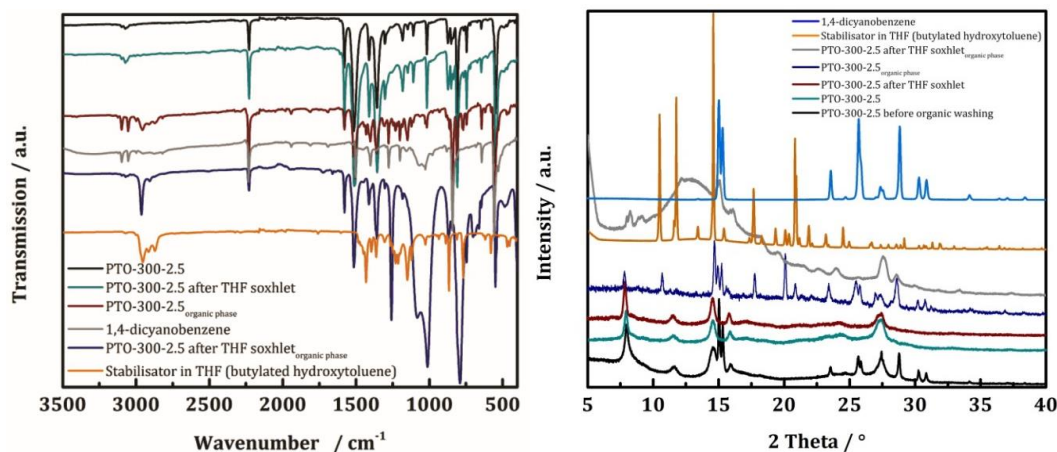
Synthesis of melon.<sup>53</sup> A porcelain crucible was loaded with dicyandiamide and heated in a muffle furnace at 600 °C for 4 hours. The synthesis yielded a yellow colored powder.

Synthesis of 16% 4-AP doped amorphous PTI.<sup>54</sup> Dicyandiamide (0.50 g, 5.95 mmol), a eutectic mixture of lithium chloride (59.2 mol%) and potassium chloride (40.8 mol%) and 4AP (72 mg, 16 % carbon-doping) as doping agent were ground and transferred in open porcelain crucibles, which were heated in a argon purged horizontal tube furnace at 12 °C min<sup>-1</sup> to 550 °C for 6 hours. After grinding the sample, the heating procedure was repeated to gain a homogenous polymerized product. The syntheses yielded in a dark orange colored product which is in accordance with the literature.<sup>54</sup>

Synthesis of TFPT-COF and PTI-nanosheets according to the literature.<sup>55,6</sup>



## Results and discussion

Characterization of PTO<sub>organic phase</sub>

**Figure S68** Exemplary IR spectra (left) and PXRDs (right) of the obtained organic phase after washing PTO-300-2.5 using THF and DCM (PTO-300-2.5<sub>organic phase</sub>) compared to pristine PTO-300-2.5, after further THF Soxhlet extraction, and of its organic phase from Soxhlet extraction. The IR spectra of the starting material 1,4-dicyanobenzene and of the THF-stabilizer butylated hydroxyl toluene is added for clarity. The first organic phase contains unreacted starting material and most likely smaller oligomers. The organic phase obtained by Soxhlet extraction includes also stabilizer impurities.

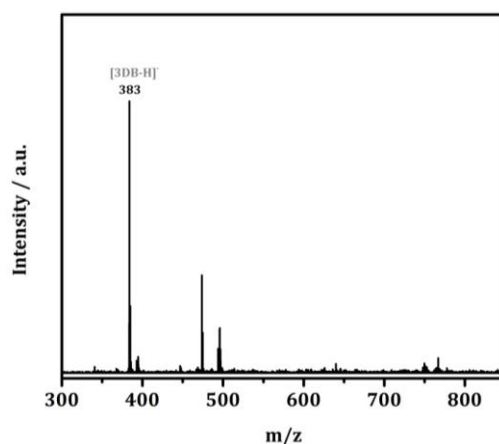


**Figure S69** MALDI-TOF spectrum (negative mode) of PTO-300-15<sub>organic phase</sub> showing a trimer fragment. No signals were observed in the mass ranges below 300 and above 850.

## XRD Characterization

**Table S8** Shift of the layer stacking from PTO-300-1 to PTO-300-15 compared to CTF-1.

sample	2 Theta / °	layer distance [Å]
CTF-1 <sup>S1</sup>	26.2	3.40
PTO-300-1	26.8	3.32
PTO-300-2.5	27.3	3.26
PTO-300-5	27.3	3.26
PTO-300-10	27.3	3.26
PTO-300-15	27.3	3.26

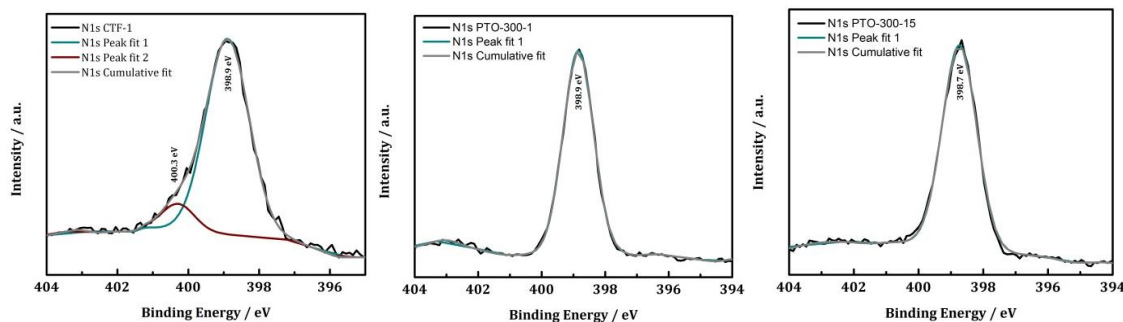
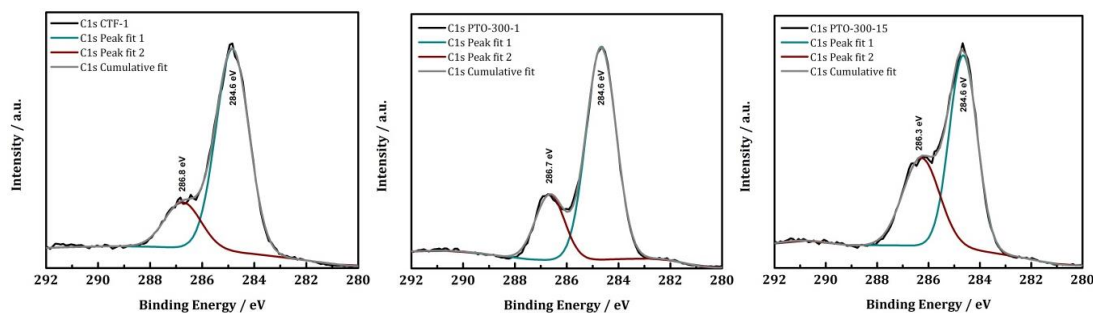
## Elemental analysis and ICP

**Table S9** Elemental analysis and BET surface areas of the presented PTOs compared to CTF-1 and calculated theoretical values of the elemental composition of 1,4-dicyanobenzene and the trimer.

sample	N	C	H	Zn	wt%	BET SA <sup>b</sup>
	[wt%]	[wt%]	[wt%]	[wt%] <sup>a</sup>	C/N	[m <sup>2</sup> g <sup>-1</sup> ]
calculated	21.86	74.99	3.15	0	3.43	-
1,4-dicyanobenzene and trimer	21.86	74.99	3.15	0	3.43	-
CTF-1 according to <i>Kuhn et al.</i> <sup>S1</sup>	19.3	72.8	3.2	-	3.77	791
CTF-1 according to <i>Ren et al.</i> <sup>c S7</sup>	20.71	74.49	3.03	-	3.60	2
CTF-1 according to <i>Ren et al.</i> <sup>d S7</sup>	22.58	72.93	3.32	-	3.23	4
PTO-300-1	21.61	74.30	3.29	0.03	3.44	116
PTO-300-2.5	21.38	73.53	3.23	0.02	3.44	12
PTO-300-5	21.57	74.25	3.28	0.04	3.44	19
PTO-300-10	21.69	74.45	3.32	0.11	3.43	13
PTO-300-15	20.99	72.75	3.48	0.03	3.47	21
PTO-350-1	21.13	73.59	3.34	0.01	3.48	10
PTO-350-10	20.39	72.93	3.15	0.01	3.58	6
CTF-1 as synthesized	18.60	70.20	3.30	0.21	3.77	610

<sup>a</sup> Measured by ICP. <sup>b</sup> From argon physisorption measurements (Figure S21-22). <sup>c</sup> TFMS catalysed synthesis and further heating step at 400 °C for 40 h. <sup>d</sup> TFMS catalysed and microwave-assisted synthesis.

## XPS measurements

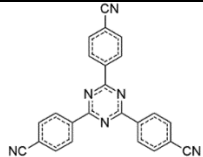
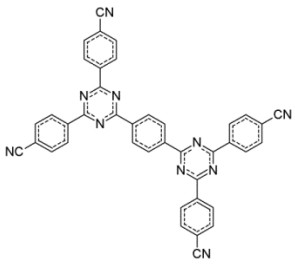
**Figure S70** N1s XPS spectra with applied peak and cumulative fits of CTF-1 (left), PTO-300-1 (middle) and PTO-300-15 (right).**Figure S71** C1s XPS spectra with applied peak and cumulative fits of CTF-1 (left), PTO-300-1 (middle) and PTO-300-15 (right).

## MALDI-TOF measurements and IR analysis

**Table S10** Summarized mass peaks observed in the MALDI-TOF spectra of PTO-300-1 and PTO-300-15.

PTO-300-1	PTO-300-15	connectivity
128	128	monomer
256		dimer
384	384	trimer
641	641	pentamer (chain, dendrimer)
897	897	heptamer (chain, dendrimer)
1153	1153	nonamer (chain, dendrimer)
-	1409	endecamer (chain, dendrimer)
1499	1551	dodecamer (chain or ring) without 1CN (PTO-300-1) or with 1N (PTO-300-15)
2049	-	16mer
2178	-	17mer (chain, dendrimer)
2306	-	18mer
2434	-	19mer (chain, dendrimer or ring)
2563	-	20mer
2690	-	21mer (chain, dendrimer)
2819	-	22mer
2947	-	23mer (chain)

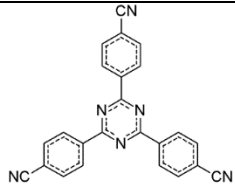
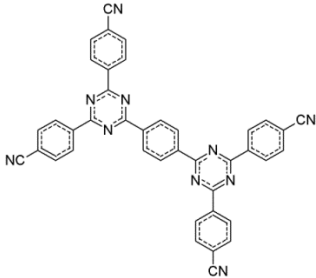
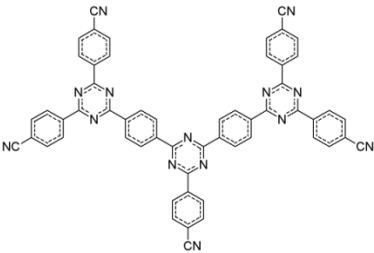
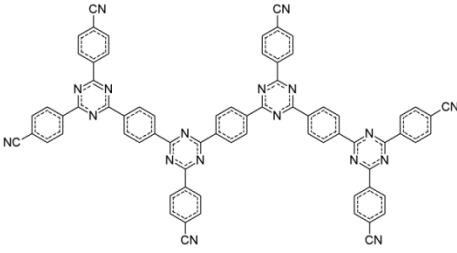
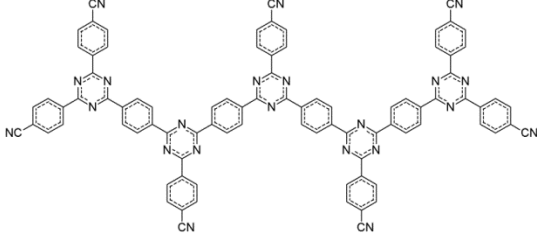
**Dendrimers:  $(3 + 2n; n = 0, 1, 2, 3,..)$  multiples of 1,4-dicyanobenzene mass ( $m/z = 128.1$ )****Table S11** Observed dendrimeric oligomers of CTF-1 and the specific nitrile-to-triazazine ratio.

dendrimeric fragments	$n$	$(3+2n)$	$m/z$	number of C≡N / number of C=N bonds
	0	3	384.4	$3 / 6 \cdot 1 = 0.50$
	1	5	640.7	$4 / 6 \cdot 2 = 0.33$

	2	7	896.9	$5 / 6 \cdot 3 = 0.28$
	3	9	1153.2	$6 / 6 \cdot 4 = 0.25$
	6	15	1922.0	$9 / 6 \cdot 7 = 0.21$
	8	19	2434.5	$11 / 6 \cdot 9 = 0.20$

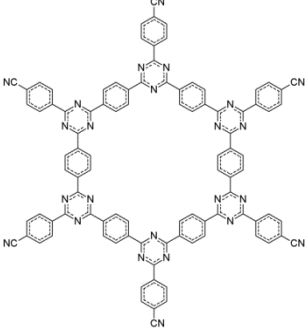
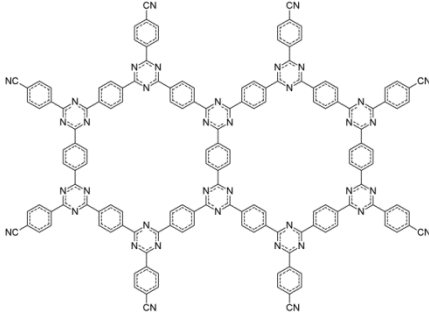
Chain fragments:  $(3 + 2n; n = 0, 1, 2, 3, \dots)$  multiples of 1,4-dicyanobenzene mass ( $m/z = 128.1$ )

**Table S12** Linear chain fragments (of CTF-1) observable in the mass spectra for the PTO samples and the specific nitrile-to-triazine ratio.

chain fragments	$n$	$(3+2n)$	$m/z$	number of C≡N / number of C=N bonds
	0	3	384.4	$3 / 6 \cdot 1 = 0.50$
	1	5	640.7	$4 / 6 \cdot 2 = 0.33$
	2	7	896.9	$5 / 6 \cdot 3 = 0.28$
	3	9	1153.2	$6 / 6 \cdot 4 = 0.25$
	4	11	1409.4	$7 / 6 \cdot 5 = 0.23$

Ring fragments:  $(12 + 7n; n = 0, 1, 2, 3,..)$  multiples of 1,4-dicyanobenzene mass ( $m/z = 128.1$ )

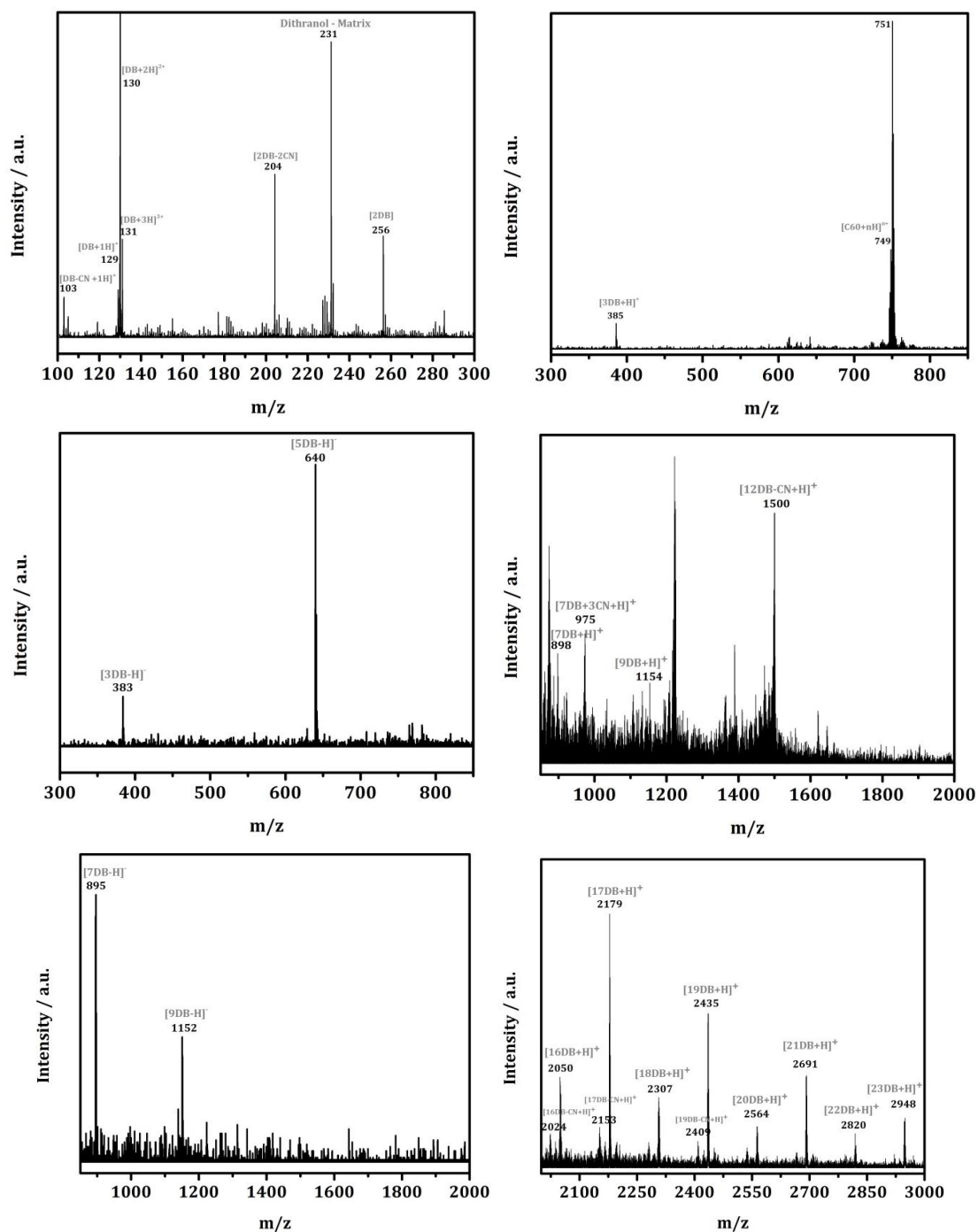
**Table S13** Ring fragments (of CTF-1) observable in the mass spectra for the PTO samples and the specific nitrile-to-triazine ratio.

ring fragments	n	$(12+7n)$	$m/z$	number of C≡N / number of C=N bonds
	0	12	1537.6	$6 / 6 \cdot 6 = 0.17$
	1	19	2434.5	$8 / 6 \cdot 10 = 0.13$

**Table S14** Nitrile-to-triazine ratios calculated from the IR signals (from signal intensities and integral, after background subtraction) of PTO-300-1 and PTO-300 synthesized with higher zinc chloride dilution: PTO-300-2.5, PTO-300-10 and PTO-300-15 in comparison to the trimer.

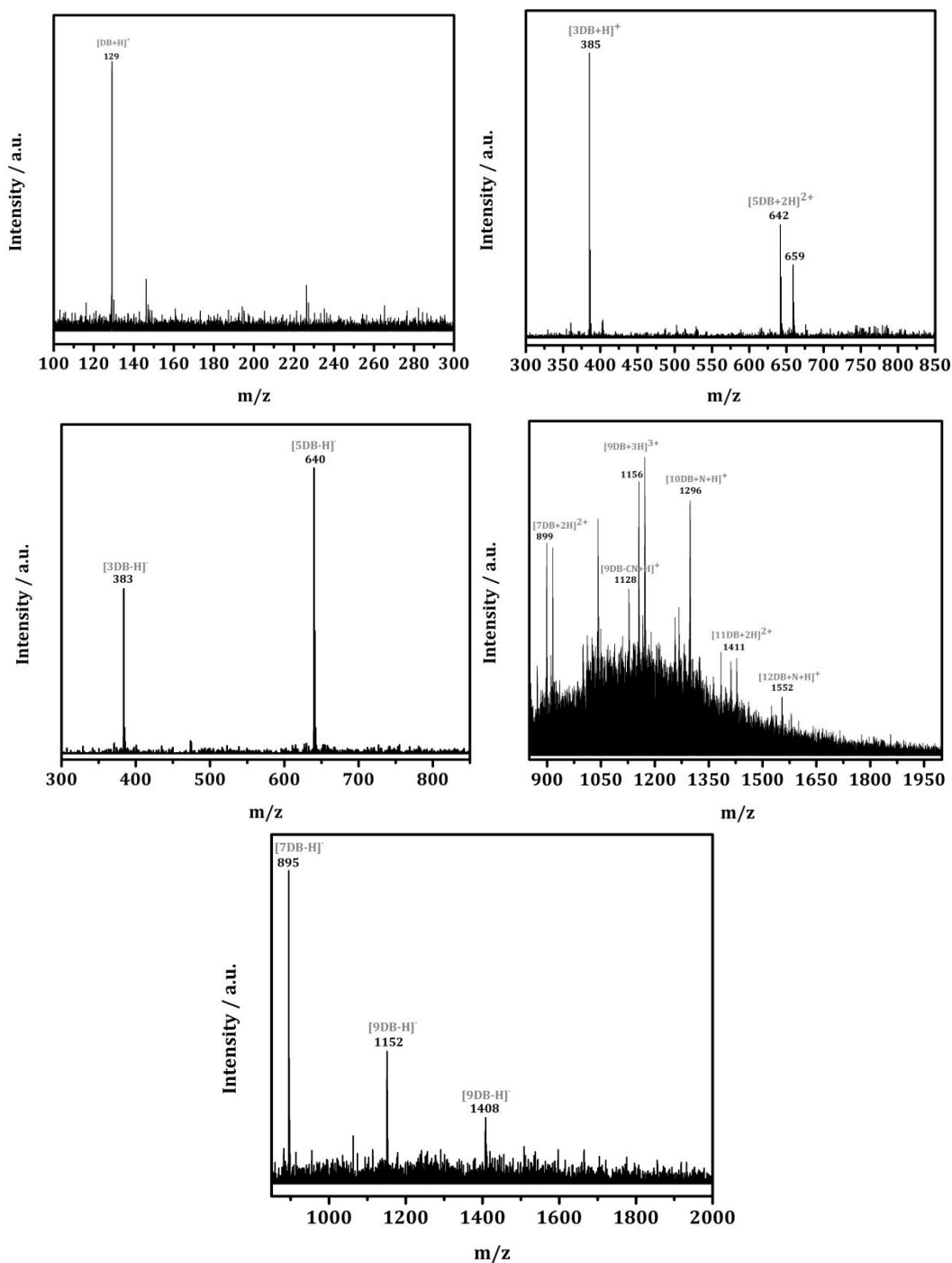
sample	nitrile-to-triazine ratio (intensity)	nitrile-to-triazine ratio (integral)
PTO-300-1	0.18 (0.18)	0.08 (0.09)
PTO-300-15	0.33 (0.32)	0.18 (0.16)
PTO-300-10	0.38 (0.46)	0.18 (0.23)
PTO-300-2.5	0.41	0.18
Trimer	0.51	0.29

Mass spectra of PTO-300-1



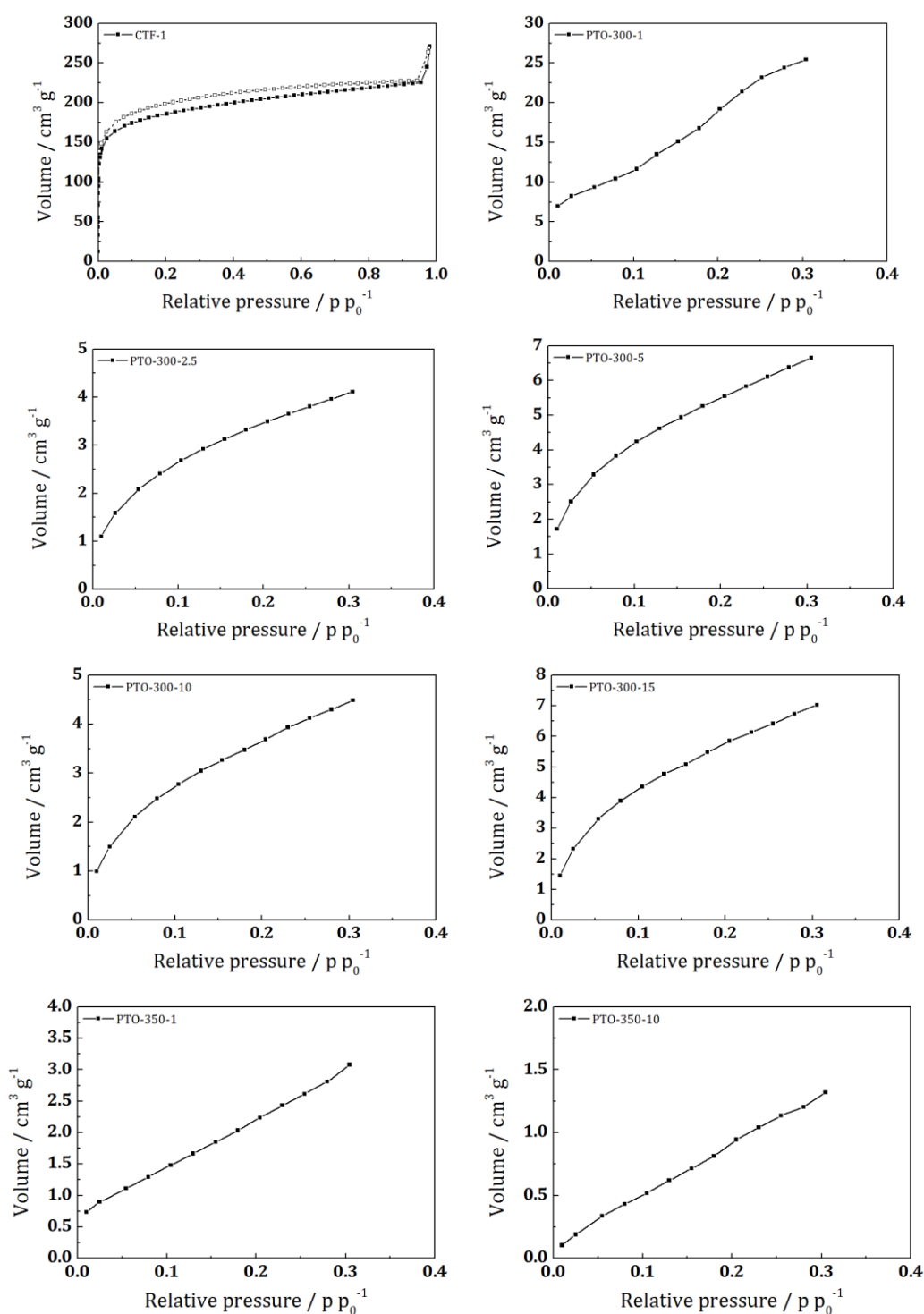
**Figure S72** Representative MALDI-TOF spectra of the PTO-300-1 sample, measured in the mass range  $>100$  and  $<3000$  (either in positive or negative mode, indicated with  $+H^+$  or  $-H^+$ , respectively). DB represents the mass of the precursor 1,4-dicyanobenzene ( $m/z = 128$ ). The signals at 230 and 750 correspond to the matrix.

Mass spectra of PTO-300-15



**Figure S73** Representative MALDI-TOF spectra of the PTO-300-15 sample, measured in the mass range  $> 100$  and  $< 2000$  (either in positive or negative mode, indicated with  $+H^+$  or  $-H^+$ , respectively). DB represents the mass of the precursor 1,4-dicyanobenzene ( $m/z = 128$ ). The signals at 230 correspond to the matrix.



*Ar-physisorption measurements*

**Figure S74** Argon adsorption (filled squares) and desorption (empty squares) isotherm of CTF-1 and 13-point argon adsorption isotherms of PTO-300s and PTO-350s for BET calculations.

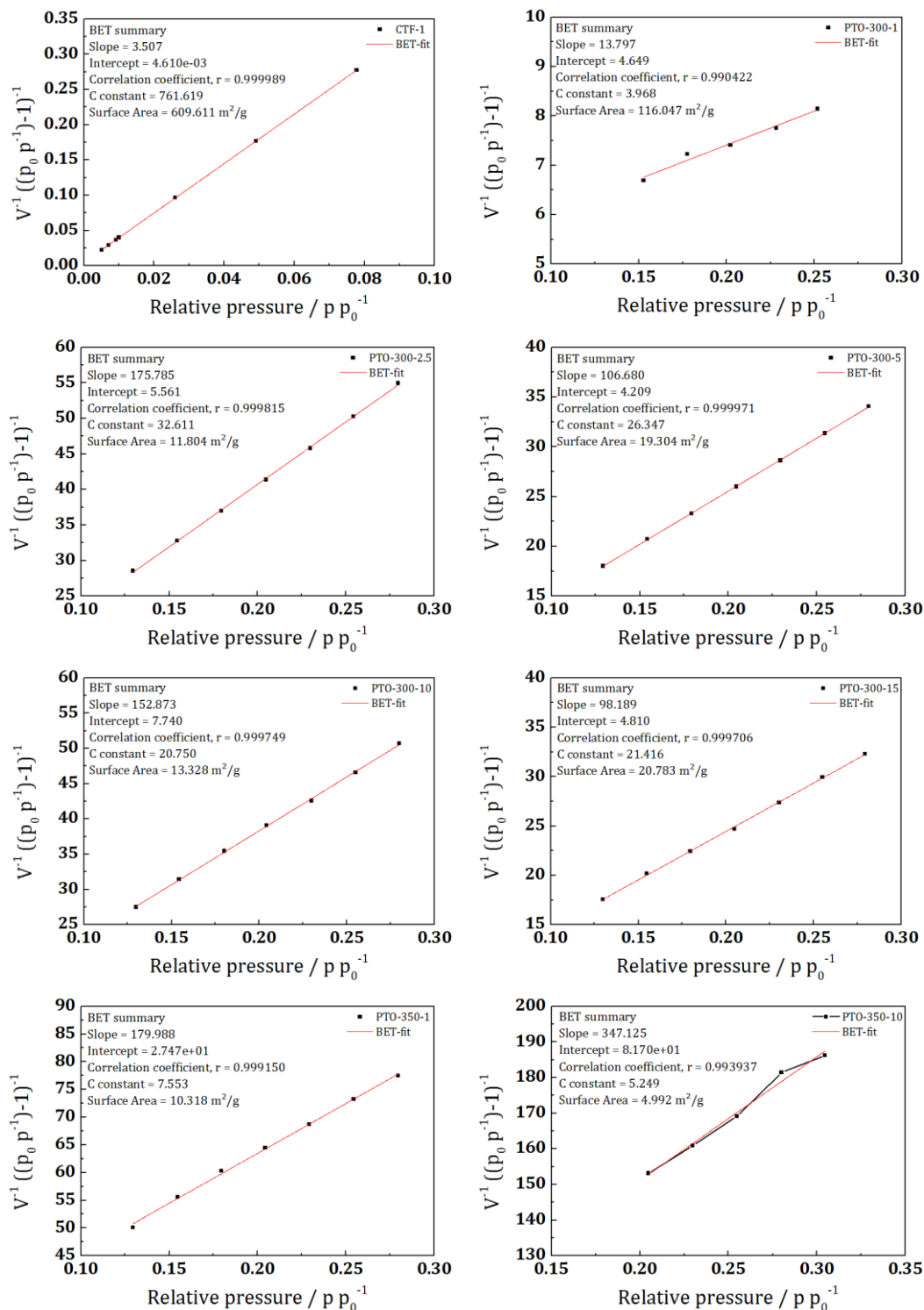


**Figure S75** BET-fits and BET calculation data of CTF-1, PTO-300s and PTO-350s. In accordance with the ISO recommendations multipoint BET tags equal or below the maximum in  $V \cdot (1 - P/P_0)$  were chosen.

## NMR measurements

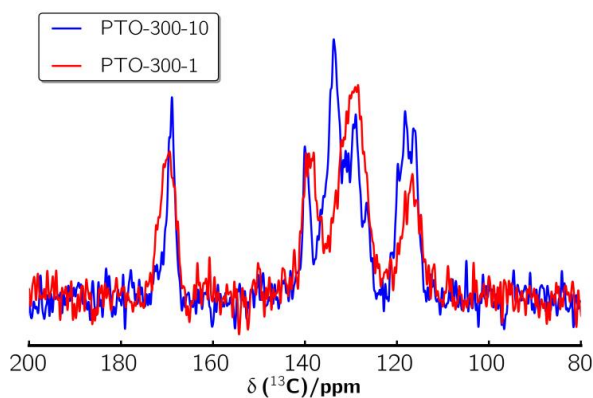


**Figure S76**  $^{13}\text{C}$  SP ssNMR spectra of PTO-300-10 and PTO-300-1 recorded with MAS using a rotational frequency of 20 kHz.

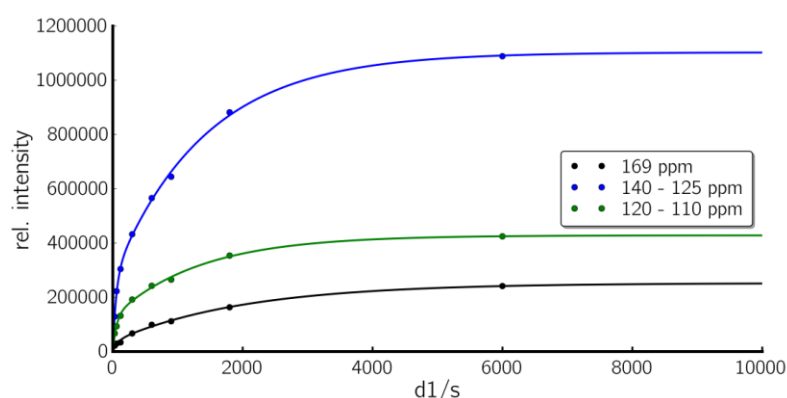


**Figure S77** Recycle delay plotted against signal intensity for  $^{13}\text{C}$  SP ssNMR spectra of PTO-300-10 and fitted with the following biexponential function  $I(x) = I_{0,1}(1 - \exp(-\frac{x}{T_{1,1}})) + I_{0,2}(1 - \exp(-\frac{x}{T_{1,2}}))$ .

The values for  $I_0$  and  $T_1$  are presented in the following table.

	$I_{0,1}$	$T_{1,1} / \text{s}$	$I_{0,2}$	$T_{1,2} / \text{s}$
169 ppm	36716	742	215416	2013
140 – 125 ppm	268771	535	833953	1406
120 – 110 ppm	126903	570	301307	1334

The underestimation of the triazine signal due to the longer spin-lattice relaxation time was calculated from the ratio of the measured intensity at 6000 s to  $I_{0,1} + I_{0,2}$  and gives about 5%. For the other signals this deviation is only about 1%.

## Photocatalytic experiments

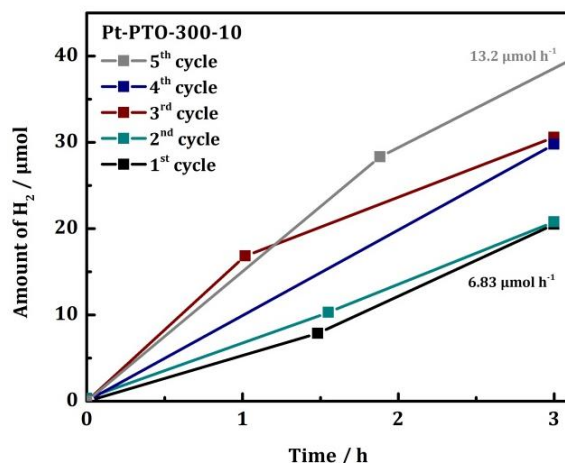


**Figure S78** Cyclic measurements with platinum-modified PTO-300-10 irradiated with simulated sunlight for three hours for each cycle. After each cycle the reactor was evacuated and purged with argon and irradiation was restarted.

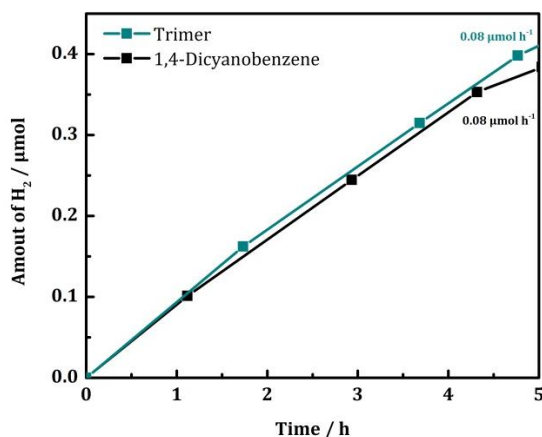


**Figure S79** Photocatalytic tests of the starting material 1,4-dicyanobenzene (black) and the trimer (cyan) using a buffered (pH 7, 0.5 M phosphate buffer) 10 vol% TEOA solution and platinum as co-catalyst during UV-Vis illumination ( $\geq 250$  nm).

**Table S15** Photocatalytic activity (with Pt as co-catalyst) versus the surface area.

sample	BET SA [m <sup>2</sup> g <sup>-1</sup> ]	HER [μmol h <sup>-1</sup> ]	HER [μmol h <sup>-1</sup> ] / BET SA [m <sup>2</sup> g <sup>-1</sup> ]
PTO-300-1	116	1.45	0.01
PTO-300-2.5	12	6.91	0.58
PTO-300-5	19	3.36	0.18
PTO-300-10	13	9.00	0.69
PTO-300-15	21	9.40	0.48
CTF-1 as synthesized	610	0.02	0.00

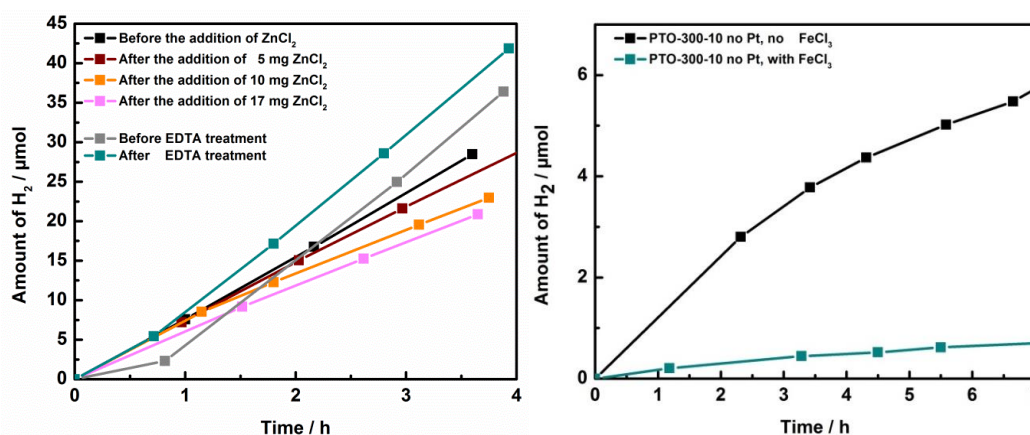


**Figure S80** Hydrogen evolution rates of Pt-PTO-300-10 before and after addition of several amounts (5, 10 or 17 mg) of ZnCl<sub>2</sub> and before and after stirring (for 2 days) / excessively washing the sample in EDTA (left). Hydrogen evolution rates (without the addition of H<sub>2</sub>PtCl<sub>6</sub>) of PTO-300-10 before and after stirring the sample in a FeCl<sub>3</sub> solution and an excessive washing procedure to achieve Fe<sup>3+</sup> modification or, more accurately “poisoning” of the active site (likely the free electron pair at the nitrogen site of the nitrile group or the triazine) by coordination. However, the coordination mode is unclear, even if we can clearly ascertain that iron is in the sample (see Table S9). The Fe<sup>3+</sup>-treated sample showed a drastically decreased activity. The addition of platinum leads to an identical rate for both materials suggesting that not all active sites are poisoned by the Fe<sup>3+</sup> or that platinum deposited on the Fe<sup>3+</sup> site still promotes the electron transfer process.

**Table S16** ICP data of the PTO-300-10 sample after/before EDTA treatment and Fe<sup>3+</sup> poisoning.

sample	Zn	Fe
PTO-300-10 before EDTA treatment	0.107	0.000
PTO-300-10 after EDTA treatment	0.079	0.000
PTO-300-10 after Fe <sup>3+</sup> -poisoning	0.107	0.960

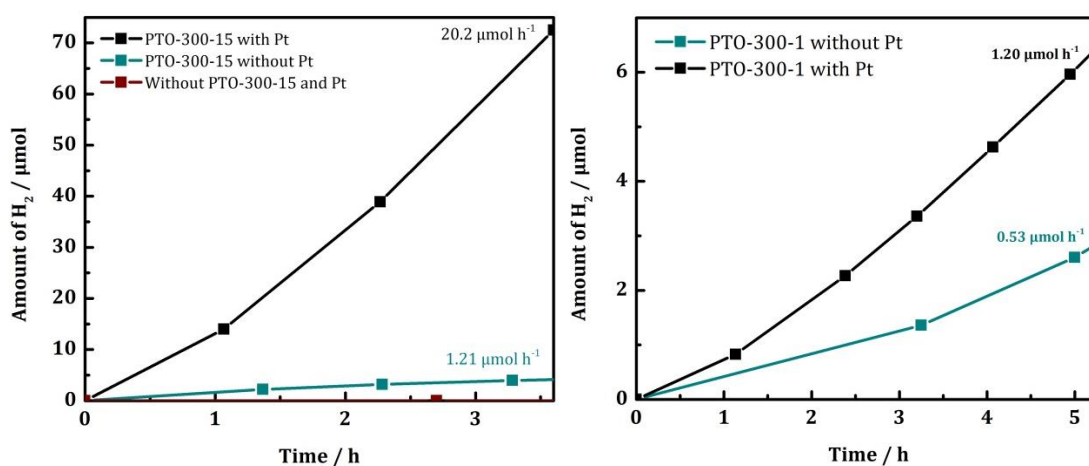


**Figure S81** Photocatalytic measurements (simulated sunlight) of dispersed PTO-300-15 (left) and PTO-300-1 (right) containing 6 μL H<sub>2</sub>PtCl<sub>6</sub> (black), in comparison to a photocatalysis run without the addition of platinum as co-catalyst (cyan). The red slope represents a control experiment showing the illuminated buffered TEoA solution without photocatalyst and platinum.

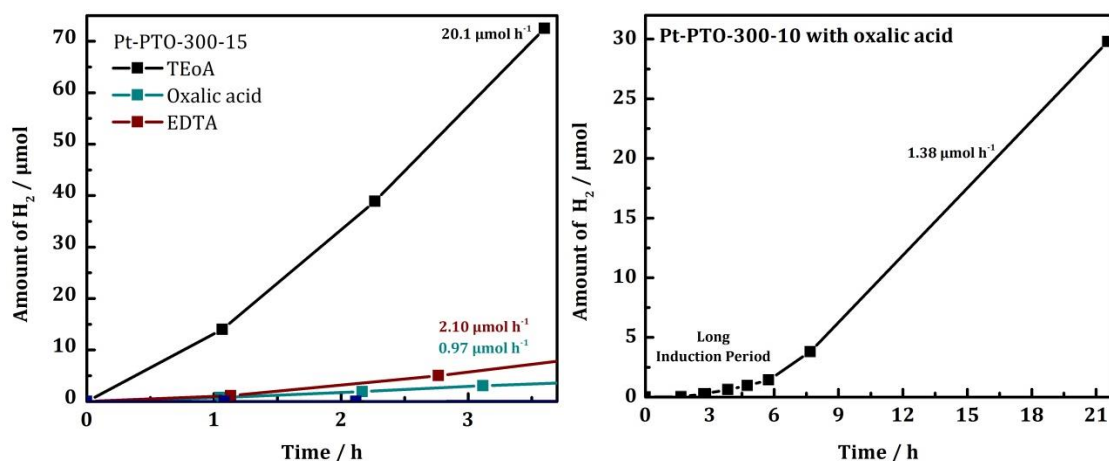


**Figure S82** Photocatalytic tests with Pt-PTO-300-15 (10 mL buffered - pH 7, 0.5 M phosphate buffer – electron donor solution, simulated sunlight, 6 μL H<sub>2</sub>PtCl<sub>6</sub>) using different electron donors: TEOA (10 vol%; black), oxalic acid (100 mg; cyan) and EDTA (10 vol%; red) (left). Stability test for more than 20 hours of Pt-PTO-300-10 using oxalic acid as electron donor (right).

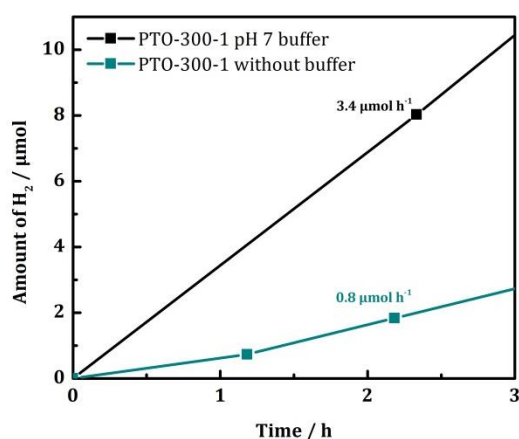


**Figure S83** Photocatalytic activity of Pt-PTO-300-1 dispersed in a phosphate buffered (pH 7, 0.5 M; black) compared to a non-buffered (cyan) 10 vol% TEOA solution illuminated with simulated sunlight.

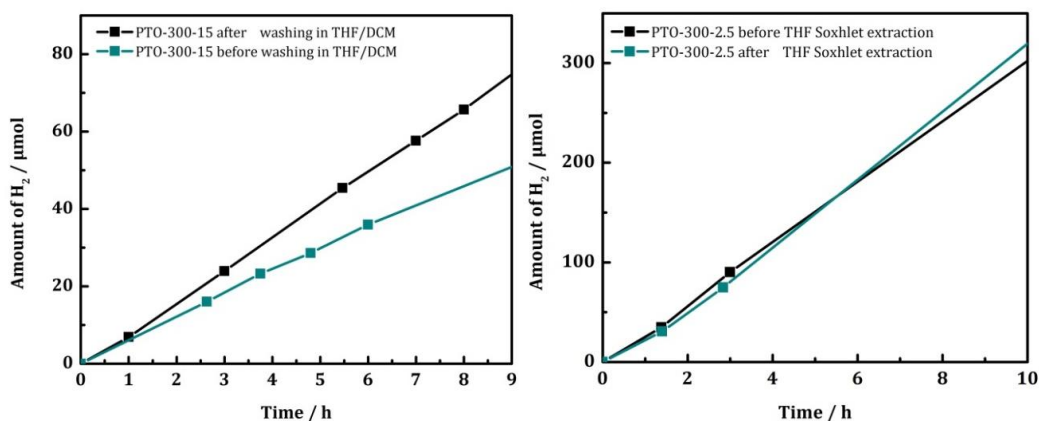


**Figure S84** Photocatalytic activity of Pt-PTO-300-15 before (cyan) and after (black) the first washing procedure with THF/DCM, showing that less active starting materials or rather small oligomers (such as trimers) are washed away (left). Photocatalytic activity of Pt-PTO-300-2.5 before (black) and after THF Soxhlet extraction (cyan) showing that the first washing procedure is sufficient to get rid of less active impurities (right).

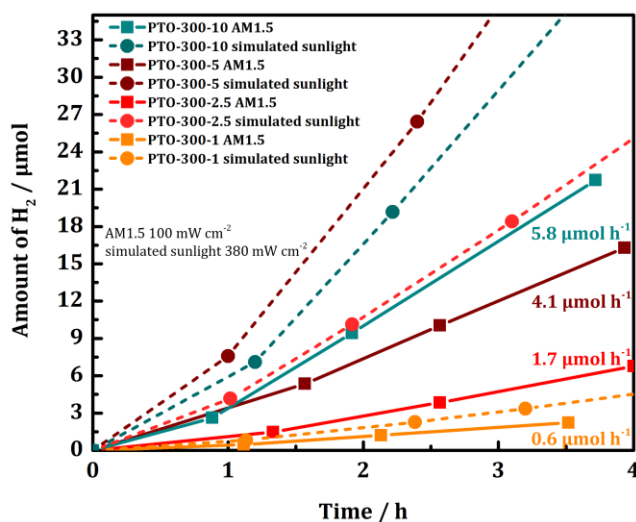


**Figure S85** Photocatalytic activity of four different PTO-300 samples under AM1.5 ( $100 \text{ mW cm}^{-2}$ ) vs. simulated sunlight conditions ( $380 \text{ mW cm}^{-2}$ ) (pH 7, 0.5 M phosphate buffer, 10 vol% TEoA solution, 2.2 wt% Pt).

*Batch-to-batch variations*

**Table S17** Hydrogen evolution rates of several PTO-300 batches (Figure S86). Bold values mark the “outlier” batches which were not used for the calculation of the “average” hydrogen evolution rate.

sample	HER* (several batches) / $\mu\text{mol h}^{-1}$
PTO-300-1	1.5, 1.5, 1.7
PTO-300-2.5	7.4, 8.0, 13.1, 15.6, <b>30.3</b>
PTO-300-5	<b>3.4</b> , <b>4.0</b> , 14.4, 15.8
PTO-300-10	8.3, 9.0, 9.9, 10.9
PTO-300-15	8.6, 8.7, 9.4, 11.6, <b>20.1</b>

\* Measurement error of 15 %.



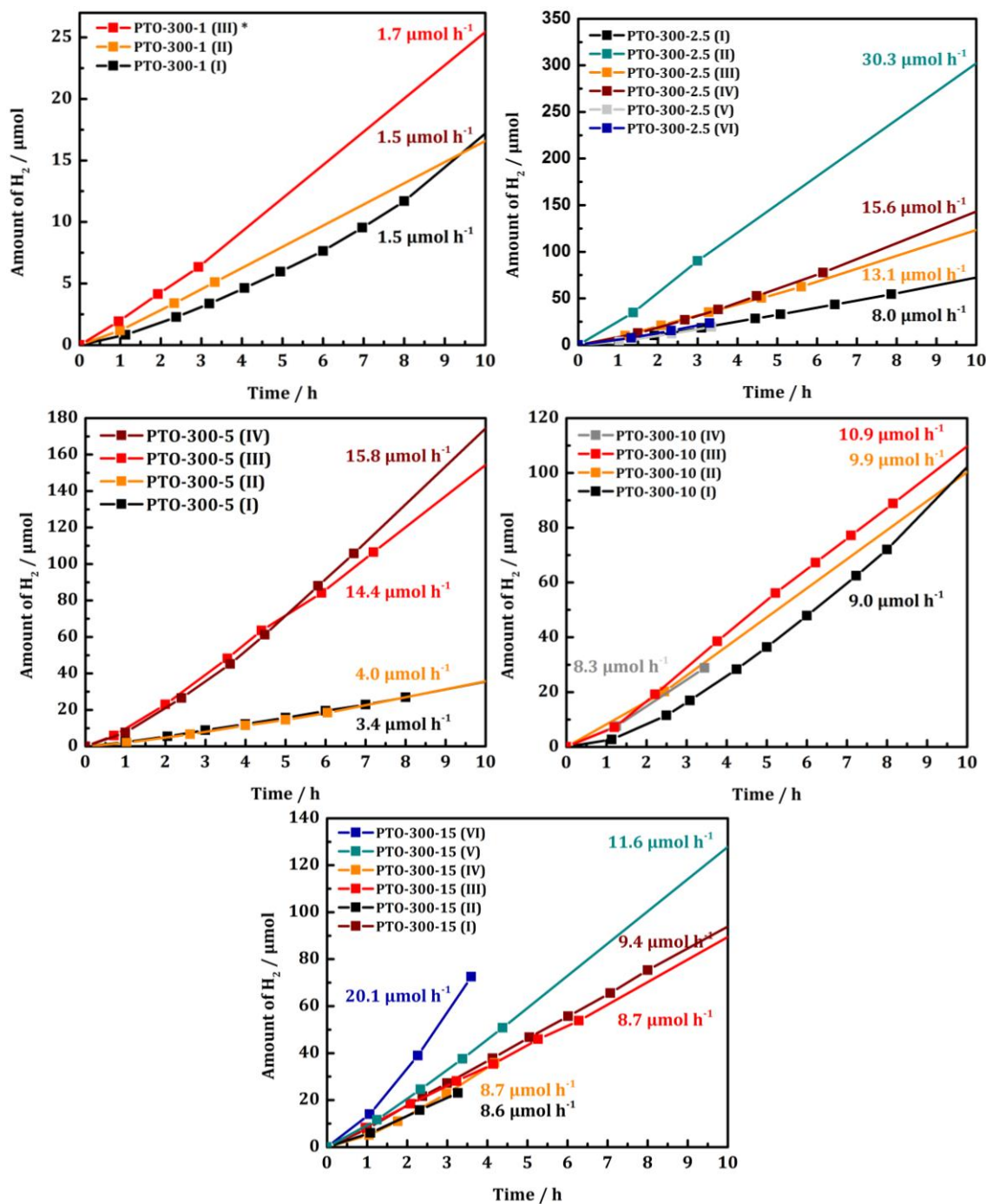


**Figure S86** Photocatalytic activity of various PTO-300 batches illuminated under simulated sunlight conditions (pH 7, 0.5 M phosphate buffer, 10 vol% TEOA solution, 2.2 wt% Pt) to illustrate batch-to-batch variations when synthesized in excess of  $ZnCl_2$ .



## Characterization of the photocatalyst after photocatalysis

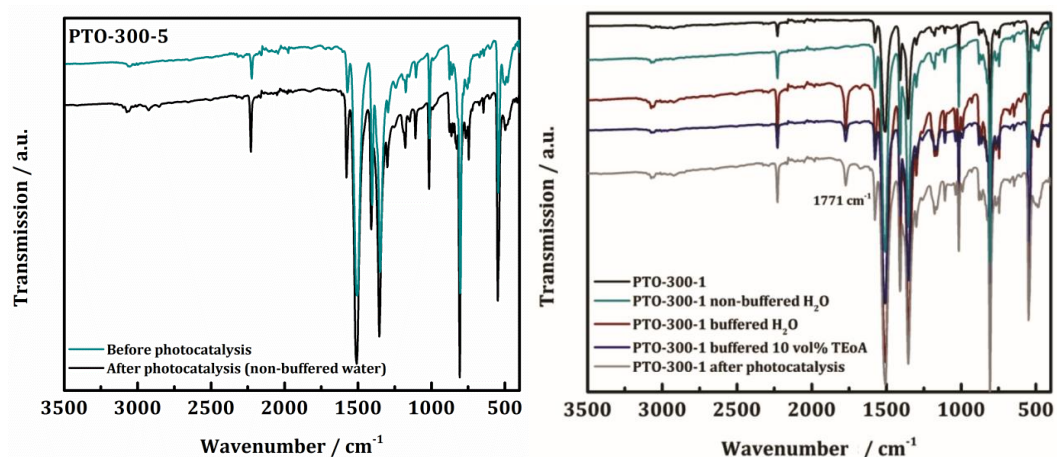


**Figure S87** IR spectroscopic characterization of the photocatalyst before (left: Pt-PTO-300-5; right: Pt-PTO-300-1) and after 24 hour of photocatalysis (left: in non-buffered water; right: in buffered water) as well as after each preparation step of the photocatalytic experiment: Stirring the photocatalyst in water or in pH 7 0.5 M phosphate buffer and after the addition of 10 vol% TEoA. A new band at  $1771\text{ cm}^{-1}$  appears due to the buffer. No changes caused by photodegradation.

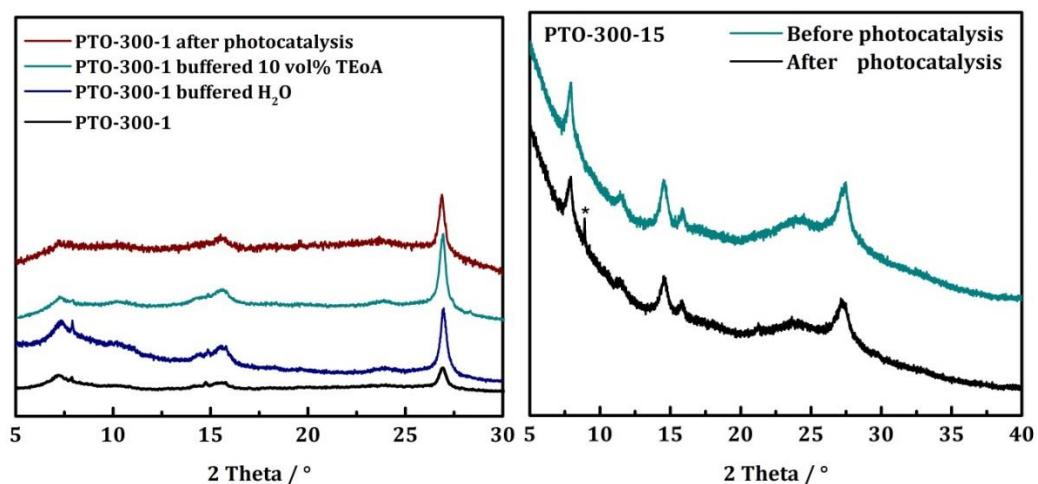


**Figure S88** PXRD of the photocatalyst PTO-300-1 (left) and PTO-300-15 (right) before and after 24 hour of photocatalysis in buffered water (left, Pt-PTO-300-1; right, Pt-PTO-300-15). In case of PTO-300-1, PXRD patterns are also shown after each preparation step of the photocatalytic experiment: Stirring the photocatalyst in pH 7 0.5 M phosphate buffer and after the addition of 10 vol% TEoA. The sharp reflection marked with an asterisk is an artefact due to the sample holder.

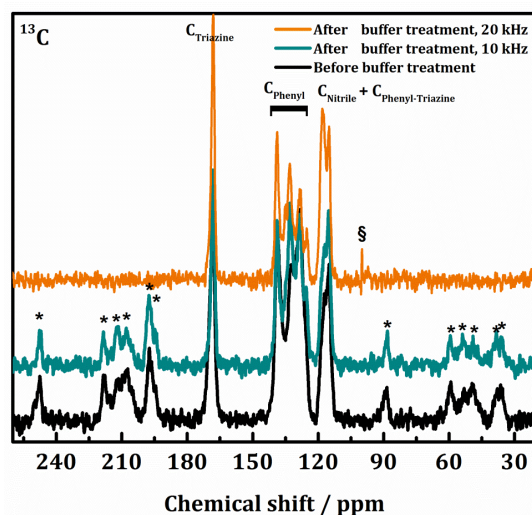


**Figure S89** Solid state NMR  $^{13}\text{C}$  spectra (contact time 5 ms) of PTO-300-15 before (spinning speed 10 kHz) and after (spinning speed 10 and 20 kHz) stirring the photocatalyst three days in buffered water (pH 7, 0.5 M phosphate buffer). Bands marked with an asterisk are rotational side bands. The sharp peak marked with “S” is an artefact. No additional carbon signals are detected after buffer treatment which makes hydrolysis of the nitrile groups unlikely.

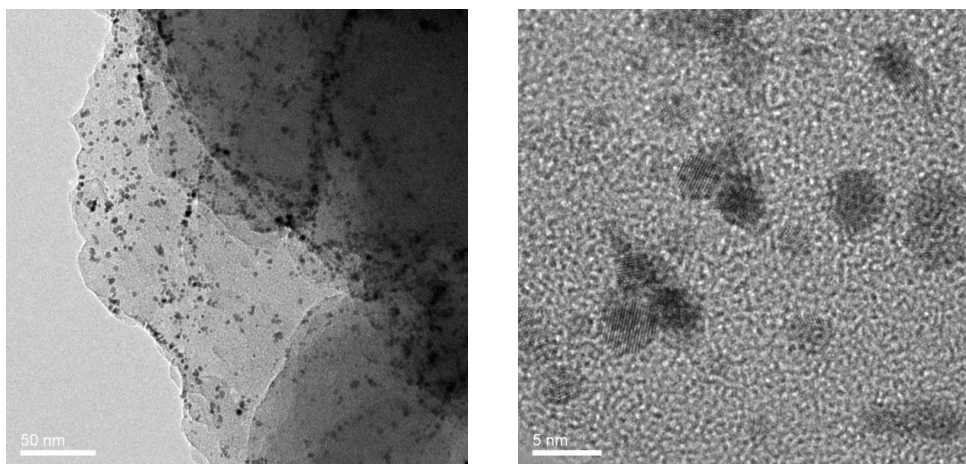


**Figure S90** TEM images of the Pt-modified PTO-300-1 sample after photocatalysis. Pt-nanoparticles around 4 nm of average size have been formed on the sample surface after photo-reduction of  $\text{H}_2\text{PtCl}_6$ .

## TEM characterization

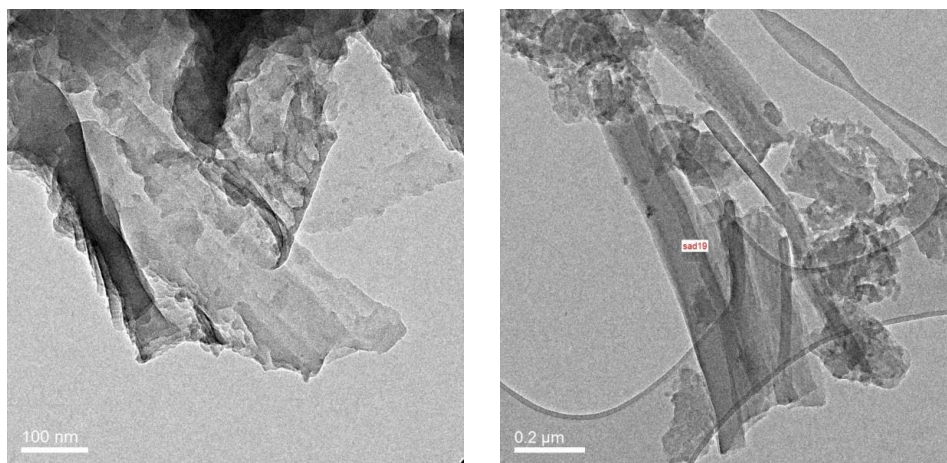


**Figure S91** TEM image of PTO-300-1 showing a layered-like material (left). TEM image of PTO-300-10 showing mixed phases of clusters and either fibers or furled layers (right).

**Bibliography**

- (S1) P. Kuhn, M. Antonietti and A. Thomas, *Angew. Chem. Int. Ed.* **2008**, *47*, 3450.
- (S2) H. Tanaka, K. Shizu, H. Nakanotani and C. Adachi, *C. Chem. Mater.* **2013**, *25*, 3766.
- (S3) X. Wang, K. Maeda, A. Thomas, K. Takanabe, G. Xin, J. M. Carlsson, K. Domen and M. Antonietti, *Nat. Mater.* **2009**, *8*, 76.
- (S4) K. Schwinghammer, B. Tuffy, M. B. Mesch, E. Wirnhier, C. Martineau, F. Taulelle, W. Schnick, J. Senker and B. V. Lotsch, *Angew. Chem. Int. Ed.* **2013**, *52*, 2435.
- (S5) L. Stegbauer, K. Schwinghammer and B. V. Lotsch, *Chem. Sci.* **2014**, *5*, 2789.
- (S6) K. Schwinghammer, M. B. Mesch, V. Duppel, C. Ziegler, J. Senker and B. V. Lotsch, *J. Am. Chem. Soc.* **2014**, *136*, 1730.
- (S7) S. Ren, M. J. Bojdys, R. Dawson, A. Laybourn, Y. Z. Khimyak, D. J. Adams, A. I. Cooper, *Adv. Mater.* **2012**, *24*, 2357.

## 7.2 Photocatalysis – calculations

It is recommended to read the PhD thesis of B. Tuffy (Max Planck Institute of Solid State Research) for further details on the applied photocatalysis setup used in this thesis.<sup>S1</sup>

### Conversion of ppm to $\mu\text{mol h}^{-1} \text{g}^{-1}$ hydrogen

The calculations are based on the ideal gas law:

$$pV = nRT;$$

$$n [\text{mol H}_2 \text{ h}^{-1}] = \frac{pV}{RT} \times \text{ppm H}_2 \text{ h}^{-1}$$

$$= \frac{1 [\text{atm}] \times V}{0.082 [\text{atm mol}^{-1} \text{ K}^{-1}] \times 293.15 [\text{K}]} \times \frac{\text{H}_2 [\text{h}^{-1}]}{1000000} = \frac{\text{H}_2 [\text{ppm h}^{-1}] \times V}{24.04 [\text{mol}^{-1}]};$$

$$n [\mu\text{mol H}_2 \text{ h}^{-1}] = n [\text{mol H}_2 \text{ h}^{-1}] \times 1000000;$$

$$n [\mu\text{mol H}_2 \text{ h}^{-1} \text{ g}^{-1}] = n [\mu\text{mol H}_2 \text{ h}^{-1}] \times \frac{1000 [\text{mg}]}{\text{amount of photocatalyst} [\text{mg}]}$$

$p$  = pressure [atm],  $V$  = volume of gas [0.220 L (large reactor) or 0.014 L (small reactor) when filled with 10 mL suspension],  $n$  = amount of hydrogen gas [mol per hour],  $T$  reaction temperature [293.15 K] and  $R$  = gas constant [0.082 atm mol<sup>-1</sup> K<sup>-1</sup>].

Under the applied conditions, the molar amounts  $n$  of produced hydrogen do not significantly differ when hydrogen is considered a “real gas” according to *Van der Waals law*.<sup>S2</sup> Only deviations within the nmol region have been noticed. The *Van der Waals law* reads as follows:

$$\left(p + \frac{n^2 a}{V^2}\right)(V - nb) = nRT$$

Since the real gas differs from the ideal gas with regards to the attraction between the particles  $a$  (J m<sup>3</sup> mol<sup>-2</sup>) and the volume excluded by a mol of particles  $b$  (m<sup>3</sup> mol<sup>-1</sup>), those values have been considered as  $a$  being 0.02476 J m<sup>3</sup> mol<sup>-2</sup> and  $b$  being 0.00002661 m<sup>3</sup> mol<sup>-1</sup>.

Thus, a realistic value of 3000 ppm H<sub>2</sub> produced per hour (in a volume of 0.220 L at 1 atm and 293.15 K) can be converted into 27.4370  $\mu\text{mol H}_2$  according to the ideal gas law and 27.4067  $\mu\text{mol}$  according to the *Van der Waals law*.

### Apparent quantum efficiency (photonic efficiency) calculations

For the calculation of the apparent quantum efficiency (AQE) of the presented photocatalysts (suspensions), the intensity of light was first measured (in mW cm<sup>-2</sup>) with a photomultiplier at the height of the sample surface through each band pass filter (400, 450, 500, 550 and 600  $\pm$  20 nm) and the used glass vial (small reactor) or quartz glass lid of the reactor (large reactor). The measured lamp power was then multiplied with the sample surface area (in cm<sup>-2</sup>) to determine the total incident power (in mW). For further calculations, the incident power was converted to W (1 W = 1 J s<sup>-1</sup>).

The sum of the photon energies (in J) per each wavelength region, or rather the peak integral (380 nm – 420 nm, 430 nm – 470 nm, 480 nm – 520 nm, 530 nm – 570 nm, etc), was then calculated. In Table S18 the photon energies per each wavelength and the sum of the used photon energies are listed. The number of incident photons per second, *i.e.* photon flux, was determined as follows.

$$\text{Number of incident photons per second} = 40 \times \frac{\text{Incident light power [J s}^{-1}\text{]}}{\text{Sum of photon energy [J]}}$$

Next, the number of incident photons per second was converted to  $\mu\text{mol}$  per hour with the help of the Avogadro constant ( $N_A$ ).

$$\text{Incident photons [mol h}^{-1}\text{]} = \frac{\text{Number of incident photons [s}^{-1}\text{]} \times 60 \times 60}{N_A [\text{mol}^{-1}]}$$

$$\text{Incident photons } [\mu\text{mol h}^{-1}] = \frac{\text{Number of incident photons} \times 3600 \text{ h}^{-1} \times 1000000}{6.022\text{E}23 [\mu\text{mol}^{-1}]}$$

Finally, the AQE for each wavelength region was computed as follows, considering that two electrons are needed to produce one molecule of hydrogen.

$$\text{AQE} = \frac{\text{Generated electrons } [\mu\text{mol}^{-1} \text{h}^{-1}]}{\text{Incident photons } [\mu\text{mol}^{-1} \text{h}^{-1}]} = \frac{2 \times \text{Amount of produced H}_2 [\mu\text{mol}^{-1} \text{h}^{-1}]}{\text{Incident photons } [\mu\text{mol}^{-1} \text{h}^{-1}]}$$

$$\text{AQE [\%]} = \text{AQE} \times 100$$

**Table S18** Photon energies (in J and eV) for a series of wavelengths (in m and nm). The colored regions are the ones used for the AQE calculations. For each wavelength region, the sum of the photon energies are given.

wavelength [m]	wavelength [nm]	photon energy [J]	photon energy [eV]	sum of photon energy [J]
3.8E-07	380	5.22757E-19	3.263149353	
3.81E-07	381	5.21384E-19	3.254584656	
3.82E-07	382	5.2002E-19	3.246064801	
3.83E-07	383	5.18662E-19	3.237589436	
3.84E-07	384	5.17311E-19	3.229158214	
3.85E-07	385	5.15967E-19	3.22077079	
3.86E-07	386	5.14631E-19	3.212426824	
3.87E-07	387	5.13301E-19	3.204125979	
3.88E-07	388	5.11978E-19	3.195867923	
3.89E-07	389	5.10662E-19	3.187652324	
3.9E-07	390	5.09353E-19	3.179478857	
3.91E-07	391	5.0805E-19	3.171347197	
3.92E-07	392	5.06754E-19	3.163257026	
3.93E-07	393	5.05464E-19	3.155208026	
3.94E-07	394	5.04181E-19	3.147199883	
3.95E-07	395	5.02905E-19	3.139232289	
3.96E-07	396	5.01635E-19	3.131304934	
3.97E-07	397	5.00371E-19	3.123417517	
3.98E-07	398	4.99114E-19	3.115569734	
3.99E-07	399	4.97863E-19	3.107761288	
4E-07	400	4.97E-19	3.099991885	<b>2.038E-17</b>
4.01E-07	401	4.9538E-19	3.092261232	
4.02E-07	402	4.94148E-19	3.08456904	
4.03E-07	403	4.92922E-19	3.076915022	

4.04E-07	404	4.91702E-19	3.069298896
4.05E-07	405	4.90488E-19	3.06172038
4.06E-07	406	4.8928E-19	3.054179197
4.07E-07	407	4.88077E-19	3.046675071
4.08E-07	408	4.86881E-19	3.039207731
4.09E-07	409	4.85691E-19	3.031776905
4.1E-07	410	4.84506E-19	3.024382327
4.11E-07	411	4.83327E-19	3.017023732
4.12E-07	412	4.82154E-19	3.009700859
4.13E-07	413	4.80987E-19	3.002413448
4.14E-07	414	4.79825E-19	2.995161242
4.15E-07	415	4.78669E-19	2.987943986
4.16E-07	416	4.77518E-19	2.980761428
4.17E-07	417	4.76373E-19	2.973613319
4.18E-07	418	4.75233E-19	2.966499412
4.19E-07	419	4.74099E-19	2.959419461
4.2E-07	420	4.7297E-19	2.952373224
4.21E-07	421	4.71847E-19	2.945360461
4.22E-07	422	4.70729E-19	2.938380934
4.23E-07	423	4.69616E-19	2.931434407
4.24E-07	424	4.68508E-19	2.924520646
4.25E-07	425	4.67406E-19	2.917639421
4.26E-07	426	4.66309E-19	2.910790502
4.27E-07	427	4.65217E-19	2.903973663
4.28E-07	428	4.6413E-19	2.897188678
4.29E-07	429	4.63048E-19	2.890435324
4.3E-07	430	4.61971E-19	2.883713382
4.31E-07	431	4.60899E-19	2.877022631
4.32E-07	432	4.59832E-19	2.870362857
4.33E-07	433	4.5877E-19	2.863733843
4.34E-07	434	4.57713E-19	2.857135378
4.35E-07	435	4.56661E-19	2.850567251
4.36E-07	436	4.55613E-19	2.844029252
4.37E-07	437	4.54571E-19	2.837521176
4.38E-07	438	4.53533E-19	2.831042817
4.39E-07	439	4.525E-19	2.824593973
4.4E-07	440	4.51472E-19	2.818174441
4.41E-07	441	4.50448E-19	2.811784023
4.42E-07	442	4.49429E-19	2.80542252
4.43E-07	443	4.48414E-19	2.799089738
4.44E-07	444	4.47404E-19	2.792785482
4.45E-07	445	4.46399E-19	2.78650956
4.46E-07	446	4.45398E-19	2.78026178
4.47E-07	447	4.44402E-19	2.774041955
4.48E-07	448	4.4341E-19	2.767849897
4.49E-07	449	4.42422E-19	2.761685421
4.5E-07	450	4.41439E-19	2.755548342

1.811E-17

4.51E-07	451	4.4046E-19	2.749438479
4.52E-07	452	4.39486E-19	2.743355651
4.53E-07	453	4.38515E-19	2.737299678
4.54E-07	454	4.3755E-19	2.731270383
4.55E-07	455	4.36588E-19	2.725267591
4.56E-07	456	4.3563E-19	2.719291127
4.57E-07	457	4.34677E-19	2.713340819
4.58E-07	458	4.33728E-19	2.707416494
4.59E-07	459	4.32783E-19	2.701517983
4.6E-07	460	4.31842E-19	2.695645118
4.61E-07	461	4.30906E-19	2.689797731
4.62E-07	462	4.29973E-19	2.683975658
4.63E-07	463	4.29044E-19	2.678178734
4.64E-07	464	4.2812E-19	2.672406798
4.65E-07	465	4.27199E-19	2.666659686
4.66E-07	466	4.26282E-19	2.66093724
4.67E-07	467	4.25369E-19	2.655239302
4.68E-07	468	4.2446E-19	2.649565714
4.69E-07	469	4.23555E-19	2.64391632
4.7E-07	470	4.22654E-19	2.638290966
4.71E-07	471	4.21757E-19	2.632689499
4.72E-07	472	4.20863E-19	2.627111767
4.73E-07	473	4.19974E-19	2.62155762
4.74E-07	474	4.19088E-19	2.616026907
4.75E-07	475	4.18205E-19	2.610519482
4.76E-07	476	4.17327E-19	2.605035198
4.77E-07	477	4.16452E-19	2.599573908
4.78E-07	478	4.15581E-19	2.594135469
4.79E-07	479	4.14713E-19	2.588719737
4.8E-07	480	4.13849E-19	2.583326571
4.81E-07	481	4.12989E-19	2.57795583
4.82E-07	482	4.12132E-19	2.572607374
4.83E-07	483	4.11278E-19	2.567281064
4.84E-07	484	4.10429E-19	2.561976765
4.85E-07	485	4.09582E-19	2.556694338
4.86E-07	486	4.0874E-19	2.55143365
4.87E-07	487	4.079E-19	2.546194567
4.88E-07	488	4.07065E-19	2.540976955
4.89E-07	489	4.06232E-19	2.535780683
4.9E-07	490	4.05403E-19	2.530605621
4.91E-07	491	4.04577E-19	2.525451638
4.92E-07	492	4.03755E-19	2.520318606
4.93E-07	493	4.02936E-19	2.515206398
4.94E-07	494	4.0212E-19	2.510114887
4.95E-07	495	4.01308E-19	2.505043948
4.96E-07	496	4.00499E-19	2.499993456
4.97E-07	497	3.99693E-19	2.494963288



4.98E-07	498	3.98891E-19	2.489953321	
4.99E-07	499	3.98091E-19	2.484963435	
5E-07	500	3.97295E-19	2.479993508	<b>1.62982E-17</b>
5.01E-07	501	3.96502E-19	2.475043421	
5.02E-07	502	3.95712E-19	2.470113056	
5.03E-07	503	3.94925E-19	2.465202294	
5.04E-07	504	3.94142E-19	2.460311102	
5.05E-07	505	3.93361E-19	2.455439117	
5.06E-07	506	3.92584E-19	2.45058647	
5.07E-07	507	3.9181E-19	2.445752967	
5.08E-07	508	3.91038E-19	2.440938492	
5.09E-07	509	3.9027E-19	2.436142935	
5.1E-07	510	3.89505E-19	2.431366184	
5.11E-07	511	3.88743E-19	2.426608129	
5.12E-07	512	3.87983E-19	2.42186866	
5.13E-07	513	3.87227E-19	2.417147669	
5.14E-07	514	3.86474E-19	2.412445047	
5.15E-07	515	3.85723E-19	2.407760687	
5.16E-07	516	3.84976E-19	2.403094485	
5.17E-07	517	3.84231E-19	2.398446333	
5.18E-07	518	3.83489E-19	2.393816128	
5.19E-07	519	3.8275E-19	2.389203765	
5.2E-07	520	3.82014E-19	2.384609142	
5.21E-07	521	3.81281E-19	2.380032157	
5.22E-07	522	3.80551E-19	2.375472709	
5.23E-07	523	3.79823E-19	2.370930696	
5.24E-07	524	3.79098E-19	2.366406019	
5.25E-07	525	3.78376E-19	2.361898579	
5.26E-07	526	3.77657E-19	2.357408278	
5.27E-07	527	3.7694E-19	2.352935017	
5.28E-07	528	3.76226E-19	2.348478701	
5.29E-07	529	3.75515E-19	2.344039233	
5.3E-07	530	3.74807E-19	2.339616517	
5.31E-07	531	3.74101E-19	2.33521046	
5.32E-07	532	3.73398E-19	2.330820966	
5.33E-07	533	3.72697E-19	2.326447944	
5.34E-07	534	3.71999E-19	2.3220913	
5.35E-07	535	3.71304E-19	2.317750942	
5.36E-07	536	3.70611E-19	2.31342678	
5.37E-07	537	3.69921E-19	2.309118723	
5.38E-07	538	3.69233E-19	2.30482668	
5.39E-07	539	3.68548E-19	2.300550564	
5.4E-07	540	3.67866E-19	2.296290285	
5.41E-07	541	3.67186E-19	2.292045756	
5.42E-07	542	3.66508E-19	2.287816889	
5.43E-07	543	3.65833E-19	2.283603599	
5.44E-07	544	3.65161E-19	2.279405798	



5.45E-07	545	3.64491E-19	2.275223402	
5.46E-07	546	3.63823E-19	2.271056326	
5.47E-07	547	3.63158E-19	2.266904486	
5.48E-07	548	3.62495E-19	2.262767799	
5.49E-07	549	3.61835E-19	2.258646182	
5.5E-07	550	3.61177E-19	2.254539553	1.482E-17
5.51E-07	551	3.60522E-19	2.25044783	
5.52E-07	552	3.59869E-19	2.246370931	
5.53E-07	553	3.59218E-19	2.242308778	
5.54E-07	554	3.58569E-19	2.238261289	
5.55E-07	555	3.57923E-19	2.234228386	
5.56E-07	556	3.5728E-19	2.230209989	
5.57E-07	557	3.56638E-19	2.226206022	
5.58E-07	558	3.55999E-19	2.222216405	
5.59E-07	559	3.55362E-19	2.218241063	
5.6E-07	560	3.54728E-19	2.214279918	
5.61E-07	561	3.54095E-19	2.210332895	
5.62E-07	562	3.53465E-19	2.206399918	
5.63E-07	563	3.52837E-19	2.202480913	
5.64E-07	564	3.52212E-19	2.198575805	
5.65E-07	565	3.51588E-19	2.19468452	
5.66E-07	566	3.50967E-19	2.190806986	
5.67E-07	567	3.50348E-19	2.186943129	
5.68E-07	568	3.49731E-19	2.183092877	
5.69E-07	569	3.49117E-19	2.179256158	
5.7E-07	570	3.48504E-19	2.175432902	
5.71E-07	571	3.47894E-19	2.171623037	
5.72E-07	572	3.47286E-19	2.167826493	
5.73E-07	573	3.4668E-19	2.164043201	
5.74E-07	574	3.46076E-19	2.160273091	
5.75E-07	575	3.45474E-19	2.156516094	
5.76E-07	576	3.44874E-19	2.152772142	
5.77E-07	577	3.44276E-19	2.149041168	
5.78E-07	578	3.43681E-19	2.145323104	
5.79E-07	579	3.43087E-19	2.141617883	
5.8E-07	580	3.42496E-19	2.137925438	
5.81E-07	581	3.41906E-19	2.134245704	
5.82E-07	582	3.41319E-19	2.130578615	
5.83E-07	583	3.40733E-19	2.126924106	
5.84E-07	584	3.4015E-19	2.123282113	
5.85E-07	585	3.39568E-19	2.119652571	
5.86E-07	586	3.38989E-19	2.116035416	
5.87E-07	587	3.38411E-19	2.112430586	
5.88E-07	588	3.37836E-19	2.108838017	
5.89E-07	589	3.37262E-19	2.105257647	
5.9E-07	590	3.36691E-19	2.101689414	
5.91E-07	591	3.36121E-19	2.098133256	

5.92E-07	592	3.35553E-19	2.094589112	
5.93E-07	593	3.34987E-19	2.091056921	
5.94E-07	594	3.34423E-19	2.087536623	
5.95E-07	595	3.33861E-19	2.084028158	
5.96E-07	596	3.33301E-19	2.080531467	
5.97E-07	597	3.32743E-19	2.077046489	
5.98E-07	598	3.32186E-19	2.073573167	
5.99E-07	599	3.31632E-19	2.070111442	
6E-07	600	3.31079E-19	2.066661257	1.358E-17
6.01E-07	601	3.30528E-19	2.063222553	
6.02E-07	602	3.29979E-19	2.059795273	
6.03E-07	603	3.29432E-19	2.05637936	
6.04E-07	604	3.28887E-19	2.052974758	
6.05E-07	605	3.28343E-19	2.049581412	
6.06E-07	606	3.27801E-19	2.046199264	
6.07E-07	607	3.27261E-19	2.04282826	
6.08E-07	608	3.26723E-19	2.039468345	
6.09E-07	609	3.26186E-19	2.036119465	
6.1E-07	610	3.25652E-19	2.032781564	
6.11E-07	611	3.25119E-19	2.029454589	
6.12E-07	612	3.24587E-19	2.026138487	
6.13E-07	613	3.24058E-19	2.022833204	
6.14E-07	614	3.2353E-19	2.019538687	
6.15E-07	615	3.23004E-19	2.016254885	
6.16E-07	616	3.2248E-19	2.012981744	
6.17E-07	617	3.21957E-19	2.009719212	
6.18E-07	618	3.21436E-19	2.00646724	
6.19E-07	619	3.20917E-19	2.003225774	
6.2E-07	620	3.20399E-19	1.999994765	

## Bibliography

(S1) B. Tuffy, *PhD thesis*, University of Munich, 2016.

(S2) Van der Waals law calculator, [http://www.webqc.org/van\\_der\\_waals\\_gas\\_law.html](http://www.webqc.org/van_der_waals_gas_law.html), accessed on 22<sup>th</sup> of January 2016.

## 7.3 List of publications and statement of contribution

The majority of the results compiled in this thesis were published in scientific journals as listed below. As the scope of this thesis is the synthesis and characterization of triazine-based frameworks for light-driven hydrogen evolution, publications beyond this scope are not explicitly listed in prior Chapters and are here referred to *as not part of this thesis*. Orals and poster presentations at scientific conferences as well as workshop participations are summarized separately.

### Publications published as part of this thesis

#### Triazine-based carbon nitrides for visible-light-driven hydrogen evolution

K. Schwinghammer, B. Tuffy, M. B. Mesch, E. Wirnhier, C. Martineau, F. Taulelle, W. Schnick, J. Senker, B. V. Lotsch

*Angew. Chem. Int. Ed.* **2013**, *52*, 2435–2439.

CeNS Publication Award **2013**.

Press releases: <http://technologiewerte.de/2013/01/24/neuer-katalysator-fur-die-wasserspaltung/>.  
<http://www.nano-initiative-munich.de/press/press-releases/meldung/n/new-catalyst-for-water-splitting/>.

*K. Schwinghammer (Max Planck Institute for Solid State Research, Stuttgart, advisor: Prof. Dr. B. Lotsch) wrote the Results and Discussion section of the manuscript, screened the literature, synthesized the samples, did most of the (commission of the) analysis, edited images, interpreted most of the analytical data. B. Tuffy (Max Planck Institute for Solid State Research, Stuttgart, advisor: Prof. Dr. B. Lotsch) has conducted part of the photocatalytic measurements such as the wavelength-depending measurements, and acted as mentor and supervisor for this publication. This work was published as part of his PhD thesis. All solid-state NMR measurements, their interpretation, as well as image editing were carried out by M. B. Mesch (University of Bayreuth, advisor: Prof. Dr. J. Senker) in the department of Prof. Dr. F. Taulelle with his student Dr. C. Martineau (Tectospin, Institut Lavoisier de Versailles, France) and will appear in M. B. Mesch's PhD thesis. Dr. E. Wirnhier (University of Munich, advisor: Prof. Dr. W. Schnick) introduced K. Schwinghammer into the synthesis of poly(triazine imide) and melon; this publications is also part of her PhD thesis. V. Duppel (Max Planck Institute for Solid State Research, Stuttgart, advisor: Prof. Dr. B. Lotsch) performed the TEM measurements of the platinum-modified photocatalyst and edited the TEM image. The sorption measurements were carried out by Dr. S. Hug (University of Munich, advisor: Prof. Dr. B. Lotsch). Elemental analysis and ICP was conducted by M.-L. Schreiber (Max Planck Institute for Solid State Research, Stuttgart, advisor: Prof. Dr. B. Lotsch). Part of the PXRD patterns were recorded by C. Stefani (Max Planck Institute for Solid State Research, Stuttgart, advisor: Prof. Dr. R. Dinnebier). Each author also revised the manuscript. C. Hohmann (NIM) designed the image shown in the front page cover.*

## Crystalline carbon nitride nanosheets for improved visible-light hydrogen evolution

K. Schwinghammer, M. B. Mesch, V. Duppel, C. Ziegler, J. Senker, B. V. Lotsch

*J. Am. Chem. Soc.* **2014**, 136, 1730–1733.

*K. Schwinghammer (Max Planck Institute for Solid State Research, Stuttgart, advisor: Prof. Dr. B. Lotsch) wrote the main part of the manuscript, synthesized the samples, screened the literature, did most of the image editing, interpreted the analytical data and did/commissioned most of the analysis. The ssNMR measurements and the water layer calculations were carried out by M. B. Mesch (University of Bayreuth, advisor: Prof. Dr. J. Senker) and will appear in her PhD thesis. She also interpreted the ssNMR results with the help of her supervisor and edited the ssNMR images. V. Duppel (Max Planck Institute for Solid State Research, Stuttgart, advisor: Prof. Dr. B. Lotsch) performed all TEM measurements, simulations and edited the TEM image. The AFM measurements and corresponding height profiles were performed by C. Ziegler (University of Munich, advisor: Prof. Dr. B. Lotsch). Dr. M. Konuma (Max Planck Institute for Solid State Research, Stuttgart, advisor: Prof. Dr. U. Starke) conducted the XPS measurements, C. Stefani (Max Planck Institute for Solid State Research, Stuttgart, advisor: Prof. Dr. R. Dinnebier) measured the PXRD patterns and M.-L. Schreiber (Max Planck Institute for Solid State Research, Stuttgart, advisor: Prof. Dr. B. Lotsch) performed the elemental analysis and ICP measurements. R. Noack (Max Planck Institute for Solid State Research, graphics service) helped design the table of content graphic. All authors revised the manuscript.*

## Cation and anion exchange of crystalline poly(triazine imide) and its effect on structural and optical properties

K. Schwinghammer, M. B. Mesch, V. Duppel, L. Schoop, E. J. McDermott, T. de Boer, A. Moewes, J. Senker, B. V. Lotsch

*To be submitted.*

*K. Schwinghammer (Max Planck Institute for Solid State Research, Stuttgart, advisor: Prof. Dr. B. Lotsch) wrote the main part of the manuscript, synthesized the samples, screened the literature, did most of the image editing, interpreted the analytical data and did/commissioned most of the analysis. The ssNMR measurements were carried out by M. B. Mesch (University of Bayreuth, advisor: Prof. Dr. J. Senker) and might appear in her PhD thesis. M. B. Mesch also interpreted the ssNMR results with the help of her supervisor. V. Duppel (Max Planck Institute for Solid State Research, Stuttgart, advisor: Prof. Dr. B. Lotsch) performed all TEM measurements, simulations and edited the TEM image. The LeBail fits and structure elucidations were performed by L. Schoop (Max Planck Institute for Solid State Research, Stuttgart, advisor: Prof. Dr. B. Lotsch). T. de Boer (University of Saskatchewan Saskatoon, SK, advisor: Prof. Dr. A. Moewes) conducted the XES and XAS measurements which were interpreted by E. J. McDermott (Vienna University of Technology, Vienna, advisor: Prof. Dr. A. Moewes). The AFM measurements were performed by D. Weber (Max Planck Institute for Solid State Research, Stuttgart, advisor: Prof. Dr. B. Lotsch). Dr. M. Konuma (Max Planck Institute for Solid State Research, Stuttgart, advisor: Prof. Dr. U. Starke) conducted the XPS measurements, C. Stefani (Max Planck Institute for Solid State Research, Stuttgart, advisor: Prof. Dr. R. Dinnebier) measured the PXRD patterns and M.-L. Schreiber (Max Planck Institute for Solid State Research, Stuttgart,*

advisor: Prof. Dr. B. Lotsch) performed the elemental analysis and ICP measurements. All authors revised the manuscript.

### **A hydrazone-based covalent organic framework for photocatalytic hydrogen production**

L. Stegbauer, K. Schwinghammer, B. V. Lotsch

*Chem. Sci.* **2014**, *5*, 2789–2793.

L. Stegbauer (University of Munich, advisor: Prof. Dr. B. Lotsch) synthesized and characterized all the necessary materials, screened the literature, wrote the majority of the manuscript, edited the images, interpreted/commissioned the analytical data. This work also appeared in his PhD thesis. K. Schwinghammer (Max Planck Institute for Solid State Research, Stuttgart, advisor: Prof. Dr. B. Lotsch) conducted and interpreted the photocatalytic measurements and the photocatalysis section. Dr. S. Hug (University of Munich, advisor: Prof. Dr. B. Lotsch) carried out the sorption measurements, C. Stefani (Max Planck Institute for Solid State Research, Stuttgart, advisor: Prof. Dr. R. Dinnebier) performed powder diffraction measurements and V. Duppel (Max Planck Institute for Solid State Research, Stuttgart, advisor: Prof. Dr. B. Lotsch) conducted TEM measurements. D. Weber (Max Planck Institute for Solid State Research, Stuttgart, advisor: Prof. Dr. B. Lotsch) supported this work. Solid-state NMR measurements were performed by C. Minke (University of Munich, advisor: Prof. Dr. W. Schnick) and M.-L. Schreiber (Max Planck Institute for Solid State Research, Stuttgart, advisor: Prof. Dr. B. Lotsch) carried out part of the syntheses. C. Hohmann (NIM) designed the table of content graphic. All authors revised the manuscript.

### **Phenyl-triazine oligomers for light-driven hydrogen evolution**

K. Schwinghammer, S. Hug, M. B. Mesch, J. Senker, B. V. Lotsch

*Energy Environ. Sci.* **2015**, *8*, 3345–3353.

Dr. S. Hug (University of Munich, advisor: Prof. Dr. B. Lotsch) and K. Schwinghammer (Max Planck Institute for Solid State Research, Stuttgart, advisor: Prof. Dr. B. Lotsch) are equally contributing authors for this manuscript, since both of the authors performed literature screening, interpretation of the analytical data, commissioned the analysis, synthesized the materials (except for “the trimer” which has been synthesized by Dr. V. Vjas (Max Planck Institute for Solid State Research, Stuttgart, advisor: Prof. Dr. B. Lotsch)), and wrote the most part. Therefore, part of this manuscript is published in Dr. S. Hug’s PhD thesis. Dr. S. Hug was further in charge of the sorption measurements and interpretation, which were performed in Munich. The photocatalytic experiments were conducted exclusively by K. Schwinghammer who also did the image editing. M. B. Mesch (University of Bayreuth, Bayreuth, advisor: Prof. Dr. J. Senker) and C. Minke (University of Munich, Munich; advisor: Prof. Dr. W. Schnick) performed the solid-state NMR measurements which will appear in M. B. Mesch’s PhD thesis. C. Stefani (Max Planck Institute for Solid State Research, Stuttgart, advisor: Prof. Dr. R. Dinnebier) performed the powder diffraction measurements, V. Duppel (Max Planck Institute for Solid State Research, Stuttgart, advisor: Prof. Dr. B. Lotsch) the TEM measurements, C. Sondermann (Max Planck Institute for Solid State Research, Stuttgart, advisor: Prof. Dr. B. Lotsch) the

MALDI-TOF measurements, Dr. M. Konuma (Max Planck Institute for Solid State Research, Stuttgart, advisor: Prof. Dr. U. Starke) the XPS measurements, and M.-L. Schreiber (Max Planck Institute for Solid State Research, Stuttgart, advisor: Prof. Dr. B. Lotsch) the elemental and ICP analyses. Dr. V. W. Lau, F. Haase (Max Planck Institute for Solid State Research, Stuttgart, advisor: Prof. Dr. B. Lotsch) and L. Stegbauer (University of Munich, Munich, advisor: Prof. Dr. B. Lotsch) contributed through helpful discussion. All authors revised the manuscript. R. Noack (Max Planck Institute for Solid State Research, graphics service) helped designing the table of content.

## **Publications published as not part of this thesis**

### **Towards rational photocatalyst design: Structure-property-activity relationships in graphitic carbon nitrides**

V. W. Lau, K. Schwinghammer, B. V. Lotsch

*to be submitted.*

### **Laser ablation of molecular carbon nitride compounds**

D. Fischer, K. Schwinghammer, C. Sondermann, V. W. Lau, J. Mannhart, B. V. Lotsch

*Appl. Surf. Sci.* **2015**, *349*, 353–360.

### **Lithium charge storage mechanisms of cross-linked triazine networks and their porous carbon derivatives**

K. See, S. Hug, K. Schwinghammer, M. Lumley, Y. Zheng, J. Nolt, G. Stucky, F. Wudl, B. V. Lotsch, R. Seshadri

*Chem. Mater.* **2015**, *27*, 3821–3829.

## **Publications published prior to this thesis**

### **Towards mesostructured zinc imidazolate frameworks**

S. C. Junggeburth, K. Schwinghammer, K. S. Viridi, C. Scheu, B. V. Lotsch

*Chem. Eur. J.* **2012**, *18*, 2143–2152.

## 7.4 Contributions to conferences

*Triazine-based systems for solar energy to hydrogen fuel conversion* (poster presentation)

K. Schwinghammer, S. Hug, B. V. Lotsch

Workshop on polymer photocatalysts for solar fuels synthesis, **2016**.

*Triazine-based frameworks for visible-driven hydrogen evolution* (oral presentation and poster presentation)

K. Schwinghammer, L. Stegbauer, S. Hug, B. V. Lotsch

1<sup>st</sup> international solar fuels conference (ISF-1 and ISF-1 Young), Uppsala (Sweden), **2015**.  
Travel award from CeNS.

*Triazine-based carbon nitrides for improved visible-light hydrogen evolution* (poster presentation)

K. Schwinghammer, B. Tuffy, M. B. Mesch, E. Wirnhier, C. Martineau, F. Taulelle, W. Schnick, J. Senker, V. Duppel, C. Ziegler, B. V. Lotsch

IPS-20: 20<sup>th</sup> international conference on photochemical conversion and storage of solar energy, Berlin (Germany), **2014**.

*Functional frameworks as scaffolds for solar energy conversion* (poster presentation)

L. Stegbauer, K. Schwinghammer, B. Tuff, B. V. Lotsch

Young ideas in nanoscience, NIM workshop, Munich (Germany), **2013**.

*Triazine-based carbon nitrides for light-driven hydrogen evolution* (oral and poster presentation)

K. Schwinghammer, B. V. Lotsch

Forum on materials for sustainable energy, Cambridge (USA), **2013** (together with the Faculty of Material Science of the Massachusetts Institute of Technology).

*Triazine-based carbon nitrides for light-driven hydrogen production* (oral presentation with presentation prize)

K. Schwinghammer, B. V. Lotsch

Joint workshop on materials chemistry, Max Planck Institute for Solid State Research, Stuttgart (Germany), **2012**.

*Photocatalysis on triazine-based carbon nitrides* (poster presentation)

K. Schwinghammer, B. Tuffy, M. B. Mesch, E. Wirnhier, C. Martineau, F. Taulelle, W. Schnick, J. Senker, B. V. Lotsch

CeNS Workshop, Nanosciences: From molecular systems to functional materials, Venice International University (VIU), San Servolo (Italy), **2011**.

## 7.5 List of abbreviations

1D	one-dimension
2D	two-dimensional
3D	three-dimensional
4AP	4-amino-2,6-dihydroxypyrimidine
Å	Ångström
AFM	atomic force microscopy
aPTI	amorphous PTI
AM	air mass ( <i>e.g.</i> AM1.5 filter)
Anal.	Analytical
a.u.	arbitrary units
AQE	apparent quantum efficiency
ATR	attenuated total reflection
BA	barbituric acid
BET	Brunauer–Emmett–Teller
C	cyanamide
calcd.	calculated
CCD	charge coupled device
CCDC	Cambridge Crystallographic Data Centre
CN	carbon nitride
COF	covalent organic framework
CP	cross polarization
CPPI	cross polarization with polarization inversion
CTF	covalent triazine framework
CVD	chemical vapor deposition
CW	continuous wave
D	dicyandiamide



DCM	dichlormethane
DFT	density functional theory
EA	elemental analysis
EDX	energy dispersive X-ray spectroscopy
eV	electron volt
DB	1,4-dicyanobenzene
DETH	2,5-diethoxy-terephthalohydrazide
DLS	dynamic light scattering
EDTA	ethylenediaminetetraacetic acid
eq	equivalent
FB	flip-back
FID	flame ionization detector
FT	Fourier transformed
FWHM	full width half maximum
<i>g</i> -C <sub>3</sub> N <sub>4</sub>	graphitic carbon nitride
G/L	Gaussian/Lorentzian
HER	hydrogen evolution reaction/ rate
HOMO	highest occupied molecule orbital
HP-HT	high pressure high temperature
ICP-AES	inductively coupled plasma – atomic emission spectroscopy
IP	isoelectrical point
IR	infrared
JEMS	Journal of the European Mathematical Society
M	melamine
MALDI-TOF	Matrix Assisted Laser Desorption Ionization – Time of Flight
MAS	magic angle spinning
MeOH	methanol
MD	molecular dynamics

MS	Material Studio
msp	mesoporous
NIR	near infrared
NLDFT	non-local density functional theory
NMR	nuclear magnetic resonance
NOESY	Nuclear Overhauser effect spectroscopy
PHI	poly(heptazine imide)
ppm	parts per million
PRC	proton reduction catalyst
PSD	pore size distribution
PTFE	polytetrafluorethene
PTI/XY	poly(triazine imide) with XY intercalation
PTO	phenyl-triazine oligomer
PVD	physical vapor deposition
PXRD	powder X-ray diffraction
RAMP	ramped amplitude
ref.	reference
RF	radio frequency
SA	surface area
SAED	selected area electron diffraction
SBU	secondary building units
SEM	scanning electron microscopy
ss	solid-state
TEM	transmission electron microscope
TEoA	triethanolamine
TFPT	1,3,5-tris-(4-formyl-phenyl)triazine
THF	tetrahydrofuran
TMS	tetramethylsilane

U	urea
UV	ultra violet
Vis	visible
<i>vs</i>	<i>versus</i>
XPS	X-ray photoelectron spectroscopy
(P)XRD	(powder) X-ray diffraction